



**HAL**  
open science

# Structural and optical characterization of green-yellow light emitting devices with high indium concentrated (In,Ga)N quantum wells

Sakhawat Hussain

► **To cite this version:**

Sakhawat Hussain. Structural and optical characterization of green-yellow light emitting devices with high indium concentrated (In,Ga)N quantum wells. Physics [physics]. Université Nice Sophia Antipolis, 2014. English. NNT: . tel-01097095

**HAL Id: tel-01097095**

**<https://theses.hal.science/tel-01097095>**

Submitted on 18 Dec 2014

**HAL** is a multi-disciplinary open access archive for the deposit and dissemination of scientific research documents, whether they are published or not. The documents may come from teaching and research institutions in France or abroad, or from public or private research centers.

L'archive ouverte pluridisciplinaire **HAL**, est destinée au dépôt et à la diffusion de documents scientifiques de niveau recherche, publiés ou non, émanant des établissements d'enseignement et de recherche français ou étrangers, des laboratoires publics ou privés.

UNIVERSITE DE NICE-SOPHIA ANTIPOLIS –UFR Sciences  
Ecole Doctorale de Sciences Fondamentales et Appliquées

T H E S E

pour obtenir le titre de

**Docteur en Sciences**

de l'UNIVERSITE de Nice-Sophia Antipolis

Discipline: Physique

présentée et soutenue par

**Sakhawat Hussain**

Propriétés optiques et structurales de dispositifs luminescents contenant des puits  
quantiques (In,Ga)N à forte concentration en indium et émettant dans le vert et le jaune

Structural and optical characterization of green-yellow light emitting devices with high  
indium concentrated (In,Ga)N quantum wells

Thèse dirigée par Philippe Vennéguès  
et co-dirigée par Benjamin Damilano  
soutenue le 12. 12. 2014

**Jury**

G. Feuillet	Directeur de recherche, CEA, Grenoble	Président
C. Bougerol	Directeur de recherche, Grenoble	Rapporteur
R. Martin	Professeur, Université de Strathclyde	Rapporteur
N. Cherkashin	Chargé de recherche, CNRS, Toulouse	Examineur
A. Dussaigne	Ingénieur-chercheur, Grenoble	Examineur
B. Damilano	Chargé de recherche, CNRS, Valbonne	Co-directeur de thèse
P. Vennéguès	Ingénieur de recherche, CNRS, Valbonne	Directeur de thèse

Centre de Recherche sur l'Hétéro-Epitaxie et ses Applications, CNRS, Valbonne



## Acknowledgements

This work has been carried out at the Center de Recherche sur l'Hetero Epitaxie et ses Applications (CRHEA), Valbonne, Sophia Antipolis, France. I have received enormous assistances and guidance from many people of this lab. I would like to convey my sincere gratitude to all of them for their kind support and concern.

I would like to extend my gratitude to Catherine Bougerol, Robert Martin, Guy Feuillet, Amélie Dussaigne and Nikolay Cherkashin for accepting to be the members of the jury board of my Ph.D. thesis. My special thanks are to Catherine Bougerol and Robert Martin, members of jury board, for agreeing to be the reporters of this work.

My sincere thanks and gratitude are to my supervisor Philippe Vennéguès for accepting me as a PhD student and for his constant guidance, motivation to do this research work. I am grateful to him to teach me how to prepare and analyze the TEM samples using various TEM techniques.

I am also grateful to my co-supervisor Benjamin Damilano for his help, support and cooperation to complete my thesis work. I am indebted to my supervisors for their endless guidance and encouragement to overcome all my difficulties during this work. I really appreciate the way they have shown their generosity and patience towards me to answer all my queries as well as to correct the manuscript.

I am thankful to Jean Yves Duboz, Director of the Laboratory, Philippe Vennéguès and Benjamin Damilano for their help to get the extension of Erasmus Mundus Mobility with Asia (EMMA) scholarship, without which it would not have been possible to complete my Ph.D. research work.

My special thanks are to Benjamin Damilano, Hyonju Kim-Chauveau, Kaddour Lekhal and Philippe de Mierry for the samples and helping me in collecting and interpreting data. I am thankful to Olivier Tottereau and Maud Nemoz for their support and cooperation especially for helping me to get familiarized with the AFM and XRD and to make me understand different aspects of the analysis. I am grateful to Thomas Neisius, who helped me to use the STEM and get valuable data of the samples. I also like to convey my special thanks to Boris Poulet for his suggestions and effort which helped me to prepare the TEM samples fast.

I also thank Borge Vinter, Mathieu Leroux and Jean Michel Chauveau for explaining the various aspects of semiconductor physics to me. I am grateful to the organizers of E-MRS spring conference-2013, the Ganex summer school-2013 and to my laboratory for organizing many seminars in nitride semiconductor.

My special thanks to all my Ph.D. laboratory mates and also to Virginie Brändli, Eric Drezet, Denis Lefebvre and Meletios Mexis for their support. I thank Isabelle Cerutti, Michèle Pefferkorn and Anne-Marie Galliana of my laboratory for their administrative support.

The coordinators of EMMA program, Francine Diener and Marc Diener and the entire EMMA team have been a constant support during my stay in France. I am thankful to them all.

I would like to thank Ezio Maggiora, Residence Manager, for his assistance and also to the Conseil Général Alpes-Maritimes for their transport support, which allows me to live in and enjoy the natural beauty and gorgeous lifestyle of the city Nice, France. Finally I thank my family and friends, especially my parents for their endless encouragement and support during my study in France.

## Abbreviations

3DAP	three dimensional atomic probe microscopy
ADF	annular dark field
AFM	atomic force microscopy
BF	bright field
BFP (bfp)	back focal plane
CB	conduction band
CL	cathodoluminescence
cs-TEM	cross sectional transmission electron microscopy
DF	dark field
DP	diffraction pattern
EDX	energy dispersive X-ray
EELS	electron energy loss spectroscopy
eV (unit)	electron volt
FWHM	full width half maximum
GPA	geometric phase analysis
HAADF	high angle annular dark field
HRSTEM	high resolution scanning transmission electron microscopy
HRTEM	high resolution transmission electron microscopy
LED	light emitting diode
LR	laser reflectometry
M/QW	multi /quantum well
MB	multi beam
MBE	molecular beam epitaxy
MD	misfit dislocation
ML	monolayer
MOCVD	metal organic chemical vapor deposition
mrad (unit)	mili radian
nm	nano meter
PM	projection method
Ppz	Polarization piezo-electric
Psp	Polarization spontaneous
QCSE	quantum confined Stark effect
RF	radio frequency
RMS	root mean square
RSM	reciprocal space map
RT-PL	room temperature photoluminescence
SBDF	strong beam dark field
SCCM (sccm)	standard cubic centimeter per minute
SF	stacking fault
SLM (slm)	standard liter per minute

STEM	scanning transmission electron microscopy
TD	threading dislocation
TDD	threading dislocation density
TEG	triethylgallium
TEM	transmission electron microscopy
TMA	trimethylaluminium
TMG	trimethylgallium
TMI	trimethylindium
VB	valence band
WBDF	weak beam dark field
XRD	x-ray diffraction
ZA	zone axis

## Résumé

Les hétérostructures InGaN/GaN sont étudiées pour la réalisation de diodes électroluminescentes émettant dans le vert et le jaune avec une forte luminosité et une bonne efficacité. Ceci requière la fabrication de puits quantiques InGaN de haute qualité, ayant une composition élevée en Indium ( $> 15\%$ ) et une largeur raisonnable, de l'ordre de 2 à 4 nm. Cependant, la réalisation de ce type de structure est extrêmement problématique en raison des écarts importants entre les températures de croissance de l'InGaN (700 à 800 °C) et du GaN (900 à 1100 °C). Cette différence de température induit notamment les défauts structuraux suivants : variation d'épaisseur, défauts ponctuels et agrégats d'Indium dans les puits quantiques. De plus, l'incorporation d'Indium en grande quantité dans la couche d'InGaN a pour effet d'augmenter la différence de paramètre de maille entre la couche d'InGaN et la couche de GaN sous-jacente. De ce fait, une contrainte compressive importante apparaît dans la couche d'InGaN. La relaxation de cette contrainte entraîne alors la génération de défauts supplémentaires.

Pour la présente thèse, les hétérostructures InGaN/GaN sont épitaxiées sur des substrats de saphir (plan c) par épitaxie en phase vapeur aux organométalliques. Chaque échantillon comporte un minimum de 10 puits quantiques  $\text{In}_x\text{Ga}_{1-x}\text{N}/(\text{Al})\text{GaN}$  en vue d'obtenir une forte luminosité dans la gamme de longueurs d'onde couverte par le vert et le jaune. Plusieurs approches ont été explorées dans le but d'étudier les propriétés structurales des échantillons, tels que des puits quantiques fins ( $< 3.0\text{ nm}$ ) à forte concentration en indium ( $\geq 20\%$ ) ou encore des puits quantiques épais ( $> 3.0\text{ nm}$ ) à faible concentration en Indium ( $\leq 20\%$ ). De plus, l'influence de la présence d'une couche d'encapsulation déposée au-dessus des puits quantiques a également été étudiée. Pour cela, la microscopie électronique en transmission (MET) a principalement été utilisée, combinée à d'autres techniques de caractérisation telles que la microscopie à force atomique, la diffraction des rayons X, et la photoluminescence à température ambiante.

Les échantillons étudiés peuvent être regroupés en 3 séries. La première série d'échantillons a pour objet d'identifier l'influence de l'épaisseur et de la composition des puits quantiques dans des structures conçues pour émettre à la longueur d'onde correspondant à la couleur jaune (570 nm). Pour ce faire, la température de croissance et le temps de déposition utilisés pour la croissance des puits d'InGaN ont été modulés. En revanche, la seconde série d'échantillons vise à étudier l'influence de la couche de protection déposée au-dessus des puits quantiques pour des structures conçues pour émettre à la longueur d'onde du vert (540 nm). Contrairement à la série précédente, tous les puits quantiques de cette série sont déposés à la même température (740 °C) pendant un temps de déposition identique (4 minutes). Cependant, une fine couche d'encapsulation (maximum 1.5 nm) en AlGaIn a également été déposée au-dessus des puits

avec des paramètres de croissance variant d'un échantillon à l'autre. En comparant les différents échantillons à l'intérieur de cette série, nous avons tenté de séparer l'influence de chaque paramètre utilisé pour la croissance de l'AlGaIn. Enfin, dans la dernière série d'échantillon, nous avons exploré un procédé d'encapsulation des structures par le GaN à basse température. Nous avons ensuite étudié l'effet de ce procédé sur la structure étudiée en comparaison avec l'encapsulation par une couche d'AlGaIn.

Les épaisseurs moyennes des couches contenues dans les échantillons ainsi que la composition des puits quantiques ont été déterminées après traitement numérique des franges du réseau cristallin obtenues sur des images MET en section transverse. De manière systématique, des images en section transverse de taille relativement grande ont été utilisées. Ceci permet d'améliorer la statistique des données recueillies par MET et d'obtenir une meilleure corrélation de ces données avec celles recueillies par photoluminescence.

Les épaisseurs moyennes des couches sont déterminées en axe de zone  $\langle 14-50 \rangle$  en le mode multi-faisceaux. Celui-ci permet d'obtenir des images MET haute résolution où peuvent se distinguer les différents plans (0002) qui composent la couche. De plus, ces images font apparaître un contraste entre les couches des différents matériaux contenues dans la structure, ce qui permet de les différencier. Ainsi, il est possible de déterminer l'épaisseur de chaque couche à la monocouche près (1 monocouche de GaN a une épaisseur de 0.259 nm). La distribution des épaisseurs déterminées pour une couche donnée est approchée par une fonction gaussienne. De cette façon, l'épaisseur moyenne est déterminée, ainsi que la largeur à mi-hauteur des pics pour chaque échantillon.

L'analyse des distributions des épaisseurs a mis en évidence qu'en l'absence d'encapsulation des puits quantiques, une ondulation apparaît à l'interface entre le puits quantique d'InGaIn et la barrière GaN supérieure, ce qui n'est pas désirable. Cette observation est confirmée par la largeur à mi-hauteur de la distribution des épaisseurs qui est plus importante sur les échantillons sans couche d'encapsulation ( $\geq 1$  nm). De plus, les analyses menées sur la deuxième série d'échantillons montrent que, quelle que soit la température de croissance de la couche d'encapsulation, cette dernière permet d'éviter l'ondulation des puits quantiques InGaIn. D'autre part, lorsque l'AlGaIn est déposée à la température de l'InGaIn, l'encapsulation limite de manière efficace l'évaporation et/ou la diffusion d'Indium à partir des puits quantiques InGaIn. Par conséquent, la croissance de puits quantiques plus épais peut être réalisée de façon à obtenir une émission à des longueurs d'ondes plus élevées. L'analyse de la troisième série d'échantillons a mis en évidence que l'AlGaIn comme le GaN déposé à basse température peuvent être utilisés comme couche d'encapsulation afin d'éviter l'ondulation des puits quantiques. Cependant, la couche d'AlGaIn permet d'obtenir les longueurs d'onde les plus élevées en émission du fait de l'effet Stark confiné quantique.

La composition des couches est déterminée par une observation MET haute résolution en coupe dans les conditions 2 ondes hors axe. La méthode d'analyse de la phase géométrique est utilisée pour l'interprétation des images MET. Cependant, cette méthode est relativement limitée pour la détermination des déformations à l'interface entre différentes couches. Afin d'éviter toute ambiguïté due à l'utilisation de cette méthode, la déformation moyenne de la couche d'InGaN par rapport à la couche de GaN a été systématiquement déterminée au centre des couches. Néanmoins, afin de relier la déformation des couches à leur composition, il est nécessaire de connaître de façon précise l'état de déformation de l'échantillon MET. En effet, l'état de contrainte dépend de l'épaisseur de l'échantillon dans la direction du faisceau électronique. Ainsi, selon que l'état de contrainte soit bi-axial, uni-axial ou intermédiaire, la détermination de la composition conduira, pour une même valeur de la déformation, à des valeurs de composition différentes. Afin d'éliminer toute incertitude liée à l'état de contrainte, plusieurs régions d'un même puits quantique ont été sondées de façon à vérifier que la déformation ne varie pas significativement. D'après ces observations, l'état de contrainte des échantillons est exclusivement bi-axial. Les compositions des puits ont donc été déterminées par la méthode correspondant à cet état de contrainte. De plus, nous avons simulé et comparé les valeurs moyennes d'épaisseur et de composition obtenues par analyse MET et par diffraction des rayons X sur la raie (0002) de façon à confirmer la pertinence de notre approche.

D'après les analyses MET, nous avons obtenu la confirmation que les paramètres de croissance utilisés pour la couche d'encapsulation n'ont d'impact que sur l'épaisseur du puits, et non sur la composition déterminée au centre de celui-ci. Cette approche nous a également permis d'observer une éventuelle variation de la composition entre différents puits quantiques d'une même structure.

L'analyse des propriétés structurales des échantillons a permis d'observer des défauts tels que des dislocations coin supplémentaires et des défauts en forme de V générés dans les puits quantiques de certains échantillons. L'origine et l'impact de ces défauts ont été étudiés. Les observations ont montré que seuls les échantillons contenant des puits InGaN/GaN avec une fraction élevée d'Indium ( $\geq 18\%$ ) et une épaisseur importante ( $\geq 3.5$  nm) contiennent des dislocations traversantes de type  $\langle a \rangle$  additionnelles générés au niveau des puits quantiques. Ces dislocations participent à la formation de défauts de type V au sein de la structure. D'après nos observations, ces dislocations ne sont pas créées à partir de fautes d'empilement ou à partir d'interfaces, mais pourraient être générées lorsque des défauts de type V atteignent l'interface entre deux couches.

Nous avons observé que de telles dislocations apparaissent sous la forme d'agrégats et qu'elles ne sont pas systématiquement générées à partir de dislocations traversantes déjà existantes. Au contraire, elles ne se forment qu'à partir de certaines régions des puits quantiques. Ainsi,

nous proposons l'hypothèse selon laquelle l'origine de ces dislocations réside dans la formation d'agrégats d'Indium et/ou de défauts ponctuels au sein du puits quantique d'InGaN. Nous avons cherché une validation qualitative de cette hypothèse à partir d'images en champ sombre annulaire aux grands angles prises au niveau ou à proximité de ces défauts. Cependant, nous n'avons pu obtenir de preuve suffisamment convaincante de la présence d'agrégats d'indium dans nos structures. Il est possible que ces agrégats soient de tailles trop petites (nanométriques ou inférieur au nanomètre) pour être détectés par cette méthode.

La cartographie de l'espace réciproque par diffraction des rayons X sur les échantillons a permis de conclure que la présence de tels défauts ne permet pas de relaxer significativement la contrainte des couches épitaxiées. En effet, le taux de relaxation déterminé pour ces structures est faible, de l'ordre de 0.02 à 0.03 %. Par conséquent, la force motrice de la formation de ces dislocations ne peut pas être la relaxation de la contrainte due aux différences de paramètres de maille. Cependant, ces défauts se sont avérés néfastes pour l'efficacité de la photoluminescence des puits quantiques InGaN/GaN mesurée à température ambiante.

Une diminution de la densité de dislocations a été observée lorsque la température de croissance de l'InGaN est augmentée. Cela a pour conséquence la réduction de la composition en Indium dans le puits qui émet ainsi à une longueur d'onde plus courte. Une solution afin de compenser cet effet indésirable consisterait à épaissir le puits. Cependant, ceci n'est pas une solution idéale car la force de l'oscillateur est réduite lorsque l'épaisseur du puits augmente, du fait de l'effet Stark confiné quantique. Il a également été observé que l'encapsulation de l'InGaN par une couche d'AlGaN avec un taux d'Aluminium relativement élevé (environ 10 %) et épais (environ 3 nm) augmente le champ électrique interne dans la région du puits. Par conséquent, l'émission à des longueurs d'onde plus longues est favorisée mais l'efficacité quantique interne s'en trouve diminuée, à cause de l'effet Stark confiné quantique. En revanche, l'évolution de l'efficacité de la photoluminescence de puits InGaN encapsulés par une couche d'AlGaN en fonction de sa composition et de son épaisseur est moins évidente. Ainsi, l'optimisation de l'efficacité de la photoluminescence mesurée à température ambiante passe par un compromis entre ces différents paramètres : la qualité cristalline de l'InGaN (la température de croissance), l'épaisseur des puits, la composition de l'AlGaN, son épaisseur et ses conditions de croissance.

En conclusion, ce travail de thèse démontre qu'il n'existe pas de solution idéale permettant de concevoir des puits quantiques efficaces émettant dans les longueurs d'onde couvertes par le jaune et le vert. Ceci provient du fait que les différents paramètres régissant l'efficacité quantique interne interagissent négativement entre eux. Cependant, grâce au travail réalisé, des pistes d'améliorations ont été identifiées afin de parvenir à un compromis entre ces différents paramètres.

## Table of contents

<b>Acknowledgements .....</b>	<b>i</b>
<b>Abbreviations .....</b>	<b>iii</b>
<b>Résumé.....</b>	<b>v</b>
<b>Introduction.....</b>	<b>1</b>
<b>Introduction (French).....</b>	<b>7</b>
<b>Chapter 1 .....</b>	<b>15</b>
Fundamentals of nitride semiconductors.....	15
Introduction .....	15
1.1 Structural properties .....	15
1.1.1 Wurtzite structure .....	15
1.1.2 Relation between lattice constant and band gap energy.....	19
1.2 Dislocation basics .....	20
1.2.1 Slip plane system in wurtzite crystal structure.....	21
1.2.2 Dislocation types.....	22
1.3 Misfit in group III-nitride hetero-structures.....	23
1.3.1 Crystal deformation: bi-axial and uni-axial case.....	24
1.4 Spontaneous and piezoelectric polarization.....	29
1.4.1 Effects of polarization on (In,Ga)N/GaN heterostructure .....	31
1.4.1.1 Electric field in InGaN/GaN quantum wells.....	31
1.4.1.2 Effect of electric field on the InGaN quantum well transition energies .....	34
1.4.1.3 Impact of electric field on the radiative efficiency of InGaN/GaN QWs .....	35
1.5 Growth processes of LED structure.....	36
1.5.1 Metal-organic chemical vapor deposition (MOCVD) technique .....	37
1.5.2 The light emitting diode (LED) structure for light converter .....	38
Summary .....	39
<b>Chapter 2 .....</b>	<b>43</b>
Basic characteristics of InGaN/GaN hetero-structures.....	43

Introduction .....	43
2.1 Phase diagram: phase separation of indium.....	44
2.2 Relaxation processes in InGaN/GaN system.....	47
2.2.1 Relaxation process through glide of dislocation.....	47
2.2.1.1 Matthews and Blakeslee model .....	48
2.2.1.2 Energy balance model .....	50
2.2.1.3 Critical thickness .....	51
2.2.1.4 Limitations of Matthews-Blakeslee and energy balance model .....	53
2.2.2 Relaxation process through generation of V defects .....	54
2.2.2.1 Shape and size of the V-defects .....	56
2.2.3 Other relaxation processes observed in wurtzite crystal structure .....	58
2.3 Quantum well thickness variation .....	58
2.4 LED performance due to these basic characteristics.....	60
Summary .....	63
<b>Chapter 3 .....</b>	<b>67</b>
Different characterization techniques.....	67
Introduction .....	67
3.1 High resolution scanning /transmission electron microscopy (HR-S/TEM).....	68
3.1.1 Principle of HRTEM: scattering and diffraction .....	69
3.1.2 Basic operational modes in TEM: Diffraction and image modes.....	73
3.1.2.1 Different imaging techniques: bright field (BF) and dark field (DF) imaging ..	75
3.1.2.2 Dark field image techniques: strong beam dark field (SBDF) and weak beam dark field (WBDF).....	77
3.1.3 Scanning transmission electron microscopy (STEM) .....	78
3.1.4 High angle annular dark field (HAADF) imaging .....	81
3.2 Determination of structural properties through HRTEM imaging techniques .....	82
3.2.1 Layer thickness measurement procedure .....	83
3.2.2 Indium composition determination within the InGaN layers.....	86
3.2.2.1 Off-axis two beam conditions in TEM .....	89
3.2.2.2 The geometrical phase analysis (GPA) method.....	90

3.2.3	Dislocation analysis through TEM.....	93
3.2.3.1	Extinction principle of dislocation contrast.....	94
3.3	X-ray diffraction.....	97
3.3.1	Working principle of XRD.....	97
3.3.2	X-ray diffraction analysis of multilayer epitaxy .....	99
3.3.2.1	The $\omega$ - $2\theta$ scan.....	99
3.3.2.2	Reciprocal space map (RSM) .....	103
3.4	Room temperature photoluminescence.....	104
3.4.1	Experimental setup and measurement .....	105
3.5	Atomic force microscope .....	107
	Summary .....	110
<b>Chapter 4</b>	<b>.....</b>	<b>113</b>
	Study of the impact of capping processes for InGaN quantum wells .....	113
	Introduction .....	113
4.1	The growth process of the samples in MOCVD reactor.....	114
4.2	Study of InGaN/GaN structure without any capping layers (sample 1 and 2).....	116
4.2.1	The growth processes of sample 1 and 2 .....	116
4.2.2	Structural and optical properties of the first sample series (sample 1 and 2) .....	117
4.2.2.1	AFM analysis .....	117
4.2.2.2	TEM and XRD analysis.....	118
4.2.2.2.1	Dislocation analysis of samples 1 and 2.....	120
4.2.2.2.2	Room temperature photoluminescence (RT-PL) analysis .....	122
4.3	Study of InGaN/GaN structure with AlGaN capping layer (sample A to D) .....	123
4.3.1	Growth process of samples A to D.....	124
4.3.2	Structural and optical properties of the second sample series (samples A to D) .....	125
4.3.2.1	AFM analysis .....	125
4.3.2.2	TEM and XRD analysis of the sample series .....	126
4.3.2.2.1	Dislocation analysis of samples A to D.....	132
4.3.2.3	Room temperature photoluminescence (RT-PL) analysis.....	134
4.4	Comparative study of low temperature capping processes: GaN Vs AlGaN .....	135

4.4.1	The growth processes of samples X to Z.....	135
4.4.2	Structural and optical properties of the last sample series (samples X to Z) .....	136
4.4.2.1	AFM analysis .....	136
4.4.2.2	TEM and XRD analysis.....	137
4.4.2.2.1	Dislocation analysis of samples X to Z .....	139
4.4.2.3	Room temperature photoluminescence (RT-PL) analysis .....	141
4.5	Strain state of some samples of the studied series .....	142
4.6	Discussion .....	143
4.6.1	Strain relaxation.....	143
4.6.1.1	V-defects and additional threading dislocations.....	143
4.6.1.2	Inclined threading dislocation .....	145
4.6.2	Indium clustering .....	149
4.6.3	QW thickness increment.....	150
4.6.4	QW thickness variation .....	152
4.6.5	Impact of AlGaIn capping layer deposition .....	153
	Summary .....	153
	<b>Conclusion and perspective .....</b>	<b>157</b>
	<b>Conclusion et perspective .....</b>	<b>161</b>
	<b>Appendix .....</b>	<b>165</b>

## Introduction

In mid-90's, the first commercialization of white light emitting diode (LED) fabricated from the blue LED chips combined with yellow phosphors-cerium doped yttrium aluminium garnet (YAG) draws the attention of many researchers and scientists for the improvement of such novel devices<sup>1,2</sup>. Since then huge progress has been made in terms of efficiencies and recently record efficiencies of exceeding 200 lm/W are reported from such devices<sup>3,4</sup>. Figure 1 schematically shows the structure of such a white light emitting diode and its light generation process in forward bias. However, phosphor-converted white LED suffers from some intrinsic problems such as color instability with time and temperature, the additional process of phosphors on top of blue LED chips complicate the LED manufacturing process, which in turn increases the production complexities and cost of such devices.<sup>5</sup>

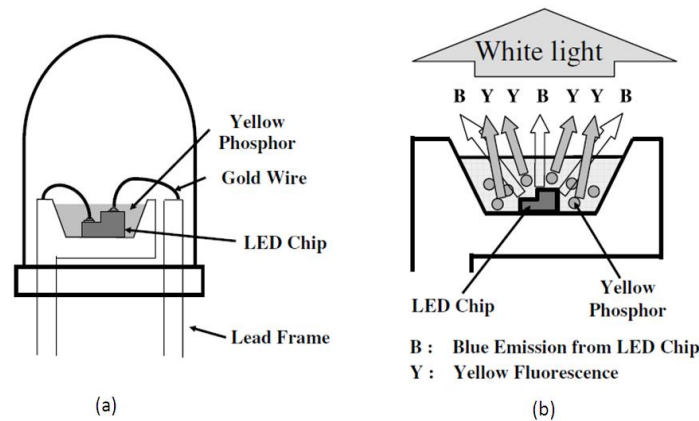


Figure 1: (a) The schematic diagram of a white light emitting diode and (b) the generation process of white light where the chip acts as a blue light source and the yellow phosphor as a light converter.<sup>3</sup>

To avoid the YAG phosphors covering process, wafer bonding of a blue (Al,Ga,In)N LED to a red (Al,Ga,In)P LED has been proposed to have the white light<sup>6</sup>. It has been also proposed to have CdSe/ZnS quantum dots (QDs) or (Al,Ga,In)P layers as semiconductor light converters to replace the YAG phosphor covering process for white LEDs<sup>7,8,9,10</sup>. But these approaches consist of adding foreign materials to the (Al, Ga, In)N material blue LED system, which complicates the overall white LED growth processes anyway.

Thus some research groups are working to realize “monolithic” or “phosphor free” white LEDs to overcome these difficulties<sup>11,12,13,14,15,16,17,18,19,20,21,22,23,24,25</sup>. Group III- nitride semiconductors play an important role in realizing such devices as their emission capability is also in the visible spectrum range<sup>26</sup>. The basic idea of such an approach is either to mix two or more color light emitting quantum wells (QWs) inside a p-n junction of an LED structure<sup>11-19</sup> or to construct a blue-violet LED as pump source on top of a light converter emitting at higher wavelength

(green-yellow) to get the white light<sup>20-25</sup>. Both these approaches have been demonstrated in our lab. For example, in 2001, the first monolithic white light emitting diode (WLED) was demonstrated by mixing the blue and the yellow quantum wells inside a p-n junction<sup>11</sup> and in 2006, the concept of pump-converter structure was proposed and a patent (French patent no. 06/50842) was made for combining a blue InGaN/GaN QW LED and a light converter (typically blue to yellow) based on stacking of nitride quantum dots or quantum wells (Al,Ga,In)N for white LED. Later in 2008, a blue LED grown on top of a yellow-green light converter was demonstrated to have a monolithic white LED.<sup>20</sup> Figure 2 schematically illustrates both approaches and presents the advantage of avoiding the process complexities associated with phosphor-based white LEDs.

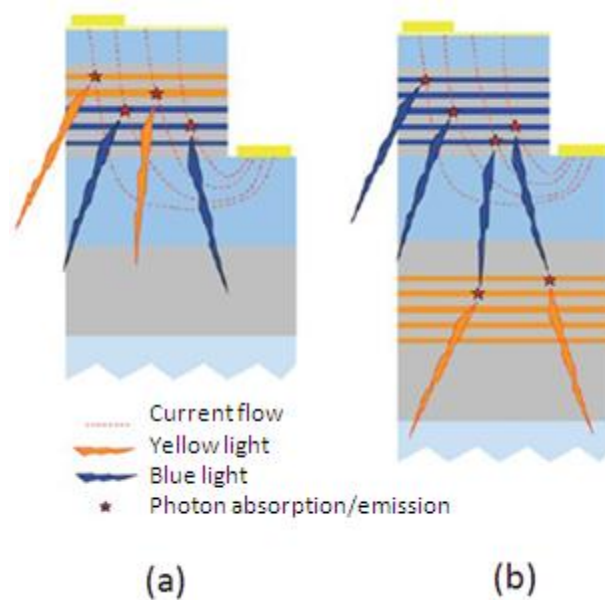


Figure 2: Schematic diagram of a (a) two different color light emitting quantum wells inside a p-n junction of a light emitting diode (LED) structure and (b) light pump-converter approach to obtain a monolithic white light emitting diode (WLED).<sup>11,20,21</sup>

However, in the first approach of monolithic white LEDs (Figure 2 (a)), crucial problems of non-uniform carrier injection among the different active QWs and ensuing strong dependence of chromaticity coordinates on the injection current level exist for the device<sup>13</sup>, whereas, in the second approach (Figure 2 (b)), such a carrier injection problem does not occur as the pump source excites the light converter optically to have a higher wavelength emission<sup>20-25</sup>. Moreover, the light converter with multiple quantum well (MQWs) structure helps to have less carrier density inside each QW of the light converter than that of current injected monolithic white LEDs, which limits the impact of efficiency droop at large operating current densities<sup>21,25</sup>.

Yet, some additional drawbacks exist with these approaches as the reported efficiencies of monolithic white LEDs are still lower than that of standard phosphor based white LEDs<sup>12,27</sup> and

it is believed that it is due to low internal quantum efficiency (IQE) of the green-yellow InGaN QWs. Thus in this work, we are going to focus on the structural and optical properties of these green-yellow InGaN QWs where they act as light converter in a monolithic white light emitting diode.

We know that the fabrication of an efficient, high brightness InGaN/GaN green-yellow light converter requires incorporating a high indium composition (>15%) within InGaN active quantum well (QW) region with reasonable well width thickness,  $L_{QW}$  (2-4 nm). But the fabrication of such high indium concentration InGaN layers by hetero-epitaxial growth processes is a very challenging task as the growth temperature of the InGaN well layer is much lower (700-800°C) than that of GaN barrier layer (900-1100°C), which induces different structural defects like QW thickness variation, point defects (vacancies, anti-sites) and Indium clustering<sup>28</sup> due to low thermal stability of InGaN alloys<sup>29,30,31</sup>. In addition, the growth of the pump LED (blue-violet) structure along with P-GaN layer for electrical contact on top of light converter may degrade the InGaN QWs inside the light converter due to high temperature<sup>32,33,34</sup>. Again, depositing high indium composition InGaN layer on GaN layer induces large compressive stress within the epilayer due to a large lattice mismatch, which can lead to additional defect formation like V-pits, misfit and threading dislocations to release the accumulated stress energy<sup>35,36,37</sup>.

These structural defects are thought to be the prime reasons for inefficient InGaN quantum wells for green-yellow light converter. Moreover, if these additional structural defects are generated while growing a green-yellow MQW structure, then they will have a detrimental impact on the performance of the pump LED, as it is grown on top of the structure, and the overall performance of the targeted monolithic white LEDs will deteriorate.

Thus the structural and optical properties of a green-yellow MQW structure are very important issues to look at for better understanding of the behavior and the performance of monolithic white LEDs.

In this work, initially we have grown 10 periods of InGaN/GaN wurtzite MQW structures by changing the growth temperature and time of the QW layers. Later several structures with at least 10 periods of InGaN/AlGaIn/GaN wurtzite MQWs are grown by metal-organic chemical vapor deposition (MOCVD) hetero-epitaxial growth process in order to achieve high brightness green, yellow-green MQW structures. In case of InGaN/AlGaIn/GaN structures, after each InGaN QW layer growth, a few monolayers of AlGaIn (less than 2 nm) are deposited as a capping layer before growing the GaN barrier layers within the structure. The deposition processes of AlGaIn as capping layers have been modified among different studied samples. The purpose of this work is to study the impact of AlGaIn capping layers and its growth processes on the structural and optical properties of such light converters. Finally, a comparative study has been made

between samples with several nm thick AlGaIn capping layers (more than 2 nm) to that of low temperature GaN capping layers on top of InGaIn QWs of a light converter structure.

In studying the structural properties, we are concerned about measuring precisely the different layer thicknesses, indium compositions within the active regions, along with identifying the different types of defects present in the grown structures. This structural information is obtained mainly from image analysis processes used in transmission electron microscopy (TEM) technique. Moreover, to confirm and verify the obtained data from TEM analysis, we conducted the X-ray diffraction (XRD) of each sample. The overall surface morphology of different samples is also observed with the help of atomic force microscopy (AFM). By analyzing this structural information of the corresponding samples, we tried to correlate them to that of their optical properties measured by room temperature photoluminescence (RTPL).

The studied results are presented in this manuscript which is organized in the following manner:

In chapter 1, we introduce the fundamental structural properties of group III-nitrides of wurtzite crystal structure. Then the slip plane systems along with different types of dislocations associated with such crystal structure are discussed. Later, the stress-strain relationship induced in the epitaxial layer and its impact on optical properties of the material is highlighted. A brief description of the metal organic chemical vapor deposition (MOCVD) technique and the studied samples structure are included.

Chapter 2 deals with the fundamental characteristics involved with InGaIn/GaN heterostructures. An overview of different characteristics such as phase separation, different relaxation processes and layer thickness variation observed with high indium composition InGaIn layers of InGaIn/ GaN system is presented. The performances of light emitting diodes (LEDs) due to these characteristics are also discussed in brief.

In chapter 3, we focus on the basics behind the experimental techniques that are used in this work. We are going to present the particular experimental methods with the goal of highlighting how and why we utilize these tools to determine the targeted properties of our studied samples. The advantage and disadvantage of these experimental procedures are also discussed in different subsections of the chapter.

In final chapter 4, we present the obtained results of our work: the importance of the deposition of AlGaIn as capping layers, the best growth process to compensate the InGaIn QW thickness variation, the indium clustering, segregation and/or evaporation due to high temperature processing involved with InGaIn/GaN LED system, and the associated optical

properties of the samples are presented in the chapter. Moreover, additional dislocations are found with very high Indium composition ( $\geq 20\%$ ) InGaN layers, so we are going to discuss the type of such additional dislocations and try to identify their origin within the InGaN layer in the chapter.

Finally, general conclusion and perspectives of this study are presented.



## Introduction (French)

Dans le milieu des années 90 ont été commercialisées les premières diodes électroluminescentes (DELs) blanches. Ces dernières sont fabriquées à partir DELs bleues combinées avec du phosphore cérium jaune dopé avec du grenat d'yttrium et d'aluminium (YAG). Dès lors, l'amélioration de tels dispositifs optiques a suscité l'engouement de la communauté scientifique<sup>1,2</sup>. Des progrès importants ont été reportés ces dernières années avec l'obtention de records d'efficacité pour ces dispositifs DELs dépassant les 200lm/W<sup>3,4</sup>. La Figure 1 montre schématiquement le fonctionnement d'une structure DEL blanche et son processus de génération de lumière en polarisation directe. Cependant les DELs dont la couleur blanche est obtenue à l'aide de phosphore souffrent de problèmes intrinsèques comme l'instabilité de la couleur au cours du temps et lorsque la température varie. Les processus permettant l'addition de phosphores sur les puces des DELs bleu ajoutent aussi des complications lors de la fabrication qui vont augmenter la complexité de production et le prix de ces dispositifs.<sup>5</sup>

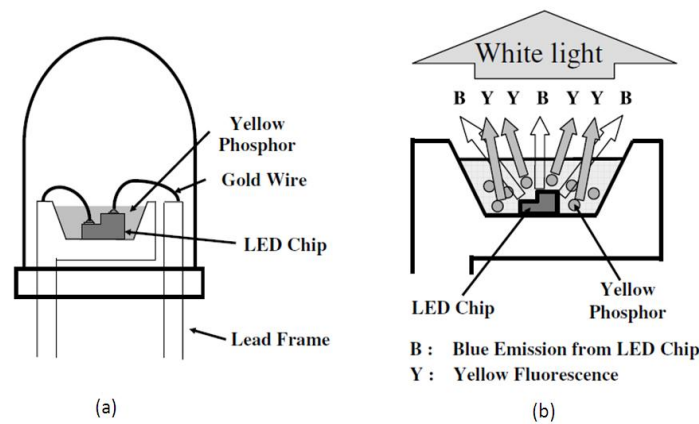


Figure 1: (a) Le schéma de principe d'une diode électroluminescente blanche et (b) le processus de génération de lumière blanche où les puces joue le rôle de source de lumière bleue et le phosphore jaune celui de convertisseur de lumière.<sup>3</sup>

Pour éviter le procédé de recouvrement par les phosphores YAG, le collage des supports des DELs bleu (Al,Ga,In)N avec des support de DELs rouge (Al,Ga,In)P a été proposé pour obtenir de la lumière blanche<sup>6</sup>. Il a aussi été proposé d'utiliser, pour l'obtention de DELs blanches, des boites quantiques (BQs) de CdSe/ZnS ou des couches de (Al,Ga,In)P comme convertisseurs de lumière à base de semi-conducteur afin de remplacer les procédés de recouvrement par phosphores YAG<sup>7,8,9,10</sup>. Mais ces approches impliquent l'addition de matériaux étrangers à la filière nitrure (Al,Ga,In)N dont sont constitués les DELs bleu. Cela complique le processus global de la croissance des DELs blanches.

En conséquence, pour dépasser ces problèmes, certains groupes de recherches concentrent leurs efforts sur la réalisation de DELs blanches dites «monolithiques» ou « sans phosphore »<sup>11,12,13,14,15,16,17,18,19,20,21,22,23,24,25</sup>. Le groupe des semi-conducteurs à base de nitrure et

d'éléments III de la classification périodique joue un rôle important dans la réalisation de ces dispositifs du fait que leur émission lumineuse se trouve aussi en partie dans la zone spectrale du visible<sup>26</sup>. L'idée sur laquelle repose cette approche est de mélanger deux ou plusieurs couleurs d'émissions lumineuses issues des puits quantiques dans la jonction p-n d'une structure DEL<sup>11-19</sup>. On peut aussi de manière complémentaire construire une DEL bleu-violet comme source de pompage optique au-dessus d'un convertisseur de lumière émettant à des longueurs d'ondes plus élevées (vert-jaune) afin d'obtenir de la lumière blanche<sup>20-25</sup>.

Ces deux méthodes ont été démontrées dans notre laboratoire. Par exemple en 2001, la première diode électroluminescente monolithique blanche a été réalisée en mélangeant à l'intérieur d'une jonction p-n des puits quantiques possédant des longueurs d'ondes d'émissions dans le bleu et dans le jaune<sup>11</sup>. Un autre exemple est en 2006, le dépôt d'un brevet (brevet Français numéro 06/50842) sur la réalisation de DELs blanches. Le concept repose sur la conversion de lumière par pompage optique afin de combiner une DEL émettant dans le bleu (puits quantiques InGaN/GaN) avec un convertisseur de lumière (typiquement du bleu au jaune) constitué de l'empilement de boîtes quantiques ou de puits quantiques de nitrures (Al,Ga,In)N. Ensuite, en 2008, une DEL bleue déposée au-dessus d'un convertisseur de lumière jaune-vert a été démontrée afin d'obtenir une DEL blanche monolithique<sup>20</sup>. La figure 2 illustre schématiquement ces approches qui présentent l'avantage d'éviter la complexité des procédés associés à la réalisation des DELs blanches issues de la conversion des DELs bleues avec des phosphores.

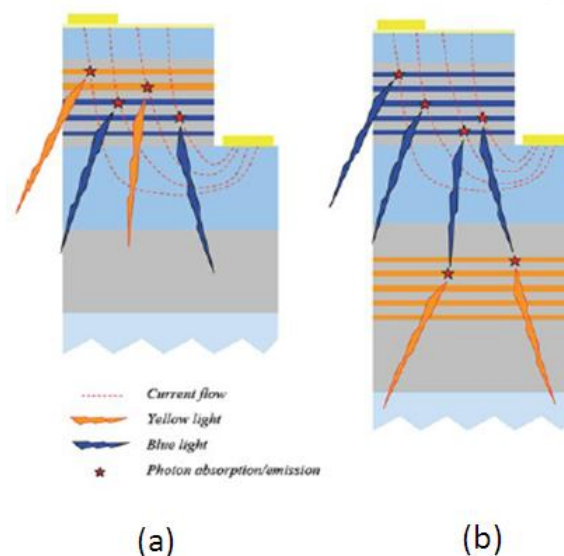


Figure 2: Schéma d'une DEL présentant (a) deux couleurs de lumière différentes émises par des puits quantiques à l'intérieur d'une jonction p-n formant la zone active d'une diode électroluminescente (DEL) et (b) l'approche de conversion par pompage optique pour obtenir une diode électroluminescente blanche monolithique (WLED).<sup>11,20, 21</sup>

Cependant, dans la première approche de DEL blanche monolithique (Figure (2a)), des problèmes cruciaux ont été mis en lumière concernant la non-uniformité de l'injection des porteurs de charges à travers les différents puits quantiques constituant la zone active. Une des principales conséquences étant une forte dépendance des coordonnées chromatiques en fonction du courant d'injection dans le dispositif<sup>13</sup>.

Dans le cas de la seconde approche (Figure (2b)), ce problème lié à l'injection des porteurs de charges n'a pas lieu d'être car la source de pompage optique excite optiquement le convertisseur de lumière pour avoir une émission dans des longueurs d'ondes plus élevées<sup>20-25</sup>. De plus, le convertisseur de lumière avec une structure de multi-puits quantiques (MPQs) contribue à la présence d'une densité de porteurs de charges plus faible dans chacun des PQ du convertisseur de lumière qu'avec des DELs blanches monolithiques injectées électriquement. Cela limite la chute de l'efficacité lors d'un fonctionnement à des larges densités de courants<sup>21,25</sup>.

Cependant, quelques désavantages liés à ces approches persistent. En effet les efficacités démontrées pour des DELs blanches monolithiques restent plus faibles que celles des DELs blanches standards à base de phosphore<sup>12,27</sup>. Cela est dû à une plus faible efficacité quantique interne (EQI) des boîtes quantiques à base d'InGaN émettant de la lumière dans le domaine spectral vert-jaune. En conséquence, dans cette étude nous allons nous concentrer sur les propriétés structurales et optiques de ces puits quantiques InGaN émettant dans le vert-jaune où elles vont jouer le rôle de convertisseur de lumière pour la réalisation de DELs blanches monolithiques.

Nous savons que la fabrication d'un convertisseur de lumière InGaN/GaN vert-jaune efficace nécessite l'incorporation d'une composition élevée d'indium (>15%) dans les zones actives composées de puits quantiques d'InGaN. De plus, ces derniers doivent aussi avoir une largeur raisonnable,  $L_{PQ}$  (2-4nm). Mais la fabrication de couches d'InGaN possédant une importante concentration d'indium n'est pas facile à réaliser en raison du fait que la température de croissance des puits d'InGaN doit être beaucoup plus faible (700-800°C) que celle de la couche barrière en GaN (900-1100°C). Cette différence de température de croissance induit des défauts structuraux tels que l'ondulation de l'épaisseur des PQs InGaN, des défauts ponctuels (lacunes, anti-site) et de la ségrégation d'indium<sup>28</sup> due à la faible stabilité thermique des alliages InGaN<sup>29,30,31</sup>.

En outre, la croissance de la structure de pompage optique (bleu-violet) de la DEL, ainsi que la croissance de la couche p-GaN servant pour le contact électrique au-dessus du convertisseur de lumière risquent éventuellement, en raison des températures de croissances importantes utilisées,<sup>32</sup> de détériorer les puits quantiques en InGaN qui sont situés à l'intérieur du convertisseur de lumière<sup>33,34</sup>.

Par ailleurs, la déposition d'une couche en InGaN avec une forte concentration d'indium sur une couche de GaN entraîne une large contrainte compressive dans la couche épitaxiée en raison de la grande différence de paramètre de maille. Cela peut conduire à la formation de

défauts additionnels. La formations de ces défauts permet de diminuer l'énergie issue de la contrainte accumulée<sup>35,36,37</sup>.

Ces défauts structuraux sont probablement identifiés comme la cause principale de l'inefficacité des puits quantiques InGaN vert-jaune qui composent le convertisseur de lumière. Par ailleurs, si ces défauts structuraux supplémentaires sont générés lors de la croissance d'une structure MPQs vert-jaune, alors ils auront aussi un impact négatif sur la performance de la DEL de pompage. En effet, cette dernière est déposée sur le dessus de la structure précédente, par conséquent la performance globale de la DEL blanche monolithiques finale va se détériorer.

Ainsi, en définitive les propriétés structurales et optiques des MPQs vert-jaune sont un sujet d'étude dont l'approfondissement est crucial pour améliorer notre compréhension du comportement et des performances des DELs blanches monolithiques.

Dans cette étude, nous avons initialement déposé 10 périodes d'empilement wurtzite InGaN/GaN en changeant la température et la durée de croissance des puits quantiques. Ensuite plusieurs structures avec au moins 10 périodes de MPQs wurtzite InGaN/AlGaIn/GaN ont été déposées heteroepitaxialement. La technique d'épitaxie utilisée est l'épitaxie en phase vapeur aux organométalliques (EPVOM) dans le but d'obtenir des MPQs vert, jaune-vert présentant une forte émission lumineuse. Dans le cas de l'empilement InGaN/AlGaIn/GaN, après chaque croissance de couche de PQ InGaN, quelques monocouches atomiques de AlGaIn (<2nm) ont été déposées comme couche de protection avant la croissance de la couche barrière en GaN. Les processus de croissance de ces couches de protection en GaN ont été explorés à travers les différents échantillons étudiés.

L'objectif de ce travail de thèse est d'étudier l'impact de la couche de protection en AlGaIn ainsi que de son processus de croissance sur les propriétés structurales et optiques du convertisseur de lumière situé au-dessus des PQs InGaN. Enfin, différents échantillons avec différentes épaisseurs de couche de protection AlGaIn (>2nm) ont été étudiés de manière comparative avec d'autres types d'échantillons utilisant une couche de GaN déposé à basse température comme couche de protection au-dessus du convertisseur de lumière.

Concernant l'étude des propriétés structurales, nous nous sommes particulièrement intéressés aux mesures précises des épaisseurs des couches, des compositions en indium dans les zones actives ainsi qu'à l'identification des différents types de défauts présents dans les structures déposées. Ces informations structurales ont été étudiées principalement à partir de processus d'analyses d'images obtenues à l'aide d'un microscope électronique à transmission (MET). Par ailleurs, pour confirmer et vérifier les résultats issus de l'analyse MET, nous avons mené des analyses de diffraction par Rayons X (DRX) sur chaque échantillon. La morphologie de surface a aussi été observée à l'aide d'un microscope à force atomique (AFM). Et finalement nous avons essayé de relier ces informations structurales aux propriétés optiques mesurées par photoluminescence à température ambiante.

Les résultats obtenus lors de cette étude sont présentés dans ce manuscrit de la manière suivante :

Dans le chapitre 1, nous introduirons les propriétés structurales fondamentales des cristaux wurtzite semi-conducteurs composés III-nitride. Ensuite nous discuterons les systèmes de plans de glissements de cette structure wurtzite ainsi que des différents types de dislocations associées. La relation contrainte déformation dans la couche épitaxiée et son influence sur les propriétés optiques du matériau seront mises en évidence. Enfin nous décrirons brièvement la technique de dépôt par EPVOM et la structure de l'empilement des échantillons étudiés.

Le chapitre 2 traite des caractéristiques fondamentales impliquées dans l'hétérostructure InGaN/GaN. Une vue d'ensemble des différentes caractéristiques associées aux couches InGaN possédant une forte concentration d'indium dans le système d'empilement InGaN/GaN seront présentées. Nous nous attarderons principalement sur la séparation de phase, les processus de relaxation et le phénomène d'ondulation des épaisseurs des couches. Enfin nous discuterons brièvement au sujet de l'impact de ces différentes caractéristiques structurales sur les performances des diodes électroluminescentes (DELs).

Dans le chapitre 3, nous nous concentrerons sur les principes de bases sur lesquels reposent les techniques expérimentales que nous avons utilisées lors de ce travail de thèse. Nous présenterons certaines méthodes expérimentales en particulier afin de mettre en évidence comment et pourquoi ces outils de caractérisations peuvent être utilisés pour déterminer précisément les propriétés de nos échantillons. Les avantages et désavantages de ces procédures expérimentales seront aussi discutés dans les différentes sous-sections de ce chapitre.

Dans le chapitre 4, dernier chapitre de ce manuscrit, nous présenterons les résultats obtenus au cours de ce travail de thèse, à savoir:

L'importance de la déposition de la couche de protection en AlGaIn. Les meilleures conditions de croissances pour compenser l'ondulation de l'épaisseur des PQs en InGaIn. La formation d'îlots d'indium, la ségrégation et/ou l'évaporation due à la température élevée utilisée lors de la réalisation de DELs composées d'empilement de type InGaIn/GaN. Les propriétés optiques associées à ces échantillons seront présentées dans ce chapitre. De plus, des dislocations supplémentaires ont été mises en évidence dans les couches en InGaIn possédant des compositions en indium très élevés (>20%). Nous discuterons donc dans ce chapitre du type de ces dislocations additionnelles et nous tenterons de définir leur origine.

Finalement, une conclusion générale ainsi que les perspectives de cette étude seront présentées.

## References:

- <sup>1</sup> Kanji BANDO, Kensho SAKANO, Yasunobu NOGUCHI, and Yoshinori SHIMIZU, *Journal of Light and Visual Environment* **22** (1), 2 (1998).
- <sup>2</sup> Shuji Nakamura and Gerhard Fasol, *The Blue Laser Diode*. (Springer, Berlin, 1997).

- 3 Narukawa Yukio, Ichikawa Masatsugu, Sanga Daisuke, Sano Masahiko, and Mukai Takashi, *Journal of Physics D: Applied Physics* **43** (35), 354002 (2010).
- 4 Narukawa Yukio, Sano Masahiko, Ichikawa Masatsugu, Minato Shunsuke, Sakamoto Takahiko, Yamada Takao, and Mukai Takashi, *Japanese Journal of Applied Physics* **46** (10L), L963 (2007).
- 5 M. Meneghini, A. Tazzoli, G. Mura, G. Meneghesso, and E. Zanoni, *Electron Devices, IEEE Transactions on* **57** (1), 108 (2010).
- 6 X. Guo, G. D. Shen, B. L. Guan, X. L. Gu, D. Wu, and Y. B. Li, *Applied Physics Letters* **92** (1), 013507 (2008).
- 7 Chen Horng-Shyang, Yeh Dong-Ming, Lu Chih-Feng, Huang Chi-Feng, Wen-Yu Shiao, C. C. Yang, I. S. Liu, and Su Wei-Fang, *Photonics Technology Letters, IEEE* **18** (13), 1430 (2006).
- 8 S. Nizamoglu, T. Ozel, E. Sari, and H. V. Demir, *Nanotechnology* **18** (6), 065709 (2007).
- 9 Ho Seong Jang, Byoung-Hwa Kwon, Heesun Yang, and Duk Young Jeon, *Applied Physics Letters* **95** (16), 161901 (2009).
- 10 Xiaoyun Guo, John W. Graff, E. F. Schubert, and Jr Robert F. Karlicek, 2000 (unpublished).
- 11 Damilano Benjamin, Grandjean Nicolas, Pernot Cyril, and Massies Jean, *Japanese Journal of Applied Physics* **40** (9A), L918 (2001).
- 12 Yamada Motokazu, Narukawa Yukio, and Mukai Takashi, *Japanese Journal of Applied Physics* **41** (3A), L246 (2002).
- 13 S. Dalmaso, B. Damilano, C. Pernot, A. Dussaigne, D. Byrne, N. Grandjean, M. Leroux, and J. Massies, *physica status solidi (a)* **192** (1), 139 (2002).
- 14 S. J. Chang, L. W. Wu, Y. K. Su, C. H. Kuo, W. C. Lai, Y. P. Hsu, J. K. Sheu, J. F. Chen, and J. M. Tsai, *Electron Devices, IEEE Transactions on* **50** (2), 519 (2003).
- 15 A. Dussaigne, J. Brault, B. Damilano, and J. Massies, *physica status solidi (c)* **4** (1), 57 (2007).
- 16 Chi-Feng Huang, Chih-Feng Lu, Tsung-Yi Tang, Jeng-Jie Huang, and C. C. Yang, *Applied Physics Letters* **90** (15), 151122 (2007).
- 17 Sung-Nam Lee, H. S. Paek, H. Kim, T. Jang, and Y. Park, *Applied Physics Letters* **92** (8), 081107 (2008).
- 18 Funato Mitsuru, Kondou Takeshi, Hayashi Keita, Nishiura Shotaro, Ueda Masaya, Kawakami Yoichi, Narukawa Yukio, and Mukai Takashi, *Applied Physics Express* **1** (1), 011106 (2008).
- 19 Lu Chih-Feng, Huang Chi-Feng, Yung-Sheng Chen, Wen-Yu Shiao, Cheng-Yen Chen, Yen-Cheng Lu, and Yang Chih-Chung, *Selected Topics in Quantum Electronics, IEEE Journal of* **15** (4), 1210 (2009).
- 20 B. Damilano, A. Dussaigne, J. Brault, T. Huault, F. Natali, P. Demolon, P. De Mierry, S. Chenot, and J. Massies, *Applied Physics Letters* **93** (10), 101117 (2008).
- 21 B. Damilano, P. Demolon, J. Brault, T. Huault, F. Natali, and J. Massies, *Journal of Applied Physics* **108** (7), 073115 (2010).
- 22 V. V. Nikolaev, M. E. Portnoi, and I. Eliashevich, *physica status solidi (a)* **183** (1), 177 (2001).
- 23 B. Damilano, N. Trad, J. Brault, P. Demolon, F. Natali, and J. Massies, *physica status solidi (a)* **209** (3), 465 (2012).
- 24 Damilano Benjamin, Kim-Chauveau Hyonju, Frayssinet Eric, Brault Julien, Hussain Sakhawat, Lekhal Kaddour, Vennéguès Philippe, Mierry Philippe De, and Massies Jean, *Applied Physics Express* **6** (9), 092105 (2013).
- 25 Dario Schiavon, Michael Binder, Andreas Loeffler, and Matthias Peter, *Applied Physics Letters* **102** (11), 113509 (2013).
- 26 Shuji Nakamura, *Solid State Communications* **102** (2–3), 237 (1997).
- 27 M. R. Krames, O. B. Shchekin, Regina Mueller-Mach, Gerd O. Mueller, Zhou Ling, G. Harbers, and M. G. Craford, *Display Technology, Journal of* **3** (2), 160 (2007).

- 28 S. Kret, F. Ivaldi, K. Sobczak, R. Czernecki, and M. Leszczyński, *physica status solidi (a)* **207** (5),  
1101 (2010).
- 29 G. T. Thaler, D. D. Koleske, S. R. Lee, K. H. A. Bogart, and M. H. Crawford, *Journal of Crystal*  
*Growth* **312** (11), 1817 (2010).
- 30 M. S. Oh, M. K. Kwon, I. K. Park, S. H. Baek, S. J. Park, S. H. Lee, and J. J. Jung, *Journal of Crystal*  
*Growth* **289** (1), 107 (2006).
- 31 W. Lee, J. Limb, J. H. Ryou, D. Yoo, T. Chung, and R. D. Dupuis, *Journal of Electronic Materials* **35**  
(4), 587 (2006).
- 32 S. M. Ting, J. C. Ramer, D. I. Florescu, V. N. Merai, B. E. Albert, A. Parekh, D. S. Lee, D. Lu, D. V.  
Christini, L. Liu, and E. A. Armour, *Journal of Applied Physics* **94** (3), 1461 (2003).
- 33 Y.S. Lin, K. J. Ma, C. Hsu, Y.Y. Chung, C. W. Liu, S. W. Feng, Y. C. Cheng, C. C. Yang, M. H. Mao, H.  
W. Chuang, C. T. Kuo, J. S. Tsang, and T. E. Weirich, *Applied Physics Letters* **80** (14), 2571 (2002).
- 34 Y. Y. Chung, Y. S. Lin, S. W. Feng, Y. C. Cheng, E. C. Lin, C. C. Yang, K. J. Ma, C. Hsu, H. W.  
Chuang, C. T. Kuo, and J. S. Tsang, *Journal of Applied Physics* **93** (12), 9693 (2003).
- 35 H. K. Cho, J. Y. Lee, G. M. Yang, and C. S. Kim, *Applied Physics Letters* **79** (2), 215 (2001).
- 36 H. K. Cho, J. Y. Lee, C. S. Kim, and G. M. Yang, *Journal of Applied Physics* **91** (3), 1166 (2002).
- 37 F.A. Ponce and D.P. Bour, *Nature* **386**, 351 (1997).



# Chapter 1

## Fundamentals of nitride semiconductors



## Chapter 1

# Fundamentals of nitride semiconductors

## Introduction

To study and understand the structural and optical properties of group III-nitrides LEDs, it is important to know some of their fundamental properties. Thus in this chapter, we present some basic structural information like lattice parameters, different crystallographic planes and directions of group III-nitride wurtzite crystals. Then the structural information is used to elaborate the idea of strain-stress relationship involved in group III-nitride hetero-epitaxial growth process.

The fundamentals of defects like dislocations involved in group III-nitride hetero-epitaxial growth are highlighted. The classification of the different types of dislocations and the different slip plane systems for the wurtzite crystal structure are introduced in this chapter.

Depending on the growth orientation of group III-nitride crystal structure, the induced strain in the epilayers has impact on their observed optical properties due to polarization fields involved within the structure. Thus the origin of these polarization fields and their effects are discussed.

Finally, we discuss the basic mechanisms involved in metal organic chemical vapor deposition (MOCVD) growth technique and conclude our chapter by describing the structure of our studied samples in brief.

## 1.1 Structural properties

Group-III nitride materials can crystallize either in the cubic zinc-blende or the hexagonal wurtzite structure. The zinc-blende structure being meta-stable, the growth of high structural and optical quality group III-nitride crystals has been only achieved in the wurtzite phase. We are going to address the structural properties of wurtzite crystal structure in the next subsection.

### 1.1.1 Wurtzite structure

In order to emphasize the hexagonal symmetry of the wurtzite crystal structure, the directions in a hexagonal structure are described by four translational vectors rather than three vectors<sup>1</sup>. Figure 1-1 (a) shows a hexagonal unit cell with primary axes, where the x and y axes are at 120° to each other. Figure 1-1 (b), shows the problem that arises when expressing the same group of planes of the hexagonal system in 3 indexed {hkl}<sub>c</sub> representations. For example, all the prismatic planes parallel to the z-axis should have the same form of representation as they are crystallographically equivalent, but in case of 3 indexed notation system, their indices differ in

representation as shown in Figure 1-1 (b). To overcome this problem a fourth axis - the  $u$  axis - is introduced at  $120^\circ$  to both the  $x$  and  $y$  axes as shown in Figure 1-1 (c). Thus the indices of the lattice for wurtzite hexagonal structure are now consisting of four numbers ( $hkil$ ). From vector summation, it is obvious that the sum of the unit distance along  $x$ ,  $y$  and  $u$  axes should result to zero (i.e.  $a+b+t=0$ , from Figure 1-1 (c)), so the first three numbers in the Miller –Bravais indices should also become zero, i.e.  $h+k+i=0$  or  $i=-(h+k)$ . This condition allows us to represent the same group of planes of the hexagonal system with the combination of first three numbers of the four indexed notation ( $hkil$ ), as shown for the six prismatic planes of the system  $\{1-100\}$  in Figure 1-1(c) without ambiguity. We are going to use the four-index notation to represent the directions and planes of our sample structure in the upcoming discussion, so for the convenience of the reader, we are summarizing the bracketing convention in Table 1-1 below.

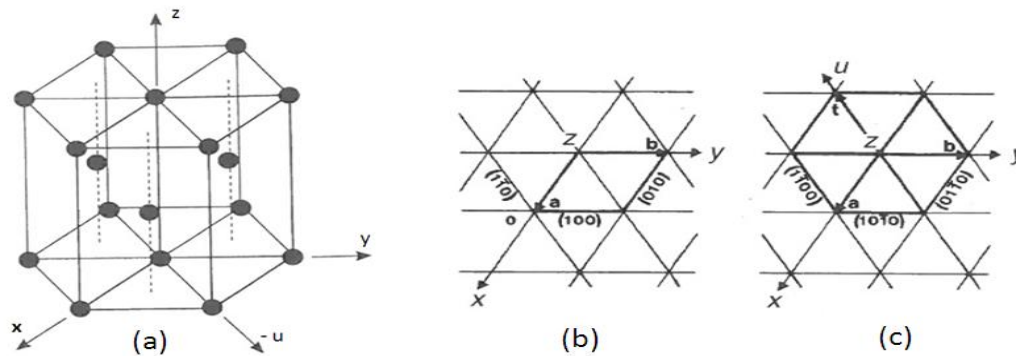


Figure 1-1: a) Unit cell of the hexagonal lattice showing the arrangement of the atoms along with the primary axes. Projected view of the unit cell structure along  $z$ -axis, b) showing the traces of the six prism faces indexed by 3 indexed system  $\{hkl\}$  and c) same planes indexed by Miller-Bravais (four-index) system<sup>2</sup>.

Table 1-1 Summary of bracketing convention for four index notation

Four-index notation	Meaning
$1\ 0\ -1\ 5$	Reflection
$(1\ 0\ -1\ 5)$	Plane
$\{1\ 0\ -1\ 5\}$	Family of planes
$[1\ 0\ -1\ 5]$	Direction
$\langle 1\ 0\ -1\ 5 \rangle$	Family of directions

The wurtzite structure has a hexagonal unit cell and each atom is in a  $sp^3$ -hybridization state and bounded to four other atoms of different types. These four atoms are located at the corners of a tetrahedron. The atoms arrangement can be represented as two hexagonal close-packed sublattices shifted with respect to each other, forming a close-packing sequence of ABAB..type. The wurtzite structure symmetry is described by the  $P6_3mc$  space group. The distance between neighboring atoms in the hexagonal plane of the wurtzite structure is

denoted as lattice parameter 'a' and the distance between the same types of atom along the perpendicular direction to that hexagonal plane is denoted as 'c' parameter of the structure. The axis along the hexagonal plane is considered to be a-axis and the perpendicular direction to that a-axis is known as c-axis of the wurtzite structure. The nearest distance between the two different atoms along the c-axis is denoted as 'u' and known as bond length. Figure 1-2 represents the atomic structure of GaN in the wurtzite structure. Here the bigger yellow balls and smaller gray ones are representing Ga atoms and N atoms, respectively, as Ga atoms have higher atomic mass than that of N atoms. The two tetrahedrons are also represented by shaded areas within the figure.

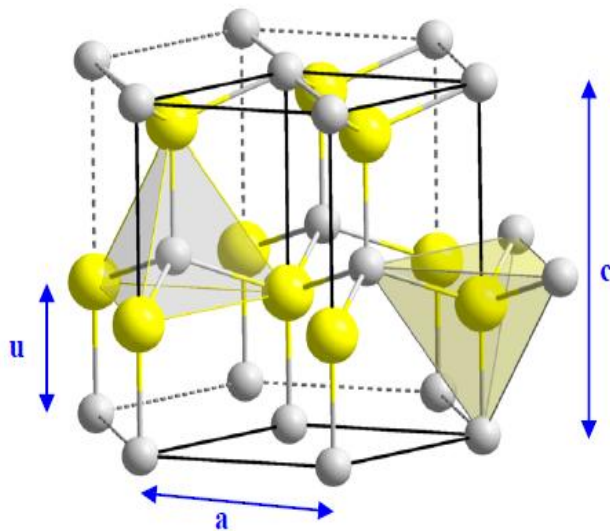


Figure 1-2: Atomic structure of GaN as wurtzite crystal. Ga atoms are represented in yellow color and are relatively larger than N atoms represented in gray. The bonds are presented in two colors. Lattice parameters along with bond length are presented in blue arrows<sup>3</sup>.

The values of the lattice parameters for binary group III-nitride compounds are listed in Table 1-2, along with the ratio of the length of the c and a axes (axial ratio) and the bond length u and c axis<sup>4,5,6,7</sup>. Considering a hard sphere model as an ideal structure, where the bond length distance of the individual atoms is considered to be equal, the c/a ratio should have the value of 1.633. But the practical values of c/a ratio vary slightly as indicated in Table 1-2 due to the fact that the atomic distance between the two different atoms along the c axis is different from the ones outside the c axis.

Table 1-2: Lattice parameters and ratios for AlN, GaN and InN crystals in wurtzite phase

	a (nm)	c (nm)	c/a	u/c
GaN	0.3189	0.5185	1.626	0.377
AlN	0.3113	0.4982	1.600	0.382
InN	0.3538	0.5703	1.612	0.377

The wurtzite structure is non-centrosymmetric, i.e. the  $[0001]$  and  $[000\bar{1}]$  directions are not equivalent. In wurtzite structure, the  $[0001]$  direction is defined as the pointing direction from III-metal atoms (Ga atoms) towards N atoms. Crystal grown along  $[0001]$  direction is known as Ga-face or metal polarity crystal and when the crystal is grown along the other direction, i.e.,  $[000\bar{1}]$  direction, it is called N polarity or N-face crystal. Figure 1-3 illustrates the two faces depending on the growth directions for GaN material.

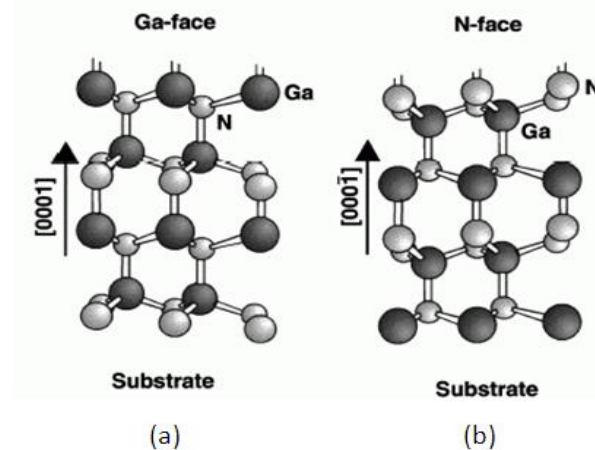


Figure 1-3: Schematic illustration of a) Ga-polarity b) N-polarity along two opposite c-axis directions for GaN wurtzite structure<sup>8</sup>.

In this work, all the samples are grown along the  $[0001]$  polar direction and the samples are observed and images are analyzed using cross section transmission electron microscopy (cs-TEM) imaging technique. Indium composition within the active region, the types of dislocations and also the thickness of different regions of the sample structures are observed and analyzed by tilting the TEM samples along three principal zone axes as  $\langle 1\bar{1}00 \rangle$ ,  $\langle 11\bar{2}0 \rangle$  and  $\langle 14\bar{5}0 \rangle$ , respectively. The details of the imaging processes and analysis techniques of TEM will be discussed later in chapter 3. The projection of the crystal structure along different zone axes has been schematically shown in Figure 1-4.

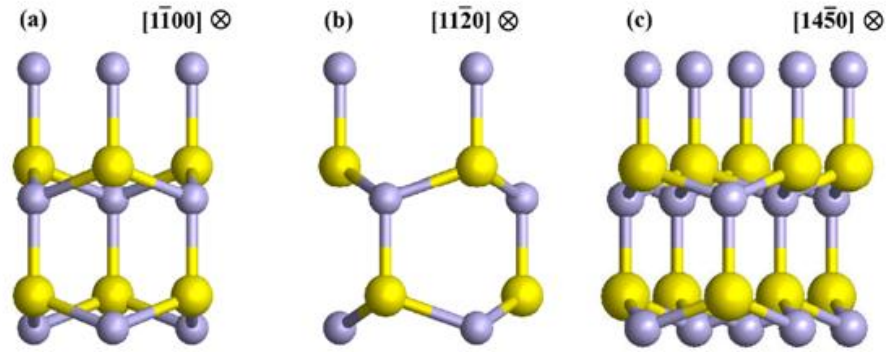


Figure 1-4: Projection of the GaN wurtzite crystal structure along a)  $\langle 1\bar{1}00 \rangle$ , b)  $\langle 11\bar{2}0 \rangle$  and c)  $\langle 14\bar{5}0 \rangle$  zone axes for a Ga polarity structure where yellow balls are for Ga atoms and the blue ones are for N atoms<sup>3</sup>.

### 1.1.2 Relation between lattice constant and band gap energy

The band gap energy  $E_g$  (eV) of group III-nitride materials can be related to their lattice constant value ( $a_0$ ) as both the band gap energy and the lattice constant values varies according to Vegard's law, depending on the composition value ( $x$ ). The lattice parameter ( $a_0$ ) of any ternary nitride, for example,  $\text{In}_x\text{Ga}_{1-x}\text{N}$  can be determined from Vegard's law as follows:

$$a_0(X_xY_{1-x}N) = xa_0(XN) + (1-x)a_0(YN) \quad (1.1)$$

where X and Y represent any of the two atoms from Al, Ga and In atoms and x corresponds to the ratio of composition within the alloy. From Table 1-2, the initial lattice constant value of binary compounds of group III-nitrides (i.e., AlN, GaN and InN) is used to interpolate the lattice constant values of other ternary alloy using equation 1.1. Similarly, the band gap energy  $E_g$  (eV) of any ternary nitride can be interpolated using the Vegard's law considering the initial band gap energy of the binary compound of group III-nitride (i.e., AlN, GaN and InN). Vurgaftman and Meyer<sup>9</sup> reported the band gap energy for the binary compounds of group III-nitride (i.e., AlN, GaN and InN) at zero Kelvin ( $T=0\text{K}$ ) temperature as shown in Table 1-3. But to correlate the theoretical<sup>10</sup> and experimental<sup>11</sup> values of the band gap energy  $E_g$  (eV) of a ternary alloy, an additional term with a parameter b is considered as shown in equation 1.2. This parameter is known as bowing parameter.

$$E_g(X_xY_{1-x}N) = xE_g(XN) + (1-x)E_g(YN) - bx(1-x) \quad (1.2)$$

The values of the bowing parameter b, for different nitride alloys are summarized in Table 1-4<sup>9</sup>.

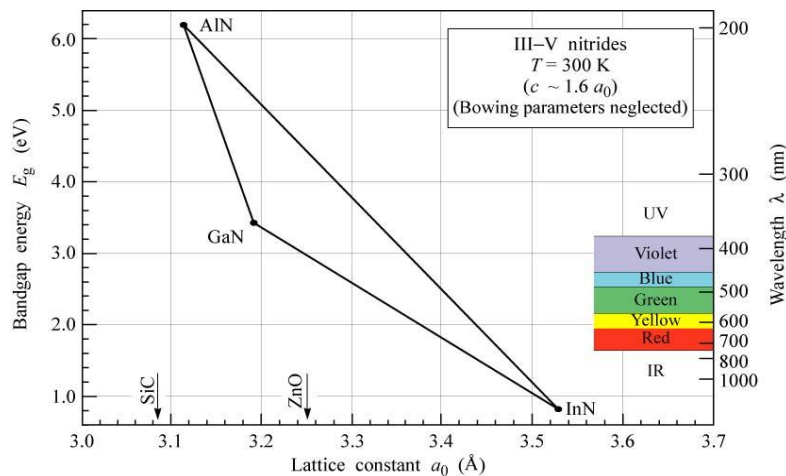
Table 1-3: Band gap energies of group III- nitride binaries at 0 K<sup>9</sup>

Material	InN	GaN	AlN
Structure	Wurtzite	Wurtzite	Wurtzite
Band gap (eV)	0.78	3.51	6.0

Table 1-4: Bowing parameters of group III-nitride alloys<sup>9</sup>

Alloy	AlGaN	InGaN	AlInN
Bowing parameter b (eV)	0.70	1.40	2.50

Now correlating the two equations 1.1 and 1.2, we can find the relation between the lattice constant ( $a_0$ ) and band gap energy (eV) of a ternary alloy. Figure 1-5 illustrates the lattice constant  $a_0$  (in Å unit) value versus the band gap energy  $E_g$  (in eV unit) for group III- nitride materials, where bowing parameters are neglected for simplicity. It is clear from Figure 1-5 that the  $\text{In}_x\text{Ga}_{1-x}\text{N}$  alloy is a very important material as it covers entire visible spectrum range from infra-red (IR) to ultra-violet (UV) depending on the Indium composition ( $x$ ).

Figure 1-5: Graph of band gap energy vs. lattice constant for group III-nitride materials<sup>12</sup>.

## 1.2 Dislocation basics

The group III- nitride multiple quantum well (MQW) structure is generally developed on top of a few micrometer thick GaN epilayer which acts as a buffer layer as it is grown on top of a foreign substrate such as sapphire. Owing to low cost and large availability, sapphire is the mostly used substrate to grow group III-nitride heterostructures. The growth process of such GaN buffer layer on top of sapphire substrate is complicated and beyond the scope of this work. So the detailed growth mechanism of such buffer layer is not discussed. But due to the high lattice mismatch ( $\sim 16\%$ )<sup>13</sup>, structural differences and growth process mechanisms, the GaN buffer layer contains a high density of dislocations of about  $5 \times 10^8$  to  $1 \times 10^9$  per  $\text{cm}^2$ , known as pre-

existing dislocations. In hetero-epitaxial growth, the dislocations that propagating through any grown epilayer are termed as threading dislocation (TD). Figure 1-6 shows a large cross sectional view of a sample, where the threading dislocations are easily seen in GaN buffer layer as indicated. It is important to know the type and the slip planes involved with these dislocations to better understand their propagation mechanism while growing the epitaxial layer. Thus in the next subsection we are going to discuss the type of dislocations and the slip plane system observed in group III-nitride wurtzite structures in brief.

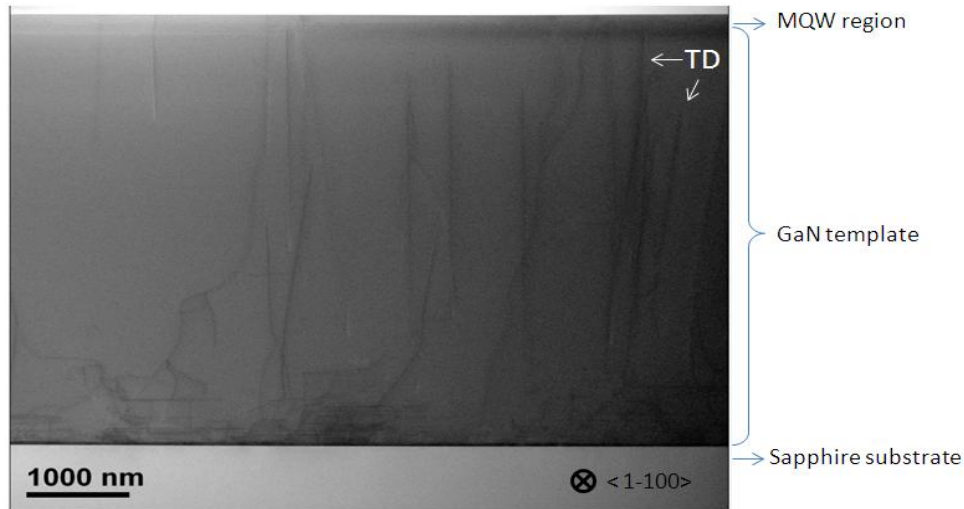


Figure 1-6: Cross-sectional transmission electron microscope (cs-TEM) imaging along  $\langle 1-100 \rangle$  zone axis, showing different regions of the sample along with the contrast for threading dislocations (TDs) as indicated by white arrows for two.

### 1.2.1 Slip plane system in wurtzite crystal structure

A slip plane is defined as a plane which contains both the Burger vector  $\mathbf{b}$  (it is defined as the dislocation-displacement vector of the crystal structure<sup>14,15</sup>) and the unit vector  $\mathbf{u}$  (which is parallel to the dislocation line direction) of a dislocation. Moreover, a slip plane and a slip direction (Burger vector) constitute a slip system. In the wurtzite crystal structure possible slip planes and slip directions are indicated as shown in Figure 1-7, where the planes are in gray color and the probable slip directions within the planes are indicated by bold arrows. Depending on the planes of the hexagonal structure, slip plane system can be classified into three groups as:

- **Basal slip system** which contains only  $\{0001\}$  basal plane and slip direction in the plane, as shown in Figure 1-7(a):  $\{0001\} \langle 11-20 \rangle$ .
- **Prismatic slip system** which contains the families of prismatic planes as  $\{1-100\}$  and  $\{11-20\}$  planes and the corresponding slip directions within the planes. Figure 1-7 (b) and (c)

shows the prismatic slip system as:  $\{1-100\} \langle 11-20 \rangle$ ,  $\{1-100\} \langle 0001 \rangle$ ;  $\{11-20\} \langle 0001 \rangle$  and  $\{11-20\} \langle 1-100 \rangle$ . And finally,

- **Pyramidal slip system** which contains the families of pyramidal planes as  $\{11-22\}$ ,  $\{1-101\}$  and  $\{1-102\}$  planes and the corresponding slip directions within those planes. Figure 1-7 (d) to (f) shows the pyramidal slip system as:  $\{11-22\} \langle 11-23 \rangle$ ,  $\{11-22\} \langle 1-100 \rangle$ ;  $\{1-101\} \langle 11-23 \rangle$ ,  $\{1-101\} \langle 11-20 \rangle$ ;  $\{1-102\} \langle 1-101 \rangle$  and  $\{1-102\} \langle 11-20 \rangle$ .

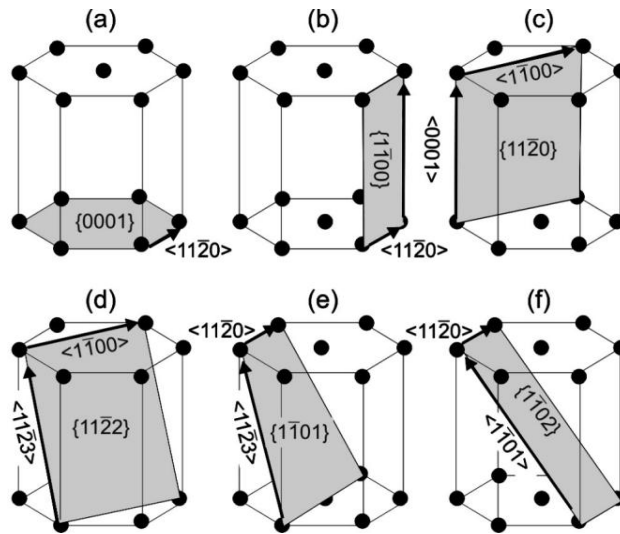


Figure 1-7: Slip systems in a hexagonal lattice. (a) basal, (b) and (c) are prismatic and (d) to (f) are pyramidal slip plane system<sup>16</sup>.

## 1.2.2 Dislocation types

In group III- nitride hexagonal structures, considering that the dislocations are propagating along  $[0001]$  direction, i.e., the unit vector  $\mathbf{u}$  is along  $[0001]$  direction, three types of dislocation are identified depending on their Burger vector  $\mathbf{b}$ . They are defined as follows:

- $\langle a\text{-type} \rangle$  or  $\langle \text{edge-type} \rangle$  dislocation, where  $\mathbf{b} = 1/3 \langle 11-20 \rangle$ ;
- $\langle c\text{-type} \rangle$  or  $\langle \text{screw-type} \rangle$  dislocation, where  $\mathbf{b} = \langle 0001 \rangle$  and
- $\langle a+c \text{ type} \rangle$  or  $\langle \text{mixed-type} \rangle$  dislocation, where  $\mathbf{b} = 1/3 \langle 11-23 \rangle$ .

In Figure 1-8, the red arrows indicate the different types of dislocation within the unit cell of a wurtzite structure, where the unit vector  $\mathbf{u}$  is along  $[0001]$  direction. Moreover, the blue arrows drawn within the  $(0001)$  plane of the figure are showing the primary axes considered to define certain families of direction of the hexagonal structure as the colorful dash lines showing families of directions  $\langle 11-20 \rangle$  and  $\langle 1-100 \rangle$  within the structure.

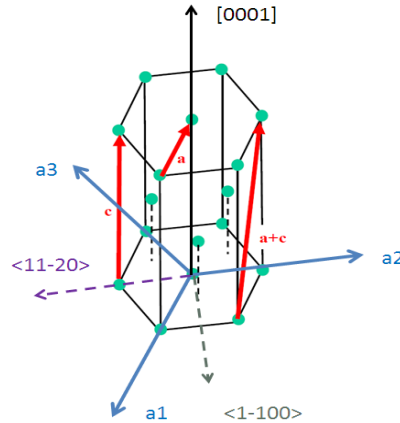


Figure 1-8: Unit cell of wurtzite structure, where the blue arrows (a1, a2 and a3) indicates the primary axes of the unit cell, the colorful dash arrows showing the particular families of direction and the red arrows shows the different types of dislocation as named beside them.

In the group III-nitride wurtzite structure, the Burger vector  $\mathbf{b}$  of  $\langle 1-100 \rangle$  and  $\langle 1-101 \rangle$  orientation are not observed, so the prismatic slip system of  $\{11-20\} \langle 1-100 \rangle$  and pyramidal slip system of  $(11-22) \langle 1-100 \rangle$  and  $\{1-102\} \langle 1-101 \rangle$  are not considered

In chapter 2, we are going to explain some relaxation processes and their limitations that have been observed in InGaN/GaN crystal growth using these slip plane systems. Later in chapter 3, we will discuss in detail the procedure how to identify the type of a dislocation by using transmission electron microscopy (TEM) techniques.

### 1.3 Misfit in group III-nitride hetero-structures

In hetero-epitaxial growth process, while growing pseudomorphically on a substrate layer the epilayer gets deformed. Both the in-plane and out of plane lattice parameters of the epilayer get changed. For example, in case of nitride alloys, the lattice mismatch between GaN ( $a_{\text{GaN}} = 3.189 \text{ \AA}$ ) and InN ( $a_{\text{InN}} = 3.538 \text{ \AA}$ ) is more than 10%. Therefore, pseudomorphic growth of InGaN on GaN will lead to strains in the InGaN layer as it suffers from a compressive stress. Figure 1-9 (a) and (b), schematically shows the pseudomorphic growth of InGaN layer on top of GaN substrate layer considering that fully relaxed InGaN layer has  $a_0$  and  $c_0$  lattice parameters, but under compression the lattice parameter changes to  $a$  and  $c$ . Note that although the Figure 1-9 represents the lattice deformation for a cubic structure, it is sufficient to illustrate the lattice deformation for a hexagonal lattice structure as well.

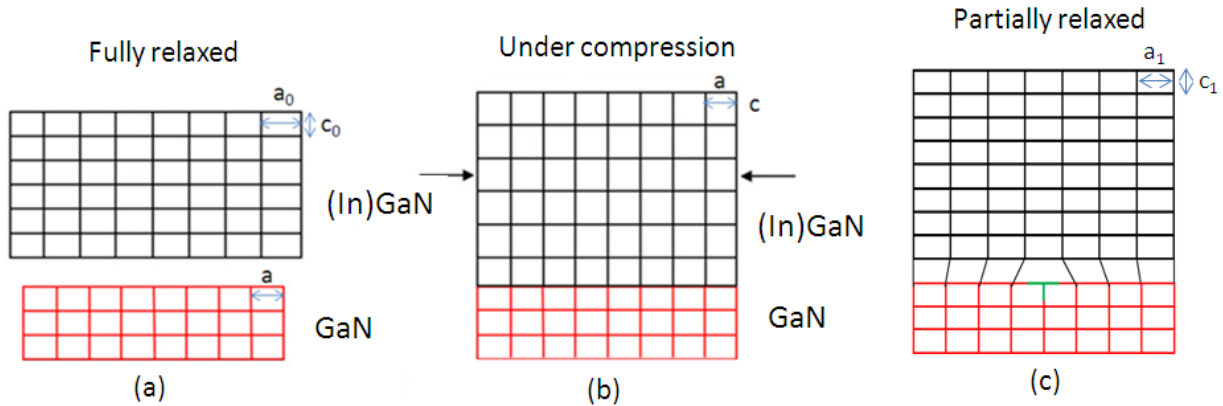


Figure 1-9: Schematic diagram showing the (a) the fully relaxed InGaN and GaN layers, (b) strained InGaN layer due to pseudomorphically growth on GaN layer and (c) misfit dislocation helping to partially relax the InGaN epilayer.

Figure 1-9 (c) shows that a dislocation at the interface of the InGaN and GaN layer helping to partially relax the induced strain of the InGaN layer, as the epilayer and the substrate layer has different lattice constant  $a_1$  and  $a$ , respectively. The generated dislocation (T mark) is known as misfit dislocation (MD).

### 1.3.1 Crystal deformation: bi-axial and uni-axial case

In a pseudomorphic wurtzite hetero-epitaxial growth process, the crystal deformation (strain) of the epilayer can be related to the stress it suffered from the fact that the in-plane lattice parameter of the epilayer changed to that of the substrate lattice parameter ( $a$ - parameter) as schematically shown in Figure 1-9 (b). Moreover, the out of plane lattice parameter ( $c$ -parameter) of the epilayer changes depending on the in plane strain induced during the growth. The stress-strain relation and also the relationship between the out of plane lattice parameter ( $c$ -parameter) to that of in-plane lattice parameter ( $a$ - parameter) can be found from the standard Hooke's law. Hooke's law allows us to relate the crystal stress to that of the crystal strain as follows:

$$\vec{\sigma} = C \cdot \vec{\epsilon} \quad (1.3)$$

where  $\vec{\sigma}$  and  $\vec{\epsilon}$  are stress and strain tensors and  $C$  is the elastic coefficient tensor. Using Voigt notation<sup>17</sup> for hexagonal crystal system, we can expressed them as follows:

$$\vec{\sigma} = \begin{bmatrix} \sigma_{xx} \\ \sigma_{yy} \\ \sigma_{zz} \\ \sigma_{yz} \\ \sigma_{zx} \\ \sigma_{xy} \end{bmatrix} \vec{\varepsilon} = \begin{bmatrix} \varepsilon_{xx} \\ \varepsilon_{yy} \\ \varepsilon_{zz} \\ 2\varepsilon_{yz} \\ 2\varepsilon_{zx} \\ 2\varepsilon_{xy} \end{bmatrix} C = \begin{bmatrix} c_{11} & c_{12} & c_{13} & 0 & 0 & 0 \\ c_{12} & c_{11} & c_{13} & 0 & 0 & 0 \\ c_{13} & c_{13} & c_{33} & 0 & 0 & 0 \\ 0 & 0 & 0 & c_{44} & 0 & 0 \\ 0 & 0 & 0 & 0 & c_{44} & 0 \\ 0 & 0 & 0 & 0 & 0 & \frac{c_{11}-c_{12}}{2} \end{bmatrix} \quad (1.4)$$

If we consider that the growth direction of an epilayer is along Z axis, then the stress in grown epilayer will take place along the two perpendicular directions of the in-plane axes (along X and Y axes). In such case the heterostructure is known to be in a bi-axial stress state. In general, the strain tensor components along different directions are expressed in terms of the lattice constants as:

$$\varepsilon_{xx} = \varepsilon_{yy} = \frac{a-a_0}{a_0}; \quad \varepsilon_{zz} = \frac{c-c_0}{c_0} \quad (1.5)$$

Where  $a_0$  and  $c_0$  are relaxed epilayer's unit cell parameters and  $a$  and  $c$  are the strained epilayer's unit cell parameters. The absence of stress along growth direction ( $\sigma_{zz} = 0$ ) and considering that the strain is equal in two lateral directions, impose the correlation between strain and stress from equations 1.3 and 1.4 as: [please see Appendix for detail derivations]

$$\sigma = \left( c_{11} + c_{12} - \frac{2c_{13}^2}{c_{33}} \right) \varepsilon \quad (1.6)$$

where,  $\sigma = \sigma_{xx} = \sigma_{yy}$ , and  $\forall i \neq j, \sigma_{ij} = 0$

$$\text{and } \varepsilon_{zz} = -2 \frac{c_{13}}{c_{33}} \varepsilon \quad (1.7)$$

where,  $\varepsilon = \varepsilon_{xx} = \varepsilon_{yy}$ ,

Therefore, for the bi-axial stress condition, equation 1.6 gives us the stress-strain relation of the epilayer and equation 1.7 correlates the extension or contraction along the growth direction  $\varepsilon_{zz}$  (Z-axis) of the epilayer to that of any lateral deformation  $\varepsilon$ .

In case of an epilayer with a very thin lateral thickness, the strain along growth axis,  $\varepsilon_{zz}$ , may not follow the equation 1.7, as the two lateral strains  $\varepsilon_{xx}$  and  $\varepsilon_{yy}$  may not be equal or even one may become zero due to surface relaxation effect along the thin thickness direction. The situation when the strain along the thin lateral thickness is zero is known as uni-axial stress condition. In uni-axial stress condition (i.e.,  $\sigma_{xx} \neq \sigma_{yy} = \sigma_{zz} = 0$ ), the correlation between  $\varepsilon_{xx}$  and  $\varepsilon_{zz}$  can be expressed from equation 1.3 and 1.4 as: [Please see Appendix for detail derivations]

$$\varepsilon_{zz} = -\frac{c_{13}(c_{11}-c_{12})}{c_{11}c_{33}-c_{13}^2} \varepsilon_{xx} \quad (1.8)$$

In transmission electron microscopy (TEM) imaging, the sample thickness should be thin enough to make the e-beam of the TEM transparent through the sample. Now to obtain the TEM images of the InGaN layer, we have to prepare and observe the samples from sideways (i.e., from the perpendicular direction to the growth axis). Such samples are known as cross-sectional transmission electron microscopy (cs-TEM) samples. Due to cs-TEM sample preparation, the thickness of such samples may become so thin that surface relaxation may take place within the sample along the e-beam direction, keeping the stress only along one direction. Figure 1-10 (a) and (b) schematically illustrate the two stress conditions, bi-axial and uni-axial stress condition, respectively. In both figures, it is considered that Z axis is the growth direction and depending on the cs-TEM sample thickness the InGaN layer may get relaxed along e-beam direction (y-axis) while the other axis (X-axis) is always in stressed state whatever the sample thickness may be. In Figure 1-10 (b), the curved surface of the InGaN layer demonstrate the surface relaxation within the sample. It has been reported for InGaN/GaN material that the cs-TEM samples of less than 50 nm thick along beam direction may suffer from surface relaxation and either may be in bi-axial or uni-axial stress condition. But samples with less than 5 nm thickness are surely in uni-axial stress condition<sup>18</sup>.

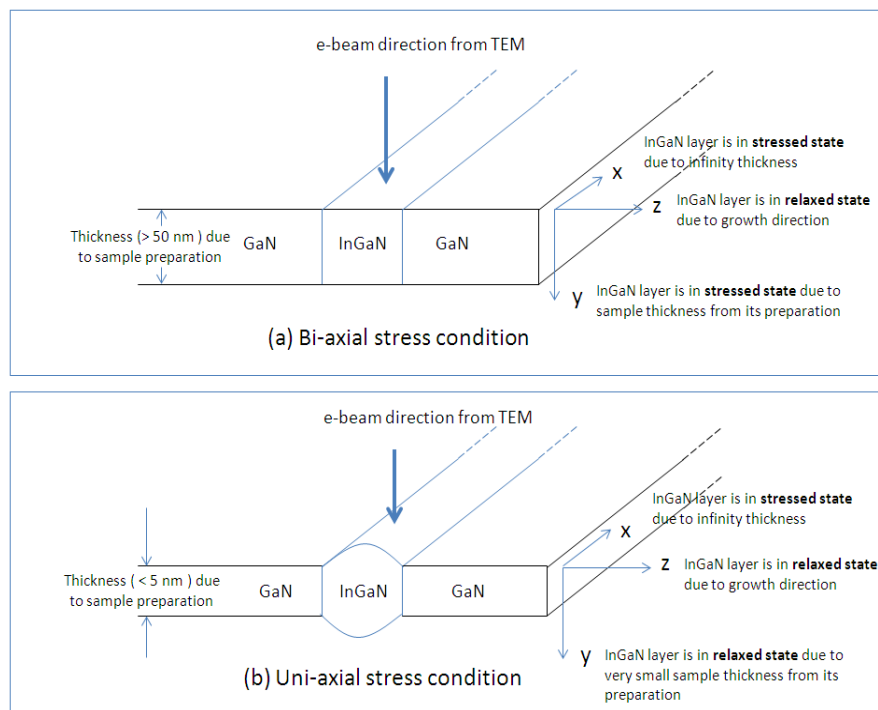


Figure 1-10: Schematic diagram showing (a) bi-axial stress and (b) uni-axial stress condition for InGaN layer depending on the sample thickness from cross sectional transmission electron microscopy sample preparation.

For an InGaN/GaN pseudomorphic heteroepitaxial growth process, from equations 1.7 and 1.8, we can express the deformed lattice parameter of any InGaN epilayer along the growth direction as: [please see Appendix for detail derivations]

$$c = c_0 \left[ 1 - \frac{2C_{13}}{C_{33}} \left( \frac{a-a_0}{a_0} \right) \right] \quad (\text{bi-axial stress condition}) \quad (1.9)$$

$$c = c_0 \left[ 1 - \left\{ \frac{C_{13}(C_{11}-C_{12})}{C_{11}C_{33}-C_{13}^2} \right\} \left( \frac{a-a_0}{a_0} \right) \right] \quad (\text{uni-axial stress condition}) \quad (1.10)$$

The change in lattice parameter between the InGaN epilayer and that of the GaN substrate layer along the growth direction (c-parameter) can be expressed as:

$$\Delta c = c - c_{\text{GaN}}$$

Thus the percentage of the InGaN lattice deformation ( $e_{zz}$ ) along the growth direction to that of GaN substrate lattice parameter ( $c_{\text{GaN}}$ ) can be expressed as:

$$e_{zz}(\%) = 100 \times \frac{(c - c_{\text{GaN}})}{c_{\text{GaN}}} \quad (1.11)$$

Using equation 1.9 and 1.10, we can determine the percentage of InGaN lattice deformation for both bi-axial and uni-axial stress condition from equation 1.11 as:

$$e_{zz}(\%) = 100 \times \left[ \frac{c_0}{c_{\text{GaN}}} \left[ 1 - \frac{2C_{13}}{C_{33}} \left( \frac{a-a_0}{a_0} \right) \right] - 1 \right] \quad (\text{bi-axial stress condition}) \quad (1.12)$$

$$e_{zz}(\%) = 100 \times \left[ \frac{c_0}{c_{\text{GaN}}} \left[ 1 - \left\{ \frac{C_{13}(C_{11}-C_{12})}{C_{11}C_{33}-C_{13}^2} \right\} \left( \frac{a-a_0}{a_0} \right) \right] - 1 \right] \quad (\text{uni-axial stress condition}) \quad (1.13)$$

By definition, in pseudomorphic growth, the in-plane lattice parameter of the strained InGaN layer ( $a$ ) takes the same lattice parameter value as that of relaxed GaN, i.e,  $a=a_{0\text{GaN}}$ , as explained in Figure 1-9 (b). Moreover, the relaxed parameters ( $a_0$  and  $c_0$ ) of the InGaN layer within these equations 1.9 to 1.13 depend on the Indium composition ( $x$ ) and can be determined from Vegard's law and the unstrained lattice parameters of GaN and InN materials<sup>19</sup> ( $c_{0\text{GaN}}=5.185 \text{ \AA}$ ,  $a_{0\text{GaN}}=3.189 \text{ \AA}$ ,  $c_{0\text{InN}}=5.718 \text{ \AA}$ ,  $a_{0\text{InN}}=3.544 \text{ \AA}$ ).

From equations 1.12 and 1.13, we can calculate the percentage of lattice deformation (%)  $e_{zz}$ , as a function of indium composition ( $x$ ) as shown in Figure 1-11.

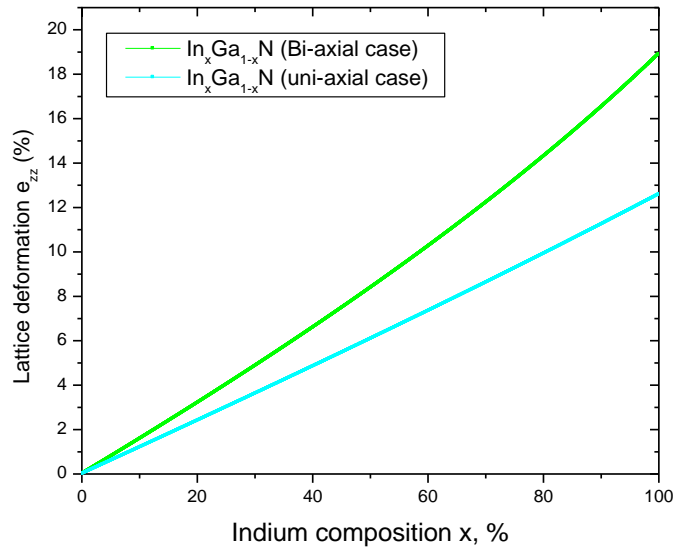


Figure 1-11: Theoretical plot of lattice deformation,  $e_{zz}$  (with respect to GaN layer using bi-axial and uni-axial stress condition) versus indium composition ( $x$ ) for InGaN quantum wells

In this work, we are going to determine the indium composition from the measurement of lattice deformation of InGaN epilayer with respect to that of GaN layer using transmission electron microscopy (TEM) imaging techniques. After calculating the percentage of lattice deformation from TEM image analysis we have used Figure 1-11 to calculate the Indium composition within the InGaN epilayer. Moreover, we compare the obtained TEM data to X-ray diffraction (XRD) data to be sure about the obtained indium composition values later on. In section 3.2.1 we are going to present the TEM imaging technique used to determine the lattice deformation value of InGaN layer to that of GaN layer.

In determining the composition within a layer, a source of inaccuracy may also arise regarding which value of elastic coefficients are used in the calculation. The elastic coefficients reported for group-III-nitrides vary in a large range<sup>20,21,22,23,24,25,26</sup>. Besides many predicted values, only theoretical calculations of Wright and Kim are available for group III-nitrides. The elastic constants reported by Wright are very frequently used for strain calculation<sup>27,28,29</sup>. Table 1-5 lists the elastic constants reported for group III-nitride crystals by different research groups and the Wright's theoretical data are highlighted as they have been used in chapter 4 to calculate the Indium composition of the InGaN active region.

Table 1-5: Elastic constants for GaN, AlN and InN crystals, all values are in GPa and the theoretical data are denoted as (th)

		C <sub>11</sub>	C <sub>12</sub>	C <sub>13</sub>	C <sub>33</sub>	C <sub>44</sub>	References
AlN	Mc Neil	411	149	99	389	125	<sup>20</sup>
	Deger	410	140	100	390	120	<sup>23</sup>
	Kim (th)	398	140	127	382	96	<sup>21</sup>
	Wright (th)	<b>396</b>	<b>137</b>	<b>108</b>	<b>373</b>	<b>116</b>	<sup>22</sup>
GaN	Polian	390	145	106	398	105	<sup>24</sup>
	Schwarz	377	160	114	209	81.4	<sup>25</sup>
	Deger	370	145	110	390	90	<sup>23</sup>
	Yamaguchi	365	135	114	381	109	<sup>26</sup>
	Kim (th)	396	144	100	392	91	<sup>21</sup>
	Wright (th)	<b>367</b>	<b>135</b>	<b>103</b>	<b>405</b>	<b>95</b>	<sup>22</sup>
InN	Kim (th)	271	124	94	200	46	<sup>21</sup>
	Wright (th)	<b>233</b>	<b>115</b>	<b>92</b>	<b>224</b>	<b>48</b>	<sup>22</sup>

#### 1.4 Spontaneous and piezoelectric polarization

In wurtzite nitride structure, strong polarization (P) exists along the c axis [0001]. This polarization is the sum of two types of polarizations known as spontaneous ( $P_{sp}$ ) and piezoelectric ( $P_{pz}$ ) polarization. Due to the non-centrosymmetric property and also the difference in electro-negativity of the metal atom to that of nitrogen atom within the wurtzite nitride structure, small electric dipoles exist along c-axis [0001]. These electric dipoles create the spontaneous polarization within the structure<sup>30</sup>.

Moreover, under stress condition, the elementary tetrahedrons of the wurtzite structures are deformed which causes the barycenters of the positive and negative charges of the crystal to move away from their usual location, creating an additional electric dipole. Polarization from such induced electric dipole is termed as piezoelectric polarization ( $P_{pz}$ ). This macroscopic polarization  $P_{pz}$  can be defined as a function of the stress as follows:

$$P_{pz} = D \cdot \vec{\sigma} \quad (1.14)$$

where D is the piezoelectric tensor. Considering the wurtzite symmetry, the above equation can be written using the Voigt notation as:

$$\begin{bmatrix} p_x^{pz} \\ p_y^{pz} \\ p_z^{pz} \end{bmatrix} = \begin{bmatrix} 0 & 0 & 0 & 0 & d_{15} & 0 \\ 0 & 0 & 0 & d_{15} & 0 & 0 \\ d_{31} & d_{31} & d_{33} & 0 & 0 & 0 \end{bmatrix} \begin{bmatrix} \sigma_{xx} \\ \sigma_{yy} \\ \sigma_{zz} \\ \sigma_{yz} \\ \sigma_{zx} \\ \sigma_{xy} \end{bmatrix} \quad (1.15)$$

Moreover, the piezoelectric polarization can also be expressed as the function of strain tensor as follows:

$$P_{pz} = E \cdot \vec{\epsilon} \quad (1.16)$$

$$\text{with, } E = \begin{bmatrix} 0 & 0 & 0 & 0 & e_{15} & 0 \\ 0 & 0 & 0 & e_{15} & 0 & 0 \\ e_{31} & e_{31} & e_{33} & 0 & 0 & 0 \end{bmatrix} \quad (1.17)$$

From equation 1.3 and 1.15, we can correlate the elements of E matrix to that of piezoelectric tensor matrix D as:  $e_{15} = d_{15}c_{44}$ ,  $e_{31} = d_{31}(c_{11} + c_{12}) + d_{33}c_{13}$  and  $e_{33} = 2d_{31}c_{13} + d_{33}c_{33}$ .

In case of bi-axial stress (i.e.  $\sigma_{xx} = \sigma_{yy} = \sigma$  and  $\sigma_{zz} = \sigma_{ij} = 0$ ), from equations 1.6, 1.7, 1.15 and 1.16, the piezoelectric polarization turns out to be oriented along the c-axis (Z axis) [0001] and can be expressed as:

$$p_{pz} = p_z^{pz} \cdot u_z = 2d_{31} \left( c_{11} + c_{12} - \frac{c_{13}^2}{c_{33}} \right) \epsilon \cdot u_z = \left( 2e_{31} - 2 \frac{c_{13}}{c_{33}} e_{33} \right) \epsilon \cdot u_z \quad (1.18)$$

where  $u_z$  is the unit vector along the c-axis and  $\epsilon$  is the in plane strain expressed as in equation 1.5. The typical value of the piezoelectric coefficients and the spontaneous polarization for III-nitrides are shown in Table 1-6<sup>30,31,32,33,34,35</sup>. Bernardini et al<sup>33,36</sup> reported that the piezoelectric polarization exhibits a non-linear behavior with respect to strain. This phenomenon has to be taken into account in order to fit with experimental works<sup>37,38</sup>. It is worth noticing that those coefficients are significantly larger in group-III nitrides than the values reported for conventional III-V semiconductors<sup>30,39</sup> and also comparable to the values reported for group II-VI wurtzite oxides (ZnO)<sup>30,34,35</sup>, so that the piezoelectric fields observed in nitrides are very intense.

Table 1-6: Piezoelectric coefficients and spontaneous polarization values for AlN, GaN and InN materials<sup>30,31,32,33,34,35</sup>

	$e_{31}(\text{C/m}^2)$	$e_{33}(\text{C/m}^2)$	$d_{31}(\text{pm/V})$	$d_{33}(\text{pm/V})$	$d_{15}(\text{pm/V})$	$P_{sp}(\text{C/m}^2)$	Relative permittivity $\epsilon_r$
AlN	-0.6	1.46	-2.1	5.4	2.9	-0.081	10.31
GaN	-0.49	0.73	-1.4	2.7	1.8	-0.029	10.28
InN	-0.57	0.97	-3.5	7.6	5.5	-0.032	14.61
ZnO	-0.51	0.89	-5.1	12.4 <sup>34</sup>	-	-0.057	10.8 <sup>35</sup>

Thus, the total polarization in strain group III-nitride crystals can be expressed as the sum of spontaneous and piezoelectric polarization as follows:

$$P = P_{pz} + P_{sp} \quad (1.19)$$

### 1.4.1 Effects of polarization on (In,Ga)N/GaN heterostructure

#### 1.4.1.1 Electric field in InGaN/GaN quantum wells

The discontinuity of the polarization within different layers of an InGaN/GaN MQW structure will lead to an accumulated surface charge at the interface of two different layers. The amount of surface charge will follow the following boundary condition:

$$\sigma_{surf} = \vec{n} \cdot (\vec{P}_1 - \vec{P}_2) \quad (1.20)$$

where  $\sigma_{surf}$  is the sheet charge density at the interface,  $\vec{n}$  is the unit vector along the normal of the interface,  $\vec{P}_1$  and  $\vec{P}_2$  represent the polarization at the two sides of the interface.

Now, considering a thin InGaN quantum well layer surrounded by thick GaN barriers in a MQW structure, where the InGaN layer is compressively strained on a strain free GaN layer grown along [0001] direction, we will have two different total polarizations  $\vec{P}_W$  and  $\vec{P}_B$  in InGaN quantum well and GaN barrier layer, respectively. As discussed in previous subsection, depending on the percentage of the Indium composition, the total polarization at the well region  $\vec{P}_W$  will be higher in value as piezoelectric polarization will dominate in that region, whereas only spontaneous polarization will have the effect in barrier GaN region as it is strain free (Figure 1-13). Thus a discontinuity of the polarization will exist in the interface of the two regions.

According to equation 1.20, the surface charge density at the barrier/ well interface would be negative,  $\sigma_{surf} = -\sigma = \vec{n} \cdot (\vec{P}_B - \vec{P}_W)$ , and at the well/ barrier interface it would be positive,  $\sigma_{surf} = +\sigma = \vec{n} \cdot (\vec{P}_W - \vec{P}_B)$ . These two opposite surface charge densities will create an electric field along [000 $\bar{1}$ ] direction within the well region.

To determine the electric field  $\vec{E}$ , we may consider the displacement field vector  $\vec{D}$  within the structure. We know that in the absence of free charge, the displacement field  $\vec{D}$  in each layer should satisfy:

$$\nabla \cdot \vec{D} = 0 \quad (1.21)$$

where the displacement field  $\vec{D}$  is expressed as a well known electrostatic equation:

$$\vec{D} = \epsilon \vec{E} + \vec{P} \quad (1.22)$$

$\vec{E}$  and  $\vec{P}$  are electric and polarization field, respectively and  $\epsilon$  is the permittivity of the media. In case of single quantum well (SQW) structure, the displacement field  $\vec{D}$  must be continuous, so we could write<sup>40</sup>:

$$\varepsilon_W \vec{E}_W + \vec{P}_W = \varepsilon_B \vec{E}_B + \vec{P}_B \quad (1.23)$$

where the indices W and the B represent the well and the barrier region of the structure, respectively. It has been pointed out by Bernardini and Fiorentini that the electric field  $\vec{E}$  becomes zero in region far from surface of a massive materials<sup>41</sup>. Therefore, we can assume that the electric field at barrier region  $\vec{E}_B$  will be zero- which in turn helps to deduce the electric field in well region from equation 1.23 as:

$$\vec{E}_W = \frac{(\vec{P}_B - \vec{P}_W)}{\varepsilon_W} \quad (1.24)$$

But for a periodic super lattice such as MQW structure, the boundary condition becomes  $L_W \vec{E}_W + L_B \vec{E}_B = 0$ , where  $L_W$  and  $L_B$  are the well and barrier layer thickness. From this boundary condition we can obtain electric field of barrier layer ( $\vec{E}_B$ ) in terms of  $\vec{E}_W$  as,  $\vec{E}_B = -\left(\frac{L_W \vec{E}_W}{L_B}\right)$  and thus putting this term in equation 1.23 and rearranging it, we can obtain the electric field within the well region as:

$$\vec{E}_W = \frac{L_B(\vec{P}_B - \vec{P}_W)}{(\varepsilon_B L_W + \varepsilon_W L_B)} \quad (1.25)$$

From equation 1.25, we can find that when the thickness of the barrier layer  $L_B$  is much larger than that of the well  $L_W$ , the electric field  $\vec{E}_W$  for the well region can be simplified to that of SQW case as expressed by equation 1.24.

However, in case of a capping layer of certain thickness  $L_C$  within a MQW structure, the displacement field  $\vec{D}$  and the boundary condition for such MQW structure become as follows:

$$\begin{aligned} \varepsilon_W \vec{E}_W + \vec{P}_W &= \varepsilon_B \vec{E}_B + \vec{P}_B = \varepsilon_C \vec{E}_C + \vec{P}_C \\ L_W \vec{E}_W + L_B \vec{E}_B + L_C \vec{E}_C &= 0 \end{aligned}$$

where,  $L_C$ ,  $\vec{E}_C$ ,  $\vec{P}_C$  and  $\varepsilon_C$  stands for capping layer thickness, electric field, polarization field and the permittivity of the capping layer, respectively. Thus considering the above mentioned conditions we can find the electric field within the well region of such three layers (QW layer/ capping layer / barrier layer) MQW structure as:

$$\vec{E}_W = \frac{\varepsilon_B L_C (\vec{P}_C - \vec{P}_W) + \varepsilon_C L_B (\vec{P}_B - \vec{P}_W)}{(\varepsilon_C \varepsilon_B L_W + \varepsilon_B \varepsilon_W L_C + \varepsilon_C \varepsilon_W L_B)} \quad (1.26)$$

Now depending on the growth orientation of the group III-nitrides, the spontaneous polarization ( $P_{sp}$ ) has a certain orientation. For example, the group III-nitride grown along [0001] orientation (Ga face) has a spontaneous polarization direction along  $[000\bar{1}]$  direction. However, due to stress on the grown epilayer, piezoelectric polarization ( $P_{pz}$ ) may have same or

opposite orientation than that of spontaneous polarization ( $P_{sp}$ ). Figure 1-12 demonstrates the different orientation of spontaneous and piezoelectric polarizations along with surface charge and electric field direction depending on the growth direction and also on compressive or tensile stress on the grown epilayer. For example, when an InGaN thin layer is grown on GaN layer along [0001] direction, the compressive stress in InGaN layer lead to a piezoelectric field ( $P_{pz}$ ) and its direction is opposite to that of spontaneous polarization ( $P_{sp}$ ) as shown in Figure 1-12. Utilizing the coefficient values from Table 1-5 and Table 1-6 and also using equations 1.18 and 1.19, we can plot the different polarization values in InGaN layer deposited on a GaN substrate depending on Indium composition, as shown in Figure 1-13. Thus it clearly demonstrates that in case of InGaN layer grown on top of GaN layer, piezoelectric polarization play the dominating role in total polarization of the layer as spontaneous polarization change very little depending on the percentage of Indium composition.

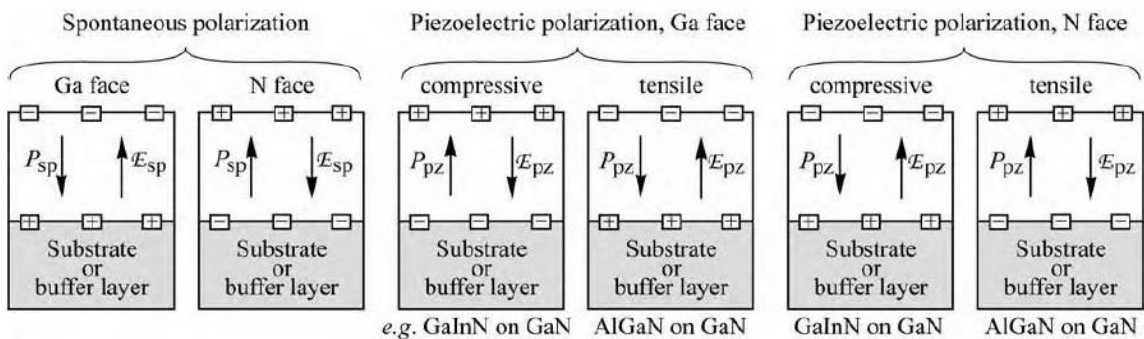


Figure 1-12: Surface charge, the direction of electric field and polarization field for spontaneous and piezoelectric polarization in group III-nitrides for Ga and N face orientation.<sup>42</sup>

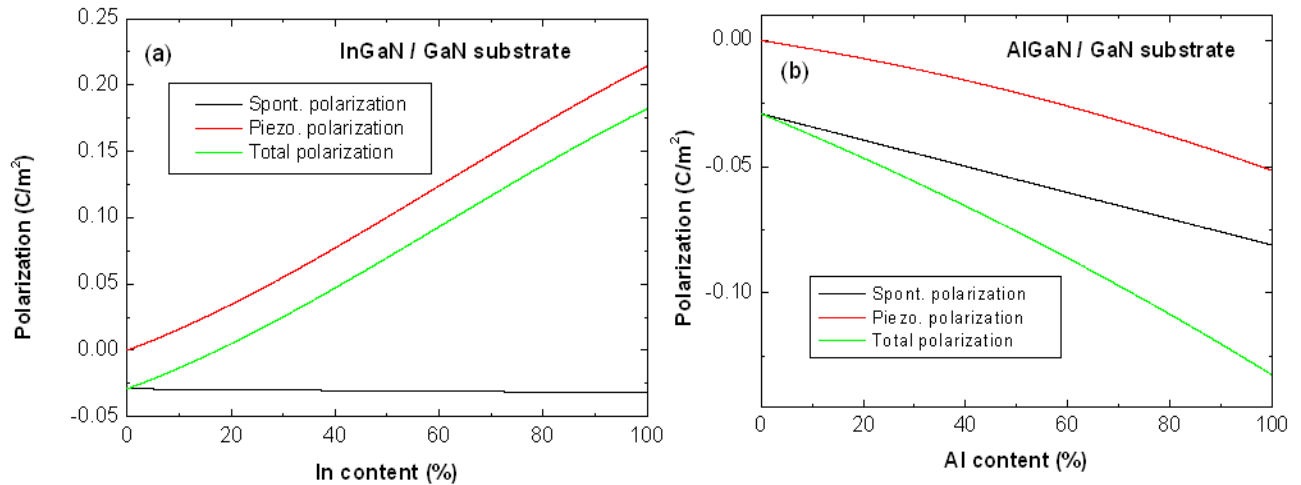


Figure 1-13: Simulated total, spontaneous and piezoelectric polarization in (a)  $\text{In}_x\text{Ga}_{1-x}\text{N}$  and (b)  $\text{Al}_x\text{Ga}_x\text{N}$  grown on GaN substrate, with different Indium and aluminium composition.

#### 1.4.1.2 Effect of electric field on the InGaN quantum well transition energies

The effects of such electric field  $\vec{E}_W$  within well region has been schematically represented in Figure 1-14, where it demonstrates that the field will deform the band structure of the InGaN/GaN system and also reduce the effective transition energy between different energy levels within the quantum wells.

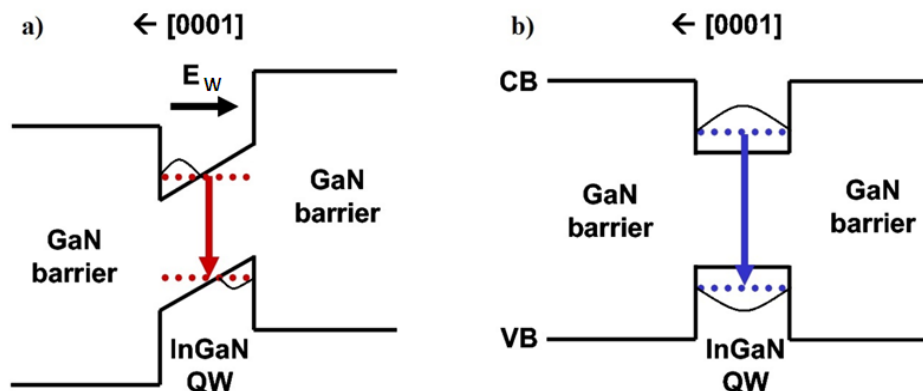


Figure 1-14: Band structure of an (In,Ga)N/ GaN quantum well (a) with and (b) without the internal electric field  $E_W$ <sup>43</sup>.

In these figures, the black lines show the conduction (CB) and the valence band (VB). The dotted colored lines indicate energy levels within the quantum wells and the bell shaped lines within the well indicate the electron and hole wave functions. It has been reported that to grow an InGaN active layer with a targeted wavelength of emission, polar (c-plane) well structure requires less indium composition than that of non-polar well structure. Piezoelectric polarization in polar well structure plays an important role to observe such phenomenon, e.g, for a targeted wavelength of 520 nm with 4 nm well width, about 3%-point less indium composition is required for polar than that of non-polar well structure<sup>44</sup>.

Moreover, due to the band bending caused by the internal electric field  $\vec{E}_W$ , the transition energy may get reduced i.e., emitted light wavelength may get red-shifted depending on the electric field  $\vec{E}_W$  and also on well thickness  $L_W$ . This effect is known as quantum confined Stark effect (QCSE) and expressed as:

$$E(eV) = E_g(GaN) + E_e + E_h - R_y - qE_W L_W \quad (1.27)$$

where,  $R_y$  is the exciton binding energy,  $q$  the elementary charge and  $L_W$  and  $E_W$  are well thickness and electric field value within the well, respectively. The  $E_g$  represents the band gap energy and  $E_e$  and  $E_h$  are the confinement energies of electrons and holes within the QW.

#### 1.4.1.3 Impact of electric field on the radiative efficiency of InGaN/GaN QWs

In presence of electric field  $\vec{E}_W$ , the electron and hole wave functions shift to opposite sides of the well and decreases the overlap area of the two envelope wave functions<sup>44,45</sup> as indicated in Figure 1-14 (a). This effect is very important because it directly impacts the radiative lifetime of carriers in the heterostructure. It has been reported that the radiative lifetime is inversely proportional to the square of the overlap of the electron and hole wave function integral as shown in equation 1.28<sup>46</sup>

$$\tau_{rad}^{-1} = \frac{nd^2 E_0^3}{3\pi\epsilon_0 h^4 c^3} |\int f_e \cdot f_h \cdot dz|^2 = \frac{E_0^3}{A} |\int f_e \cdot f_h \cdot dz|^2 \quad (1.28)$$

where  $d$  is the inter-band optical dipole of GaN,  $E_0$  is the transition energy,  $f_e$  and  $f_h$  are wave functions of electron and hole, respectively. The  $A$  value of  $90\text{eV}^3 \cdot \text{s}$  has been experimentally determined by Bretagnon et al<sup>47</sup>. For any light source short radiative lifetime is desirable since the internal quantum efficiency is directly related to the ratio of the radiative lifetime over the non-radiative lifetime. The presence of the electric field in polar InGaN/GaN QWs increases the radiative lifetime. Therefore, to keep large efficiencies in the presence of an electric field, it is mandatory to have thin QWs. The typical thickness of InGaN QWs for high efficiency light emitting devices is generally smaller than 3 nm.

Figure 1-15 shows that the external quantum efficiency (EQE) of LED devices decrease rapidly when the emission wavelength increases towards the green-yellow range i.e. wavelength greater than 500 nm. This phenomenon is known as “green gap” in nitride LEDs and LDs structure. It is assumed that for a [0001] polar InGaN/GaN light structure, QCSE is one of the main reasons behind such efficiency drop as for green and yellow light source, the indium composition is higher or the QW thickness larger which causes a higher impact of the electric field  $\vec{E}_W$  within the well region and increases the lifetime of the radiative recombination process.

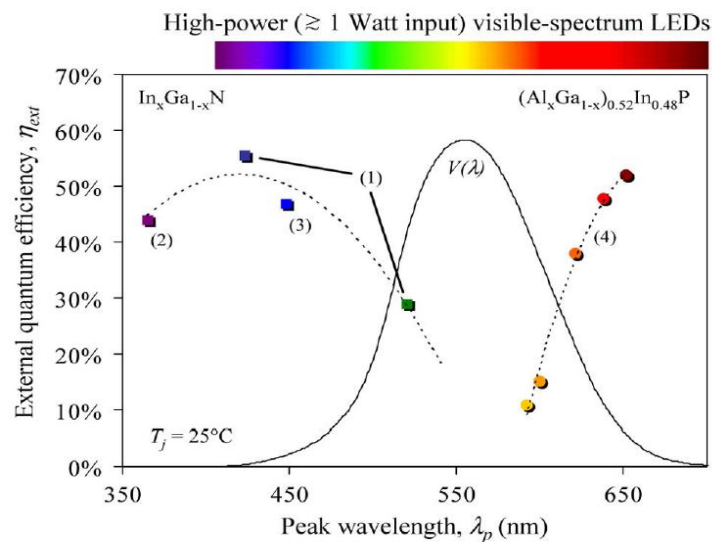


Figure 1-15: External quantum efficiency of light emitting diodes as a function of the emission wavelength: (1) InGaN thin film flip chip LEDs, 350 mA<sup>48</sup>; (2) InGaN vertical thin film LED, 1000 mA<sup>49</sup>; (3) InGaN conventional chip LEDs employing patterned substrates<sup>50</sup> and (4) Production performance AlGaInP truncated inverted pyramid LEDs<sup>51</sup>, Philips Lumileds Lighting Co., 350 mA.  $V(\lambda)$  is the luminous eye response curve from CIE (Commission Internationale de l’Eclairage). Dashed lines are guides to the eye<sup>48</sup>.

## 1.5 Growth processes of LED structure

The growth processes of LED structure are generally conducted either by molecular beam epitaxy (MBE) or metal-organic chemical vapor deposition (MOCVD) techniques. Both techniques allow monocrystalline layer growth. The advantage of the MOCVD technique is its higher growth rate (about 3-5  $\mu\text{m}$  per hour) than that of MBE technique (typically less than 1  $\mu\text{m}$  per hour). Moreover, MOCVD is performed at high temperature (1000-1100°C for GaN) which allows having better crystalline quality of the grown heterostructures. Thus compared with MBE, MOCVD technique is a more suitable growth technique for industrial needs. As all

the studied samples in this work are grown entirely by MOCVD, the following subsection describes the reactor and the grown LED structures in brief.

### 1.5.1 Metal-organic chemical vapor deposition (MOCVD) technique

The first vapor phase epitaxy with metal-organic compound was successfully conducted for (Al,Ga)As back in year 1972<sup>52</sup>. The process of such growth is that different reagents arrive to the reactor in vapor metal organic form, such as trimethylgallium (TMG), trimethylindium (TMI), trimethylaluminium (TMA) as precursors for Ga, In and Al respectively and also ammonia (NH<sub>3</sub>) for nitrogen atoms. These gaseous compounds are supplied to the substrate by carrier gas like nitrogen or hydrogen. Pyrolysis of the organic compounds occurs on the heated substrate surface and the epitaxial layer forms from chemical reactions of the released reagents.

Both horizontal and vertical reactors for MOCVD growth technique are available. In this work all the samples are grown using a home-made vertical reactor. Figure 1-16 shows the schematic diagram of a vertical MOCVD reactor, where the essential parts of the reactor is indicated. The wafer on which different layers of the LED structure are deposited is placed on the graphite sample holder. The RF heating system is used to heat up the holder to the required temperature of the growth process. A thermocouple underneath the holder or the laser beam from the top is used to read the temperature of the growth system. The laser beam is also used to determine the growth rate of the epitaxial layer from the beam reflectivity from the wafer surface using the laser reflectometry (LR) system. The LR system has a laser source at 632.8 nm (He-Ne laser) mechanically modulated and a detection system with a synchronous demodulator. Since the nitrides are transparent at 632.8 nm source and grown epitaxial nitride layer has different refractive index from the substrate, the reflected light intensity follows a periodic function with the period  $\tau$  expressed as follows:

$$\tau = \frac{\lambda \times \cos(\theta)}{2nV} \quad (1.29)$$

where  $\lambda$  is the wavelength of the laser source,  $n$  is the refractive index of the epitaxial layer at growth temperature,  $\theta$  the angle of the incidence and  $V$  is the growth rate of the layer.

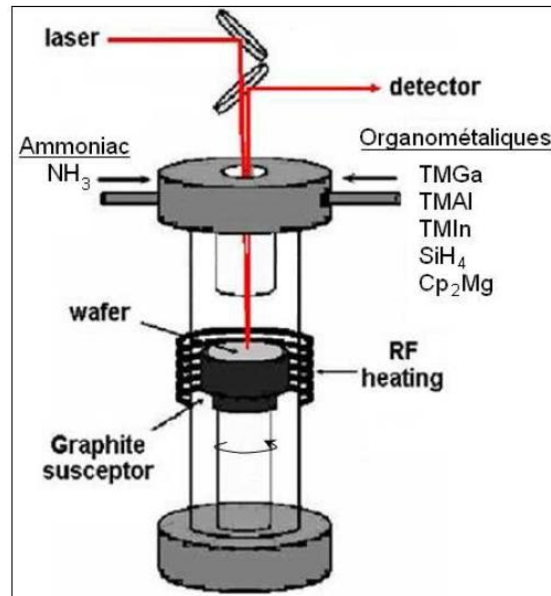


Figure 1-16: Schematic diagram of vertical MOCVD reactor<sup>53</sup>

Monitoring the pattern of the reflected laser light with time one can easily estimate the growth rate and layer morphology while growth.

### 1.5.2 The light emitting diode (LED) structure for light converter

Using the MOCVD growth technique, all the studied LED structures as light converters in this work have been grown on a commercially available 2 inch, n-type GaN on c-plane sapphire ( $\text{Al}_2\text{O}_3$ ) substrate. Most of the grown LEDs have the structure as schematically shown in Figure 1-17 where, the GaN layer act as a barrier layer, the InGaN layer as the active quantum well (QW) region and the AlGaIn layer as a capping layer. In two samples instead of AlGaIn as capping layer, low temperature GaN layer has been grown as capping layer after each InGaN QW and some samples have been grown without any capping layer for comparison purpose in this work. In each sample 10 periods of such layers have been grown. To achieve a high brightness light source of InGaN/ GaN system with an emission wavelength of more than 500 nm we have manipulated the growth processes of the studied light converter structures.

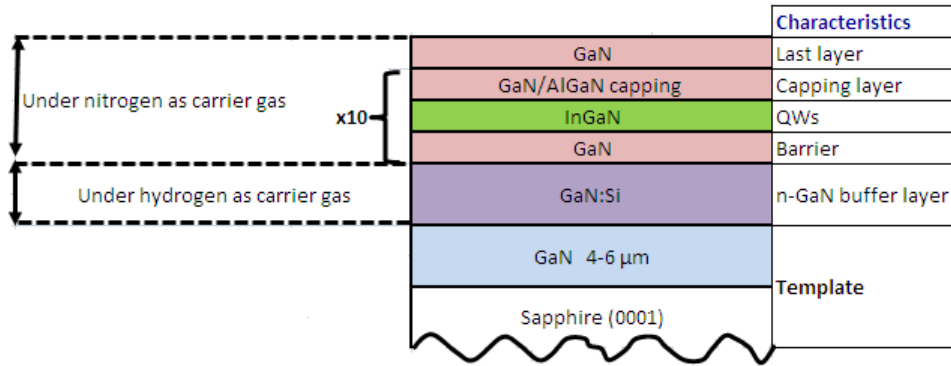


Figure 1-17: Schematic diagram of the light converter structures

In our grown samples we have used either trimethylgallium (TMG) or triethylgallium (TEG) as precursor for Ga atoms and trimethylindium (TMI), trimethylaluminum (TMA) as precursor for In and Al atoms, respectively. We used ammonia (NH<sub>3</sub>) gas for N atoms. In all the cases nitrogen (N<sub>2</sub>) is used as carrier gas for the growth of the whole light converter structure in the home made vertical MOCVD reactor.

The growth rate and growth temperature of the InGaN active QW layer of the structure are quite low as compared to that of the GaN barrier layer. We have managed to maintain the deposition rate for InGaN layer at around 1.4 nm to 2 nm/min, while growing the layer either at 680°C or 740°C. The deposition rate for the GaN layer is set around 6-7 nm/min, growing at 940°C or 970°C. In case of InGaN layer growth, we used TEG and for GaN layer growth we used TMG as precursor for Ga atoms. This is intentionally done as TEG has higher decomposition rate than TMG at low temperature and also it allows us to manage two different flow rates for the two different layers in our reactor. All the growth temperature values correspond to the thermocouple reading of the home made reactor.

The details of the growth parameters and the structural and optical properties of the studied LEDs are going to be presented in chapter 4.

## Summary

Some of the fundamental properties of group III-nitrides of wurtzite crystal structure have been discussed in this chapter. Different types of dislocations and slip plane systems for hexagonal wurtzite structure have been described. The ideas developed here are referred to explain some characteristic issues observed in InGaN/GaN heterostructure in the next chapter and also for our samples later on.

The stress-strain relationship in group III-nitrides crystal system has been discussed in details to highlight the fact that it may be an issue in determining the In composition in our samples. Moreover, for group III-nitride material of (0001) growth orientation, the impact of this stress-strain relation on optical properties has been discussed as polarization fields are involved in such wurtzite crystal. It has then been pointed out briefly that depositing high indium (> 15%) composition in InGaN quantum well has limitation in providing the green-yellow light emission with sufficient intensity due to QCSE. The idea of QCSE is referred to explain the obtained room temperature photoluminescence (RT-PL) spectrum for our samples in later chapters (chapter 4).

In this work, as all the samples are grown from home made metal-organic chemical vapor deposition (MOCVD) vertical reactor, so we introduced the reactor and described the studied LED structures very briefly in this chapter.

In the next chapter, we are going to introduce the basic characteristics involved in InGaN/GaN grown LEDs. The fundamental properties of group III-nitrides introduced in this chapter are intensively used to discuss the reported characteristics involved in InGaN/GaN crystal growth.

## References

- 1 F. Frank, *Acta Crystallographica* **18** (5), 862 (1965).
- 2 Christopher Hammond, *The Basics of Crystallography and Diffraction* Second ed. (Oxford university press, New York, 2001).
- 3 M. Korytov, PhD thesis, Universite de Nice- Sophia Antipolis, France, 2010.
- 4 H. P. Maruska and J. J. Tietjen, *Applied Physics Letters* **15** (10), 327 (1969).
- 5 W. M. Yim, E. J. Stofko, P. J. Zanzucchi, J. I. Pankove, M. Ettenberg, and S. L. Gilbert, *Journal of Applied Physics* **44** (1), 292 (1973).
- 6 Heinz Schulz and K. H. Thiemann, *Solid State Communications* **23** (11), 815 (1977).
- 7 S. Strite and H. Morkoç, *Journal of Vacuum Science & Technology B* **10** (4), 1237 (1992).
- 8 O. Ambacher, J. Smart, J. R. Shealy, N. G. Weimann, K. Chu, M. Murphy, W. J. Schaff, L. F. Eastman, R. Dimitrov, L. Wittmer, M. Stutzmann, W. Rieger, and J. Hilsenbeck, *Journal of Applied Physics* **85** (6), 3222 (1999).
- 9 I. Vurgaftman and J. R. Meyer, *Journal of Applied Physics* **94** (6), 3675 (2003).
- 10 O Madelung, *Data in science and technology: semiconductors*. (Springer-Verlag, Berlin, 1991).
- 11 Shuji Nakamura, *Solid State Communications* **102** (2–3), 237 (1997).
- 12 E. Fred Schubert, *Light-Emitting Diodes*, 2nd ed. (Cambridge university press, Cambridge, 2006).
- 13 J. Narayan, Punam Pant, A. Chugh, H. Choi, and J. C. C. Fan, *Journal of Applied Physics* **99** (5) (2006).
- 14 D. J. Bacon D. Hull, *Introduction to Dislocations*, Fourth edition ed. (Butterworth- Heinemann, 2001).
- 15 J.P. Hirth and J. Lothe, *Theory of Dislocations*, 2nd Edition ed. (John Wiley and Sons, New York).
- 16 S. Srinivasan, L. Geng, R. Liu, F. A. Ponce, Y. Narukawa, and S. Tanaka, *Applied Physics Letters* **83** (25), 5187 (2003).

- 17 J. F. Nye, *Physical Properties of Crystals* (Oxford University Press, New York, 1985).
- 18 A. Rosenauer, D. Gerthsen, and V. Potin, *physica status solidi (a)* **203** (1), 176 (2006).
- 19 Bougrov V., Levinshtein M.E., Rumyantsev S.L., and Zubrilov A., *Properties of Advanced*  
20 *Semiconductor Materials GaN, AlN, InN, BN, SiC, SiGe*. (John Wiley & Sons, Inc., New York, 2001).
- Laurie E. McNeil, Marcos Grimsditch, and Roger H. French, *Journal of the American Ceramic*  
21 *Society* **76** (5), 1132 (1993).
- Kwiseon Kim, Walter R. L. Lambrecht, and Benjamin Segall, *Physical Review B* **53** (24), 16310  
22 (1996).
- A. F. Wright, *Journal of Applied Physics* **82** (6), 2833 (1997).
- 23 C. Deger, E. Born, H. Angerer, O. Ambacher, M. Stutzmann, J. Hornsteiner, E. Riha, and G.  
Fischerauer, *Applied Physics Letters* **72** (19), 2400 (1998).
- 24 A. Polian, M. Grimsditch, and I. Grzegory, *Journal of Applied Physics* **79** (6), 3343 (1996).
- 25 R. B. Schwarz, K. Khachatryan, and E. R. Weber, *Applied Physics Letters* **70** (9), 1122 (1997).
- 26 M Yamaguchi, T Yagi, T Azuhata, T Sota, K Suzuki, S Chichibu, and S Nakamura, *Journal of*  
*Physics: Condensed Matter* **9** (1), 241 (1997).
- 27 D. Gerthsen, E. Hahn, B. Neubauer, V. Potin, A. Rosenauer, and M. Schowalter, *physica status*  
*solidi (c)* **0** (6), 1668 (2003).
- 28 E. Sarigiannidou, E. Monroy, B. Daudin, J. L. Rouvière, and A. D. Andreev, *Applied Physics Letters*  
**87** (20) (2005).
- 29 H. P. D. Schenk, M. Nemoz, M. Korytov, P. Vennéguès, A. D. Dräger, and A. Hangleiter, *Applied*  
*Physics Letters* **93** (8) (2008).
- 30 Fabio Bernardini, Vincenzo Fiorentini, and David Vanderbilt, *Physical Review B* **56** (16), R10024  
(1997).
- 31 Fabio Bernardini and Vincenzo Fiorentini, *Physical Review B* **64** (8), 085207 (2001).
- 32 Fabio Bernardini, Vincenzo Fiorentini, and David Vanderbilt, *Physical Review Letters* **79** (20),  
3958 (1997).
- 33 Fabio Bernardini and Vincenzo Fiorentini, *Applied Physics Letters* **80** (22), 4145 (2002).
- 34 J. A. Christman, R. R. Woolcott, A. I. Kingon, and R. J. Nemanich, *Applied Physics Letters* **73** (26),  
3851 (1998).
- 35 W. Tjhen, T. Tamagawa, C. P. Ye, C. C. Hsueh, P. Schiller, and D. L. Polla, presented at the Micro  
Electro Mechanical Systems, 1991, MEMS '91, Proceedings. An Investigation of Micro Structures,  
Sensors, Actuators, Machines and Robots. IEEE, 1991 (unpublished).
- 36 Fabio Bernardini and Vincenzo Fiorentini, *Physical Review B* **65** (12), 129903 (2002).
- 37 M. Leroux, N. Grandjean, M. Laügt, J. Massies, B. Gil, P. Lefebvre, and P. Bigenwald, *Physical*  
*Review B* **58** (20), R13371 (1998).
- 38 N. Grandjean, J. Massies, and M. Leroux, *Applied Physics Letters* **74** (16), 2361 (1999).
- 39 Stefano de Gironcoli, Stefano Baroni, and Raffaele Resta, *Physical Review Letters* **62** (24), 2853  
(1989).
- 40 David Vanderbilt and R. D. King-Smith, *Physical Review B* **48** (7), 4442 (1993).
- 41 F. Bernardini and V. Fiorentini, *physica status solidi (b)* **216** (1), 391 (1999).
- 42 E. Fred Schubert, *Light-emitting diodes*, 2nd edition ed. (Cambridge university press, 2006).
- 43 Yuanyang XIA, UNIVERSITE DE NICE-SOPHIA ANTIPOLIS, 2013.
- 44 Uwe Strauß, Adrian Avramescu, Teresa Lermer, Désirée Queren, Alvaro Gomez-Iglesias,  
Christoph Eichler, Jens Müller, Georg Brüderl, and Stephan Lutgen, *physica status solidi (b)* **248**  
(3), 652 (2011).
- 45 N. Grandjean, B. Damilano, S. Dalmaso, M. Leroux, M. Laugt, and J. Massies, *Journal of Applied*  
*Physics* **86** (7), 3714 (1999).
- 46 A. Thränhardt, C. Ell, G. Khitrova, and H. M. Gibbs, *Physical Review B* **65** (3), 035327 (2002).

- 47 T. Bretagnon, P. Lefebvre, P. Valvin, R. Bardoux, T. Guillet, T. Taliercio, B. Gil, N. Grandjean, F.  
Semond, B. Damilano, A. Dussaigne, and J. Massies, *Physical Review B* **73** (11), 113304 (2006).
- 48 Michael R. Krames, Oleg B. Shchekin, Regina Mueller-Mach, GerdO Mueller, Ling Zhou, Gerard  
Harbers, and M. George Craford, *J. Display Technol.* **3** (2), 160 (2007).
- 49 Daisuke Morita, Masashi Yamamoto, Kazuyuki Akaishi, Kousuke Matoba, Katsuhiko Yasutomo,  
Yoshio Kasai, Masahiko Sano, Shin-ichi Nagahama, and Takashi Mukai, *Japanese Journal of  
Applied Physics* **43** (9R), 5945 (2004).
- 50 Yukio Narukawa, Junya Narita, Takahiko Sakamoto, Kouichiro Deguchi, Takao Yamada, and  
Takashi Mukai, *Japanese Journal of Applied Physics* **45** (10L), L1084 (2006).
- 51 M. R. Krames, M. Ochiai-Holcomb, G. E. Höfler, C. Carter-Coman, E. I. Chen, I.-H. Tan, P. Grillot,  
N. F. Gardner, H. C. Chui, J.-W. Huang, S. A. Stockman, F. A. Kish, M. G. Craford, T. S. Tan, C. P.  
Kocot, M. Hueschen, J. Posselt, B. Loh, G. Sasser, and D. Collins, *Applied Physics Letters* **75** (16),  
2365 (1999).
- 52 H. M. Manasevit, *Journal of Crystal Growth* **13–14** (0), 306 (1972).
- 53 P. DeMierry; P. Mottier, *Les diodes électroluminescentes pour l'éclairage*. (Editions Lavoisier,  
2008).

## Chapter 2

Basic characteristics of InGaN/GaN hetero-structures



## Chapter 2

### Basic characteristics of InGaN/GaN hetero-structures

#### Introduction

It is well reported that despite the presence of a high dislocation density ( $> 10^8 \text{cm}^{-2}$ )<sup>1</sup>, InGaN/GaN quantum well-based LEDs are very efficient light emitters. Whereas, for other group III-V material devices, light intensity quenches even when the dislocation density is only just over  $\sim 10^3 \text{cm}^{-2}$ . Dislocation act as non-radiative recombination centers as found from cathodoluminescence (CL) experiment on GaN layers<sup>2</sup>. Yet, high brightness blue and green LED, of InGaN/GaN crystal system are commercially available<sup>3</sup>. The limited impact of dislocation density on LED efficiency draws the attention of research community. This remarkable feature of InGaN/ GaN system is assumed to be due to carrier localization within the layers. It was proposed that localization of carriers are occurring either due to Indium clustering and/or few monolayer of quantum well thickness variation as they cause potential fluctuation within the quantum wells. Carrier localization can be evidenced through the temperature dependent photoluminescence (PL) experiments- as it appeared to have “S” shaped behavior (redshift-blueshift-redshif) deviated from the standard Varshni law behavior<sup>4,5,6</sup>. Moreover, a large Stokes shift between the absorption edge and the emission energy for InGaN/GaN heterostructure has been observed by several research groups and the phenomenon was explained by referring to carrier localization due to indium clustering within the InGaN layers<sup>7,8,9,10</sup>.

We know that to incorporate an indium composition higher than 15% in InGaN QWs, the growth temperature should be around 700-800°C, which is quite low as compared to the growth temperature of GaN (900-1100°C). It has been reported that high indium composition (>15%) InGaN alloys have a low thermal stability<sup>11,12,13</sup> and the growth temperature difference between InGaN and capping GaN layer induces structural changes in InGaN QWs such as QW thickness fluctuations and indium clustering<sup>14,15</sup>. Moreover, due to the large lattice mismatch between the high indium (>15%) InGaN and GaN template, stress energy in grown InGaN layer induces the formation of defects such as V-pits and misfit dislocations (MDs) along with threading dislocations (TDs) to release the stress energy in the epilayer<sup>16,17,1</sup>.

Thus in this chapter, we are going to present some basic issues involved in InGaN/GaN heterostructures, grown along the [0001] growth orientation. Firstly, we will try to explain the reason behind the indium clustering which may occur in InGaN epilayers through the phase diagram of the wurtzite crystal system. Then from the concept of different types of dislocation and slip plane systems discussed in chapter 1, we will discuss the different relaxation processes reported for InGaN/GaN system. Later, the cause of quantum well thickness variation will be

highlighted. Finally, we will discuss the observed effects in LED performance due to these characteristics in InGaN/GaN hetero-structure.

## 2.1 Phase diagram: phase separation of indium

In earlier work, many authors identify and claim that they have observed chemical de-mixing of InGaN within their grown ternary alloy structure, emitting from UV to green light<sup>18,19,20,21,22,23</sup>. It is believed that due to the high miscibility gap between InN and GaN<sup>24</sup>, chemical de-mixing occurs in the ternary alloy. This high miscibility gap should lead to an InGaN layer composed of In-rich areas in an In-deficient matrix. The basic reason behind such de-mixing mechanism is nothing but thermodynamics.

Thermodynamics explain that the phase separation of a mixture can occur to minimize the free energy of the system. In a phase diagram (Figure 2-1), the spinodal (dashed line) and binodal line (black line) can be calculated using Gibbs function  $G = H - TS$  of a system, where H being the enthalpy, S the entropy, and T the temperature of the system. The enthalpy H and entropy S of the system depend on the indium composition x. The binodal line in the phase diagram denotes the absolute minima of the Gibbs function ( $\frac{\partial G}{\partial x} = 0$ ) and the spinodal line is calculated from the second derivative of the Gibbs function with respect to the composition x as ( $\frac{\partial^2 G}{\partial^2 x} = 0$ ). These two lines in phase diagram distinguish the three mixing regions as stable, meta-stable and unstable of the alloy following the standard theory<sup>25</sup>. The region above binodal line is known as the stable region, the region between binodal and spinodal line is known as the meta-stable and the region underneath the spinodal line is known as the unstable region of the phase diagram.

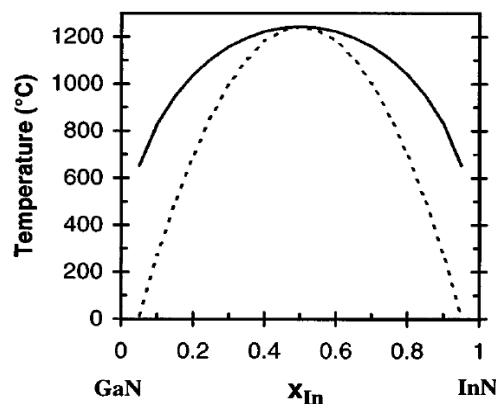


Figure 2-1: Binodal (black line) and spinodal (dashed line) curves for  $\text{In}_x\text{Ga}_{1-x}\text{N}$  system<sup>24</sup>

Ho and Stringfellow<sup>24</sup> have calculated and showed a phase diagram (Figure 2-1) for free-standing InGaN layer i.e., they do not consider the pseudomorphic growth of the InGaN layer

on top of GaN layer or even for some percentage of relaxation within the InGaN layer. According to their phase diagram, it is impossible to have an InGaN layer with a uniform composition for Indium composition above 10% at growth temperatures around 700°C-800°C. At such growth temperature the system is either in meta-stable or in unstable state of the phase diagram.

But later C. Tessarek et al<sup>26</sup> reported that both the spinodal and binodal line of a phase diagram change their position depending on the strain state of the grown InGaN layer. The critical temperature (i.e., the maximum of the spinodal line) decreases and the unstable region shifts toward higher indium composition  $x$ . Similarly, the binodal line also shift to higher composition ( $x$ ) values depending on fully relaxed to fully strained InGaN layer as shown in Figure 2-2.

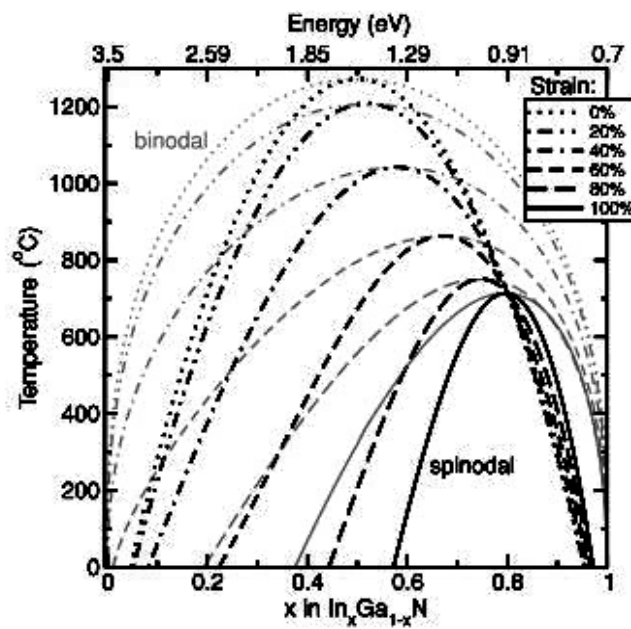


Figure 2-2: Spinodal (black) and binodal (gray) lines calculated for different strain states of the InGaN layer on a GaN substrate. The unstable region (under the spinodal line) is significantly reduced depending on the strain state of the grown InGaN layer<sup>26</sup>

From their presented graph (Figure 2-2), it is interesting to note that InGaN epilayer can be grown on a GaN substrate, up to 60% of Indium composition without any phase separation in the InGaN layer at around 700°C provided that the InGaN epilayer is pseudomorphically strained onto GaN.

Yet, many research groups demonstrate the phase separation in their grown samples with much less average indium composition with the help of x-ray diffraction (XRD)<sup>27,27,28,29,20,30</sup> (scanning) transmission electron microscopy (S/TEM)<sup>20,30,31,32,33,34</sup> in combination with energy-dispersive x-ray (EDX)<sup>33,35</sup>, photoluminescence (PL)<sup>33</sup> or energy filtered transmission electron

microscopy (EFTEM)<sup>36</sup> and three-dimensional atom probe field ion microscope (3DAP)<sup>37</sup> which is believed to be the cause of carrier localization within the sample.

To identify the exact size and amount of indium clustering within the layer, several research groups have come to the conclusion that their samples have In-rich areas or In clustering with 1-3 nm size observed by S/TEM<sup>31,36,38</sup>. For example, D. Gerthsen et al<sup>31</sup> reported that In clustering with more than 65% (66-98%) of indium composition within less than 3 nm in width has occurred, where the average indium composition is only of 12 to 18% depending on growth temperature ranging from 800°C to 840°C in their samples. Figure 2-3 shows the color coded map deduced from the local lattice parameter using digital analysis of lattice fringe image (DALI) technique of one sample grown at 800°C, demonstrating indium clustering within the sample.

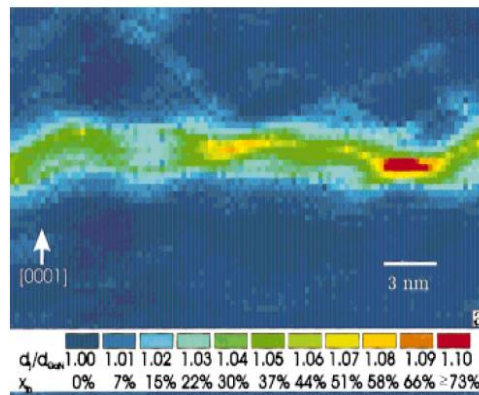


Figure 2-3: Color coded map showing the local indium clustering within the sample grown at 800°C deduced from the local lattice parameter<sup>31</sup>.

Yet, there are debates whether such In clustering seen through S/TEM experiments is due to genuine In clustering or from the electron beam damage done from the experiment. Smeeton et al<sup>39,40,41</sup> and O'Neill<sup>42</sup> demonstrated that they have observed In clustering in their samples due to electron beam damage. On the other hand, Kisielowski group<sup>43</sup> claim that they have observed indium-rich clustering with negligible electron beam energy and beam current density of 20-40 A-cm<sup>-2</sup> by TEM<sup>44</sup>. They have reported that green In<sub>x</sub>Ga<sub>1-x</sub>N quantum wells with average indium composition of 20% have genuine indium-rich clusters of 1-3 nm wide with In content up to about 40%<sup>32</sup>. Thus by reducing the exposure time and lowering the beam current density, one may still obtain S/TEM images to analyze whether they have In-rich clustering or not in their InGaN quantum wells. To avoid the TEM beam damage other experimental processes such as three dimensional atom probe field Ion microscopy (3DAP) imaging can be used. For example, Mark J. Galtrey et al<sup>37</sup> concluded from 3DAP analysis that no indium clustering exist in

their grown sample. Recently, T. Schulz et al<sup>45</sup> and T. Mehrrens et al<sup>46</sup> also reported that they do not find any Indium clustering within their samples (indium composition of ~17% and ~31%, respectively) while trying to observe clustering from very thin part of the prepared samples using scanning /transmission electron microscopy (S/TEM) and atom probe tomography (APT).

Thus we can conclude that with proper growth parameters InGaN quantum well with no indium clustering or huge composition variation may be achievable but still some random variation of indium composition may exist in place to place within the layer.

In this work, we tried to grow our InGaN epilayer at around 740°C temperature with about 17-20% of average indium composition, so according to what is reported in the literature we don't expect to find strong phase-demixion. However, it is likely that we may have some small indium composition variation within our grown InGaN epilayer.

## **2.2 Relaxation processes in InGaN/GaN system**

The next critical issue involved in InGaN/GaN system is the relaxation process of strain of the grown epilayer due to the high lattice mismatch by formation of different kinds of defects-such as V-pits, misfit dislocations (MDs) along with threading dislocations (TDs), which act as non-radiative recombination centers in the LED structure. In the following subsections the relaxation processes are described in details. Firstly, with the help of the ideas developed about different types of dislocation and its slip planes for wurtzite structure in chapter 1, relaxation processes of strained epilayer through glide of dislocation is discussed. Then, relaxation of strain through formation of V-defects and lastly, other observed relaxation processes are described.

### **2.2.1 Relaxation process through glide of dislocation**

Within last several decades different mechanisms have been proposed to explain the plastic relaxation process observed in the hexagonal crystal structure. Even some proposals are initially developed for cubic crystal structure such as Matthews-Blakeslee model and energy balance model. But later they have been modified to cover the wurtzite crystal system.

The schematic diagram of Figure 2-4 (a) and (b), illustrates the idea of Matthews-Blakeslee and the energy balance model, respectively to relax the strain of the epilayer in a cubic system. In these relaxation processes the dislocation glides through a slip plane as shown by gray plane.

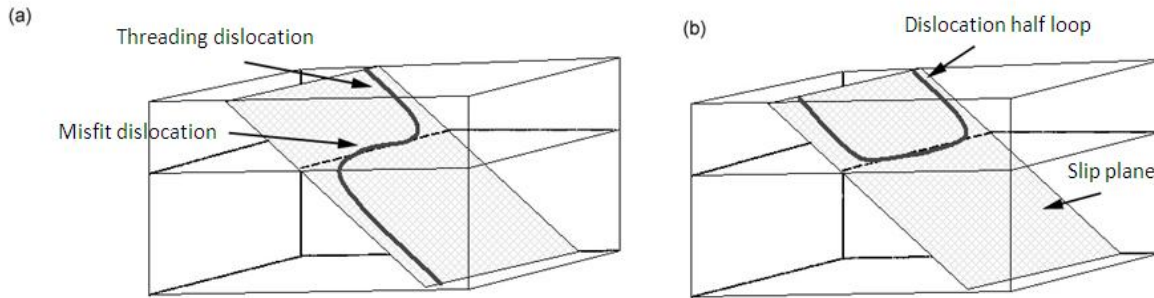


Figure 2-4: (a) Illustration of Matthews and Blakeslee model for relaxation of strain, (b) Energy balance model through glide of a misfit dislocation from free surface.

In the following subsections, both models are described in details in case of the wurtzite crystal system.

### 2.2.1.1 Matthews and Blakeslee model

Matthews and Blakeslee<sup>47</sup> model describes the mechanism of bending of a pre-existing threading dislocation at the interface of two different epilayers on a slip plane. According to the model, when an epilayer is grown on top of a substrate layer with sufficient thickness, a pre-existing TD within the substrate layer may not propagate straight through the epilayer but get bent and propagate along the interface of the two layers creating misfit dislocation within the slip plane before being thread through the epilayer. Figure 2-4 (a) schematically shows the whole mechanism as a pre-existing threading dislocation in the substrate layer gets bent at the interface of the two layers within the slip plane before being propagated through the epilayer. The forces involved in such mechanism are two forces known as the misfit force,  $F_{\text{misfit}}$  and the line tension force,  $F_{\text{line tension}}$ . The  $F_{\text{misfit}}$  is due to the misfit strain developed in the epilayer and the  $F_{\text{line tension}}$  corresponds to the line tension of the misfit segment deposited in the interface. In addition to these two forces another force known as Peierls force  $F_{\text{Peierls}}$ , was introduced in the model later on, which acts as a frictional force on threading segment of the dislocation due to the Peierls barrier<sup>48</sup>.

When the  $F_{\text{misfit}}$  is higher than the sum of the other two forces, then a pre-existing threading dislocation can bent in the interface of two layers and create a misfit dislocation (MD) in the interface as shown in Figure 2-4 (a). The condition for creating such a MD is as follows:

$$F_{\text{misfit}} = F_{\text{line tension}} + F_{\text{Peierls}}, \quad (2.1)$$

And the expression for the driving shear force  $F_{misfit}$  is as<sup>47</sup>

$$F_{misfit} = \frac{2G_{InGaN}(1+\nu)}{(1-\nu)} fbl \cos \lambda \cos \beta, \quad (2.2)$$

where  $G_{InGaN}$  is the bulk modulus and  $\nu$  is poisson's number of the InGaN layer, respectively.  $b$  is the magnitude of the Burgers vector,  $f$  is the misfit at the InGaN/GaN interface, which is defined as  $f = \frac{a-a_0}{a_0}$ , where  $a$  and  $a_0$  are strained and relaxed epilayer parameters, respectively and  $l$  is the length of the threading segment in the hetero-epitaxial layer. The product of the two cosine terms is known as the Schmid factor.

The different angles involved in the calculation are shown schematically in Figure 2-5. Two arbitrary Burgers vectors are shown as **AB** and **BC** in the figure having  $\langle 11\bar{2}3 \rangle$  and  $\langle 11\bar{2}0 \rangle$  direction, respectively. It is assumed that the pre-existing dislocation (not shown in the figure) is gliding on the slip plane  $\{1\bar{1}01\}$  indicated by the gray plane ABCD. The additional gray plane BCHG is considered to be normal to that slip plane. The two vectors  $i$  (**AJ** or **CF**) are defined as they should lie on the interfacial plane (either on AED or BCF plane) and their direction are perpendicular to the line of intersection (DA) of the interfacial plane and the slip plane<sup>49</sup>. The angle  $\lambda$ , is defined as the angle between the Burgers vector and vector  $i$ . Here for  $\langle 11\bar{2}3 \rangle$  Burger vector, the angle  $\lambda$  is defined as angle  $\angle JAB$  and for  $\langle 11\bar{2}0 \rangle$  Burger vector, the angle  $\lambda$  is not shown as it will make  $90^\circ$  angle with the corresponding vector  $i$  (**CF**). The angle  $\beta$ , is defined as angle  $\angle FCH$ , which is the angle between the vector  $i$  (**CF**) and the normal to the slip plane ABCD. (i.e., the normal direction (CH) to the slip plane (ABCD), which lies in the plane BCHG as shown in the figure).

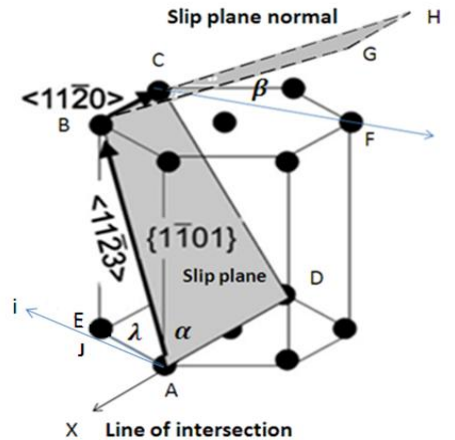


Figure 2-5: Schematic diagram showing the different angles ( $\alpha$ ,  $\beta$  and  $\lambda$ ) considered for the calculation of different forces.

The expression for line tension force along MD is defined as<sup>47</sup> :

$$F_{line\ tension} = \frac{G_{InGaN}G_{GaN}}{\pi(1-\nu)(G_{InGaN}+G_{GaN})} b^2(1 - \nu\cos^2\alpha) \left[ \ln\left(\frac{h}{b}\right) + 1 \right], \quad (2.3)$$

where,  $G_{GaN}$  is the bulk modulus of the thick GaN layer, serving as a substrate.  $h$  represents the thickness of the InGaN layer, and  $\alpha$  is the angle between the Burgers vector and the line direction of the misfit segment.

The frictional force acting on threading segment of a dislocation is expressed as<sup>48</sup> :

$$F_{Peierls} = 2blG_{InGaN} \frac{1-\nu\cos^2\chi}{1-\nu} \omega \exp\left[-2\pi \frac{d}{b} \frac{1-\nu\cos^2\chi}{1-\nu} \omega\right], \quad (2.4)$$

where  $d$  is the spacing of the slip plane and  $\chi$  is the angle between the Burgers vector and the line direction of the threading segment.  $\omega$  is a material constant given as :

$$\omega = \exp\left[\frac{4}{5}\pi^2 \frac{nkT}{G_{InGaN}V}\right], \quad (2.5)$$

where the number of atoms per unit cell is represented by  $n$ , the volume of the unit cell by  $V$ .  $T$  is the growth temperature of the InGaN layer in absolute degree, and  $k$  is the Boltzmann's constant.

### 2.2.1.2 Energy balance model

People and Bean<sup>50</sup> and Freund and Suresh<sup>51</sup> described energy balance models for infinite MDs in cubic SiGe or GaAs systems. The models were later adopted for III-nitride system with some modification. According to the proposal of Freund and Suresh a simple energy balance model is shown in Figure 2-6 as a cross-sectional view of the Figure 2-4(b). In this model a misfit dislocation infinitely long was considered to be placed in the system from free surface to the substrate-epilayer interface through a slip plane.

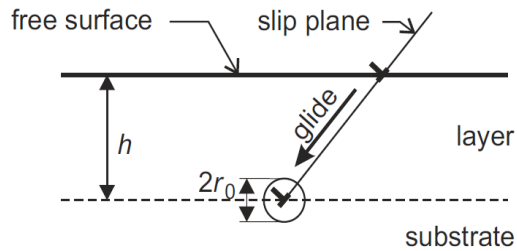


Figure 2-6: A cross sectional view of a film-substrate hetero-interface illustrating the glide of an infinitely long straight dislocation (perpendicular to the plane of the page) from a free surface.<sup>52</sup>

Compared to the elastically strained pseudomorphic epilayer, one straight infinitely long dislocation, which has glided from the free surface down into the hetero-interface, changes the total energy (per unit length) of the system by

$$\Delta E = \frac{dE_d}{dl} + \frac{dW}{dl}, \quad (2.6)$$

The energy introduced within the system by this infinite long MD was considered as dislocation energy  $\frac{dE_d}{dl}$  and the work done  $\frac{dW}{dl}$  by the system during this dislocation glide to partially relax the misfit strain.

The formula of dislocation energy  $\frac{dE_d}{dl}$  for an infinitely long straight dislocation lying on the hexagonal c-plane can be expressed following the procedure described by Steed<sup>53</sup> as :

$$\frac{dE_d}{dl} = (Ab_{e,\parallel}^2 + Bb_{e,\perp}^2 + Cb_s^2) \ln \frac{R}{r_0}, \quad (2.7)$$

where  $b_{e,\parallel}$ ,  $b_{e,\perp}$  and  $b_s$  are components of the Burgers vector as an edge component lying on (0001) plane, an edge component perpendicular to (0001) plane and a screw component respectively. And the symbol R and  $r_0$  represent the outer and inner cut-off radii of the elastic media adjoining the dislocation<sup>54</sup>. For  $\frac{1}{3}\langle 11\bar{2}3 \rangle / \{11\bar{2}2\}$  slip system, the expression for work done  $\frac{dW}{dl}$  by the system, is given by

$$\frac{dW}{dl} = \frac{(c_{11}+c_{12})c_{33}-2c_{13}^2}{c_{33}} \varepsilon_m b_{e,\parallel} h, \quad (2.8)$$

where h is the deposit layer thickness,  $c_{ij}$  are the elastic constants and  $\varepsilon_m$  is the misfit strain.

Here we express the expression for work done function  $\frac{dW}{dl}$  by a system only for  $\frac{1}{3}\langle 11\bar{2}3 \rangle / \{11\bar{2}2\}$  slip system as S. Srinivasan et al<sup>55</sup> proposed that MD can glide down from a free surface most actively along this slip system than any other pyramidal slip system. And moreover we intentionally avoid expressing the work function  $\frac{dW}{dl}$  for other slip systems -basal and prismatic plane system as explained in section 2.2.1.4.

### 2.2.1.3 Critical thickness

The epilayer thickness above which a system just gains sufficient energy either to create a MD in the interface of two layers from a pre-existing threading dislocation or has sufficient strain

energy to allow the glide of a long MD from the free surface into the interface plane, to relax the build in stress energy developed due to epilayer growth, is called the critical thickness.

According to Matthew and Blakeslee model, from equation 2.1, the critical thickness (CT) is the epilayer thickness, at which the misfit force ( $F_{\text{misfit}}$ ) is just equal to the other two forces. Similarly, according to energy balance model, from equation 2.6, the condition for critical thickness of the epilayer is as follows:

$$\Delta E = 0, \quad (2.9)$$

It is because when,  $\Delta E > 0$ , the energy involved in introducing the MD to the system is higher than that of energy supplied by the system to do that work, so the creation of a MD is energetically unfavorable, MD will not create in the hetero-interface through the slip plane as shown in Figure 2-4 (b). On the other hand, if  $\Delta E < 0$ , then the system has sufficient strain energy and can use the required energy from the system to introduce the MD and relax the system.

D. Holec et al<sup>52</sup> have shown for  $\frac{1}{3}\langle 11\bar{2}3 \rangle / \{11\bar{2}2\}$  slip system, the energy balance model with proper hexagonal symmetry of wurtzite materials describes the critical thickness of the InGaN/GaN material system more appropriately than that of other models developed by Fischer et al<sup>56</sup> and People and Bean<sup>50</sup>. They also showed that changing the isotropic approximation<sup>47</sup> to more appropriate hexagonal symmetry of wurtzite materials for calculating the critical thickness value, may reduce the value by 10%-20%. Figure 2-7 shows the comparison graph for such two calculations and Figure 2-8 shows the 10-20% less in CT value while considering indium composition of up to 30% within the layer. For example, for Indium composition of 16-25%, the critical thickness is below 4 nm.

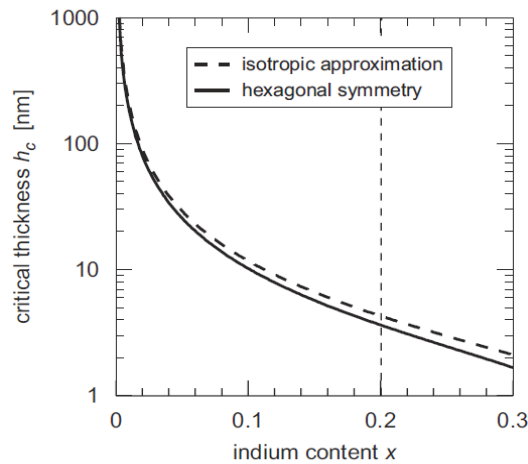


Figure 2-7: The calculation of critical thickness against composition curves for the single-layer  $\text{In}_x\text{Ga}_{1-x}\text{N}/\text{GaN}$  system. The two curves correspond to the isotropic approximation<sup>47</sup> and to the energy balance model with the proper hexagonal symmetry of wurtzite materials.<sup>52</sup>

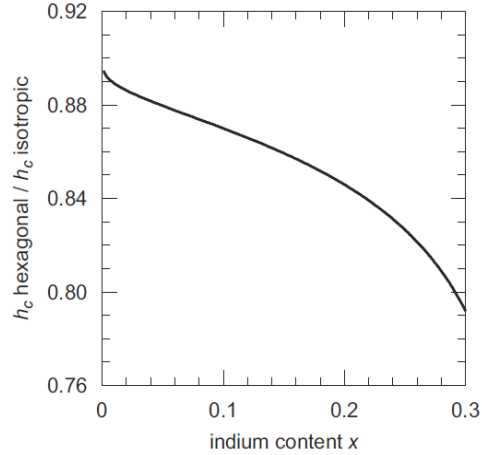


Figure 2-8: The effect of the hexagonal symmetry on the critical thickness values for the  $\text{In}_x\text{Ga}_{1-x}\text{N}/\text{GaN}$  single-layer system. The hexagonal symmetry lowers the critical thickness values by about 10-20% when compared to the isotropic case<sup>52</sup>.

#### 2.2.1.4 Limitations of Matthews-Blakeslee and energy balance model

Considering Figure 2-5 along with equation 2.2, we can find that the driving shear force  $F_{\text{misfit}}$  has zero value for both basal plane and prismatic plane slip systems (described in chapter 1) due to the fact that the term  $\cos \lambda$  of the Schmid factor becomes zero for both the two plane systems. But for the pyramidal slip system it has non-zero value. Table 7, gives the value of the effective shear factor for different slip systems. From Table 7, it can be concluded that the Matthew and Blakeslee model is effective only for  $\langle a+c \rangle$  type dislocation in pyramidal planes. This is also why the work done function  $\frac{dW}{dt}$  by a system has not been derived for the basal and prismatic plane slip system in energy balance model in section 2.2.1.2.

Table 7: Effective shear factor,  $\cos \lambda$ , for different slip system<sup>55</sup>

	Slip system	$\cos \lambda$
Basal plane	$\{0001\}\langle 11\bar{2}0 \rangle$	0
Prism planes	$\{1100\}\langle 1120 \rangle$	0
	$\{1100\}\langle 0001 \rangle$	0
	$\{1120\}\langle 0001 \rangle$	0
	$\{1120\}\langle 1100 \rangle$	0
Pyramidal planes	$\{11\bar{2}2\}\langle 1100 \rangle$	0
	$\{1101\}\langle 1120 \rangle$	0
	$\{1102\}\langle 1120 \rangle$	0
	$\{11\bar{2}2\}\langle 1123 \rangle$	0.524
	$\{1101\}\langle 1123 \rangle$	0.454
	$\{1102\}\langle 1101 \rangle$	0.730

Very few research groups have claimed to observe the relaxation for their grown epilayer through above described models (Matthews-Blakeslee and energy balance model). For example, S. Srinivasan et al<sup>55</sup> reported that pre-existing dislocation has glide through  $\{1\ 1\ \bar{2}\ 2\}\{1\ 1\ \bar{2}\ 3\}$  slip system, leaving  $\langle 1\ \bar{1}\ 0\ 0 \rangle$  line direction mark on the (0001) plane of the surface, obeying Matthews-Blakeslee model in their samples. They have calculated and showed that for  $\text{In}_{0.10}\text{Ga}_{0.90}\text{N}$  layer  $\sim 100$  nm thick deposited on an epitaxial lateral overgrown GaN template, has the highest net force  $F_{\text{net}} = F_{\text{misfit}} - F_{\text{line tension}} - F_{\text{Peierls}}$ , to create MD through  $\{11\bar{2}2\}\{11\bar{2}3\}$  slip system. Similarly, R. Liu et al<sup>57</sup> also reported MDs generation by energy balance model for their sample having  $\text{In}_{0.17}\text{Ga}_{0.83}\text{N}$  layer of  $\sim 100$  nm thick deposited on GaN substrate with lower than  $\sim 10^7$  cm<sup>-2</sup> threading dislocation density. In both cases, the calculated CT would be around 9.6 nm and 5.5 nm, respectively. So the creation of MDs via  $\{1\ 1\ \bar{2}\ 2\}\{1\ 1\ \bar{2}\ 3\}$  slip system are well justified as both the samples have much larger layer thickness of about 100 nm than calculated critical thickness.

The occurrence of such plastic relaxations in wurtzite crystals of polar orientation is rare because the length of the Burger vector for  $\langle a+c \rangle$  type dislocation is high. As we can find from both equations 2.3 and 2.4, the line tension force  $F_{\text{line-tension}}$  and the Peierls force,  $F_{\text{Peierls}}$  increase as the length of the Burger vector ( $b$ ) gets increased. In case of line tension  $F_{\text{line-tension}}$ , it has a square term dependency of Burger vector length and Peierls force,  $F_{\text{Peierls}}$ , increases exponentially with the increasing value of Burger vector length. Both line tension force and the Peierls force oppose the occurrence of MDs through any pyramidal plane of the hexagonal structure. Moreover, generally the pre-existing threading dislocations have vertical orientation i.e., they are in prismatic plane of the hexagonal structure. Thus it is believed that epilayer gets relaxed through other plastic relaxation processes first - such as formation of V-defects at the end of a vertically oriented pre-existing threading before being relaxed through Matthews-Blakeslee or energy balance model relaxation processes described above.

So in the next subsection, we are going to describe the relaxation of epilayer through formation of V-defects and also other relevant features of V-defects.

### 2.2.2 Relaxation process through generation of V defects

V defect (also known as V-pits or pinholes) itself is a plastic deformation but it helps to elastically relax the strain of the layer at or near its surface. Figure 2-9 shows the schematic model of elastic relaxation at V-defects, where it indicates that at the surface of V-defects the strain is relaxed while the other parts of the layer are in strain state. Thus the formation of V-defects in InGaN epitaxial layer is assumed to be due to the elastic relaxation of strain within the surface area of the layer<sup>58</sup>. It is also proposed that the formation of V-defects could be due to the kinetic effects of growth process along different crystallographic planes<sup>59</sup>. Two-

dimensional finite-element calculations of pit like structures show that such pits may efficiently reduce the strain by elastic relaxation<sup>60</sup>.

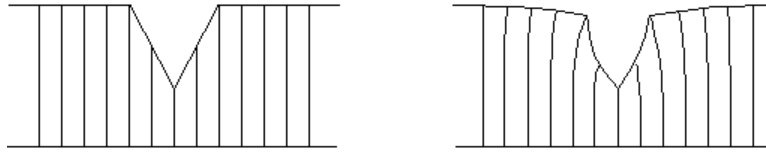


Figure 2-9: Model of elastic relaxation at V-defects. Left image shows the fictitious situation with rigid lattice planes and right image shows the elastic relaxation<sup>49</sup>

Again several research groups have already observed and suggest that threading dislocations (TDs) may help to relax the InGaN active layer by assisting to grow V-defects in the layer. It is generally reported that the vertex of a V-defects is connected to a TD. The type of such dislocations can be of any type such as pure  $\langle a \rangle$ ,  $\langle c \rangle$  and/or  $\langle a+c \rangle$  type of dislocations<sup>49,16,61,62</sup>.

V-defects are also reported to be found in epilayers where there are no TDs associated with them but the generation of such defects are from stacking fault (SF)<sup>16</sup>. Figure 2-10 shows the schematic model for V-defects formation mechanism.

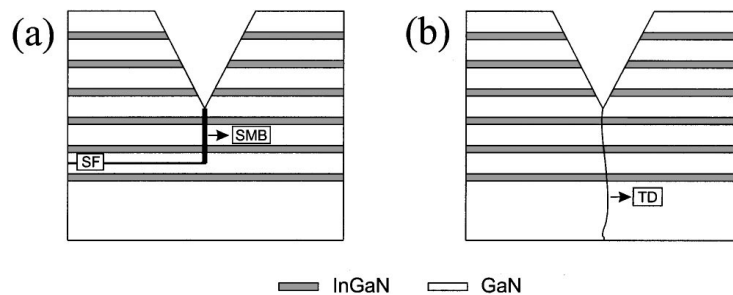


Figure 2-10: Schematic models for V-defect formation connected with (a) a stacking mismatch boundary induced by stacking faults and (b) a threading dislocation (TD).<sup>16</sup>

Figure 2-11 schematically shows the cross sectional view along [11-20] direction of a wurtzite structure, where the site at which growing epilayer with ABABAB lattice sequence is altered to ABCBCB lattice sequence. This site is known as stacking fault (SF) of the structure. After such SF, epilayer may grow with two different lattice sequences- ABABAB and ABCBCB in two different parts of the layers, which eventually creates a junction at the two different lattice sequence layer parts. This junction is known as stacking mismatch boundary (SMB). Later from such SMB, V defects can be initiated as shown in the Figure 2-11. H. K. Cho et al<sup>16</sup> reported V defects generated both from SF and from TD in their highly strained  $\text{In}_{0.3}\text{Ga}_{0.7}\text{N}/\text{GaN}$  MQW sample. Figure 2-12(a) shows the HRTEM image of an area with SF and SMB region within the sample

and Figure 2-12(b) shows the cross-section view of the sample which demonstrates the origin of the V-defects from both threading dislocation (TD) and stacking fault (SF) regions.

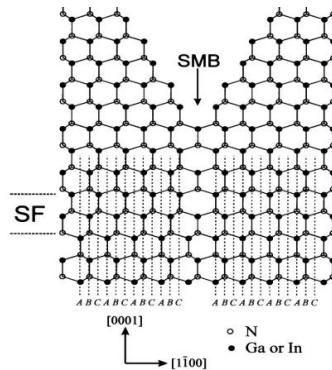


Figure 2-11: Schematic diagram showing the generation process of V- defects from the stacking fault of the grown epilayer<sup>16</sup>.

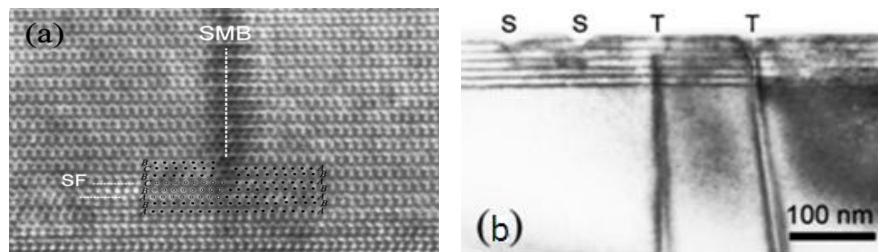


Figure 2-12: (a) HRTEM images confirming the stacking fault (SF) and the stacking mismatch boundary (SMB) of a sample, (b) Cross-sectional bright field TEM images from the highly strained  $\text{In}_{0.3}\text{Ga}_{0.7}\text{N}/\text{GaN}$  MQW sample. Where 'S' indicating the pits generated from stacking fault and 'T' for pits connected with TDs<sup>16</sup>.

It is assumed that when the concentration of impurity atoms increases to a certain degree, it may slow down or inhibit the crystal growth at that place and form V-defects. Z. Liliental-Weber et al<sup>59</sup> reported that when oxygen content was increased from  $5 \times 10^{17} \text{ cm}^{-3}$  to  $4 \times 10^{18} \text{ cm}^{-3}$  in the layer, the density of V-defects increased from  $1 \times 10^7$  to  $3 \times 10^7 \text{ cm}^{-2}$  without any measurable change in the dislocation density or lattice parameter.

### 2.2.2.1 Shape and size of the V-defects

Cross sectional transmission electron microscopy (cs-TEM) and atomic force microscopy (AFM) measurements confirm that V-defects have hexahedron cone morphology with  $\{1\bar{1}01\}$

sidewalls<sup>63</sup>. Figure 2-13 shows the schematic view of a hexagonal V-defect emerging at the apex of a threading dislocation. When the pits are observed from the  $\langle 0001 \rangle$  direction, the six boundary lines of the hexagon are found to be perpendicular to the  $\langle 1\bar{1}00 \rangle$  direction<sup>64,65</sup>. Figure 2-14 shows the schematic diagram and also the AFM image of a V-defect.

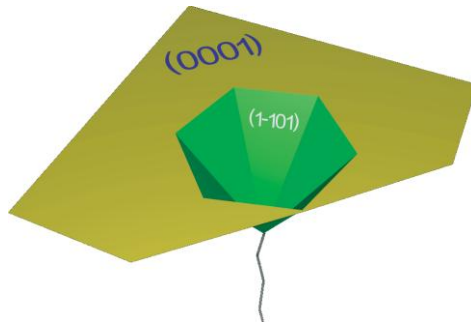


Figure 2-13: Schematic diagram of V-defects having  $\{1\bar{1}01\}$  sidewalls and emerging from the apex of a threading dislocation.<sup>63</sup>

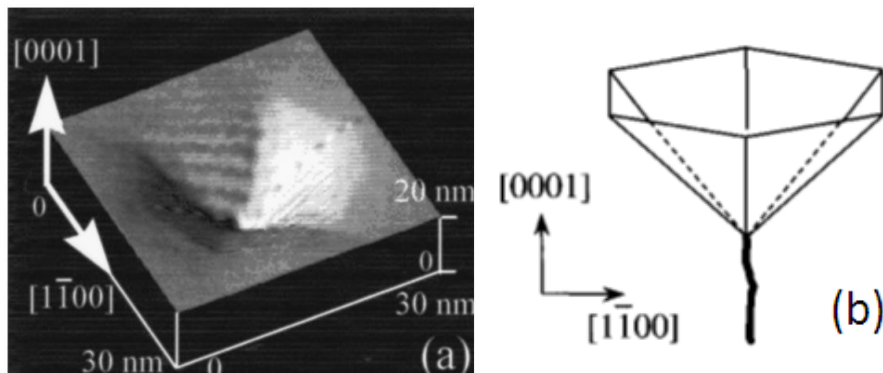


Figure 2-14: (a) An AFM image and (b) schematic diagram illustrating the three-dimensional (3D) morphology<sup>64</sup>

Y. Chen et al<sup>64</sup> demonstrated that the number of QWs has an impact on the size of the V-defects. They have reported that before any InGaN layer deposition, the GaN buffer layer has  $\sim 1 \times 10^8 - 10^9 \text{ cm}^{-2}$  TDs and estimated V-defect density of less than  $10^6 \text{ cm}^{-2}$  in their wafers. But when several InGaN layers of  $\sim 30\%$  of Indium have been deposited, the V-defect density increased drastically to  $\sim 2.1 \times 10^9 \text{ cm}^{-2}$  and the size of pits also increased from  $\sim 10 \text{ nm}$  on the surface of three QWs to  $\sim 25 \text{ nm}$  on the surface of five QWs<sup>64</sup>. Moreover, they have also found that while growing the same structure with less Indium ( $\sim 20\%$ ) composition, the V-pit density is approximately one order of magnitude less ( $\sim 2 \times 10^8 \text{ cm}^{-2}$ ) whereas the total numbers of TDs are quite same as that of high In composition ( $\sim 30\%$ ) samples. This suggests that the size and number of V-defects also help to relax the strain of the epilayer at the surface of the V-defects.

### 2.2.3 Other relaxation processes observed in wurtzite crystal structure

It has been clearly demonstrated in section 2.2.2 that no threading dislocation of either <a-type> or <c-type>, is involved in relaxing the build-in stress of the epilayer following Matthews-Blakeslee model. Even an infinitely long misfit dislocation will rarely glide through {11-22} slip plane from the free surface to relax the strain. Yet, B. Jahnke et al<sup>49</sup> reported that when the V-pits reach the heteroepitaxial interface, <a-type> misfit dislocations are created and propagate through the basal {0001} plane as schematically demonstrated in Figure 2-15 to relax the stress at the apex of V-pits.

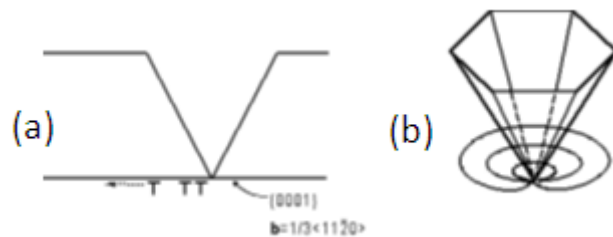


Figure 2-15: (a) Schematic diagram showing edge type dislocation generated from a V-pit, which intersects the interface of two different layers, (b) Perspective view showing how the misfit dislocation glides away from the deep V-pit<sup>49</sup>

A similar type of relaxation has also been observed by R. Lui et al<sup>57</sup>, where they describe the propagation of <a-type> dislocations as radial-shape dislocation half loops. They clearly identified that an <a-type> dislocation has been created at the interface of the two layers exposed by V-defects, while the diameter of the half loops in basal plane depends on the amount of stress relaxation. Mesa patterning on the GaN substrate can also help to form the radial shape dislocation half loops within the basal plane of the InGaN/ GaN interface - if the mesa patterning expose the hetero-interface to free surface<sup>66</sup>.

Finally, P. Cantu et al<sup>67</sup> and A. E. Romanov et al<sup>68</sup> reported a mechanism of stress relaxation by inclination or bending of threading dislocation for GaN/AlGaIn system. But for the InGaIn/GaN system such type of stress relaxation of epilayer has not been reported so far.

We are going to present whether our studied samples have such relaxation processes involved in them in chapter 4.

### 2.3 Quantum well thickness variation

The in-plane variation of the QW thickness is observed in any semiconducting crystal due to the variable size of the terraces<sup>69,70,71,72</sup>. In InGaIn/GaN hetero-structures more severe variation of the QW thickness can be observed. It is assumed that due to growth temperature differences in InGaIn QWs and GaN barrier layer, InGaIn layers suffer from thickness variation.<sup>15,73</sup> Indium

atoms out-diffuse and/or evaporate from the upper part of deposited InGaN layer due to high temperature ramp. S. Kret et al<sup>14</sup> clearly demonstrated InGaN QW thickness variation caused by high temperature ramp by comparing two samples, one grown at a single temperature (780°C) and other grown with a two temperature processes, i.e., the InGaN QW grown at 730°C and GaN barrier at 900°C. Comparing the two images in Figure 2-16, it is evident that the sample with higher barrier growth temperature has more QW thickness variation. They have also observed local disappearing of QWs and very low Indium composition within less thick part of the QWs.

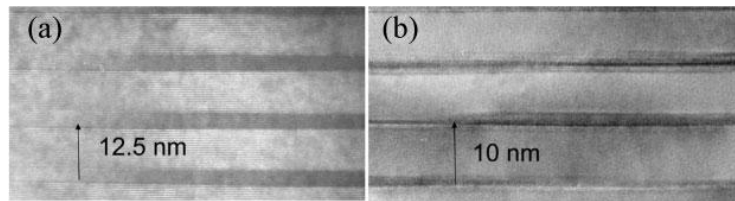


Figure 2-16: Comparison of two MQW structures- a) grown at single temperature process 780°C b) a two temperature process 730/900°C, demonstrating the high growth temperature effect to QW thickness.<sup>14</sup>

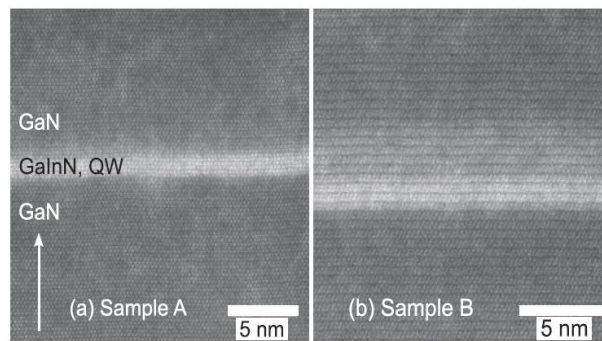


Figure 2-17: Scanning transmission electron microscopy images a) sample with 24% indium composition and b) sample with 30% of indium composition.<sup>74</sup>

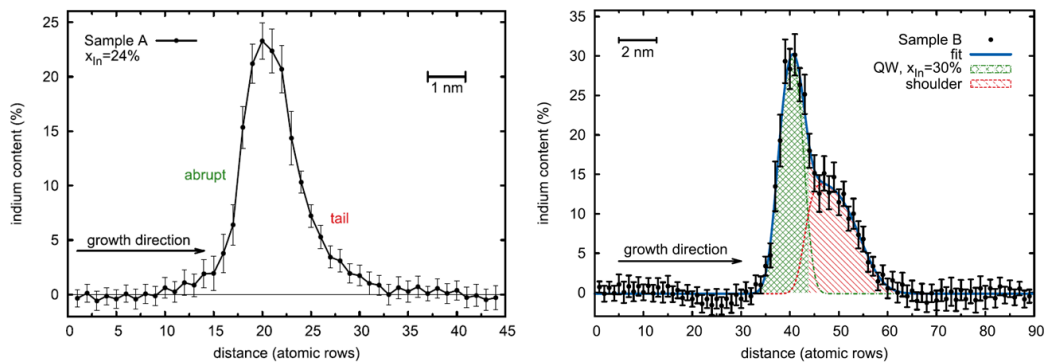


Figure 2-18: Indium content distribution along growth direction for sample A and B shown in Figure 2-17.<sup>74</sup>

L. Hoffmann et al.<sup>74</sup> also suggested that due to high temperature ramp, Indium from the QWs gets out diffused and appear in the barrier layer. From high angle annular dark field – scanning transmission electron microscopy (HAADF-STEM) imaging (the HAADF-STEM imaging technique will be described more precisely in chapter 3) they demonstrated that (Figure 2-17), the lower interface of GaN- InGaN layer shows abrupt change in contrast but the upper interfaces are not that sharp. Moreover, calculating the indium distribution for both images in Figure 2-17 along the growth direction they have confirmed that the Indium gets out-diffused from the InGaN QW layer to GaN barrier layer (Figure 2-18). In both cases, the lower interface has abrupt change in Indium composition but either a tail or a shoulder type distribution is found in the top interface of InGaN –GaN layers, which indicate the out diffusion of Indium from the QWs. The explanation of such shoulder type indium distribution is thought to be due to the incorporation of indium adlayer during the growth process.

Furthermore, many researchers have reported that indium diffusion from the InGaN well layer into the GaN barrier layer in the MQW active layer occurs during the thermal annealing at temperature above 1000°C.<sup>75</sup> Therefore, high temperature p-GaN layer deposition in LED structure may also degrade the MQW structures<sup>76,77</sup>.

In chapter 4, we are going to present the QW thickness variation phenomena in our studied samples in details.

## 2.4 LED performance due to these basic characteristics

We know that the PL intensity  $I_{PL}(T)$  can be expressed as follows:

$$I_{PL}(T) = \frac{g}{1 + \frac{\tau_R(T)}{\tau_{NR}(T)}} \quad (2.10)$$

where,  $\tau_R(T)$  and  $\tau_{NR}(T)$  represent temperature dependent radiative and non-radiative life time of carriers, respectively and  $g$  is the exciton generation rate. From equation 2.10, it is obvious that to have high intensity PL, we have to have very low radiative life time ( $\tau_R(T)$ ) and high non-radiative life time ( $\tau_{NR}(T)$ ) of the excited carriers within the structure. Generally, at higher temperature the non-radiative life time ( $\tau_{NR}(T)$ ) of the excited carriers becomes low as the carriers have sufficient energy to move and find defects within the structure before being radiatively recombined. Thus any defect such as TD, MD along with V-pits is undesirable for light emitting structure as they act as non-radiative recombination centers and reduce the overall intensity.

However, both advantage and disadvantage of such defects are reported for InGaN/GaN system. For example, in case of indium composition variation (phase separation) within QW

layers, it has been reported that InGaN/GaN system has lower sensitivity of TDDs compared to the other III-V semiconductor materials light structure due to carrier localization within InGaN QW layers.<sup>78</sup> On the other hand, several research groups also demonstrated that due to phase separation, they observed a broad line spectrum from their samples<sup>26,14,73</sup>. Z. Z. Chen et al<sup>19</sup> demonstrated through electroluminescence (EL) experiment that the sample emits green light (due to high In composition) from few areas while injecting with low current density, as the injected carriers occupy the lower energy state within the structure but increasing the injection current level, the EL spectrum dominates with blue light (due to low In composition), where green spots become dimmed compared to the blue emission from the whole sample as the injected carriers started to occupy not only lower energy states but also higher energy states within the structure.

Similarly, for V-defects, it has been reported that QWs grown on the side walls  $\{1-101\}$  of V-defects act as energy barrier for carriers to get non-radiatively recombines at the core of the V-defects. For example, A. Hangleiter et al<sup>63</sup> identify that sidewalls of the V-defects has much less QW thickness than that of (0001) planer region QWs. Figure 2-19 shows the thickness of QW and barrier layers of 3.5 nm and 11 nm, respectively on the (0001) plane region but much less thickness on the  $\{1\bar{1}01\}$  side walls of the V-defect as 1.1 nm and 2.3 nm for QW and barrier layers, respectively. Thus this QW thickness variation creates the band gap variation between the two regions and helps carriers to recombine in (0001) planer region of the structure with higher probability.

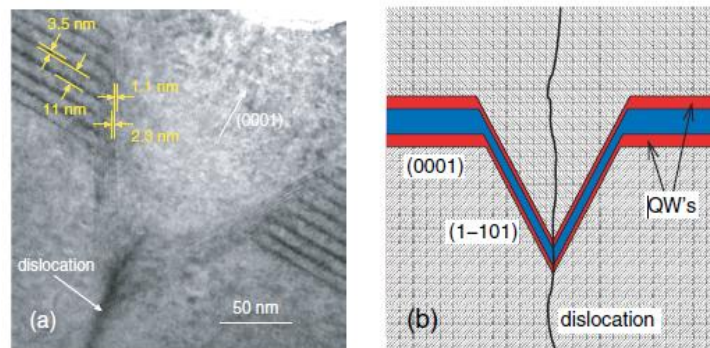


Figure 2-19: (a) Transmission electron microscopy images of an InGaN/ GaN multiple quantum well structure. In the planer region high quality QW's with well-defined sharp interfaces are visible. In the vicinity of a threading dislocation, a V-defect appears with sidewall QW's thickness much lower than for the (0001) QW's. This is also schematically shown in (b) <sup>63</sup>.

On the other hand, the presence of V defects also causes broader line spectrum emission as the sidewalls  $\{1\bar{1}01\}$  of the V-defects has higher band gap energy than that of (0001) planer

region. Low temperature scanning near-field optical microscope (SNOM) data confirms that band gap variation within the two regions near the vicinity of the V-defects<sup>63,79</sup>, as the emission wavelength from the region in between V-defects has approximately 430 nm of wavelength emission (black line) and the spectra from areas close to the defects shows additional emission peaks in the 380-410 nm range (Figure 2-20) in addition to the main emission for In<sub>0.12</sub>Ga<sub>0.88</sub>N MQW structure.

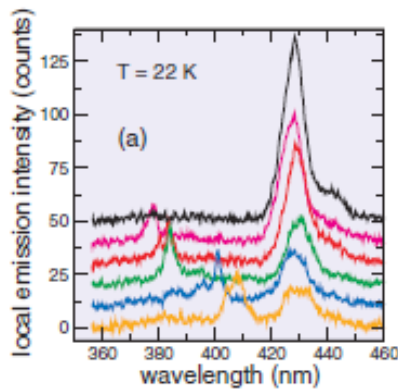


Figure 2-20: Low temperature emission spectra obtained from nm-size areas close to threading dislocations with a near field microscope<sup>63,79</sup>. Besides the main emission at 430 nm (black line – corresponds to the emission from the area in between the V defects) multiple sharp peaks from different locations near V-defects appear in the range 380–410 nm.

Again from cathodoluminescence (CL) experiment, it has been suggested that V-defect areas have higher indium composition than defect free planer area as V-defect regions emit higher wavelength light (shoulder peak emission) than that of planer region (main peak) of the LED structure<sup>80,62</sup>. Thus V defects within the structure causes to emit broad line spectrum.

InGaN/ GaN samples with high TDD ( $\sim 10^9 \text{ cm}^{-2}$ ) but very low Indium composition ( $< 10\%$ ) (UV – blue light) may not have any indium clustering within the active region but still they are able to emit relatively higher brightness light<sup>3</sup>. The possible explanation of such phenomenon may be due to carrier localization from quantum well thickness variation. Though it has been reported, for a sample with 25% of In composition, 3.3 nm of InGaN well width and large internal electric field of 2MV/cm, that only one monolayer of thickness change can cause 58 meV of band gap energy change in InGaN/GaN system<sup>81</sup>, so InGaN well thickness is also a great issue in obtaining a desired line spectrum from such structure.

Thus we can conclude that though these characteristics allow us to explain the better performance of InGaN/GaN LEDs than that of other III-V semiconductor light devices but still they have overall detrimental impact on efficiency, emitted light intensity and line spectrum from the structure.

## Summary

In this chapter an overview of different characteristics involved in InGaN/ GaN system with high indium composition and their impact on LED performance has been discussed. To have an efficient LED with higher wavelength (> 500 nm) emission, we have to have high Indium composition (>15%) InGaN QWs with few structural defects. It is therefore, a very challenging task to have multi quantum well crystal structure with few defects. In our analyzed sample, we grow the active InGaN layers within 16% to 25% of indium composition at 680°C to 740°C growth temperature. Moreover, we keep the InGaN layer thickness within 2-3 nm to make sure that they are quite below the critical thickness value. The target of such growth process is to be in a stable state of the phase diagram to avoid any spinodal decomposition to occur in our pseudomorphically grown InGaN layer.

In this work few monolayers of different types of capping layers are deposited after InGaN quantum well to investigate whether the capping layer compensates the QW thickness variations, indium clustering, segregation and/or evaporation due to the high temperature GaN barrier growth.

Atomic force microscopy (AFM), x-ray diffraction (XRD), photo-luminescence (PL), (scanning) transmission electron microscopy ((S)TEM) has been utilized to analyze the grown samples.

In the next chapter, the basics of the measurement instruments and characterizing techniques used in this work are discussed.

## References

- <sup>1</sup> F.A. Ponce and D.P. Bour, *Nature* **386**, 351 (1997).
- <sup>2</sup> S. J. Rosner, E. C. Carr, M. J. Ludowise, G. Girolami, and H. I. Erikson, *Applied Physics Letters* **70** (4), 420 (1997).
- <sup>3</sup> S. Nakamura, M. Senoh, N. Iwasa, and S. Nagahama, *Japan Journal of Applied Physics* **34** (Part 1), L797 (1995).
- <sup>4</sup> Yong-Hoon Cho, G. H. Gainer, A. J. Fischer, J. J. Song, S. Keller, U. K. Mishra, and S. P. DenBaars, *Applied Physics Letters* **73** (10), 1370 (1998).
- <sup>5</sup> K. L. Teo, J. S. Colton, P. Y. Yu, E. R. Weber, M. F. Li, W. Liu, K. Uchida, H. Tokunaga, N. Akutsu, and K. Matsumoto, *Applied Physics Letters* **73** (12), 1697 (1998).
- <sup>6</sup> P. Lefebvre, T. Taliencio, A. Morel, J. Allègre, M. Gallart, B. Gil, H. Mathieu, B. Damilano, N. Grandjean, and J. Massies, *Applied Physics Letters* **78** (11), 1538 (2001).
- <sup>7</sup> S. F. Chichibu, A. C. Abare, M. S. Minsky, S. Keller, S. B. Fleischer, J. E. Bowers, E. Hu, U. K. Mishra, L. A. Coldren, S. P. DenBaars, and T. Sota, *Applied Physics Letters* **73** (14), 2006 (1998).
- <sup>8</sup> B. Damilano, N. Grandjean, J. Massies, L. Siozade, and J. Leymarie, *Applied Physics Letters* **77** (9), 1268 (2000).

- 9 R. W. Martin, P. G. Middleton, K. P. O'Donnell, and W. Van der Stricht, *Applied Physics Letters* **74** (2), 263 (1999).
- 10 L. Siozade, P. Disseix, A. Vasson, J. Leymarie, B. Damilano, N. Grandjean, and J. Massies, *physica status solidi (a)* **183** (1), 139 (2001).
- 11 G. T. Thaler, D. D. Koleske, S. R. Lee, K. H. A. Bogart, and M. H. Crawford, *Journal of Crystal Growth* **312** (11), 1817 (2010).
- 12 M. S. Oh, M. K. Kwon, I. K. Park, S. H. Baek, S. J. Park, S. H. Lee, and J. J. Jung, *Journal of Crystal Growth* **289** (1), 107 (2006).
- 13 W. Lee, J. Limb, J. H. Ryou, D. Yoo, T. Chung, and R. D. Dupuis, *Journal of Electronic Materials* **35** (4), 587 (2006).
- 14 S. Kret, F. Ivaldi, K. Sobczak, R. Czernecki, and M. Leszczyński, *physica status solidi (a)* **207** (5), 1101 (2010).
- 15 Nicole K. van der Laak, Rachel A. Oliver, Menno J. Kappers, and Colin J. Humphreys, *Applied Physics Letters* **90** (12) (2007).
- 16 H. K. Cho, J. Y. Lee, G. M. Yang, and C. S. Kim, *Applied Physics Letters* **79** (2), 215 (2001).
- 17 H. K. Cho, J. Y. Lee, C. S. Kim, and G. M. Yang, *Journal of Applied Physics* **91** (3), 1166 (2002).
- 18 Z. Z. Chen, Z. X. Qin, X. D. Hu, T. J. Yu, Z. J. Yang, Y. Z. Tong, X. M. Ding, and G. Y. Zhang, *Physica B: Condensed Matter* **344** (1–4), 292 (2004).
- 19 Z. Z. Chen, P. Liu, S. L. Qi, K. Xu, Z. X. Qin, Y. Z. Tong, T. J. Yu, X. D. Hu, and G. Y. Zhang, *Journal of Crystal Growth* **298** (0), 731 (2007).
- 20 N. A. El-Masry, E. L. Piner, S. X. Liu, and S. M. Bedair, *Applied Physics Letters* **72** (1), 40 (1998).
- 21 D. Gerthsen, E. Hahn, B. Neubauer, V. Potin, A. Rosenauer, and M. Schowalter, *physica status solidi (c)* **0** (6), 1668 (2003).
- 22 Christian; Liliental-Weber Kisielowski, Zuzanna; Nakamura, Shuji, *Japan Journal of Applied Physics* **36** (Part 1 No.11), 6932 (1997).
- 23 Yen-Sheng Lin, Kung-Jeng Ma, C. Hsu, Shih-Wei Feng, Yung-Chen Cheng, Chi-Chih Liao, C. C. Yang, Chang-Cheng Chou, Chia-Ming Lee, and Jen-Inn Chyi, *Applied Physics Letters* **77** (19), 2988 (2000).
- 24 I-hsiu Ho and G. B. Stringfellow, *Applied Physics Letters* **69** (18), 2701 (1996).
- 25 R. A. Swalin, *Thermodynamics of Solids*. (John Wiley & Sons, New York, 1961).
- 26 C. Tessarek, S. Figge, T. Aschenbrenner, S. Bley, A. Rosenauer, M. Seyfried, J. Kalden, K. Sebald, J. Gutowski, and D. Hommel, *Physical Review B* **83** (11), 115316 (2011).
- 27 Y. Guo, X. L. Liu, H. P. Song, A. L. Yang, X. Q. Xu, G. L. Zheng, H. Y. Wei, S. Y. Yang, Q. S. Zhu, and Z. G. Wang, *Applied Surface Science* **256** (10), 3352 (2010).
- 28 Akihiro Wakahara, Takashi Tokuda, Xiao-Zhong Dang, Susumu Noda, and Akio Sasaki *Applied Physics Letters* **71** (7), 906 (1997).
- 29 R. Singh, D. Doppalapudi, T. D. Moustakas, and L. T. Romano, *Applied Physics Letters* **70** (9), 1089 (1997).
- 30 D. Doppalapudi, S. N. Basu, K. F. Ludwig, and T. D. Moustakas, *Journal of Applied Physics* **84** (3), 1389 (1998).
- 31 D. Gerthsen, E. Hahn, B. Neubauer, A. Rosenauer, O. Schön, M. Heuken, and A. Rizzi, *physica status solidi (a)* **177** (1), 145 (2000).
- 32 J. R. Jinschek, R. Erni, N. F. Gardner, A. Y. Kim, and C. Kisielowski, *Solid State Communications* **137** (4), 230 (2006).
- 33 Yukio Narukawa, Yoichi Kawakami, Mitsuru Funato, Shizuo Fujita, Shigeo Fujita, and Shuji Nakamura, *Applied Physics Letters* **70** (8), 981 (1997).
- 34 L. Nistor, H. Bender, A. Vantomme, M. F. Wu, J. Van Landuyt, K. P. O'Donnell, R. Martin, K. Jacobs, and I. Moerman, *Applied Physics Letters* **77** (4), 507 (2000).

- 35 S. Einfeldt, T. Bottcher, D. Hommel, H. Selke, P.L. Ryder, F. Bertram, T. Riemann, D. Rudloff, and  
J. Christen, *MRS Internet Journal Nitride Semiconductor Research* **4S1**, G3.33 (1999).
- 36 H. K. Cho, J. Y. Lee, N. Sharma, C. J. Humphreys, G. M. Yang, C. S. Kim, J. H. Song, and P. W. Yu,  
*Applied Physics Letters* **79** (16), 2594 (2001).
- 37 Mark J. Galtrey, Rachel A. Oliver, Menno J. Kappers, Colin J. Humphreys, Debbie J. Stokes, Peter  
H. Clifton, and Alfred Cerezo, *Applied Physics Letters* **90** (6) (2007).
- 38 T. Li, E. Hahn, D. Gerthsen, A. Rosenauer, A. Strittmatter, L. Reißmann, and D. Bimberg, *Applied  
Physics Letters* **86** (24) (2005).
- 39 T. M. Smeeton, M. J. Kappers, J. S. Barnard, M. E. Vickers, and C. J. Humphreys, *Applied Physics  
Letters* **83** (26), 5419 (2003).
- 40 T. M. Smeeton, M. J. Kappers, J. S. Barnard, M. E. Vickers, and C. J. Humphreys, *physica status  
solidi (b)* **240** (2), 297 (2003).
- 41 T. M. Smeeton, C. J. Humphreys, J. S. Barnard, and M. J. Kappers, *J Mater Sci* **41** (9), 2729  
(2006).
- 42 J. P. O'Neill, I. M. Ross, A. G. Cullis, T. Wang, and P. J. Parbrook, *Applied Physics Letters* **83** (10),  
1965 (2003).
- 43 J. R. Jinschek and C. Kisielowski, *Physica B: Condensed Matter* **376–377** (0), 536 (2006).
- 44 T. Bartel, J. R. Jinschek, B. Freitag, P. Specht, and C. Kisielowski, *physica status solidi (a)* **203** (1),  
167 (2006).
- 45 T. Schulz, A. Duff, T. Remmele, M. Korytov, T. Markurt, M. Albrecht, L. Lympirakis, J.  
Neugebauer, C. Chèze, and C. Skierbiszewski, *Journal of Applied Physics* **115** (3) (2014).
- 46 T. Mehrtens, M. Schowalter, D. Tytko, P. Choi, D. Raabe, L. Hoffmann, H. Jönen, U. Rossow, A.  
Hangleiter, and A. Rosenauer, *Applied Physics Letters* **102** (13) (2013).
- 47 J. W. Matthews and A. E. Blakeslee, *Journal of Crystal Growth* **27**, 118 (1974).
- 48 D. Chidambarao, G. R. Srinivasan, B. Cunningham, and C. S. Murthy, *Applied Physics Letters* **57**  
(10), 1001 (1990).
- 49 B. Jahnen, M. Albrecht, W. Dorsch, S. Christiansen, H. P. Strunk, D. Hanser, and Robert F. Davis,  
*MRS Internet Journal Nitride Semiconductor Research* **3**, 39 (1998).
- 50 R. People and J. C. Bean, *Applied Physics Letters* **47** (3), 322 (1985).
- 51 L. B. Freund and S. Suresh, *Thin Film Materials: Stress, Defect Formation and Surface Evolution*.  
(Cambridge University Press, Cambridge, 2003).
- 52 D. Holec, P. M. F. J. Costa, M. J. Kappers, and C. J. Humphreys, *Journal of Crystal Growth* **303** (1),  
314 (2007).
- 53 J. W. Steeds, *Introduction to Anisotropic Elasticity Theory of Dislocations*. (Clarendon Press,  
Oxford, 1973).
- 54 J.P. Hirth and J. Lothe, *Theory of Dislocations* (Krieger Publishing Company, Malabar, FL, 1982).
- 55 S. Srinivasan, L. Geng, R. Liu, F. A. Ponce, Y. Narukawa, and S. Tanaka, *Applied Physics Letters* **83**  
(25), 5187 (2003).
- 56 A. Fischer, H. Kühne, and H. Richter, *Physical Review Letters* **73** (20), 2712 (1994).
- 57 R. Liu, J. Mei, S. Srinivasan, F. A. Ponce, H. Omiya, Y. Narukawa, and T. Mukai, *Applied Physics  
Letters* **89** (20) (2006).
- 58 F. C. Frank, *Acta Crystallographica* **4** (6), 497 (1951).
- 59 Z. Liliental-Weber, Y. Chen, S. Ruvimov, and J. Washburn, *Physical Review Letters* **79** (15), 2835  
(1997).
- 60 D. Vanderbilt and LK. Wickham, *Material Research Society Symposium Proceedings* **202**, 555  
(1991).

- 61 C. J. Sun, M. Zubair Anwar, Q. Chen, J. W. Yang, M. Asif Khan, M. S. Shur, A. D. Bykhovski, Z.  
Liliental-Weber, C. Kisielowski, M. Smith, J. Y. Lin, and H. X. Jiang, *Applied Physics Letters* **70**  
(22), 2978 (1997).
- 62 X. H. Wu, C. R. Elsass, A. Abare, M. Mack, S. Keller, P. M. Petroff, S. P. DenBaars, J. S. Speck, and  
S. J. Rosner, *Applied Physics Letters* **72** (6), 692 (1998).
- 63 A. Hangleiter, F. Hitzel, C. Netzel, D. Fuhrmann, U. Rossow, G. Ade, and P. Hinze, *Physical*  
*Review Letters* **95** (12), 127402 (2005).
- 64 Y. Chen, T. Takeuchi, H. Amano, I. Akasaki, N. Yamada, Y. Kaneko, and S. Y. Wang, *Applied*  
*Physics Letters* **72** (6), 710 (1998).
- 65 Guillaume Perillat-Merceroz, Gatien Cosendey, Jean-François Carlin, Raphaël Butté, and Nicolas  
Grandjean, *Journal of Applied Physics* **113** (6) (2013).
- 66 J. Mei, R. Liu, F. A. Ponce, H. Omiya, and T. Mukai, *Applied Physics Letters* **90** (17) (2007).
- 67 P. Cantu, F. Wu, P. Waltereit, S. Keller, A. E. Romanov, S. P. DenBaars, and J. S. Speck, *Journal of*  
*Applied Physics* **97** (10) (2005).
- 68 A. E. Romanov and J. S. Speck, *Applied Physics Letters* **83** (13), 2569 (2003).
- 69 Masahiro Yoshita, Naoki Kondo, Hiroyuki Sakaki, Motoyoshi Baba, and Hidefumi Akiyama,  
*Physical Review B* **63** (7), 075305 (2001).
- 70 Jongseok Kim, Soohaeng Cho, A. Sanz-Hervás, A. Majerfeld, G. Patriarcho, and B. W. Kim,  
*Journal of Crystal Growth* **248** (0), 359 (2003).
- 71 W. S. Fu, G. R. Olbright, A. Owyong, J. F. Klem, R. M. Biefeld, and G. R. Hadley, *Applied Physics*  
*Letters* **57** (14), 1404 (1990).
- 72 A. V. Filinov, C. Riva, F. M. Peeters, Yu E. Lozovik, and M. Bonitz, *Physical Review B* **70** (3),  
035323 (2004).
- 73 P. M. F. J. Costa, R. Datta, M. J. Kappers, M. E. Vickers, C. J. Humphreys, D. M. Graham, P.  
Dawson, M. J. Godfrey, E. J. Thrush, and J. T. Mullins, *physica status solidi (a)* **203** (7), 1729  
(2006).
- 74 L. Hoffmann, H. Bremers, H. Jönen, U. Rossow, M. Schowalter, T. Mehrrens, A. Rosenauer, and  
A. Hangleiter, *Applied Physics Letters* **102** (10) (2013).
- 75 M. D. McCluskey, L. T. Romano, B. S. Krusor, N. M. Johnson, T. Suski, and J. Jun, *Applied Physics*  
*Letters* **73** (9), 1281 (1998).
- 76 S. M. Ting, J. C. Ramer, D. I. Florescu, V. N. Merai, B. E. Albert, A. Parekh, D. S. Lee, D. Lu, D. V.  
Christini, L. Liu, and E. A. Armour, *Journal of Applied Physics* **94** (3), 1461 (2003).
- 77 Y. Y. Chung, Y. S. Lin, S. W. Feng, Y. C. Cheng, E. C. Lin, C. C. Yang, K. J. Ma, C. Hsu, H. W.  
Chuang, C. T. Kuo, and J. S. Tsang, *Journal of Applied Physics* **93** (12), 9693 (2003).
- 78 S Nakamura, *Science* **281**, 956 (and references therein) (1998).
- 79 F. Hitzel, G. Klewer, S. Lahmann, U. Rossow, and A. Hangleiter, *physica status solidi (c)* **1** (10),  
2520 (2004).
- 80 S. Srinivasan, F. Bertram, A. Bell, F. A. Ponce, S. Tanaka, H. Omiya, and Y. Nakagawa, *Applied*  
*Physics Letters* **80** (4), 550 (2002).
- 81 D. M. Graham, A. Soltani-Vala, P. Dawson, M. J. Godfrey, T. M. Smeeton, J. S. Barnard, M. J.  
Kappers, C. J. Humphreys, and E. J. Thrush, *Journal of Applied Physics* **97** (10) (2005).

## Chapter 3

### Different characterization techniques



## Chapter 3

### Different characterization techniques

#### Introduction

To evaluate structural properties of the different samples, different techniques such as X-ray diffraction (XRD), atomic force microscopy (AFM), and scanning /transmission electron microscopy (S/TEM) are intensively used in this work. And for optical characterization, room temperature photoluminescence (RTPL) has been conducted.

In the different sections of this chapter, firstly, we are going to discuss the basics behind each technique in brief, and then we present the particular experimental methods by which we evaluate our samples in details. The aim of such discussion is to highlight how and why we have utilized these particular processes to determine the targeted properties of the samples. The advantages and disadvantages of the conducted experimental procedures are also discussed.

In this work, high resolution transmission electron microscopy (HRTEM) imaging techniques are intensively used to evaluate the structural properties of different samples depending on their growth technique. The main concerns about the structural properties of the samples are as follows: the average thickness of different layers, the QW thickness variation, indium composition within the InGaN layers, indium clustering, segregation and/or evaporation due growth process differences within the samples. Moreover, the origin of additional dislocations within the QWs, their types and their propagation methods through the samples are investigated by TEM techniques. That is why, in this chapter, we are going to discuss the experimental methods we have used for TEM analysis in detail.

In addition, to confirm the obtained results for each sample, we have conducted some complementary experiments such as 0002  $\omega$ - $2\theta$  XRD scan. In this chapter we will discuss that the simulation fit of the 0002  $\omega$ - $2\theta$  scan XRD data may not provide sample's structural information unambiguously as several combinations of structural parameters (such as active QW layer thickness ( $t_w$ ), barrier layer thickness ( $t_b$ ) or indium composition ( $x_{In}$ )) can provide the same simulation fit. To confirm the best fit, we have to know at least one of the structural parameters in advance while simulating. In this work, we have relied on different layer thickness value to evaluate the fit as the HRTEM imaging techniques allow us to have thickness values within 1-2 monolayer (1 ML=0.259 nm for GaN) accuracy. On the other hand, the prediction of indium composition only through TEM analysis is questionable as the stress state condition (bi-axial, uni-axial or in between state) of the sample along e-beam direction cause uncertainty in the prediction as discussed in chapter 1. This confusion has been solved by fitting the 0002  $\omega$ - $2\theta$  XRD scan data for each sample. These crucial points are discussed in detail in this chapter.

Finally, we will discuss the experimental processes involved in room temperature photoluminescence (RT-PL) experiment and atomic force microscopy (AFM) in individual sections of the chapter. We will highlight the importance of such experiments to better understand and correlate the optical and structural properties of our studied samples.

### 3.1 High resolution scanning /transmission electron microscopy (HR-S/TEM)

The ability to distinguish adjacent structural details by unaided human eye is only about 0.08 mm apart; thus we cannot see an object which is thinner than a human hair. On the other hand, a microscope helps us to see things that are impossible to see by an unaided eye. The spatial resolution  $\Delta l$  (ability to distinguish a minimum distance of two points) of any microscope can be expressed according to Rayleigh criterion as<sup>1</sup>:

$$\Delta l = \frac{0.6\lambda}{n \sin \theta} \quad (3.1)$$

where,  $\lambda$  is the wavelength of the source,  $n$  is the refractive index of the medium and  $\theta$  is the collection semi-angle of the magnifying lens.

In early twentieth century, when the optical microscopes were operated in the visible spectrum range, the spatial resolution was only around 0.2  $\mu\text{m}$  according to equation 3.1. Yet it was impossible to see things in nanometer (nm) resolution. The wavelength of X-rays (varying from 0.005 nm to 10 nm) may give a very attractive spatial resolution value but the application of such illuminating source is not practical as the absence of focusing systems for X-rays limits its application.

In 1924 Louis de Broglie formulated the hypothesis of wave-particle duality<sup>2</sup>, which was confirmed experimentally three years later<sup>3</sup>. He proposed that any accelerated particle with mass  $m$  and velocity  $v$ , will have a wavelength  $\lambda$  associate with it and that can be related by the Plank's constant  $h$  as:

$$\lambda = \frac{h}{mv} \quad (3.2)$$

This has motivated scientists to employ electrons as microscope probe by using magnetic or electrostatic fields as lenses by which we can achieve very small wavelength  $\lambda$  from accelerated electron beams.

In this work, a JEOL 2010F TEM with an operating voltage of 200 keV and a Titan 80-300 S/TEM with an operating voltage of 300 keV were used to make structural characterizations. In both cases, from equation 3.2, the wavelength of the electron beams are  $2.74 \times 10^{-3}$  nm and  $2.24 \times 10^{-3}$  nm, respectively, which are several orders of magnitude lower than the inter-atomic distances

in most semiconductor materials ( $\approx 0.2$  nm). But, the geometric and chromatic aberrations related to the electron optics used in a S/TEM limits the overall spatial resolution. However, the detail discussion of the types of aberrations and their effects on electron microscopy are avoided in the chapter. For JEOL 2010F TEM the spatial resolution is only about 0.19 nm and for Titan 80-300 S/TEM with spherical aberration correction ( $c_s$ -corrector) the spatial resolution becomes 0.08 nm.

### 3.1.1 Principle of HRTEM: scattering and diffraction

In transmission electron microscopes two fundamentally different types of electron sources (thermionic and field emission) are used to illuminate the sample with electron beams. In thermionic emission, the electrons are ejected by heating a metal filament to high temperature to overcome its potential barrier (called work function) and applying a positive voltage to extract the electrons, whereas in field emission process, electrons are withdrawn from a sharp tip using a high electric field. In both cases the target is to have electron beam with high spatial coherency and short energy spread. The field emission process has higher spatial coherency and shorter energy spread than that of thermionic process. Thus a field emission gun (FEG) as an electron source is used in our TEM for high resolution imaging.

The main objective of such highly coherent electron beam to impinge on a sample is to detect the variations in the coherency of the scattered beams, induced by the sample properties. Under typical illumination conditions in an electron microscope, the incoming electron can be treated as a plane wave as expressed:

$$\psi = A_0 \exp[2\pi i(\mathbf{k}_0 \cdot \mathbf{r} + \varphi_0)] \quad (3.3)$$

where  $A_0$  is the amplitude of the wave,  $\mathbf{k}_0$  is the wave vector and  $\varphi_0$  is the phase of the incoming plane wave. This incoming plane wave undergoes different types of scattering processes while propagating through the sample.

At the beginning of twentieth century, Thomson et al<sup>3</sup> first discovered experimentally, the ability of atoms to scatter incoming electrons. The scattering process is classified into two types: if the re-radiation of electron beam has the same energy as that of the incoming beam then the scattering process is term as elastic, and in all other cases, the process is termed as inelastic process. The probability of an electron to be elastically scattered by an isolated atom is given by the scattering cross section  $\sigma$  as:

$$\sigma = \pi \left( \frac{Ze}{V\theta} \right)^2 \quad (3.4)$$

where  $Z$  is the atomic number,  $e$  is the electron charge,  $V$  is the potential of the incoming electron and  $\theta$  is the angle of scattering. However, an exact analytical description of the elastic

scattering cross section is not available, since the interaction potential has to take into account the nucleus of the target atom as well as the electrons associated with it. But yet one can simplify the elastic scattering process with the atomic number  $Z$  of the target atoms, i.e. the heavier the atom, the more probable is the scattering event to occur. As a result the intensity of the transmitted electron beam will decrease and the different directional scattering beams will arise. Moreover, the thickness of a sample also has an impact on the scattering process as the thicker areas of a sample will scatter more electrons than the thinner ones.

Depending on the samples' crystalline properties, the scattered electron waves from different atomic planes of the samples may create constructive as well as destructive interferences in different directions, which cause an inhomogeneous distribution of intensity of the scattering event. This phenomenon is known as diffraction. The constructive interference of different electron waves in a certain direction only occurs when the phase difference between the waves is a multiple of  $2\pi$  or the path difference is an integer ( $n$ ) multiple of wavelength  $\lambda$  of the incoming wave. Figure 3-1 schematically illustrates both the constructive and destructive interference of diffraction phenomenon individually. The criterion for constructive interference is expressed by the Bragg's law as:

$$2d\sin\theta = n \cdot \lambda \quad (3.5)$$

where  $\theta$  is the angle between the incoming wave and the scattering planes,  $d$  is the spacing between the scattering planes,  $\lambda$  is the wavelength of the incoming electron beam and  $n$  is an integer. The same condition can be expressed in terms of wave vector and the reciprocal lattice vector of the sample as (Laue equation):

$$\mathbf{k}_0 - \mathbf{k}_D = \mathbf{g} \quad (3.6)$$

Where  $\mathbf{g}$  is the reciprocal lattice vector and  $\mathbf{k}_0$  and  $\mathbf{k}_D$  are the incident and diffracted beam vectors, respectively. Please note that in electron microscopy, the diffraction phenomenon occurs for transmitted electron beams, though here we illustrate the phenomenon by wave reflection for clearer representation and understanding.

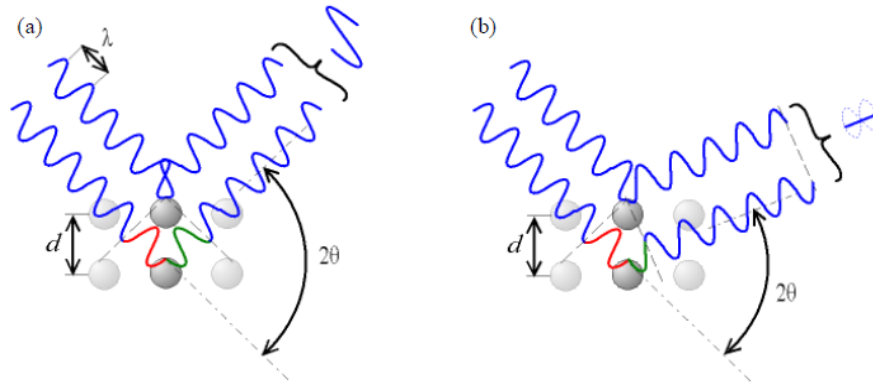


Figure 3-1: Schematic diagram of (a) constructive and (b) destructive interferences within a sample where the atomic plane difference is  $d$ , angle between the incoming wave and the atomic plane is  $\theta$  and the wavelength of the incoming wave is  $\lambda$ .<sup>4</sup>

In a transmission electron microscopy, the objective lens focuses all the diffracted beams and thus forms a diffraction pattern associated with the sample in the back focal plane of the lens. Selecting certain beam spots on the focal plane of the lens by an objective aperture, we can form the TEM image associated with the selected beam spots on the image plane. The operational mode associated with different types of electron microscopy is discussed in the next subsection in detail.

Now let us assume that one diffraction beam is passing through the objective aperture in addition to the transmitted beam as shown in Figure 3-2. The transmitted direct beam has the same wave vector ( $\mathbf{k}_T$ ) as that of the incident wave vector ( $\mathbf{k}_0$ ) and can be expressed as:

$$\psi_T = A_T \exp[2\pi i(\mathbf{k}_0 \cdot \mathbf{r} + \varphi_T)] \quad (3.7)$$

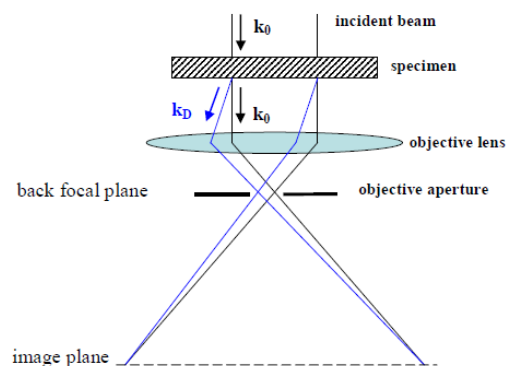


Figure 3-2: Schematic representation of transmitted two beams through the sample where the incident and diffracted beam wave vectors are represented as  $\mathbf{k}_0$  and  $\mathbf{k}_D$ , respectively. The objective lens is focusing the two beam vectors and the objective aperture helping to select a particular diffraction beam spot to form an image on the image plane<sup>4</sup>.

Similarly, the diffracted beam wave  $\psi_D$  can also be expressed as equation 3.7 with wave vector  $\mathbf{k}_D$ , which is related to  $\mathbf{k}_0$  as shown in equation 3.6. Note that for elastic scattering both beams have the same magnitude (i.e.  $|\mathbf{k}_D|=|\mathbf{k}_0|=2\pi/\lambda$ ) but different directions. Thus when the objective lens converges the two beams they will interfere and the interference image will be formed in the image plane with intensity  $I$ , expressed as:

$$I = \psi_{\Sigma} \cdot \psi_{\Sigma}^*, \quad \text{where, } \psi_{\Sigma} = \psi_T + \psi_D \quad (3.8)$$

The final image intensity ( $I$ ), contains the item  $(\psi_T^* \cdot \psi_D + \psi_T \cdot \psi_D^*)$ , which is proportional to the expression as follows:

$$\begin{aligned} & \exp[2\pi i((\mathbf{k}_0 - \mathbf{k}_D) \cdot \mathbf{r} + (\psi_T - \psi_D))] + \exp[-2\pi i((\mathbf{k}_0 - \mathbf{k}_D) \cdot \mathbf{r} + (\psi_T - \psi_D))] \\ & = 2 \cos (2\pi(\mathbf{g} \cdot \mathbf{r} + (\psi_T - \psi_D))) \end{aligned} \quad (3.9)$$

The term  $(\psi_T^* \cdot \psi_D + \psi_T \cdot \psi_D^*)$  is responsible for the appearance of a sinusoidal oscillation in the intensity of the interference image. The fringe periodicity within the image is equal to the value  $1/g$ , which represents the spacing between the atomic planes from which the incident beam gets diffracted. Therefore, the inter-planar distances of a certain plane (hkl) of the studied material can be visualized by means of the high resolution contrast in the interference constructed from the corresponding diffraction beam spot  $\mathbf{g}_{hkl}$ . However, the overall image contrast from the diffracted beams is more complex than just the superposition of fringes formed by each diffracted beam. Many factors such as sample preparation, compositional variation, thickness variation of the sample, incident beam direction, optical lenses aberration as well as microscope defocus have impacts on the image contrast of the interference image, thus care should be taken to interpret the image contrast of the image to evaluate the corresponding data from the image. Figure 3-3 illustrates a well focused cross-sectional transmission electron microscopy (cs-TEM) image along  $\langle 14-50 \rangle$  zone axis, where due to compositional variation of different regions (barrier and quantum well) of the sample, we can identify the regions from the image contrast. Moreover, the individual line contrast (enlarged view of part of the sample is shown in the inset) within the sample also corresponds to the (0002) plane monolayer of the sample. However, some part of the image as indicated by white brackets does not have the individual line contrast. This noise within the image is most probably due to sample preparation effects occurred in that region and due to spatial resolution limitation of the used TEM (For JEOL 2010F TEM, the spatial resolution is only about 0.19 nm) we are not able to see the individual atomic position along (0002) plane in the image.

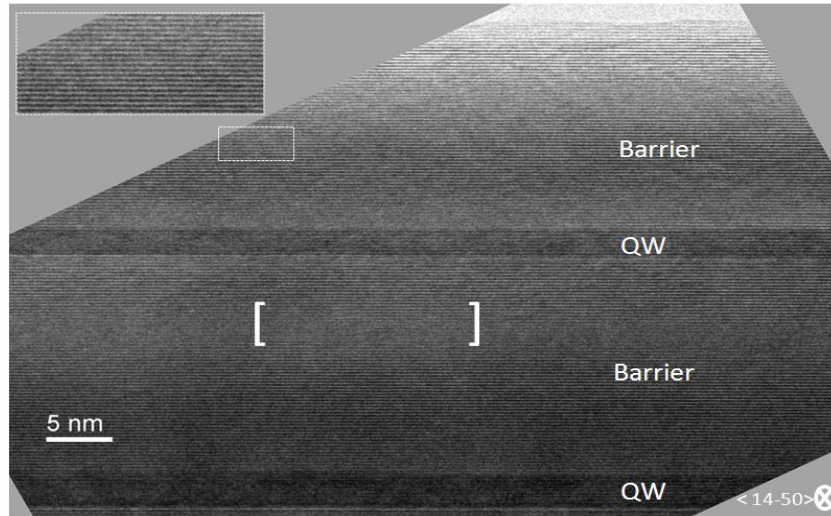


Figure 3-3: A well focused cross-sectional transmission electron microscopy image along  $\langle 14-50 \rangle$  zone axis: the image contrast in different areas is due to the compositional variation of different regions of the sample such as barrier and quantum well. The inset shows the enlarge view of the small white rectangle area (about 5 nm wide) of the sample; the individual lines within the image correspond to the (0002) plane (monolayer) of the sample. The region within white brackets does not show individual line contrast due to sample quality.

### 3.1.2 Basic operational modes in TEM: Diffraction and image modes

There exist two types of operational modes in TEM, known as (a) diffraction mode and (b) image mode. Figure 3-4 illustrates the two basic modes in TEM system. In 'diffraction mode' (Figure 3-4(A)), the strength of the intermediate lens is set automatically in such a way that it takes the back focal plane (bfp) of the objective lens as its object and allows the diffraction pattern (DP) of the sample to be projected on to the viewing screen with high magnification. In 'image mode' (Figure 3-4(B)), the intermediate lens takes the image plane of the objective lens as its object and allows the image of the sample to be projected on to the viewing screen of the system.

In order to have a diffraction pattern from a particular region of the sample, selected area diffraction (SAD) aperture may be used in diffraction mode, whereas in image mode, to obtain image from particular diffraction beam spots objective aperture is used. Depending on the objective of the observation with TEM, the apertures are either inserted or retracted in between the objective and intermediate lens as shown in Figure 3-4 for both modes.

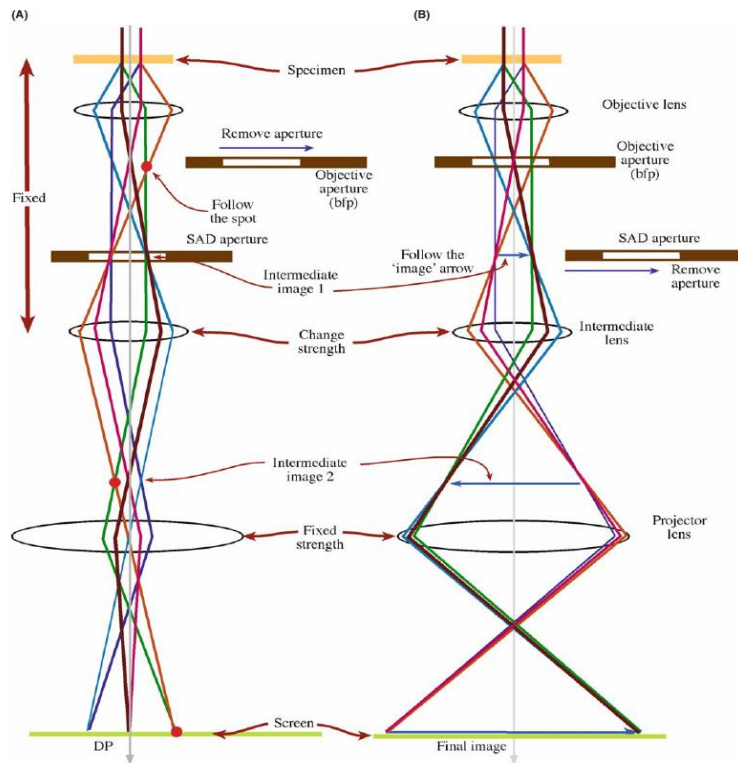


Figure 3-4: Simplified illustration of two basic operations of TEM imaging system (A) diffraction mode: projecting the diffraction pattern (DP) into the screen and (B) image mode: projecting the image into the viewing screen<sup>5</sup> (chapter 9, page 153).

In diffraction mode, by tilting the sample to a certain orientation, we may get particular diffraction pattern (DP) associated with the sample. For example Figure 3-5 schematically illustrates two particular DPs associated with two zone axes orientations of a hexagonal crystal sample. Thus observing the DP in the diffraction mode we can be sure about the orientation of the sample and then by switching to image mode, we can have the image of the sample at a particular zone axis of our interest.

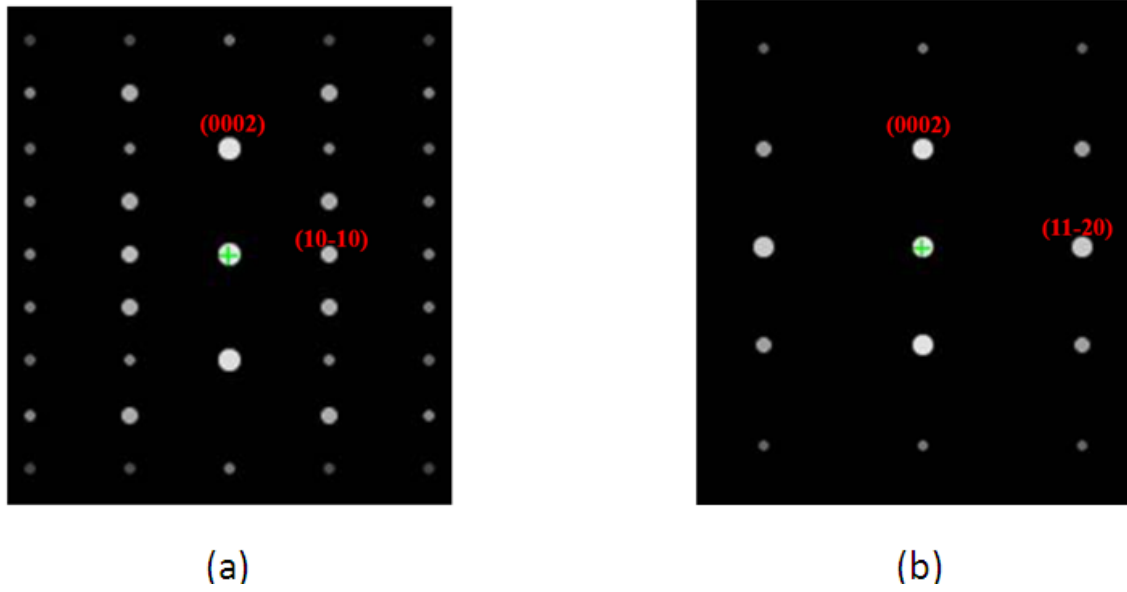


Figure 3-5: The diffraction pattern of the hexagonal crystal structure along (a)  $\langle 11-20 \rangle$  and (b)  $\langle 1-100 \rangle$  zone axes.

### 3.1.2.1 Different imaging techniques: bright field (BF) and dark field (DF) imaging

In the image mode, an objective aperture is placed on the back focal plane (bfp) of the objective lens to select a particular diffraction spot of the DP to form an image in the display screen as shown in Figure 3-4 (B). Depending on which diffraction spot is selected to form the image, the obtained image is classified differently. For example, an image is called bright field (BF) image, when the objective aperture is set to select the direct beam spot of the DP, which appears due to the direct transmission of the incident beam ( i.e., without diffraction) through the sample and have the highest intensity within all the diffraction spots of the DP. But selecting any other diffraction beam spot, other than the direct beam spot, to form an image is known as dark field (DF) image.

Figure 3-6 schematically illustrates the two imaging techniques (BF and DF imaging) used in TEM. When the incident beam is allowed to pass through the optic axis of the lenses, the direct beam passes through the sample and does not get off axis. But beams diffracted by certain planes of the sample get off axis from the optical axis before the objective lens collects them to generate the DP as shown in Figure 3-6(a). In order to allow any diffracted beam to pass through the optic axis, the incident beam is tilted with respect to the optic axis as illustrated in Figure 3-6(b). Such operational condition is known as off axis condition in TEM technique and image obtained from such condition is known as dark field image. Figure 3-7 illustrates the two images obtained using the diffraction beam spot  $g=0000$  and  $g=000-2$  to have bright field (Figure 3-7(a)) and dark field (Figure 3-7(b)) images, respectively.

Moreover, while the sample is at a particular zone axis, the diffraction pattern (DP) of the sample has uniform intensity for different complementary diffraction beam spots, e.g., the 0002 and the 000-2 beam spots will have uniform intensity while the sample is along  $\langle 11-20 \rangle$  zone axis (Figure 3-5(a)). By tilting the sample, we can manipulate the DP of the sample in such a way that one of the diffraction beam spots may become stronger in intensity than the other complementary diffraction beam spot. Such sample orientation condition is known as two beam conditions in TEM image technique<sup>5</sup>. We have used this two beams condition to take images to analyze our samples.

Again, in the image mode, when an objective aperture with large diameter is used to select more than two diffraction beam spots on the back focal plane of the objective lens to form an image, it is known as multi beam (MB) image. We have also used multi beam imaging techniques to observe and study our samples.

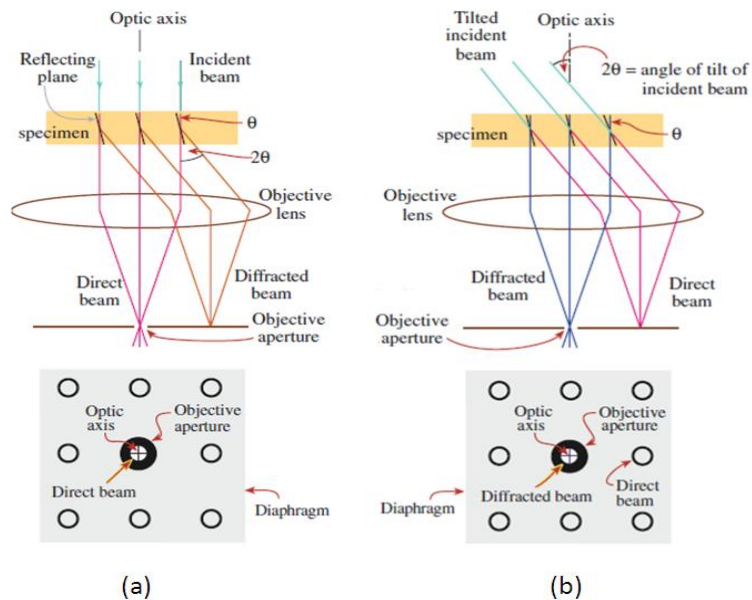


Figure 3-6: Schematic diagram for (a) bright field and (b) dark field imaging in TEM system.<sup>5</sup>

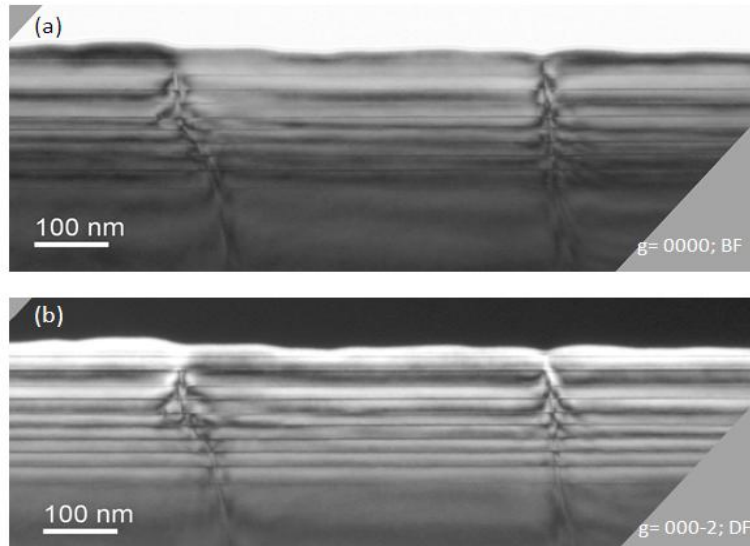


Figure 3-7: (a) Bright field and (b) dark field images obtained using direct beam spot  $g=0000$ , diffracted beam spot  $g=000-2$ , respectively.

### 3.1.2.2 Dark field image techniques: strong beam dark field (SBDF) and weak beam dark field (WBDF)

The DF image is classified into two, known as i) strong beam dark field (SBDF) and ii) weak beam dark field (WBDF) image. In Figure 3-8, the two types of dark field images are illustrated for a TEM system. In Figure 3-8 (a), we initially considered that illuminating a sample with an incident beam parallel to the optical axis may allow a particular set of  $(hkl)$  planes of the sample to fulfill the Bragg condition and provide a stronger diffraction beam spot ( $+\mathbf{g}_{(hkl)}$  strong spot) in the DP. In order to move the  $+\mathbf{g}_{(hkl)}$  spot along the optic axis, the incident beam has to be tilted  $2\theta$  from the optic axis as shown in Figure 3-8 (b) ( $3\theta$  from the  $hkl$  plane). But in this case the spot ( $+\mathbf{g}_{(hkl)}$ ) becomes weak and the  $+\mathbf{3g}_{(hkl)}$  spot becomes strong as it fulfills the Bragg's condition. Forming an image from that on axis diffraction spot ( $+\mathbf{g}_{(hkl)}$  weak spot), is known as weak beam dark field (WBDF) image or ( $\mathbf{g}-\mathbf{3g}$ ) image. But instead of having weak diffraction beam spot ( $+\mathbf{g}_{(hkl)}$  weak) along the optical axis, if we wish to have a bright diffraction beam spot along the optic axis, we have to tilt the incident beam in such a way that the  $-\mathbf{g}_{(hkl)}$  spot becomes strong and appears along the optic axis as shown in Figure 3-8 (c). Image obtained from such a diffraction beam spot ( $-\mathbf{g}_{(hkl)}$ ), is known as strong beam dark field (SBDF) image or simply termed dark field (DF) image.

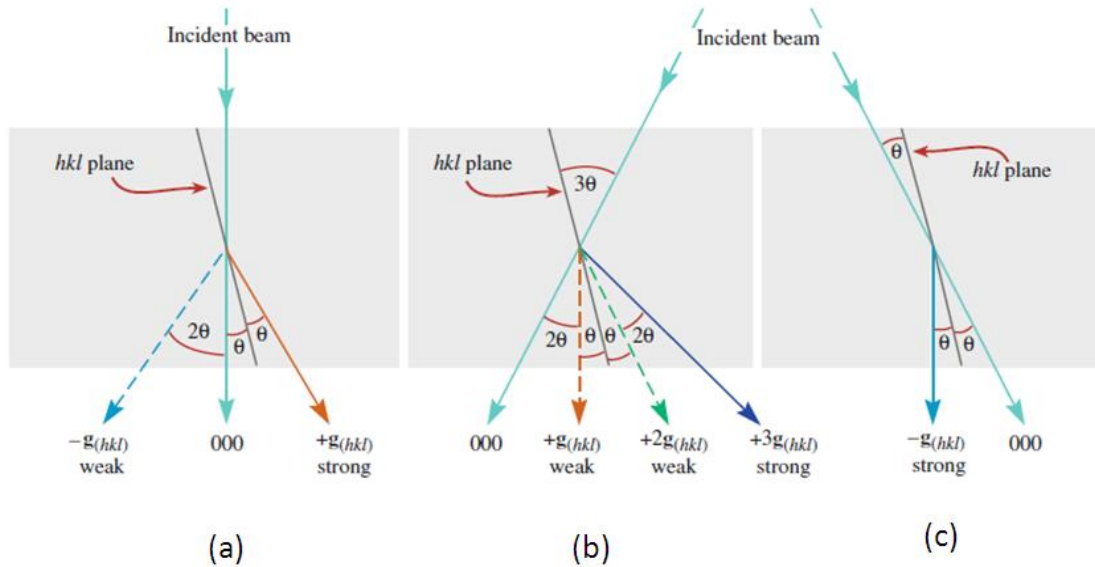


Figure 3-8: Schematic diagram for (a) bright field (BF), (b) weak beam dark field (WBDF) and (c) strong beam dark field (SBDF) imaging condition<sup>5 (chapter 22, page 384)</sup>.

In this work, different imaging techniques have been utilized to evaluate the structural properties of the samples while tilted the samples mainly in three zone axes, at or around  $\langle 11-20 \rangle$ ,  $\langle 1-100 \rangle$  and  $\langle 14-50 \rangle$  respectively. The goal of such zone axes orientation and the imaging condition used to study the structural properties will be discussed in the relevant subsections later on.

### 3.1.3 Scanning transmission electron microscopy (STEM)

In this work, we have used not only transmission electron microscopy (TEM) but also scanning transmission electron microscopy (STEM) to analyze our studied samples. Thus in this section we are going to discuss the basics of STEM along with the differences to that of conventional TEM in brief.

The main differences between the conventional TEM to that of the STEM are that in conventional TEM (from now on we will simply term it as TEM) the optical lenses before the sample makes the incoming electron beam appear parallel to the optical axis ( $\alpha_T \approx 0$ ) before illuminating the sample, whereas in STEM the lenses converge the incoming beam at larger angle ( $\alpha_s > 0$ ) with the optical axis. Thus the possible probe size in STEM ranges from 0.2 to 2.4 nm depending on the operational condition. In STEM the small beam probe is allowed to scan through the sample surface without changing its direction to the optical axis with the help of scan coils. Figure 3-9 schematically illustrates the operation of such scan coils within the STEM which do not exist in TEM system.

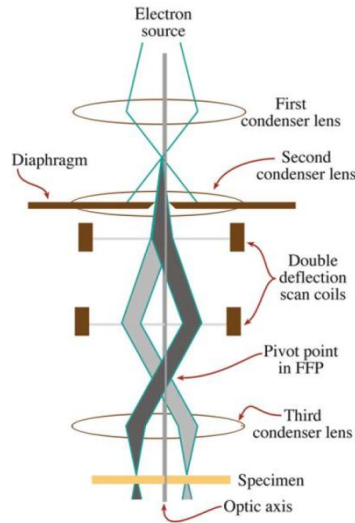


Figure 3-9: Schematic diagram showing the deflection scan coils function in STEM, as it makes the incoming beam to pivot at the first focal plane of the final condenser lens. It allows the beam probe to scan through the sample without changing its direction<sup>5</sup>.

The TEM images have more contrast effects than that of STEM images.<sup>6</sup> This is because in TEM when the incoming parallel beam (unidirectional) is allowed to pass through in large area of the sample, the transmitted beam intensity may become spatially non-uniform as it may suffer from path and diffraction differences in place to place of the sample due to its thickness variation, bend contour and scattering events within the planes. On the other hand, in STEM, the same sample area is scanned through step by step with a small beam probe formed from convergent incident beam (multi-directional beam within small convergent angle  $\alpha_s$ ). These features allows to have more uniform transmitted beam intensity from the sample and help to form the image with less contrast effects than that of TEM images. This also allows to analyze relatively thick TEM samples in STEM than in TEM. Figure 3-10 illustrates the advantage of STEM over TEM for a bent sample. In TEM due to uni-directional incident beam, some regions of the sample may fulfill the diffraction condition more than the other regions (as small misorientation within the particular planes of the sample may exists) as illustrated in Figure 3-10 (b), whereas in STEM, due to multi-directional incident beam all the particular planes within the sample will fulfill the diffraction condition and allow us to have uniform diffracted beam intensity from the whole sample, as illustrated in Figure 3-10 (a).

In STEM, the collection process of the diffracted electron beam from the sample is also different from the TEM system. Different types of electron detectors are placed underneath the sample along the optical axis of the objective lens of the system. The circular disk shape detector centered along the optical axis of the system is known as bright field (BF) detector. Another detector with annular shape and placed around the BF detector is known as annular dark field (ADF) detector of the system. Figure 3-11 illustrates the general procedure of two

imaging techniques in STEM where the BF detector is use to form the BF image and ADF detector to form DF image.

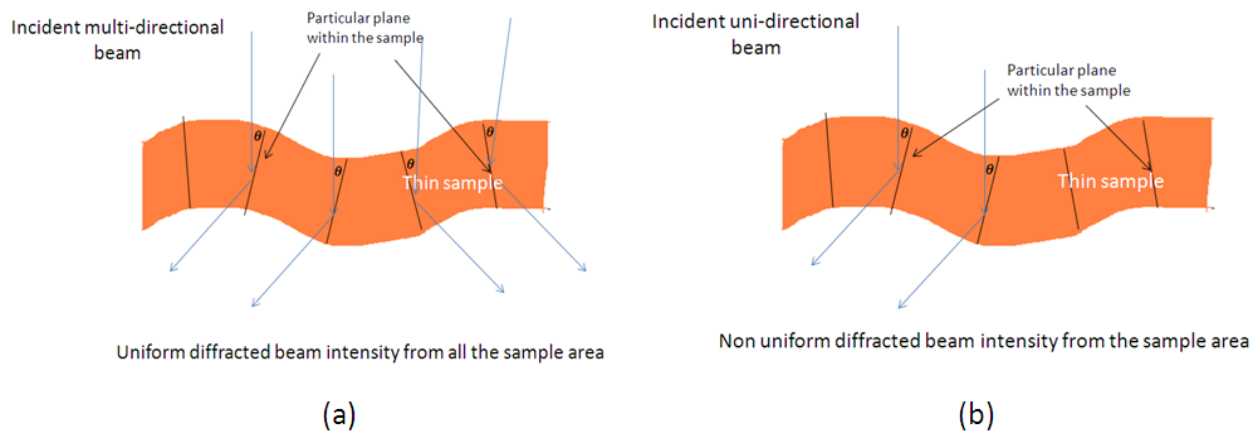


Figure 3-10: Schematic diagram showing the advantage of (a) STEM to that of (b) TEM in case of a bent sample.

Depending on the angle of the incoming convergent beam ( $\alpha_s$ ) in STEM, the radius of the transmitted and the diffracted beam spots changes. By adjusting the convergent beam angle and the distance between the sample and the detector plane, known as camera length, one can manipulate different diffracted beam spots to fall on the detectors. The camera length also controls the BF and ADF detector acceptance angle and may change the image contrast accordingly<sup>7,8</sup>. Moreover, the DP can be shifted to allow any diffracted beam spot to fall on a detector to form an image and thus we may get strong beam dark field (SBDF) or weak beam dark field (WBDF) images as discussed in section 3.1.3 in STEM system. Note that in a STEM system the incoming convergent beam is never tilted to obtain such images whereas in TEM tilting of the incoming beam is necessary.

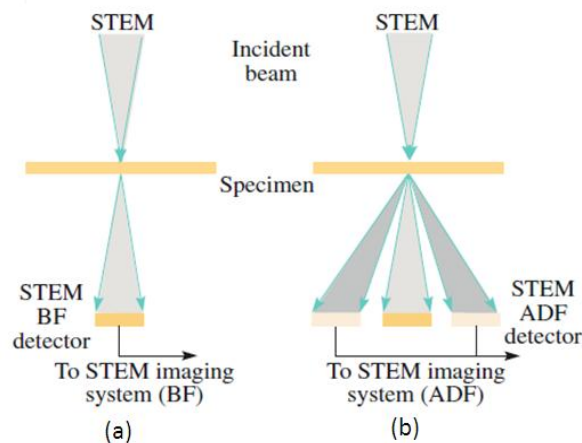


Figure 3-11: Schematic diagram for (a) bright field and (b) dark field imaging in STEM system.<sup>5</sup>

### 3.1.4 High angle annular dark field (HAADF) imaging

In STEM in addition to ADF detector, another electron detector with large central aperture may exist which is known as high angle annular dark field (HAADF) detector. The purpose of such a detector is to collect the high off-axis ( $> 50$  mrad) incoherently scattered electron from a sample. According to Rutherford's law, the probability of an incoming electron to be get scattered by an atom to a high angle is proportional to the square of its atomic number ( $Z$ )<sup>9</sup>. Thus forming an image by collecting the scattered electrons through HAADF detector is termed as HAADF image or Z-contrast image. And the interpretation of HAADF image is simple as heavier atoms will exhibit higher brightness. Figure 3-12 schematically represents the position of the HAADF detector and the general electron scattering angles gathered by each detector in a STEM.

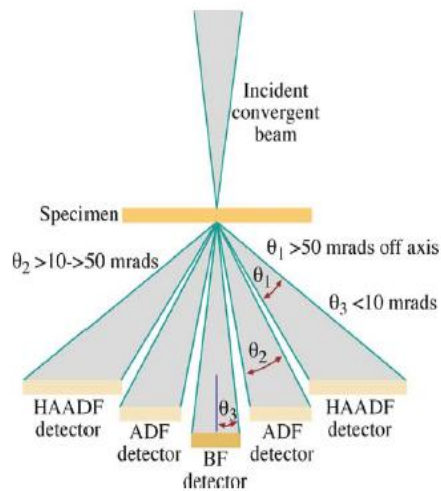


Figure 3-12: Schematic diagram of HAADF detector setup along with other detectors. The range of different scattering angles gathered by each detector is also shown.<sup>5</sup>

Now the intensity of the HAADF image depends on how many scattered electrons are collected by the HAADF detector. Thus depending on the placement of the detector, sample thickness and most importantly the amount of elastically scattered electrons reaching the HAADF detector, the image contrast may change.<sup>10</sup> The contribution of elastically scattered electrons in forming the HAADF image can be reduced by placing the HAADF detector near the sample but in that case the overall intensity of the image decreases. Moreover, the orientation of the sample in any major crystalline axis also has impact on the Z-contrast image as the incoming electron may pass through along the atomic columns with higher probability. This is known as channeling effect in HAADF imaging.

A quantitative analysis to determine the chemical composition is much more complicated than qualitative analysis from HAADF images. Extensive calculation and HAADF image simulation is

required to interpret the compositional data from HAADF images<sup>11,12,13,14</sup>. Thus in this work, we have used HAADF images just to have an idea about whether the quantum well has more or less uniform composition from the image contrast and to qualitatively identify any existence of large scale indium clustering.

In a HRTEM image, a threading dislocation causes contrast change around it which makes it difficult to observe sample properties such as QW thickness near it. On the other hand, the HAADF image does not suffer from such a contrast problem as the HAADF image contrast does not depend on diffraction conditions. Figure 3-13 illustrates this fact by comparing the two images taken at the same place of an InGaN/AlGaN/GaN sample structure. Comparing the two images, one can easily see the strong contrast appears due to different layers composition values (as mentioned in the Figure 3-13 (b)) rather than from the presence of threading dislocations which is common for HRTEM image (Figure 3-13 (a)). Note that a slight contrast still appears in the HAADF image from a threading dislocation which is most probably due to the elastically scattered electrons from the dislocation area that are yet reaching the HAADF detector.

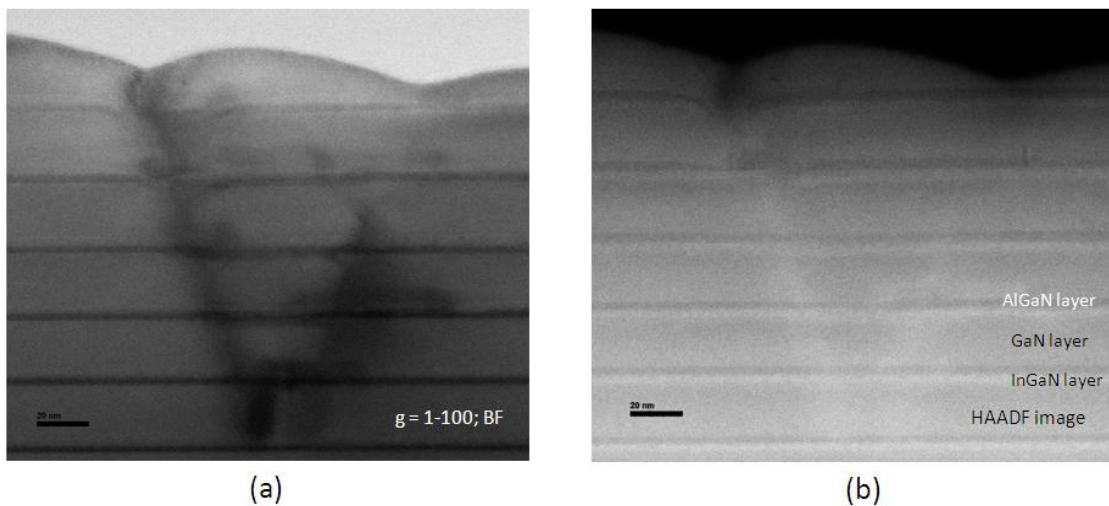


Figure 3-13: (a) Image contrast is present due to dislocation in a bright field image taken with two beam conditions (with  $g=1-100$  diffraction beam spot in higher intensity) and (b) the HAADF image of the same place where different layer contrast can easily be seen (as mentioned in the image) without the any additional contrast from dislocation.

### 3.2 Determination of structural properties through HRTEM imaging techniques

In this work, transmission electron microscopy (TEM) has been used to characterize the structural properties of grown samples. Using different TEM techniques we tried to determine the different layer thickness, thickness variation, origin of dislocations and their types and most importantly Indium composition within InGaN QW layers of the structure.

In determining the average layer thickness and indium composition within QWs through TEM, we have considered several HRTEM images taken from different parts (several  $\mu\text{m}$  apart from each other) of each sample. For each sample we have observed from first QW to last QW and even observed different regions of same QW to obtain good statistics for the thickness and composition values.

In case of average thickness measurement of different layers, we have considered at least  $2\ \mu\text{m}$  lengths laterally for each sample to have good statistical data on thickness distribution (detail in section 3.2.1).

Similarly, in determining average indium composition of a sample, we have considered several places of a QW as well as from first QW to the last QW of the sample. We are able to analyze the sample in such a way because of the fact that at and/or near the hole of the prepared cs-TEM sample, large electron beam transparent regions are available for the whole structure. Figure 3-14 schematically demonstrates the way we have obtained the average indium composition value of a sample. Note that the oval shape areas within the image indicates that we have considered several places of a QW, as well as in different QWs of the sample to identify the composition value of each QWs and finally average out them to have the overall sample's indium composition value.

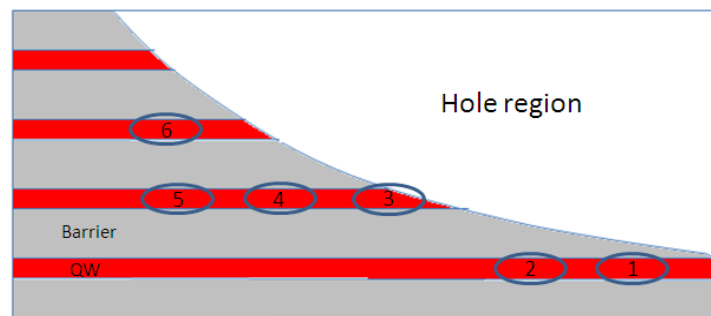


Figure 3-14: Schematic diagram of a sample as observed in TEM at relatively low magnification with several QW regions (in red) as well as barrier regions (in gray). The numbered blue oval shape areas indicate the fact several regions of a QW as well as different QWs are considered to determine the average indium composition of the sample.

In the following subsections we are going to discuss the procedure involved in determining the above mentioned criteria of the samples in detail.

### 3.2.1 Layer thickness measurement procedure

To measure the different layer thicknesses of the structure, we tilt our sample to  $\langle 14-50 \rangle$  zone axis. The cs-TEM images are taken along  $\langle 14-50 \rangle$  zone axis while setting the objective aperture with relatively large diameter to take the three diffraction beam spots of  $g = 0002$ ,  $g = 0000$  and

$g=000-2$  of the diffraction pattern to form the multi-beam (MB) image. It helps us to have the different (0002) plane of the structure as lines in the high resolution TEM image, as along such orientation the distance between the atomic column positions within a plane is smaller (104 pm) than the spatial resolution of microscope we have used for HRTEM (spatial resolution: 0.194 nm for JEOL 2010F TEM). Thus the individual atomic position within a plane does not appear as individual dot spots rather they appear as lines in the HRTEM image (Figure 3-3).

Because of different layer composition, contrast differences are observed within different layers of the image. Using digital micrograph image analysis software<sup>15</sup>, by selecting certain part of the image, we have an intensity contrast profile of the HRTEM image. Figure 3-15 (a) shows a multi beam (MB) image taken along  $\langle 14-50 \rangle$  zone axis of the sample. Two quantum wells and the barrier layer in between the quantum well regions are clearly identifiable as the intensity contrasts differ from QW region to that of the barrier region of the image. Now an intensity contrast profile is obtained from the area indicated by blue box as shown in Figure 3-15(b).

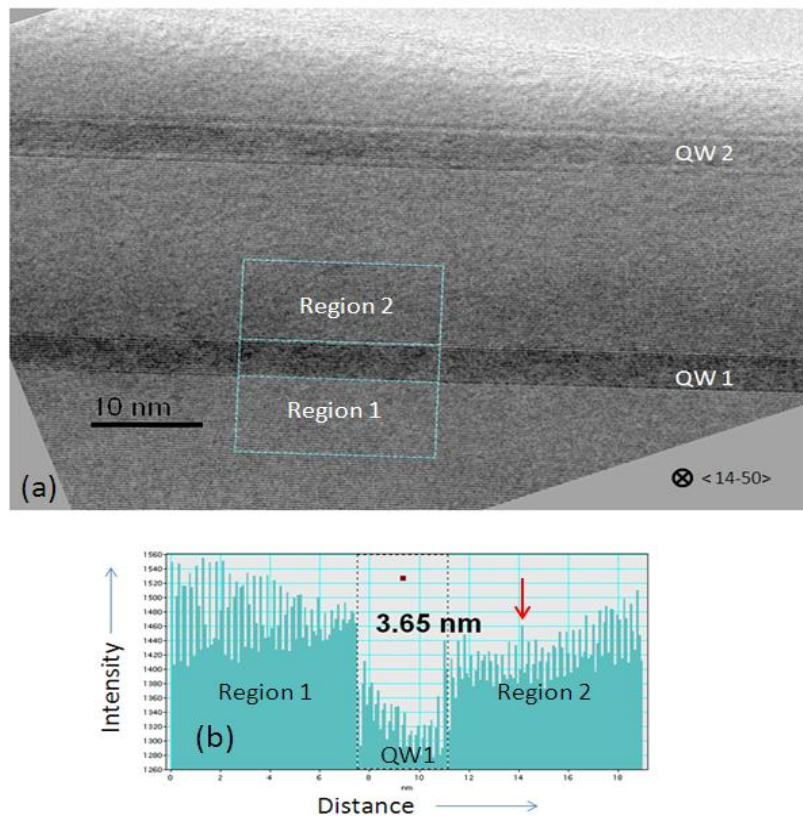


Figure 3-15: (a) Cross-sectional transmission electron microscopy (cs-TEM) image of a sample along  $\langle 14-50 \rangle$  zone axis. A certain area (blue box) is considered to draw the intensity contrast profile from bottom to top of the selected area as shown in (b). The thickness about 3.7 nm indicated in (b) correspond to the first quantum well (QW1) thickness of the sample. The individual intensity peak (indicated by red arrow) corresponds to the (0002) atomic plane of the structure.

The individual intensity peaks of the profile (indicated by red arrows in Figure 3-15 (b)) correspond to the average intensity of the individual (0002) plane layer of the selected region of the image. The distance between the two intensity peaks thus corresponds to 1 monolayer (1 ML= 0.259 nm) of the structure.

Now as the QW region is darker than that of the barrier layer regions (region 1 and 2) within the blue box, the average intensity of the QW region is much smaller than that of the other two nearby regions. Therefore, measuring the width of average low intensity area within the profile, we are able to identify the quantum well (QW) thickness within 1-2 monolayer (ML) accuracy.

In this work, to have good statistical data about different layer thicknesses, we have determined the thickness distribution of a particular layer using the method described for QW layers of a structure as follows:

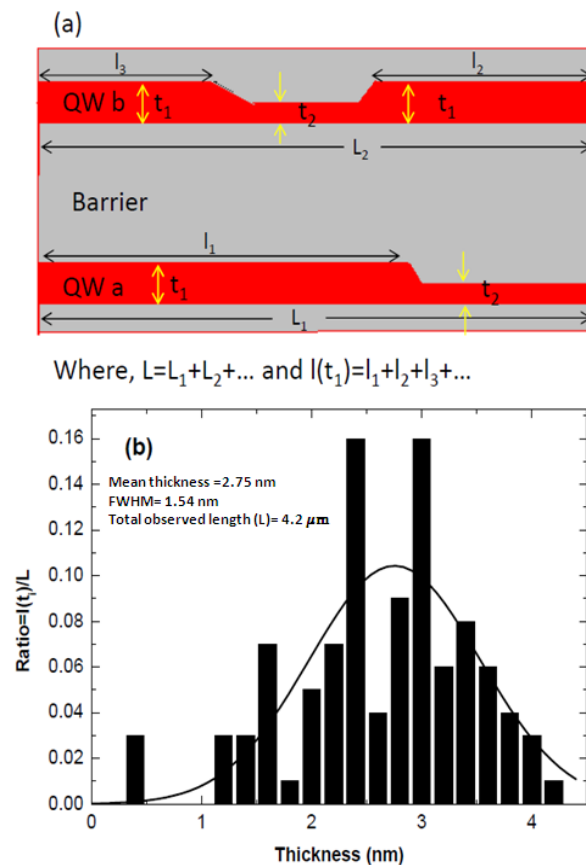


Figure 3-16 a) Schematic diagram showing the method to measure the total lateral length ( $l(t_1)=l_1+l_2+\dots$ ) for a certain quantum well thickness range ( $t_1$ ) (for example,  $2.2 \leq t_1 \leq 2.4$  nm) and the total observed lateral length ( $L=L_1+L_2+\dots$ ) of the whole sample to plot quantum well thickness distribution graph. (b) Quantum well thickness distribution graph for sample, X- axis has thickness range (with 0.2 nm width of each block) in nm and Y- axis is the ratio of total measured lateral length ( $l(t_1)$ ) to that of total observed lateral length (L).

The schematic diagram of Figure 3-16 (a) shows the derivation process of two important parameters that are used to plot the QW thickness distribution graph, namely the total lateral length ( $l(t_i)$ ) with a thickness range of ( $t_i$ ) of a sample structure and the total observed lateral length ( $L$ ). We measure the lateral length of each place ( $l_1, l_2, \dots$ ) that has the same thickness range of ( $t_1$ ) (for example  $2.2 \text{ nm} \leq t_1 \leq 2.4 \text{ nm}$ ) within the structure. We then add them all up to have the total lateral length ( $l(t_1)=l_1+l_2+\dots$ ). At the same time, we add up all the lateral observed distances ( $L_1, L_2, \dots$ ) to have the total observed lateral length ( $L= L_1+L_2+\dots$ ). Using these two parameters, we then plot as in Figure 3-16 (b), the ratio of total lateral length ( $l(t_i)$ ) to that of total observed lateral length ( $L$ ) as a function of the thickness ( $t_i$ ) for a sample.

The plot (Figure 3-16 (b)) is then fitted with a Gaussian fit curve to identify the mean QW thickness value along with the full width at half maximum (FWHM) of the distribution. Thus the measurement procedure allows us to have an overall idea of the QW thickness distribution of the whole structure. For example, from the distribution plot (Figure 3-16(b)) obtained from considering a total observed lateral length ( $L$ ) of  $4.2 \mu\text{m}$ ; we can conclude that the mean QW thickness of the whole structure is about  $2.75 \text{ nm}$  with FWHM value of Gaussian fit is of  $1.54 \text{ nm}$ , which is an indication about the amount of QW thickness variation within the structure. The QW thickness distribution graph also gives us information about the highest and lowest QW thickness present within the structure.

Moreover, following the procedure described above, we have measured the thickness of individual QW regions, the barrier thicknesses in between two QWs and the capping layer thicknesses of all our studied samples. The obtained data from each sample are analyzed and the results are discussed in later chapter (chapter 4).

### 3.2.2 Indium composition determination within the InGaN layers

In determining the indium composition within the QWs different techniques such as high angle annular dark field-scanning transmission electron microscopy (HAADF-STEM), electron energy loss spectroscopy (EELS), three dimensional atomic probe microscopy (3DAP), energy dispersive X-ray (EDX), X-ray diffraction (XRD) and/or transmission electron microscopy (TEM) techniques are available. However, the HAADF-STEM, EELS, 3DAP and EDX techniques require serious extensive calculation and image simulations to determine the chemical composition and different research groups used these techniques mainly to identify indium clustering and/or determine composition value of QWs within very small volume of their sample as discussed in section 2.1.

However, several research groups used the HRTEM images and treat them either in direct or reciprocal spaces to obtain the lattice parameter values of the layer from the image and then relate the information to the composition values. For example, T. schulz et al<sup>16,17</sup> treat the

HRTEM images in direct space to identify the composition value, whereas Maxim Korytov et al<sup>18</sup> treat the HRTEM images in reciprocal space to identify the compositional change within their samples.

The HRTEM images with high magnification allow us to have an array of intense spots within the image. The distance between the spots corresponds to the distance between atomic positions of the structure, thus the basic idea in direct space treatment is to determine the lattice parameter values of the structure by calculating the nearest neighboring spot distances along in plane and out of plane directions of the image to have a and c lattice parameters, respectively. But the accuracy in determining the lattice parameter values depends on HRTEM image quality and also on identifying the maximum intensity spot positions with sub-pixel accuracy as noise signal may blur the exact position of the maximum intensity spot within the image. Figure 3-17 illustrates this fact by showing a slight change in the measured distance (a and a') of the adjacent intensity spots due to uncertainty in locating the exact maxima positions.

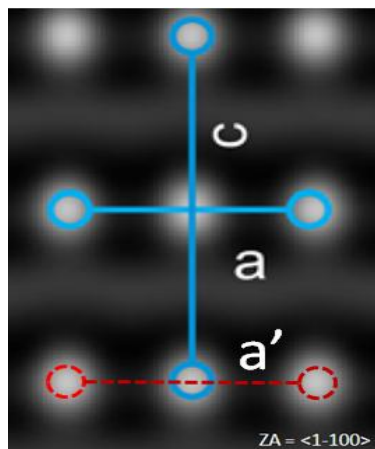


Figure 3-17: Schematic diagram of a high resolution transmission electron microscopy (HRTEM) image along  $\langle 1-100 \rangle$  zone axis, showing the difficulty of identifying the maximum intensity position by solid blue and dashed red bar along  $\langle 11-20 \rangle$  direction.

To compensate the noise impact and calculate the lattice parameters accurately, T. Schulz et al<sup>16</sup> suggest and demonstrate that by taking a series of at least 30 HRTEM images of a thin c-TEM sample along  $\langle 1-100 \rangle$  zone axis and at identical image conditions using an aberration corrected TEM, one can determine all the maximum intensity spots with sub-pixel accuracy using a peak finding algorithm (using an iterative center of gravity approach) of each image of the series. Thus calculating the nearest neighboring spot distances along  $\langle 11-20 \rangle$  and  $\langle 0001 \rangle$  direction of the images, one can obtain a series of data about in-plane (a lattice parameter) and out of plane (c lattice parameter) parameters, respectively. Finally, averaging out the obtained

data one can obtain the lattice parameters precisely and correlate the information to identify the compositional value of the studied region.

Again, Maxim Korytov<sup>4</sup> in his thesis work compares and demonstrates the drawbacks of both direct space and reciprocal space treatment of HRTEM images for determining the composition value of an epilayer through strain deformation measurements along the growth direction between epilayer and the substrate layer. He used projection method (PM) and the geometric phase analysis (GPA) method for treating the HRTEM images in direct space<sup>19</sup> and reciprocal space<sup>20</sup>, respectively. Through image simulation, he proposed that the projection method, where it directly measure the distance between the intensity maxima of a profile obtained from a studied region, has limitation in identifying accurately the intensity maxima position due to noise in an image. Moreover, the identification process of the peak intensity position of the profile also depends on which type of polynomial, its order and number of points are used to fit the intensity profile. On the other hand, GPA works well in noisy images as a particular mask is used while selecting one diffraction beam spot, which helps to reduce the noise impact, on the reciprocal space<sup>20</sup> treatment. The detail of the GPA technique is going to be discussed in section 3.2.2.2.

Yet, the GPA technique also suffers from some drawbacks as Maxim Korytov<sup>4</sup> demonstrated through HRTEM image simulation that the change in intensity contrast at the interface of two different layers causes an unwanted amplitude fluctuation of the strain profile map at positions which correspond to the interface of two different layers. He suggested that ignoring the strain values at the interface of the strain profile, it is still possible to identify an even very small amount of composition variation (0.2% of indium in InGaN/GaN) within two different layers with the GPA technique.

In this work, we are concerned about the overall average indium composition value of the samples, which drives us to consider different QWs of the sample structure (from first QW to the last QW) as well as at several places of each QW as illustrated in Figure 3-14. This is the reason why we did not follow the direct space method described by T. Schulz et al<sup>16</sup>. In that case, we have to prepare thin cs-TEM sample for each QW region, which makes the sample preparation very challenging in our study as we have at least 10 QWs in each sample. Moreover, noise may exist in the HRTEM images due to sample preparation as well as cs-TEM sample thickness variation.

However, T. Schulz et al<sup>17</sup> also demonstrate and suggest that it is possible to quantitatively measure the indium clustering from the lattice parameter values (a and c parameters) obtained from a HRTEM images of a very thin sample. They showed that by measuring weighted average distance between the individual atomic positions of an HRTEM image, one can correlate the indium composition variation within the sample from the measured c/a ratio. By comparing the

simulation and experimental images, they have showed that the limitation of this approach is that the sample should be very thin with small probe volume (12 nm X 12nm X 8 nm with only 8 nm thickness along the e-beam direction of the TEM) and the HRTEM image should be taken with an aberration corrected TEM at a particular zone axis  $\langle 1-100 \rangle$  to maximize the phase contrast and minimize the contrast delocalization within the image<sup>21</sup>. But our motivation is to study large sample areas to get more statistical data about individual QWs and overall data for each sample, so we have prepared thick cs-TEM samples to analyze different regions of each QW of the 10 MQW samples as illustrated in Figure 3-14. Moreover, for such analysis we do not use any aberration corrected TEM to obtain and analyze HRTEM images. Considering these limitations and to overcome the significant issues in our analysis, we have used the GPA technique to determine the average Indium composition within the QWs and tried to qualitatively identify the indium clustering by Z-contrast imaging (HAADF imaging) as explained in section 3.1.4.

In determining the indium composition within our samples, we have taken the HRTEM images at particular off-axis two beam conditions and analyzed the HRTEM images to identify the lattice deformation value along the growth direction within InGaN QWs with respect to GaN layer as reference. As discussed in section 1.3.1, we then use the concept of the percentage of lattice deformation,  $e_{zz}$  as a function of indium composition ( $x$ ) to identify the compositional value within the QWs. In the following subsections, we are going to discuss the methods that we have employed to take the HRTEM images and analyze the images for indium composition determination.

### 3.2.2.1 Off-axis two beam conditions in TEM

D. Gerthsen et al<sup>22</sup> reported that in a two beam conditions with 0004 diffracting beam spot in strong intensity and the 0002 diffracting beam centered on the optic axis (off-axis), the fringe image formed by selecting the 0000 and 0002 beam spots provide the most reliable lattice deformation information of the  $\text{In}_x\text{Ga}_{1-x}\text{N}$  layer depending on the indium composition ( $x$ ) in TEM technique. In this work, we have utilized exactly the same off-axis two beam conditions described by D. Gerthsen et al by tilting the sample about  $6^\circ$  from  $\langle 11-20 \rangle$  zone axis to take the HRTEM images for quantitative analysis of our samples. The HRTEM images are then treated by geometrical phase analysis (GPA) method to find out the lattice deformation of InGaN layer with respect to that of GaN layer as a reference.

The basics behind the GPA method and the operational procedure are discussed in detail in the following subsection.

### 3.2.2.2 The geometrical phase analysis (GPA) method

The geometrical phase analysis (GPA) method allows us to obtain the local strain present in a layer with respect to a reference region. For a 1D case, Figure 3-18 schematically illustrates the basics behind the technique involved in determining the strain. Here two fringe images are considered where one is totally unstrained and termed as reference and another one has both strained and unstrained regions with respect to reference image. Due to the local change in lattice periodicity of the strained layer, a phase shift of  $p_0$  may occur between the two fringe images. This phase shift of  $p_0$  is directly proportional to the magnitude of the change in fringe periodicity within the strained region. Thus taking the derivative of this phase shift, it will provide us the local strain involved in that particular region.

As GPA treats data in reciprocal space,<sup>20</sup> after choosing a particular Bragg's reflection of the contributing waves of the image, it will calculate the phase shift present within the treated image from that selected Bragg's reflection and will provide the strain map associated to that image through digital image processing.

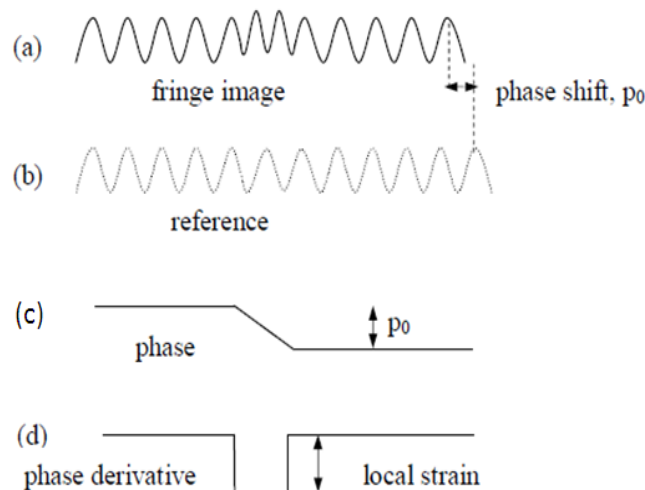


Figure 3-18: (a) Fringe image of a region where local displacement is present, (b) correspond to the fringe image of a reference region where there exist no local displacement, (c) illustrate the phase change between the two fringe images (a) and (b), (d) provides the local strain calculated from the phase derivative of (c)<sup>4</sup>.

The steps that are followed in identifying the local strain within an HRTEM image are described as follows:

- Step one: the Fourier transformation of the HRTEM image (Figure 3-19 (a)) is calculated which reveals the Bragg-reflections of the waves contributing to the image. One Bragg reflection is selected as a reciprocal lattice vector  $g$  (in our case we have selected the 0002 diffraction spot) with a certain symmetric mask of particular

size and shape around the spot (Figure 3-19 (b)). The size and shape of the used mask is discussed later.

- Step two: A complex inverse Fourier transformation is calculated to obtain the phase image which only deals with phase component (Figure 3-19 (c)).
- Step three: A region with known lattice parameter within the phase image is selected as reference region. Then the reciprocal vector is refined in order to minimize the phase variation within the selected reference region (Figure 3-19 (d)).
- Step four: Taking the derivative of the refined phase image, the deformation map of the considered HRTEM image is obtained (Figure 3-19 (e)).
- Step five: Drawing a profile within the deformation map in the [0001] direction will give us the value of the lattice deformation with respect to a reference region (Figure 3-19 (f)).

As discussed earlier the advantage of the GPA technique is that it is less sensitive to noise in the images than any direct space method in determining the strain deformation values, this noise reduction is governed by the mask size used in the GPA technique. The smaller the mask size, the smoother the image would be. But a smaller mask also averages out the details of the map as the spatial resolution of the strain map is inversely related to the mask size<sup>23</sup>. In this work, a commercially available plug-in GPA v2.0 for Digital Micrograph has been used. It has three standard mask sizes: the largest one of  $g/2$ , medium one of  $g/3$  and the smallest one of  $g/4$  radius. We used a cosine mask of  $g/3$  radius to select the 0002 diffraction spot to obtain the strain map of the image as discussed above.

In this work, the drawbacks of the GPA technique generated due to change in image contrast at the interface of two different layers, as discussed by Maxim Korytov<sup>4</sup> and Eirini Sariginnidou<sup>39</sup>, are avoided by considering the strain profile value coming from the middle of the InGaN layer region. For example, we have considered the lattice deformation values from the center region of the profile and approximate the average lattice deformation value for the InGaN layer with respect to GaN substrate layer (Figure 3-19(f)). We then used Figure 1-11 to correlate the averaged lattice deformation value  $e_{zz}$  to that of indium composition value ( $x$ ) to conclude about the percentage of indium composition present in the studied InGaN layers. For example, from Figure 3-19 (f), we have found the average lattice deformation value of about 2.8% for InGaN layer to that of GaN layer, which corresponds to an indium composition of about 17% within that InGaN layer while considering the sample in bi-axial stress state.

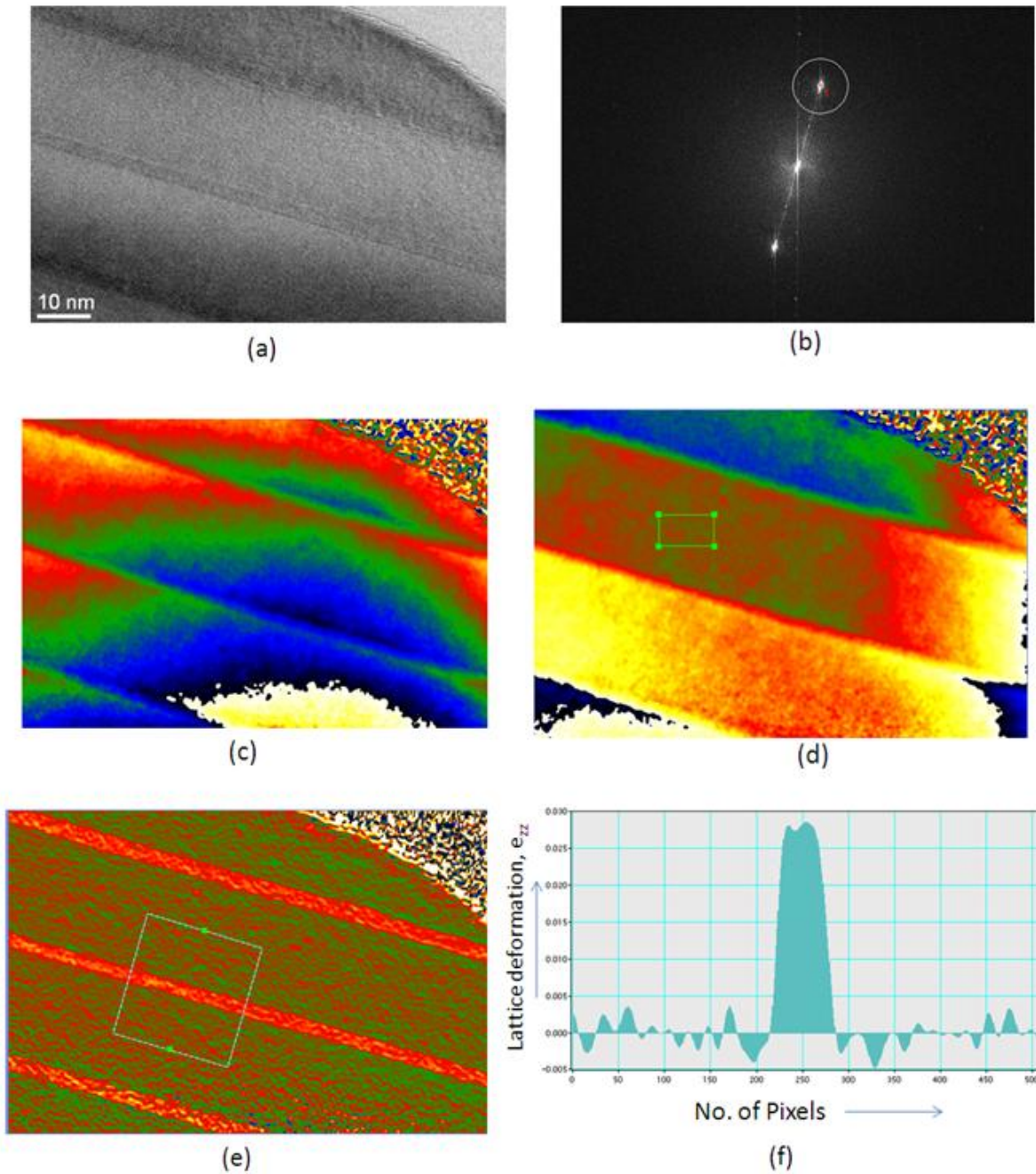


Figure 3-19: **(a)** High resolution transmission electron microscopy (HRTEM) image of a sample taken at a particular off-axis two beam condition, **(b)** Fourier Transformation of the image (a) and selecting the (0002) diffracting spot with a medium sized cosine mask, **(c)** Phase image found from Inverse Fourier Transformation calculation, **(d)** refined phase image obtained by refining the phase within a selected (green rectangle) reference area, **(e)** deformation map of the image (a) after taking the phase derivative of image (d), and **(f)** lattice deformation profile from the selected region of image (e) as indicated by white square.

Now as all cs-TEM samples are prepared using a standard mechanical polishing process followed by dimpling from one side and finally a focused ion beam thinning process, the thickness along the e-beam direction at different parts of the sample is not uniform. This thickness non-uniformity along the e-beam direction may cause the surface relaxation of the QW regions at or near the edge of the sample as discussed in section 1.3.1 and increase the uncertainty between the uni-axial and bi-axial or in between stress state conditions of the studied areas, which in turn may raise the question about the validity of the obtained composition value since the same strain value ( $e_{zz}$ ) indicates a different composition value depending on uni-axial or bi-axial state condition (Figure 1-11). To be sure about the stress state condition of the studied area of the sample, we have analyzed the sample at different places from the very edge to the thick part of the sample as schematically illustrated by blue oval shaped marks, numbered from 3 to 5 in Figure 3-14. We have found that for our studied samples the lattice deformation value ( $e_{zz}$ ) does not change its value while changing the position of the studied regions from very edge to thick part of the sample for each QW (Note that for a QW with certain percentage of composition value, while suffering from both bi-axial and uni-axial stress state conditions due to sample thickness change, should have different lattice deformation value ( $e_{zz}$ ) from place to place within the QW just to indicate the same composition value). Thus it confirms that the samples are only in one stress state condition and we may predict that the QWs are in a bi-axial stress state as we analyzed in relatively thick parts of the samples.

In order to confirm the indium compositions obtained from HRTEM images assuming biaxial stress condition, we systematically conducted x-ray diffraction  $\omega$ - $2\theta$  scans of all the samples and simulations to verify the obtained TEM data. The details of the XRD scan and simulation processes are discussed in section 3.3.

### 3.2.3 Dislocation analysis through TEM

Any defect in a crystal deforms the perfect crystal structure and induces a strain field around that defect. Figure 3-20 schematically illustrates one situation where the planes of the crystal are considered not to be in Bragg's condition but due to the presence of a dislocation, the strained field near the dislocation may bend back the plane to Bragg's condition and provide high intensity from the strained region. Thus depending on the TEM imaging condition, change in image contrast can be obtained from such defects and they can be identified. For example, from cs-TEM images in Figure 3-7, we can easily identify the existence of two threading dislocations in the sample from both BF and DF imaging condition. In this work, the weak beam dark field (WBDF) imaging technique is used to identify the type of dislocation from the image contrast obtained, while taking the image at a particular diffracted beam spot  $\mathbf{g}$ . The appearance of such contrast within the image depends on the extinction principle of dislocation

contrast. Thus we are going to discuss the visibility criteria of dislocation contrast in detail in section 3.2.4.

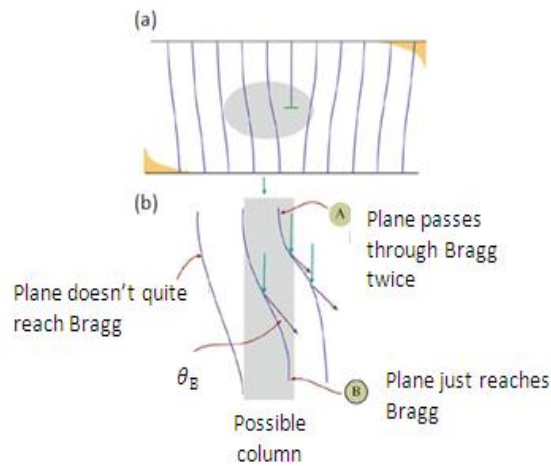


Figure 3-20: (a) Schematic diagram showing an edge dislocation inducing strain in planes near it, (b) depending on the imaging condition the strained region of the specimen may provide high intensity as the diffracting planes may bend back to Bragg's diffraction condition<sup>5(chapter 27, page 469)</sup>.

### 3.2.3.1 Extinction principle of dislocation contrast

In presence of a dislocation, using the modified Howie- Whelan equation<sup>5</sup>, the amplitude of a diffracted beam can be expressed as:

$$\frac{d\phi_g}{dz} = \frac{\pi i}{\xi_g} \phi_0 + 2\pi i S_R \phi_g \quad (3.10)$$

$$\text{with,} \quad S_R = S + \mathbf{g} \cdot \frac{d\mathbf{R}}{dz} \quad (3.11)$$

Where,  $\phi_g$  is the amplitude for the diffracted beam,  $\phi_0$  is the amplitude of the direct beam,  $\xi_g$  is the extinction distance,  $z$  is the thickness of the sample in the beam direction,  $\mathbf{g}$  represents the diffraction vector for beam  $G$ ,  $S_R$  is a vector representation of the deviation measured for exact Bragg condition in Ewald sphere representation for the system and most importantly the  $\mathbf{R}$  corresponds to the displacement vector in presence of a dislocation. It is also known that in polar coordinates ( $r$  and  $\phi$ ) system, the displacement vector  $\mathbf{R}$  can be represented as:

$$\mathbf{R} = \frac{1}{2\pi} \left( \mathbf{b}\phi + \frac{1}{4(1-\nu)} \{ \mathbf{b}_e + \mathbf{b} \times \mathbf{u} (2(1-2\nu) \ln r + \cos 2\phi) \} \right) \quad (3.12)$$

where  $\mathbf{b}$  is the Burger vector,  $\mathbf{b}_e$  is the edge component of the Burger vector,  $\mathbf{u}$  is the unit vector along the dislocation line and  $\nu$  is the Poisson's ratio.

The amplitude of the diffraction beam  $\phi_g$ , directly depends on the value of  $\mathbf{R}$ , more precisely on the type of dislocation involved. For example, in case of a screw type dislocation, we know that  $\mathbf{b}_e=0$  and  $\mathbf{b} \times \mathbf{u} = 0$ , as  $\mathbf{b}$  and  $\mathbf{u}$  are in parallel to each other, thus the equation 1.23 become as:

$$\mathbf{R} = \frac{b\phi}{2\pi} \quad (3.13)$$

In equation 3.13,  $\phi$  is a function of sample thickness  $z$  along the beam direction, so the term  $\mathbf{g} \cdot \frac{d\mathbf{R}}{dz}$  in equation 3.11 becomes proportional to  $\mathbf{g} \cdot \mathbf{b}$  for screw type dislocations, Similarly, for edge type dislocations where  $\mathbf{b}=\mathbf{b}_e$ , the term  $\mathbf{g} \cdot \frac{d\mathbf{R}}{dz}$  in equation 3.11 becomes dependent on both  $\mathbf{g} \cdot \mathbf{b}$  and  $\mathbf{g} \cdot (\mathbf{b} \times \mathbf{u})$  terms, where the term  $\mathbf{g} \cdot (\mathbf{b} \times \mathbf{u})$  originates from the curvature of the slip plane involved with an edge type dislocation.<sup>5</sup>

Thus from the above discussion, we can conclude that the general criterion for invisibility of a dislocation in an image is:  $\mathbf{g} \cdot \mathbf{b} = 0$ . However, the dislocations become invisible when  $\mathbf{g} \cdot \mathbf{b} < \frac{1}{3}$  and also on the other hand dislocations become visible even if  $\mathbf{g} \cdot \mathbf{b} = 0$  when  $\mathbf{g} \cdot (\mathbf{b} \times \mathbf{u}) \neq 0$ .

Therefore, by selecting different diffracting beam spots  $\mathbf{g}_{(hkl)}$  and calculating  $(\mathbf{g} \cdot \mathbf{b})$ , we can observe and determine the type of a dislocation present in a sample from TEM images. Table 3-1 summarizes the visibility criteria for the different types of dislocation present in hexagonal wurtzite structure. Thus in WBDF imaging condition (discussed in section 3.1.2.2), if we take images with both  $\mathbf{g}= 11-20$  and  $\mathbf{g}= 0002$  diffracting beam spots, then dislocation of  $\langle a+c \rangle$  type will appear bright in both images but for  $\langle a \rangle$  and  $\langle c \rangle$  type dislocations they will appear bright only in one of the two images. The  $\langle a \rangle$  type will appear bright in the image taken with  $\mathbf{g}= 11-20$  diffraction beam spot (as  $\mathbf{g} \cdot \mathbf{b} = 2$ ) and similarly the  $\langle c \rangle$  type dislocation will appear in the image taken with  $\mathbf{g}= 0002$  diffraction beam spot only (as  $\mathbf{g} \cdot \mathbf{b} = 2$ ).

Table 3-1: Criteria for the dislocation contrast for a, c and a+c types of dislocation. Dislocation become invisible when  $\mathbf{g} \cdot \mathbf{b} = 0$  and visible when  $\mathbf{g} \cdot \mathbf{b} \neq 0$

$\mathbf{g} \cdot \mathbf{b}$		$\mathbf{b}$		
		$a = 1/3 \langle 11-20 \rangle$	$c = \langle 0001 \rangle$	$a+c = 1/3 \langle 11-23 \rangle$
$\mathbf{g}$	11-20	2	0	2
	0002	0	2	2

In this work, to observe and locate the threading dislocation positions within the cs-TEM samples, we tilt the samples along  $\langle 1-100 \rangle$  zone axis (ZA) first and use a large objective aperture to select multiple diffracted beam spots (selected diffracted beam spots are: 0002, 0000, 11-20 and their complimentary ones) on the back focal plane of the objective lens to form the multi-beam (MB) images. As explained, any threading dislocation present within the

samples will provide a change in image contrast, thus we can identify the positions of the threading dislocations within the cs-TEM samples through these  $\langle 1-100 \rangle$  zone axis MB images. Then we tilt the samples from the  $\langle 1-100 \rangle$  zone axis and maneuver the TEM machine to obtain the WBDF images both with  $g = 11-20$  and  $g = 0002$  beam spots at the located threading dislocation positions. Thus using the dislocation visibility criteria discussed above, we are able to identify the type of the dislocation by analyzing the obtained images. For example, Figure 3-21 illustrates the identification process of dislocation type through different images. The blue arrows indicate  $\langle a \rangle$  type and the yellow arrow indicates  $\langle a+c \rangle$  type dislocation present within the image following the dislocation visibility criteria.

Following the same procedure described for TEM, we have used STEM to observe and characterize the dislocations in relatively thick regions and in large field of view of the sample, as STEM images are less sensitive to sample thickness.<sup>6</sup>

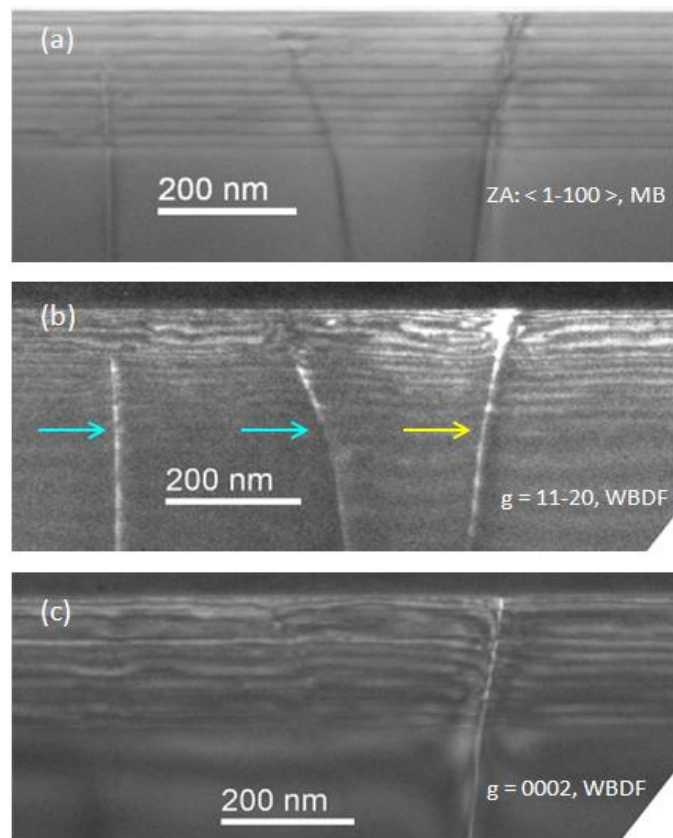


Figure 3-21: (a) Multi-beam (MB) imaging along  $\langle 1-100 \rangle$  zone axis (ZA). Weak beam dark field (WBDF) imaging with (b)  $g = 11-20$  and (c)  $g = 0002$  diffracted beam spots. Following the dislocation visibility criteria, the blue and yellow arrows indicate  $\langle a \rangle$  and  $\langle a+c \rangle$  type dislocations, respectively in the image (b).

### 3.3 X-ray diffraction

#### 3.3.1 Working principle of XRD

X-ray diffraction is a non destructive experimental procedure used to determine the structural properties of a sample. In this process, x-ray radiation of certain wavelength ( $\lambda$ ), close to the crystal lattice spacing, is allowed to probe a sample surface. In general, the x-ray beam is generated by bombarding a Cu target by accelerated electron in a vacuum tube and a monochromator is used to select the  $K\alpha_1$  line of the Cu of wavelength  $\sim 1.54 \text{ \AA}$ . The working principle of XRD is exactly same as that discussed for TEM system in section 3.1.1. The differences in between the two systems are that in case of XRD the diffracted beam is collected from the same side of the incoming incident beam and the wavelength of the incoming wave for XRD is much higher than that of TEM system.

In X-ray diffraction, the sample acts as a 3D grating, so when the sample and/or the detector is moved, a 3D array of diffraction maxima related to the sample can be investigated. Each set of crystal planes will produce one diffraction spot of the 3D array of diffraction maxima associated with the sample. The spot position is inversely related to the spacing of the corresponding planes and its direction is perpendicular to the plane. This 3D array reflects the information of the reciprocal lattice, from which the inter-plane spacing 'd' of the crystal in real space can be determined.

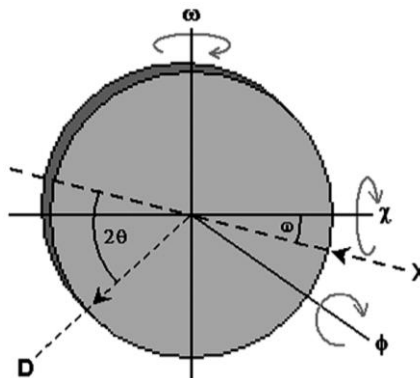


Figure 3-22: The different rotational axes of the sample used in X-ray diffraction, where  $\phi$  axis projects out of the plane of the page; the  $\omega$  and  $\chi$  axes lie within the plane of the page. X refers to the x-ray source and D to the detector of the system<sup>24</sup>.

Figure 3-22 illustrates the different rotational axes of the sample that can be changed to evaluate the different diffraction spots associated with a crystal sample along with the position of the detector D. The  $\omega$  and  $\chi$  rotational axes lie within the sample surface and the other axis  $\phi$  is perpendicular to the sample surface. In Figure 3-22, the X and D correspond to the x-ray source and the detector of the XRD system. Moreover, the angle  $\omega$  is the angle between the

sample surface and the incoming x-ray direction and the  $2\theta$  correspond to the angle between the transmitted X ray direction and the detector position direction as illustrated by the Figure 3-22.

By changing any one of the parameters discussed above of an XRD system, one particular type of scan data can be achieved. Moreover, to investigate different diffraction spots related to the different planes of the sample, several diffraction geometries are used in XRD. Figure 3-23 shows the two type of diffraction geometries used in this work. A symmetric geometry is used to investigate the crystal planes parallel to the sample surface, in this case  $2\theta=2\omega$ . And in asymmetric geometry, those diffraction spots are observed which are coming from planes not parallel to the sample surface. An offset in  $\omega$  is applied (offset= $\theta\pm\omega$ ) to obtain a grazing incidence or exit configuration.

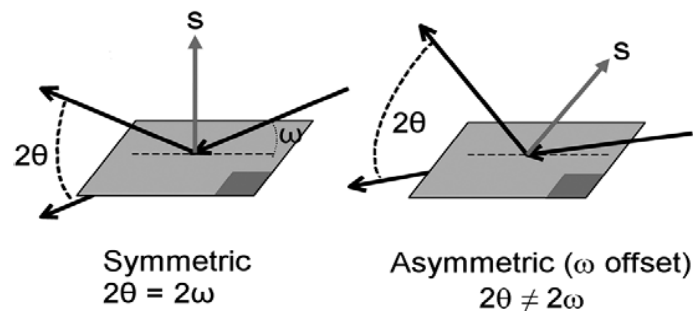


Figure 3-23: The two diffraction geometries used in this work: symmetric geometry is used for  $\omega$ - $2\theta$  scan and asymmetric geometry for reciprocal space mapping (RSM) scan.<sup>24</sup>

In this work, using symmetric diffraction geometry we have performed the 0002  $\omega$ - $2\theta$  scan for each of our samples. In such scan type, the sample is rotated around  $\omega$  axis and the detector is rotated by  $2\theta$  with an angular ratio of 1:2. Considering the reciprocal space, such scan allows to probe a small volume around the corresponding diffraction spot (in our case the diffraction spot is 0002) depending on the amount of deviation applied to  $\omega$  scan value. In graphical representation of the scan, the x axis is in units of  $\omega$  angle.

The asymmetric diffraction geometry is applied to evaluate the reciprocal space map (RSM) at 20-25 diffraction spot of our studied sample in order to evaluate the strain state of the samples.

In the following subsection, we are going to discuss the X-ray diffraction analysis processes used in determining the structural information of our samples, in brief.

### 3.3.2 X-ray diffraction analysis of multilayer epitaxy

#### 3.3.2.1 The $\omega$ - $2\theta$ scan

In this work as all the samples are grown on a GaN template layer deposited on sapphire substrate with at least 10 periods of InGaN/AlGaIn/GaN layers (MQWs), so conducting the  $\omega$ - $2\theta$  scan of (0002) plane of the samples allow us to have a distribution of super lattice (SL) fringe pattern centered along the sharp peak from (0002) plane of GaN template layer. The peak at lower angle relative to that of the GaN template layer peak is known as zero-order peak, which appears depending on the average indium composition value within one period of the structure. The other satellite peaks appear on both side of the zero-order peak due to repetition of the InGaN/AlGaIn/GaN layers. Figure 3-24 illustrates the 0002  $\omega$ - $2\theta$  scan data for 3 samples with different QW numbers in them<sup>25</sup>. The main sharp peak is indicated as GaN as it is from the thick GaN template layer and the second highest peak as zero-order peak (0). The other satellite peaks are numbered depending on the positional values of the satellites as increasing positive integer number are used for higher angles and negative integers are used for lower angle positional values than the zero order peak position (0). It is clear from the figure that when the number of the repetition period increases the intensity of the satellite peaks increases and they are easily distinguishable.

The relation between the different interference fringe distances to that of the corresponding thickness of the sample can be related as<sup>26,27</sup>:

$$T = \frac{(n_i - n_j)\lambda}{2(\sin\theta_i - \sin\theta_j)} \quad (3.14)$$

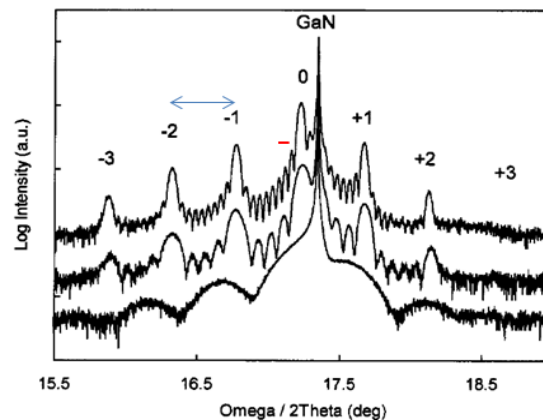


Figure 3-24: Experimental 0002  $\omega$ - $2\theta$  scan data of a InGaIn-GaN single quantum well (bottom), 5 QWs (middle) and 10 QWs (top), obtained using an analyzer crystal<sup>25</sup>.

where  $T$  corresponds to the thickness determined from the corresponding angles  $\theta_i$  and  $\theta_j$  of the two adjacent interference fringes  $i$  and  $j$  of order  $n$  in the  $0002 \omega-2\theta$  scan data and the  $\lambda$  is the wavelength of the X-ray ( $\lambda=1.54 \text{ \AA}$ ). Note that if we consider the two adjacent satellite peaks of the  $0002 \omega-2\theta$  scan data (blue arrow in Figure 3-24), the  $T$  value corresponds to the thickness of one period of the sample ( $T=t_w+t_b$ ), where  $t_w$  and  $t_b$  represent the thickness of well and barrier layer, respectively. But if we consider the angular distance (red bar in the Figure 3-24) of two adjacent interference fringes within two satellite peaks, then it corresponds to the total thickness of the sample ( $T=n(t_w+t_b)$ , where  $n$  is the total number of periods)<sup>28</sup>.

Now the position of satellite peaks in  $\omega-2\theta$  scan data depends on different parameters of the sample such as composition ( $x$ ), well thickness ( $t_w$ ), barrier layer thickness ( $t_b$ ) and/or the ratio between the barrier layer thickness to that of well layer thickness,  $R=(t_b/t_w)$  of the sample. Moreover, the intensity of the different higher order satellite peaks also depends on the thickness ratio ( $R=(t_b/t_w)$ ) and the composition ( $x$ ) value of the sample. To fit an experimental  $0002 \omega-2\theta$  scan data of a MQW sample with that of a simulation data, unfortunately, there may exist not only one but several possible combinations of these parameter values to have the same simulation fit.<sup>29</sup>

M.E. Vickers et al<sup>25</sup> demonstrates these facts by considering the following equations:

$$d_{av}T = d_{GaN}t_{GaN} + d_{InGaN}t_{InGaN} \quad (3.15)$$

$$T = t_{GaN} + t_{InGaN} \text{ and } R = t_{GaN}/t_{InGaN} \quad (3.16)$$

where  $t_i$  is thickness of a layer  $i$  and  $T$  the thickness of one period,  $d$  is the inter-planar spacing of a layer which in other words depends on composition value of the layer and  $R$  is the thickness ratio of the GaN barrier to the InGaN well layer. They have simulate the  $0002 \omega-2\theta$  scan data for a 10 QW InGaN/GaN structure by changing different parameters as illustrated in Figure 3-25 and Figure 3-26.

In Figure 3-25, the simulation result is for a fixed indium composition of 15% ( $x_{in}=0.15$ ), but changing the GaN/ InGaN thickness ratio ( $R$ ) from 4 to 2 with  $1 \text{ \AA}$  step size for both layers is presented. Note that the GaN barrier and InGaN well layer thicknesses are set to  $80 \text{ \AA}$  and  $20 \text{ \AA}$ , respectively for highest thickness ratio of  $R=4$  for bottom scan, whereas the GaN layer and InGaN layer thicknesses are of  $67 \text{ \AA}$  and  $33 \text{ \AA}$ , respectively for lowest thickness ratio of  $R=2$  presented in top scan.

Again, the simulation result for same sample structure with fixed  $In_xGa_{1-x}N$  well and GaN barrier layer thicknesses at  $25 \text{ \AA}$  and  $75 \text{ \AA}$ , respectively, while varying indium composition ( $x_{in}$ ) is shown in Figure 3-26.

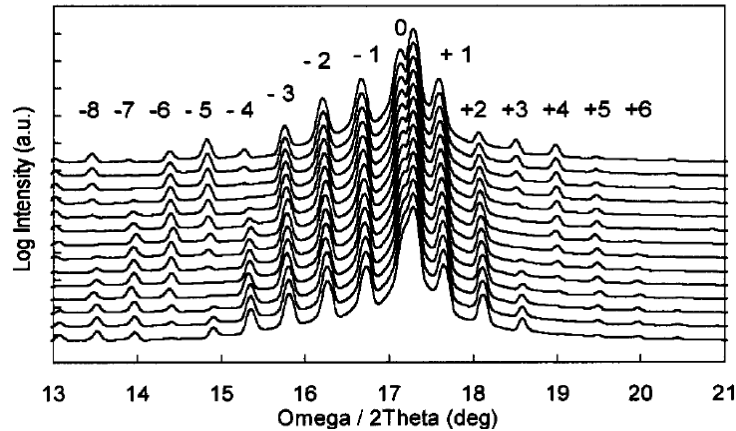


Figure 3-25: Simulated 0002 data for 10 QW structures with fixed In composition of 15% within InGaN layer ( $x_{In}=0.15$ ) but with a range of thickness ratios  $R$ . The bottom scan is for GaN/ $In_xGa_{1-x}N$  ratio of  $R=80/20=4$ , whereas the top scan has GaN/ $In_xGa_{1-x}N$  ratio of  $R=63/33=2$  while changing the ratio by 1 Å steps towards the top. Here each scan is offset vertically for clarity and without analyzer crystal in the detector<sup>25</sup>.

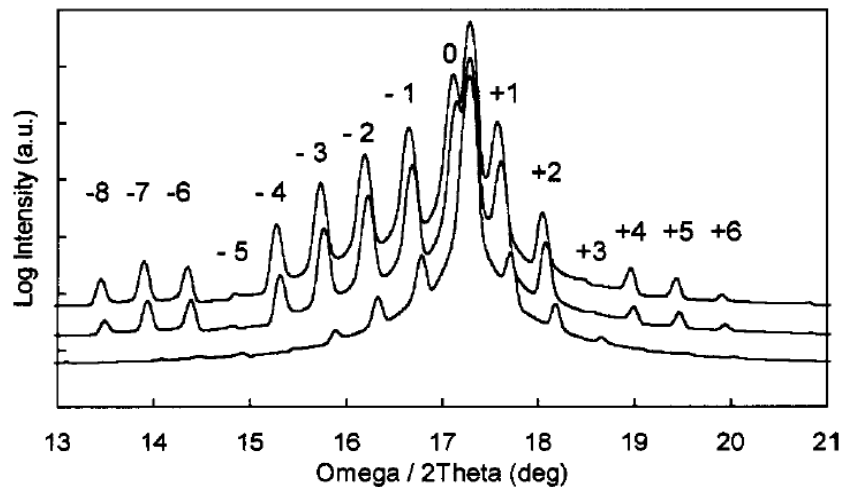


Figure 3-26: Simulated 0002 data for 10 QW structures with a range of  $x_{In}$ , where  $In_xGa_{1-x}N$  well layer and the GaN barrier layer thicknesses are set at 25 Å and 75 Å respectively. The bottom scan data is for  $x_{In}=0.05$ , middle one is for  $x_{In}=0.15$  and the top one is for  $x_{In}=0.25$ , each scan is offset vertically for clarity and without any analyzer crystal in the detector<sup>25</sup>.

They have concluded that for a certain thickness ratio  $R$  and indium composition ( $x_{In}$ ) certain satellite peaks become very weak and the intensity of higher order satellite peaks (-8 to -3 and +3 to +6) are more sensitive to the change of the thickness ratio ( $R$ ) and Indium composition ( $x_{In}$ ) values for such sample structure. The intensity of all the satellite peaks increases when the thickness of the InGaN layers ( $t_w$ ) and higher indium content ( $x_{In}$ ) is increased. Moreover, the satellite peaks (including the zero-order peak) shift towards lower angular position of the 0002  $\omega$ - $2\theta$  scan data, while increasing the Indium composition ( $x_{In}$ ) values as shown in Figure 3-26

25,27,30

Thus comparing the relative intensities of higher order satellite peaks of several simulated scan data to that of experimental scan data one may predict structural information of the sample unambiguously<sup>25</sup>. This analyzing process is lengthy and difficult. But if one knows one of the simulating parameters in first hand, then it is much easier to fit the experimental scan data to determine the other structural information of the sample unambiguously and easily.

In this work, we have utilized HRTEM imaging techniques (as discussed in section 3.2.1 and section 3.2.2) and analyzed quite large sample areas of each sample to identify the average thickness of different layers (within 1-2 ML of accuracy) as well as the Indium composition of the sample. But as discussed in section 1.3.1, because of the uncertainty in predicting the average Indium composition ( $x_{In}$ ) of each sample from TEM image analysis, we do not use the obtained indium composition ( $x_{In}$ ) value as a known parameter, but instead used different layers' average thickness value to fit the 0002  $\omega$ - $2\theta$  scan experimental data because of their reliability (1-2 ML accuracy).

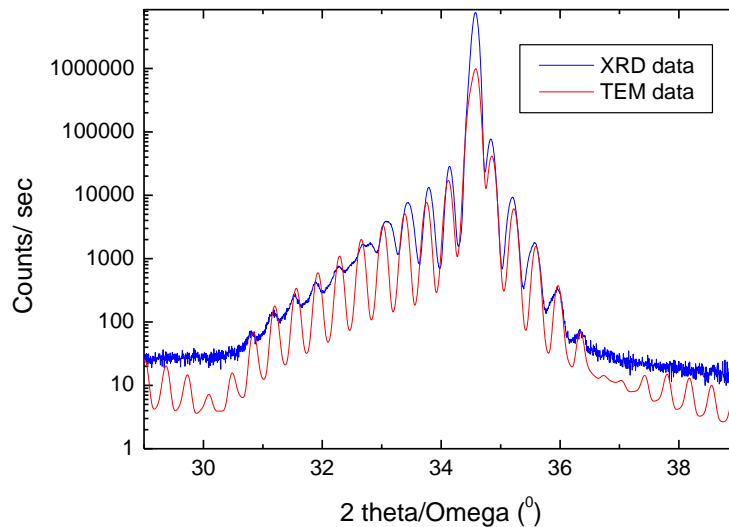


Figure 3-27: Fit of the  $\omega$ - $2\theta$  x-ray diffraction scan data for one sample (sample Z), using thickness and composition data deduced from the quantitative transmission electron microscopy analysis.

After obtaining the Indium composition ( $x_{In}$ ) value from the 0002  $\omega$ - $2\theta$  scan data fit, we are able to identify whether the obtained indium composition ( $x_{In}$ ) from TEM analysis is reliable or not. Moreover, the indium composition ( $x_{In}$ ) value from the XRD fit allows us to confirm in which stress state (bi-axial or uni-axial) the cs-TEM samples are in. For example, Figure 3-27 illustrates the simulation fit of XRD data to that of TEM data for one sample (sample Z- discussed in chapter 4) which has 10 periods of InGaN/AlGaIn/GaN multi-quantum wells. In this

simulation we have considered the indium and aluminium composition of 20% and 8% respectively, along with different layer thickness values obtained from TEM analysis as known parameters. From the fit we can say that the used simulation data are relevant and thus by comparing the composition values of the fit to that of obtained TEM data we are able to verify our analysis.

However, the TEM analysis helps us not only to determine the average Indium composition of the samples but also the individual composition value of each QW and compare whether the composition value changes from QWs to QWs due to change in growth techniques. Eventual lateral Indium composition changes in individual QW may also be detected by TEM analysis.

In the next chapter, we are going to present in detail the results of our studied samples.

### 3.3.2.2 Reciprocal space map (RSM)

The RSM data is obtained by taking a series of  $\omega$ - $2\theta$  scans at successive  $\omega$  values (or vice versa) and presented in a map form. The coordinates of such plot is in reciprocal lattice units ( $1\text{RLU}=1\text{\AA}^{-1}= 2(\sin\theta)/\lambda$ ), so the scan angles used to construct such plot are converted into reciprocal lattice units  $s$  using the following two formulae<sup>31</sup>:

$$S_x = \frac{Q_x}{2\pi} = \frac{1}{\lambda} \{ \cos \omega - \cos (2\theta - \omega) \} \quad (3.17)$$

$$S_z = \frac{Q_z}{2\pi} = \frac{1}{\lambda} \{ \sin \omega + \sin (2\theta - \omega) \} \quad (3.18)$$

It is conventional in crystallography to use the units  $S_x$  and  $S_z$  and a wave-vector  $|k|=1/\lambda$ . However, in solid state physics the other two units  $Q_x$  and  $Q_z$  are generally used, where the wave-vector is considered to be  $|k|= 2\pi/\lambda$ . Anyway, the  $S_x$  or  $Q_x$  axis and the  $S_z$  or  $Q_z$  axis of the RSM can inversely related to the in-plane lattice parameter ( $a$ ) and out of plane lattice parameter ( $c$ ), respectively of the sample.

Figure 3-28 illustrates one RSM conducted around the diffraction spot of (20-25) plane of a sample with 10 periods of InGaN/(Al)GaN multi quantum well structure (sample Z), grown on top of thick GaN buffer layer where all the beam spots of the RSM are labeled as shown. Within the image the solid black line is drawn through the center of all super lattice (SL) spots and the dashed red line is drawn through the center of the GaN buffer layer spot of the RSM. We know that in case of a pseudomorphic structure, such lines drawn in a RSM image taken at a non-symmetric diffraction spot (for example the diffraction spot of (20-25) plane) should be well aligned. But if there is some in-plane relaxation within the InGaN epilayers then some misalignment between the lines will appear. Depending on the percentage of relaxation of the InGaN epilayer, the line passing through SL spots will move to left than that of the line passing through GaN spot as we know the relaxed InGaN epilayer has higher in-plane lattice parameters

than that of GaN layer ( $a_{\text{GaN}} < a_{\text{InGaN}}$ ). Thus determining the amount of misalignment on the line along X-axis of the RSM, one can calculate the percentage of relaxation within the epilayers of the structure.

Following the same analysis procedure on the RSM images of our studied samples we determine whether our sample is relaxed or not and if relaxed then of what percentage. We are going to present the percentage of relaxation of our studied samples in the next chapter.

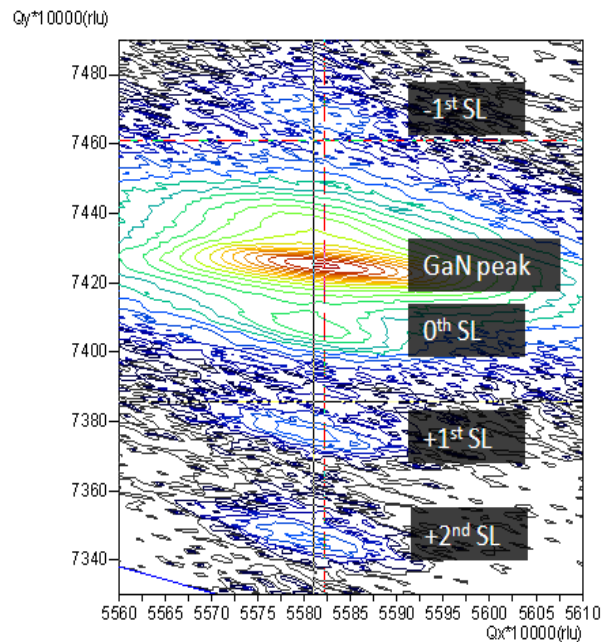


Figure 3-28: Reciprocal space map (RSM) of a sample with 10 periods of InGaN/GaN multi quantum well (Sample Z). The misalignment between the lines passing through different super lattice (SL) spots (black line) and the GaN buffer layer spot (red dashed line) indicate that there is some in-plane relaxation present in the InGaN epilayers of the structure.

### 3.4 Room temperature photoluminescence

In a photoluminescence (PL) experiment a direct band-gap semiconductor sample is excited with a high energy laser source. The electrons within the valence band of the sample get excited to the conduction band creating excited electron-hole pairs within the sample. The system then tends to come to its equilibrium state through the recombination process of these excited electron-hole pairs. This recombination process is achieved through either band-to-band transitions, or through discrete energy level transitions within the band gap of the sample, which are related to the dopants or defects that exist in the sample. These recombination processes are radiative in nature. Thus recording the spectrum of the whole radiation allows us to have peaks at different energies which correspond to different recombination processes.

Analyzing the photoluminescence (PL) spectrum gives information about the electronic band structure of the sample.

In this work, all the PL experiments are conducted at room temperature. The samples are placed in a translation stage to have the room temperature photoluminescence (RT-PL) at different positions of the samples, i.e. from center to the edge of the sample wafer.

### 3.4.1 Experimental setup and measurement

Figure 3-29 illustrates the experimental setup of the room temperature photoluminescence (RT-PL) experiment. A laser beam from a source is guided and focused on the sample surface with the help of mirrors and lenses, and different regions of the sample are excited by moving the position of the sample with a translation stage. The emitted light from the sample is then collected through an optical system which is placed along the surface normal in front of the sample. The first lens of the optical system is placed in such a distance from the sample surface that the sample surface is at the focal distance of the lens. So the emitted light from that particular point of the sample is guided and transferred as a parallel beam to the second lens. Similarly, the second lens converges the incoming parallel beam and focuses it to a particular point (focal point) where the signal is coupled into an optical fiber connected to a multichannel photo-detector. Finally, the spectrum is analyzed by a computer as shown in Figure 3-29.

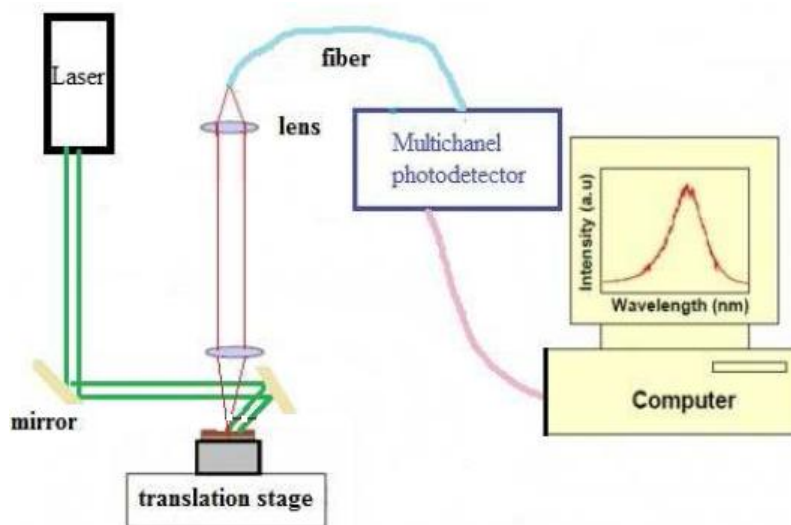


Figure 3-29: Schematic diagram of the room temperature photoluminescence (RT-PL) setup.

In our case, we have used a frequency-doubled argon ion ( $\text{Ar}^+$ ) laser as a source which emits at 244 nm. The intensity of the laser beam within the sample depends on the absorption coefficient ( $\alpha$ ) of the material and also on the depth of the sample ( $d$ ). We can relate the

intensity at any particular depth  $I(d)$  to that of incoming intensity ( $I_0$ ) of the laser beam according to the Beer-Lambert law<sup>32</sup>:

$$I(d) = I_0 \exp(-\alpha d) \quad (3.19)$$

Moreover, the penetration depth  $D$ , is defined as the inverse of the absorption coefficient ( $\alpha$ ) of a material, i.e.  $D = 1/\alpha$ , which allow us to define a particular depth at which the intensity of the incoming laser beam becomes ( $1/e = 0.367$ ) about 36% of the initial intensity ( $I_0$ ). Thus it is this depth at which the energy of the incoming laser beam becomes too weak to excite any further electron-hole pair in the sample.

It has been reported by O. Ambacher et al<sup>33</sup> and J.F. Muth<sup>34</sup> that the absorption coefficient ( $\alpha$ ) of a sample varies with the sample structure, doping levels, wavelength of the incident beam and also with the temperature. Moreover, J.F. Muth et al<sup>34</sup> reported the absorption coefficient ( $\alpha$ ) of a thick GaN layer grown on c plane sapphire substrate by MOCVD at different excitation energy at room temperature ( $T=295$  K). Figure 3-30 shows their obtained graph for the absorption coefficient ( $\alpha$ ) versus the incident beam energy for GaN material at room temperature (295 K).

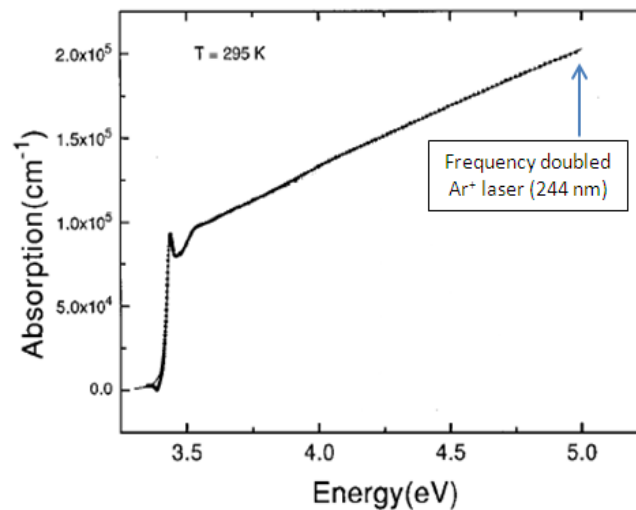


Figure 3-30: Absorption coefficient versus the incident beam energy for GaN at room temperature (295 K), where the energy position of Ar<sup>+</sup> laser (244 nm) is indicated by arrow<sup>34</sup>.

Table 3-2: Penetration depth  $D$  of the Ar<sup>+</sup> laser in a GaN layer

Laser	Temperature (K)	Wavelength (nm)	Absorption coefficient (cm <sup>-1</sup> )	Penetration depth (nm)
Frequency doubled Ar <sup>+</sup> laser	295	244	2.0X10 <sup>5</sup>	50.0

From the above discussion, we can find that the penetration depth ( $D$ ) for GaN material with  $\text{Ar}^+$  laser is only of 50 nm (Table 3-2). It means that only a thin layer close to the sample surface is excited and the PL spectrum correspond the response from such a thin layer. In all our studied samples, we have MQW structure with at least 10 QWs, so the total thickness of our sample is much more than 50 nm from the surface, which is why the RTPL spectrum is thought to originate from only 2-3 QWs from the surface of the sample. From the spectrum we identify the energy at which the spectrum has its maximum intensity and attribute the energy as the band to band transition energy for electron-hole pair recombination processes within the confined QW region as it has the highest probability. We evaluate the total integral intensity of the spectrum and assign that value to the energy (or wavelength) position at which the intensity is highest of the spectrum.

### 3.5 Atomic force microscope

Atomic force microscopy (AFM) is one of the different types of scanning probe microscopy (SPM), which is used to observe the morphology of the surface of a sample with few nm (1 nm to 5 nm) of lateral resolution. It is also known as scanning force microscopy (SFM). It consists of a cantilever with a sharp tip at the end. Generally the length of the cantilever is of 100 to 200  $\mu\text{m}$  and the tip radius is of few (5-60 nm) nm.<sup>35</sup> The lateral resolution of the system depends on the probing tip shape as the radius of curvature and sidewall angles of the tip limits its lateral resolution. It is obvious that the smaller the radius of curvature and the sidewall angles of a tip, the higher the resolution of the AFM system would be.

In this work, surface morphology of the sample has been observed using an AFM working in tapping mode. In such operating mode, the cantilever of the system is oscillating at or near its resonance frequency with amplitude ranging typically from 20 nm to 100 nm. A laser light beam is allowed to get reflected from the top of the cantilever and fall on a split photodiode detector as shown in the Figure 3-31. When the tip of the system is not even close to the sample but vibrating with its resonance frequency, the root mean square (RMS) value of the photodiode detector signal allows us to recognize the initial stage of the system. Then allowing the tip to lightly 'tap' on the surface of the sample, we may reduce the amplitude of the oscillation owing to atomic forces between the tip and the sample surface, including the Van der Waals forces, dipole-dipole interaction, electrostatic forces, etc-which in turn alters the RMS value of the detector signal from its initial value. This change in RMS value is detected by detector electronics and used to manipulate the feedback control system to change the vertical position of the cantilever-tip system so that the RMS value of the detector can gain its initial set point value at each data point (X,Y) of the sample. The change in the vertical position of the

cantilever-tip system is then used to form the topographic image of the sample through computer software. Tapping mode AFM allow us to have higher lateral resolution of 1 nm to 5 nm and the vertical resolution of approximately 1 Å for surface images of the sample<sup>35</sup>.

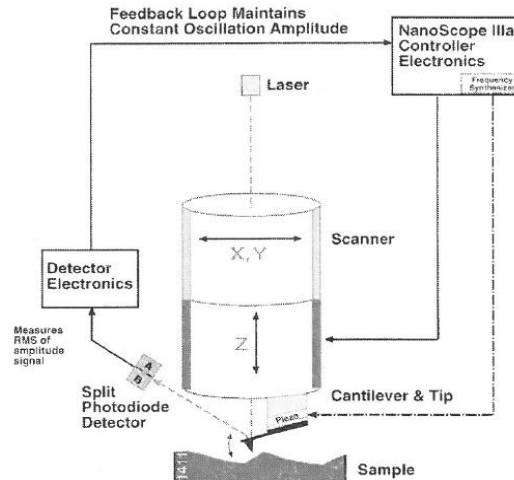


Figure 3-31: Schematic diagram for working principle of tapping mode atomic force microscopy<sup>35</sup>

In this work, to observe the surface roughness and to determine the average threading dislocation density (TDD) of a sample, several images have been acquired by AFM. The AFM allows us to take images in topographical image mode which records the height variation of the tip and allows us to measure the surface roughness and observe the surface topography to distinguish specific surface features such as threading dislocations and V-pits. Threading dislocations can be easily identified by AFM, as they create depressions (pits) on the sample surface. These depressions on the sample surface result from a balance between the surface energy and the TD line energy<sup>36</sup>. Moreover, the surface of samples grown by MOCVD are quite smooth and these depressions within the samples can be easily detected by AFM<sup>37</sup>. As an example, Figure 3-32 (a) shows the surface morphology of a ~20 nm thick GaN layer of an InGaN/AlGaIn/GaN multiple quantum well structure grown on sapphire substrate. The black points are related to the threading dislocations.<sup>38</sup> Figure 3-32 (b) shows the height scale of image (a). Analyzing the images, we can determine the root mean square (RMS) value of the surface roughness and also count the number of emerging threading dislocations; we can determine the average threading dislocation density (TDD) per  $\text{cm}^2$  of the sample. For example, the RMS value of the surface roughness of Figure 3-32 (a) is about 0.36 nm with average height of about 3.43 nm and the total TDD (considering both <a> and <a+c> type of dislocations) is about  $1.2 \times 10^9$  per  $\text{cm}^2$ .

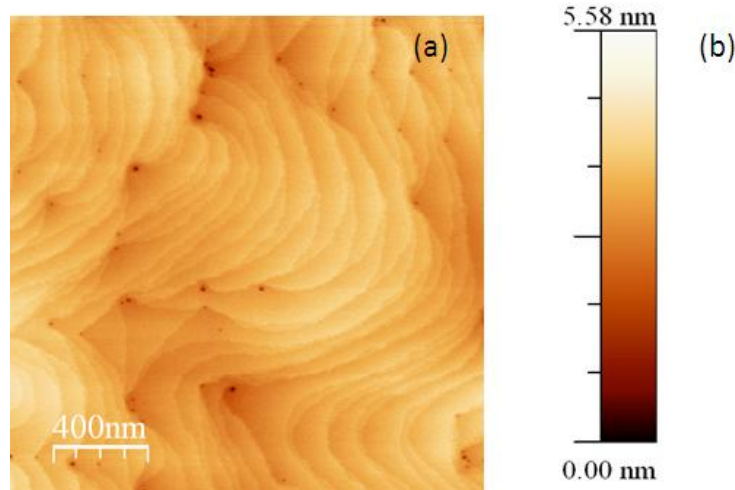


Figure 3-32: Atomic Force Microscopy (AFM) imaging of a  $2 \times 2 \mu\text{m}^2$  surface area of a multiple quantum well (MQW) sample: (a) Surface morphology, where black dots represent the threading dislocations, (b) height profile of the image in (a).

To measure the average threading dislocation density (TDD) and the root mean square (RMS) surface roughness values of the sample series more precisely, we have considered at least 8 AFM images with scan size of  $2 \times 2 \mu\text{m}^2$  at or near the center of the sample wafers. From each image we have calculated the TDD and the surface roughness and determine the cumulative average of the data to get the overall average. Figure 3-33 illustrates the TDD per  $\text{cm}^2$  and the surface roughness (RMS) values in nm scale measured for each image as well as the cumulative average of the data for one sample (sample C-discussed in chapter 4). Moreover standard deviation was measured from the data to show the overall range of the measured values. Table 3-3 summarizes the measured values of both the TDD and the RMS surface roughness of the sample.

Table 3-3: Measured threading dislocation density (per  $\text{cm}^2$ ) and root mean square (RMS) values of the surface roughness of one sample.

Sample	Threading dislocation density per $\text{cm}^2$	RMS surface roughness (nm)
Sample C	$1.0 \times 10^9 (\pm 2.5 \times 10^8)$	0.33 ( $\pm 0.08$ )

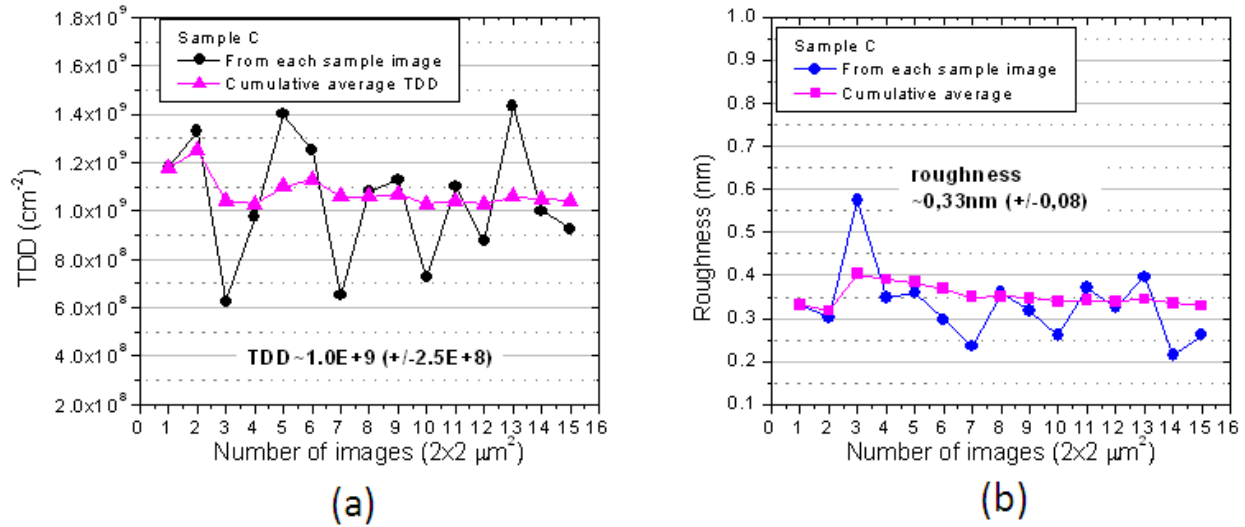


Figure 3-33: Graph presenting the measured (a) threading dislocation density and (b) surface roughness of each image along with the cumulative average values for one sample (sample C). From both graph we can conclude that the sample has overall average TDD of  $1.0 \times 10^9 \text{ cm}^{-2}$  and surface roughness (in rms) of  $0.33 \text{ nm}$  with a range of  $\pm 2.5 \times 10^8 \text{ cm}^{-2}$  and  $0.08 \text{ nm}$  for TDD and surface roughness, respectively.

From Figure 3-33, we can find that it is always better to consider at least 8 AFM images of  $2 \times 2 \mu\text{m}^2$  scan size and calculate the cumulative average to identify the overall average TDD and surface roughness values. Otherwise, there is a chance to have error in measured values as the cumulative average values are fluctuating and they become stable only after 8 images.

In this work, considering the TDDs of samples and observing the surface morphology, we have predicted the impact of the growth process differences within the samples. By comparing the TDD of the template used for the samples and the counted TDD of individual samples we were able to notify that additional emerging threading dislocations were generated in some samples. Moreover, we have seen some clustering of emerging threading dislocations at place to place for some samples, which motivates us to observe the samples through TEM techniques and try to find the origin of such additional threading dislocations in our samples in this work. Finally, we tried to relate the overall integral intensity of the RTPPL of the sample to that of TDDs.

## Summary

In this chapter, we have discussed the different characterization techniques such as HRTEM, XRD, AFM and RTPPL that are involved in this work. In each section of the chapter, we tried to present some basics behind each experimental process and then presented the individual experimental methods used in this work. Their necessities and importance to evaluate the properties of the samples are also discussed in detail. The correlations between individual experiments are also highlighted while discussing them in this chapter.

In the next chapter, we are going to present the obtained results of our studied samples through these experimental processes.

## References

- 1 Christopher Hammond, *The Basics of Crystallography and Diffraction* Second ed. (Oxford university press, New York, 2001).
- 2 L. de Broglie, Vol. 3, p. 22.
- 3 G.P.Thomson and A.Reid, *Nature* **119** (3007), 890 (1927).
- 4 M. Korytov, PhD thesis, Universite de Nice- Sophia Antipolis, France, 2010.
- 5 David B. Williams and C. Barry Carter, *Transmission Electron Microscopy A Textbook for Materials Science*. (Springer).
- 6 S.J. Pennycook and P.D. Nellist, *Z- Contrast Scanning Transmission Electron Microscopy*. (Kluwer Academic Publishers, The Netherlands, 1999).
- 7 P. J. Phillips, M. J. Mills, and M. De Graef, *Philosophical Magazine* **91** (16), 2081 (2011).
- 8 P. J. Phillips, M. C. Brandes, M. J. Mills, and M. De Graef, *Ultramicroscopy* **111** (9–10), 1483 (2011).
- 9 E. Rutherford, *Philosophical Magazine* **21**, 669 (1911).
- 10 T. Walther, *Journal of Microscopy* **221** (2), 137 (2006).
- 11 Tim Grieb, Knut Müller, Rafael Fritz, Marco Schowalter, Nils Neugebohrn, Nikolai Knaub, Kerstin Volz, and Andreas Rosenauer, *Ultramicroscopy* **117** (0), 15 (2012).
- 12 Andreas Rosenauer, Katharina Gries, Knut Müller, Angelika Pretorius, Marco Schowalter, Adrian Avramescu, Karl Engl, and Stephan Lutgen, *Ultramicroscopy* **109** (9), 1171 (2009).
- 13 Andreas Rosenauer, Thorsten Mehrstens, Knut Müller, Katharina Gries, Marco Schowalter, Parlapalli Venkata Satyam, Stephanie Bley, Christian Tessarek, Detlef Hommel, Katrin Sebald, Moritz Seyfried, Jürgen Gutowski, Adrian Avramescu, Karl Engl, and Stephan Lutgen, *Ultramicroscopy* **111** (8), 1316 (2011).
- 14 V. Grillo, *Ultramicroscopy* **109** (12), 1453 (2009).
- 15 <http://www.gatan.com/>.
- 16 T. Schulz, T. Remmele, T. Markurt, M. Korytov, and M. Albrecht, *Journal of Applied Physics* **112** (3) (2012).
- 17 T. Schulz, A. Duff, T. Remmele, M. Korytov, T. Markurt, M. Albrecht, L. Lymperakis, J. Neugebauer, C. Chèze, and C. Skierbiszewski, *Journal of Applied Physics* **115** (3) (2014).
- 18 M. Korytov, M. Benaissa, J. Brault, T. Huault, T. Neisius, and P. Vennéguès, *Applied Physics Letters* **94** (14) (2009).
- 19 R. Bierwolf, M. Hohenstein, F. Phillipp, O. Brandt, G. E. Crook, and K. Ploog, *Ultramicroscopy* **49** (1–4), 273 (1993).
- 20 M. J. Hÿtch, E. Snoeck, and R. Kilaas, *Ultramicroscopy* **74** (3), 131 (1998).
- 21 M. Lentzen, B. Jahnen, C. L. Jia, A. Thust, K. Tillmann, and K. Urban, *Ultramicroscopy* **92** (3–4), 233 (2002).
- 22 D. Gerthsen, E. Hahn, B. Neubauer, V. Potin, A. Rosenauer, and M. Schowalter, *physica status solidi (c)* **0** (6), 1668 (2003).
- 23 J. L. Rouvière and E. Sarigiannidou, *Ultramicroscopy* **106** (1), 1 (2005).
- 24 M A Moram and M E Vickers, *Reports on Progress in Physics* **72** (3), 036502 (2009).

- 25 M. E. Vickers, M. J. Kappers, T. M. Smeeton, E. J. Thrush, J. S. Barnard, and C. J. Humphreys, *Journal of Applied Physics* **94** (3), 1565 (2003).
- 26 P F Fewster, *X-Ray Scattering from Semiconductors*, 2nd ed. (Imperial College Press, London, 2003 ).
- 27 D K Bowen and B K Tanner, *High Resolution X-Ray Diffractometry and Topography*. (Taylor and Francis, London, 1998).
- 28 P. Fewster, *Journal of Applied Crystallography* **21** (5), 524 (1988).
- 29 T. M. Smeeton, M. J. Kappers, J. S. Barnard, M. E. Vickers, and C. J. Humphreys, *physica status solidi (b)* **240** (2), 297 (2003).
- 30 A. Krost, J. Bläsing, M. Lünenbürger, H. Protzmann, and M. Heuken, *Applied Physics Letters* **75** (5), 689 (1999).
- 31 Pietsch U, Hol’y V, and Baumbach, *High Resolution X-Ray Scattering From Thin Films and Multilayers* 2nd ed. (Springer, New York, 2004).
- 32 B. D. Cullity and S. R. Stock, *Elements of X-Ray Diffraction*, 3rd ed. (Prentice-Hall, Englewood Cliffs, NJ, 2001 ).
- 33 O. Ambacher, W. Rieger, P. Ansmann, H. Angerer, T. D. Moustakas, and M. Stutzmann, *Solid State Communications* **97** (5), 365 (1996).
- 34 J. F. Muth, J. H. Lee, I. K. Shmagin, R. M. Kolbas, H. C. Casey, B. P. Keller, U. K. Mishra, and S. P. DenBaars, *Applied Physics Letters* **71** (18), 2572 (1997).
- 35 *Scanning Probe Microscopy Training Notebook*. (Digital Instruments, Veeco Metrology Group 2000).
- 36 F. C. Frank, *Acta Crystallographica* **4** (6), 497 (1951).
- 37 B. Heying, E. J. Tarsa, C. R. Elsass, P. Fini, S. P. DenBaars, and J. S. Speck, *Journal of Applied Physics* **85** (9), 6470 (1999).
- 38 M. Khoury, A. Courville, B. Poulet, M. Teisseire, E. Beraudo, M. J. Rashid, E. Frayssinet, B. Damilano, F. Semond, O. Tottereau, and P. Vennéguès, *Semiconductor Science and Technology* **28** (3), 035006 (2013).
- 39 Eirini Sarigiannidou, PhD thesis, Université Joseph Fourier – Grenoble ISciences & Géographie, France 2004

## Chapter 4

Study of the impact of capping processes for InGaN  
quantum wells



## Chapter 4

### Study of the impact of capping processes for InGaN quantum wells

#### Introduction

In this chapter, we are going to study three sample series, where all the samples were grown using a homemade metalorganic chemical vapor deposition (MOCVD) vertical reactor. The motivation of such a sample series analysis is to determine the impact of different growth processes on the green, yellow InGaN/GaN multi quantum well structure. We have used the different techniques that are discussed in chapter 3 to obtain the structural and optical properties of the samples.

For the first sample series, two samples (samples 1 and 2) have been grown with no capping layer deposition after InGaN QW layers. The idea behind this sample series study is to achieve one specific wavelength (yellow) emission from a sample with a large InGaN QW thickness and low indium composition (sample 1) and another one with a relatively small InGaN QW thickness but higher Indium composition (sample 2). Figure 4-1 illustrates the calculated wavelength emission as a function of QW thickness and indium composition for the InGaN/ GaN system. As shown in the figure, yellow emission (570 nm) can be achieved with the following couples of QW thickness/Indium composition combination, for example: 6 nm/ 0.16, 3 nm/ 0.23, and 1.2 nm/ 0.43. To achieve such samples both the QW growth temperature and deposition time of the two samples have been modified. We have analyzed these two samples and present the obtained results in section 4.2.

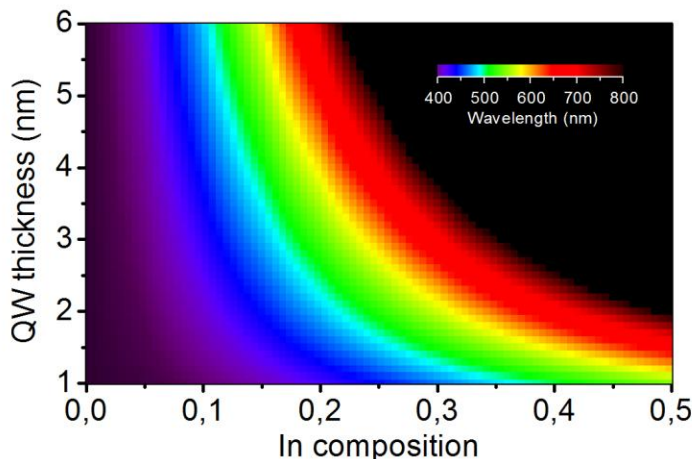


Figure 4-1: Calculated wavelength as a function of indium composition and quantum well thickness for InGaN/GaN system. (Courtesy from Dr. Benjamin Damilano)

Next, to evaluate the impact of a few monolayers of AlGaIn capping after each QW, three samples (sample B to D) have been grown in the second series. The growth process of AlGaIn

capping layer has been modified from sample to sample. However, one additional sample without any capping layer deposition has been grown as a reference sample (sample A) to compare the impact of growth process differences within the second sample series. The obtained structural and optical properties of this sample series are going to be presented in section 4.3.

Finally, in the last sample series, we have investigated three more samples (sample X to Z) to identify the impact of thick capping layer deposition processes at low growth temperature. Two of the samples were grown with GaN and the other one with AlGaIn as capping layer after each InGaN QW. We are going to present the obtained results in section 4.4 for this sample series.

Please note that we have grown all our samples using a 20 years old homemade vertical MOCVD reactor. The use of such a reactor has advantages and disadvantages. On one hand, this reactor is very versatile. It is for example relatively simple to change the gases, the growth pressure and temperatures. On the other hand, the samples grown on this reactor suffer from inhomogeneities. These inhomogeneities may be spatial inhomogeneities (change of thickness and composition with the position on the wafer) or inhomogeneities between different growth runs. We have thus found (see later) that using the same growth conditions for InGaN QWs, their thicknesses and composition may differ between the different runs. This is why we are going to analyze and compare the samples within each sample series to identify the impact of the growth process differences while considering one sample of each series as a reference one.

After growing the samples, we have conducted the XRD experiments at the center of the 2 inch sample wafer. Then we have conducted the AFM imaging at several places at or near the center for each sample. Room temperature photoluminescence (RT-PL) experiments have been conducted step by step from center to edge of the wafer as explained in section 3.4 and finally for TEM analysis we have managed to prepare all our cross-sectional TEM samples within  $2\pm 1$  mm from the center of the wafer except for one (sample C) which is from about  $5\pm 1$  mm away from the center.

We are going to describe the general growth process mechanism and the precursors used to grow all our studied samples in a homemade MOCVD reactor in section 4.1 and the discussion of the obtained results is presented in detail later in section 4.6.

#### **4.1 The growth process of the samples in MOCVD reactor**

All the samples are grown on commercially available n-type GaN on c-plane sapphire substrates by metalorganic chemical vapor deposition (MOCVD). Before growing the InGaIn/GaN multi quantum well structure, a few hundred nanometers (about 700 nm) thick Si doped GaN buffer layer was grown at high temperature (1080°C). Trimethylgallium (TMG), ammonia (NH<sub>3</sub>) are used as precursors for gallium and nitrogen atoms and hydrogen (H<sub>2</sub>) was used as carrier gas to

grow such thick buffer layers. The flow rates of these gases are of 5 standard cubic centimeters per minute (sccm), 3.5 standard liters per minute (slm) and 5 slm for TMG,  $\text{NH}_3$  and  $\text{H}_2$ , respectively. The growth was conducted for a total time of 18 minutes at a  $2.35 \mu\text{m}$  per hour growth rate.

After one first GaN barrier layer growth on top of the thick GaN:Si buffer layer, at least 10 periods of InGaN/(Al)GaN multiple quantum wells were grown with different capping processes on top of the InGaN QW layer. Figure 4-2 shows the general structure of the studied samples along with the growth temperature and the growth time. The whole MQW was grown utilizing nitrogen ( $\text{N}_2$ ) as carrier gas with a flow rate of 5 slm. Note that the growth time for the GaN barrier layers for all the samples was kept the same for 2 minutes (the thickness is about 14 nm or 20 nm) but the growth temperature was different ( $940^\circ\text{C}$  and  $970^\circ\text{C}$ ) from one sample series to another. For InGaN QW and capping layers, both the growth time and temperature were different from one sample series to another. The growth process differences of each sample will be discussed in detail in their relevant sections.

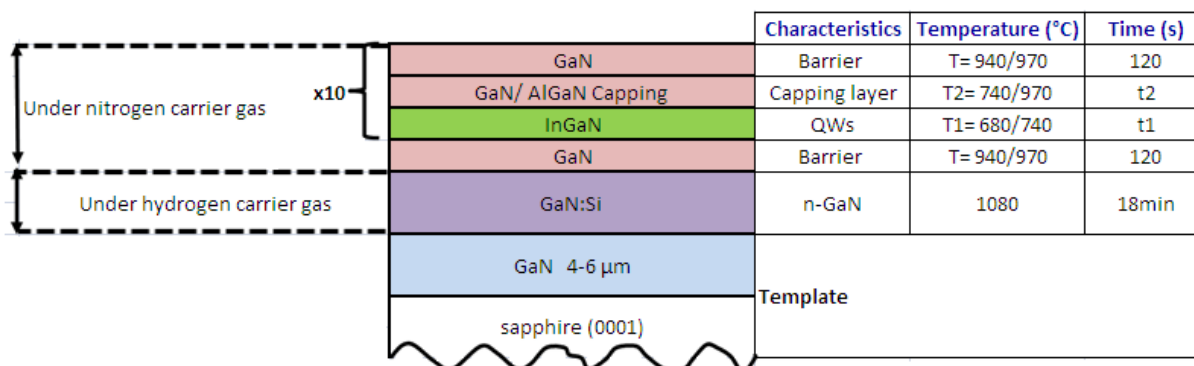


Figure 4-2: Schematic diagram of the multiple quantum well structures of the studied samples.

As mentioned in chapter 1, to grow the InGaN/(Al)GaN layers, trimethylindium (TMI), trimethylaluminium (TMA) and ammonia ( $\text{NH}_3$ ) are used as precursor for indium, aluminium and nitrogen, respectively. And both trimethylgallium (TMG) and triethylgallium (TEG) are used as precursor for gallium atoms in the growth processes. Note that we have used TEG for InGaN layers and TMG for GaN barrier and AlGaN capping layers growth in our samples. This was intentionally done as TEG has higher decomposition rate than TMG at low temperature and it allows us to have two different flow rates for two different layers in our reactor.

For all the samples in our study, we kept the group V/III gas flow ratio high. For example, while growing the GaN barrier, we used a flow rate of 1 or 5 sccm for TMG and 3.5 slm for  $\text{NH}_3$  gases. Similarly, while growing the InGaN QW layers, we used the flow rates of 100 sccm for TMI, 5 or

10 sccm for TEG and 3.5 slm for  $\text{NH}_3$  gases. In order to grow AlGaN as capping layer we used the flow rates of 4 sccm for TMA, 1 sccm for TMG and 3.5 slm for  $\text{NH}_3$  gases, respectively.

## **4.2 Study of InGaN/GaN structure without any capping layers (sample 1 and 2)**

As we mentioned in the introduction section, in this first sample series we targeted yellow emission from a sample with a large InGaN QW thickness and a low indium composition value (sample 1) and from another sample with a small InGaN QW thickness and a high indium composition values (sample 2), thus we have modified the QW growth temperature and time between the two samples. We intentionally kept the QW growth temperature and deposition time lower for one sample than that of the other one.

The growth process difference and its impact are analyzed in detail in the following subsections.

### **4.2.1 The growth processes of sample 1 and 2**

Both of the two samples were grown following the procedure described in section 4.1. But the basic differences between the two samples were that the growth time and temperature of the InGaN layers differ from each other. For sample 1, we have set the growth temperature for InGaN QW layer at  $740^\circ\text{C}$  with a total deposition time of 4 minutes to have low indium composition but high QW thickness whereas, for sample 2, the InGaN QW layers were grown at  $680^\circ\text{C}$  with a total deposition time of 2 minutes to have high indium composition but low QW thickness values. Figure 4-3 schematically illustrates the two growth processes of the two samples. Note that in both cases after the InGaN QW layer growth, no growth interruption was conducted as the precursor TEG and  $\text{NH}_3$  were kept 'ON' while the temperature of the reactor increased from lower temperature (either  $680^\circ\text{C}$  or  $740^\circ\text{C}$ ) to the higher temperature ( $940^\circ\text{C}$ ) within 2.5 minutes (corresponding thickness about 2 nm). No additional capping layer has been deposited before growing the GaN barrier layer. The flow rates of the different precursors were set to the values as mentioned in section 4.1 along with TMG and TEG of 1 and 10 sccm, respectively for this sample series.

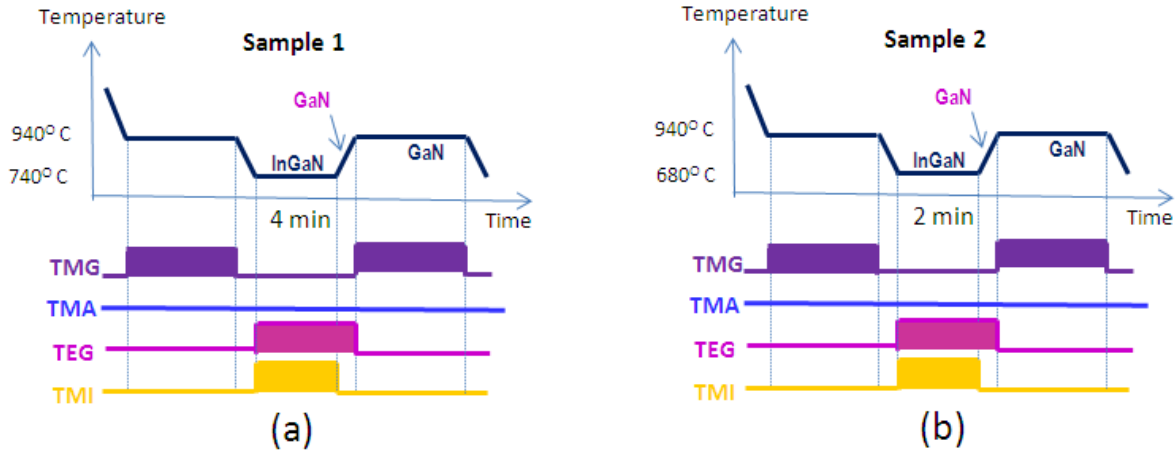


Figure 4-3: The growth process of (a) sample 1 and (b) sample 2. The color bar below the graph indicates the 'ON' and 'OFF' state of different gas flows. The 'ON' state corresponds to filled rectangles.

## 4.2.2 Structural and optical properties of the first sample series (sample 1 and 2)

### 4.2.2.1 AFM analysis

Following the process described in section 3.5, we have measured the RMS surface roughness and the threading dislocation density (TDD) per  $\text{cm}^2$  of the two samples. Sample 1 has surface roughness and TDD of 1.40 nm and  $2.0 \times 10^9 \text{ cm}^{-2}$ , respectively, whereas for sample 2, the values were determined to be 1.80 nm and  $7.8 \times 10^9 \text{ cm}^{-2}$ , respectively. Figure 4-4 shows the corresponding AFM images of both samples. For both surface roughness and the threading dislocation density (TDD) of sample 2 higher values than those of sample 1 were found. The TDD values of the two samples are significantly larger than that of the GaN template, which is about a few  $10^8 \text{ cm}^{-2}$ . We did not observe V-defects on the surface of the two samples but we found clustering of TDs in their surface as shown in Figure 4-4 (c).

Thus to determine the origin of such additional threading dislocations and to analyze the structural properties, we have conducted the TEM and XRD analysis of the two samples.

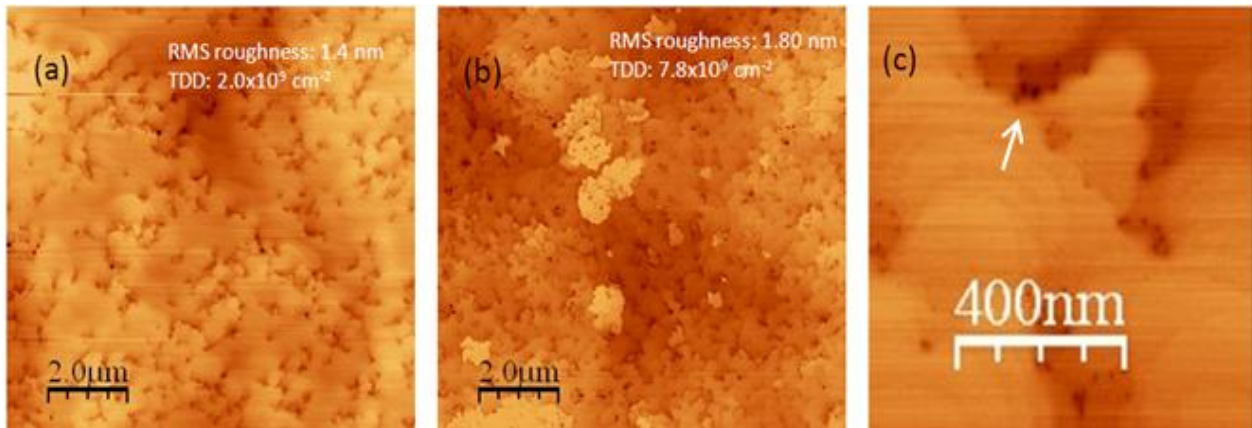


Figure 4-4: Surface morphology of the samples at the center of the wafer for (a) sample 1 and (b) sample 2. The calculated RMS surface roughness and the threading dislocation density (TDD) are also mentioned for both samples. (c) clustering of threading dislocations on the surface as shown by one white arrow.

#### 4.2.2.2 TEM and XRD analysis

We followed the procedure described in section 3.2 of chapter 3 to identify the impact of growth process differences on different structural properties such as different layer thicknesses and composition values of the InGaN QW layers of the two samples. We have found that for both samples the individual InGaN QW layer thickness increases from the 1<sup>st</sup> QW to 4-5<sup>th</sup> QW before having stable QW thicknesses. For example, Figure 4-5 (a) illustrates this fact for sample 1 in large field of view, which allows us to see almost all the QWs from QW 1 to QW 8 of the sample. Figure 4-5 (b) indicates the different QW thicknesses and clearly reveals this fact that the QW thicknesses increased from 1.46 nm to 3.50 nm for QW 2 to QW 4, respectively in sample 1.

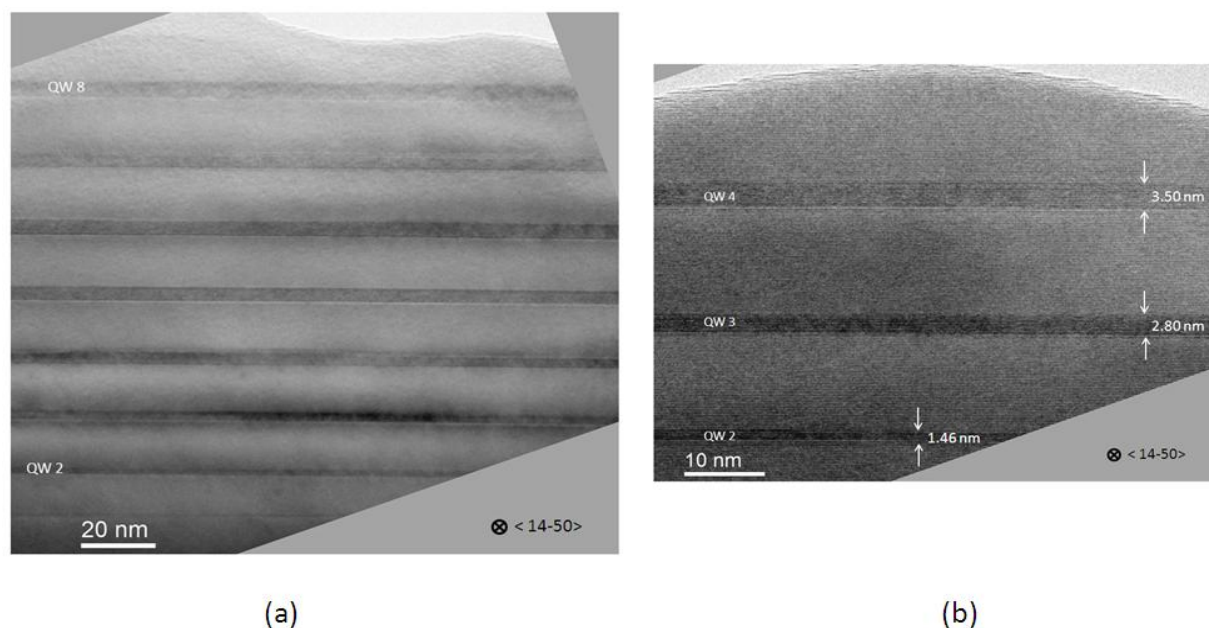


Figure 4-5: The cross-sectional transmission electron microscopy imaging along  $\langle 14-50 \rangle$  zone axis: (a) trend of average QW thickness increment from QW to QW can be observed from large field of view for sample 1 and (b) arbitrarily chosen small area of the sample 1 and the thickness of individual QWs has been indicated by white arrows.

Figure 4-6 summarizes the measured average QW layer thickness values for both samples. The data plots in black and red colors correspond to sample 1 and 2, respectively. This graph confirms that after the 4-5<sup>th</sup> QW the samples have stable QW thicknesses. But we did not observe any indium composition increment from lower to higher QW for both samples. The differences in the indium composition were only about 1% between QWs, which were in the error bar limit. We are going to discuss more about these issues later in the discussion section.

Table 4-1 summarizes the analyzed data for this sample series. Due to growth temperature and deposition time differences between the two samples, It is quite expected to have higher overall average QW thickness (4.3 nm) and lower average indium composition values (about 17%) for sample 1 than that of sample 2 (about 2.8 nm QW thickness and 25% of indium composition for sample 2). However, the average GaN barrier layer thicknesses for both samples are about 14 nm as expected.

While observing the individual QWs of each sample, we found frequent occurrence of QW thickness variation within each QW for both samples (similar to sample A as shown in Figure 4-13). The full width at half maximum (FWHM) values from the Gaussian fit of the QW thickness distribution plots (the evaluation process is described in section 3.2.1) confirms the observed phenomenon as its value is relatively high ( $\geq 1.0$  nm) for both samples. Note that the tabulated FWHM values (Table 4-1) of this sample series were calculated from higher QWs (From QW no. 4 to the last one) thickness distribution data as they have stable average thickness. Moreover,

sample 1 has a higher FWHM value (1.7 nm) than that of sample 2 (1.0 nm) which indicates that the step size of the QW thickness variation is relatively larger for sample 1.

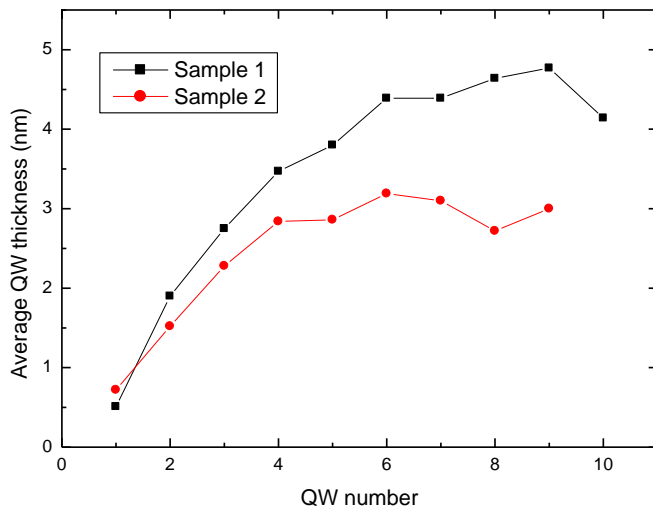


Figure 4-6: Graph displaying the average thickness value of each QW for sample 1 and 2.

Table 4-1: Summary data of the two samples

Sample	Mean Indium composition within QWs % In	Mean barrier thickness $L_{\text{BARRIER}}$ (nm)	Mean QW thickness value $L_{\text{QW}}$ (nm)	FWHM value of Gaussian fit of QW thickness distribution	InGaN growth temp. T ( $^{\circ}\text{C}$ )	InGaN growth time t (mins.)	Observed total lateral length L (nm)
Sample 1	17 $\pm$ 1	14 $\pm$ 1	4.30	1.7	740	4	3604
Sample 2	25 $\pm$ 1	14 $\pm$ 1	2.80	1.0	680	2	2152

#### 4.2.2.2.1 Dislocation analysis of samples 1 and 2

To observe the dislocations and analyze their types, we have conducted the experiment as described in section 3.2.3 of chapter 3, at different places of the two samples. The pre-existent threading dislocations were observed in both samples with either of  $\langle a \rangle$  or  $\langle a+c \rangle$  type and majority were of  $\langle a \rangle$  type. We have observed only very few  $\langle c \rangle$  type pre-existing threading dislocations in our samples. Figure 4-7 shows two images taken at the same place of sample 1 where Figure 4-7 (a) and (b) are taken with  $g=0002$  and  $g=11-20$  diffraction beam spot in weak beam dark field (WBDF) imaging condition. First of all, it is clear from these images that additional dislocations are formed from pre-existing ones in the GaN layer. Considering the

invisibility criteria ( $\mathbf{g} \cdot \mathbf{R} \neq 0$ ) of dislocation contrast summarized in table 3-1 of chapter 3, it is obvious from the images that the additional dislocations were generated within the QWs (sample 1) and they were all of  $\langle a \rangle$  type, as we can see bright contrast only in the image taken with  $g=11-20$  diffraction beam spot. However, from the figure, we can also observe that some  $\langle a \rangle$  type threading dislocations also bent into the interface of two layers creating a small segment of misfit dislocation (MD).

We are going to discuss the assumed generation process of these additional  $\langle a \rangle$  type dislocation and their impact on the strain state of the samples in detail later in discussion section.

Please note that such additional  $\langle a \rangle$  type threading dislocations were observed in different places of both samples and we found comparatively higher density in sample 2 than that of sample 1.

Note that the elastic stress energy is higher in sample 2. We know that the elastic stress energy per unit area ( $E_{elastic}$ ) within one QW epilayer can be expressed as for bi-axial stress state condition as<sup>1</sup>:

$$E_{elastic} = \left( C_{11} + C_{12} - 2 \frac{C_{13}^2}{C_{33}} \right) \times \left( \frac{a - a_0}{a_0} \right)^2 \times QW \text{ thickness} \quad (4.1)$$

where,  $C_{ij}$  are the elastic coefficients and  $a$  and  $a_0$  are strained and relaxed in plane lattice parameters of the epilayer. These parameters ( $C_{ij}$  and  $a$ ) depend on the composition values of the epilayer. Using Vegard's law (equation 1.1) and tabulated values in chapter 1 (table 1.2 and 1.5), we can easily calculate these parameters for any composition value. Then we can use the parameters to calculate the elastic stress energy of our samples from equation 4.1. The built-in elastic stress energy per unit area within one QW of our samples is found to be about  $0.6 \text{ J/m}^2$  and  $0.8 \text{ J/m}^2$  for sample 1 and 2, respectively.

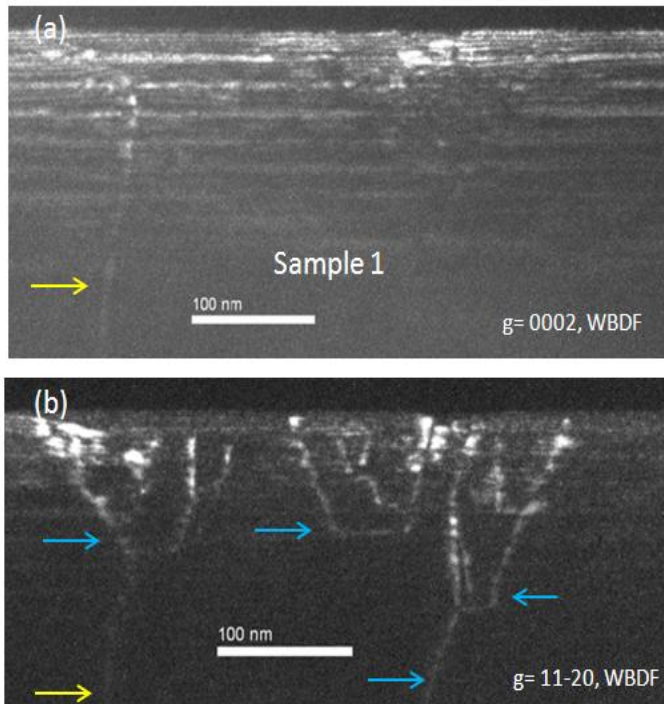


Figure 4-7: Dislocation analysis of sample 1: Weak beam dark field image (WBDF) images (a) with  $g=0002$  and (b) with  $g=11-20$  diffraction spots, which confirms that the additional dislocations generated within the grown structure are of  $\langle a \rangle$  type as indicated by blue arrows and the pre-existent threading dislocations are either  $\langle a \rangle$  or  $\langle a+c \rangle$  type as indicated by blue and yellow arrows at the bottom of image (b).

#### 4.2.2.2 Room temperature photoluminescence (RT-PL) analysis

The room temperature photoluminescence (RT-PL) of the two samples shows that both samples have the maximum intensity almost at same wavelength of emission around 570 nm ( $\lambda=570$  nm and  $\lambda=568$  nm for sample 1 and sample 2, respectively). As we have found that sample 1 has a higher average QW thickness (4.30 nm) but lower indium composition value ( $17\pm 1$  %) than sample 2 (average thickness 2.8 nm and Indium composition  $25\pm 1$  %), thus they both emit light of around 570 nm wavelength.

Under RT-PL experiment, it is most likely that we should have much higher intensity from sample 1 as it has lower TDD than that of sample 2 ( $2.0 \times 10^9$  and  $7.8 \times 10^9$  per  $\text{cm}^{-2}$  for sample 1 and sample 2 respectively). But we observed slightly higher intensity from sample 1 as shown in Figure 4-8 and assume that it is due to the fact that sample 1 has relatively higher QW thickness (4.3 nm) than sample 2 (2.8 nm), which makes the oscillator strength smaller for sample 1 due to QCSE. These two opposite effects ultimately allow us to have almost same intense emission from the two samples.

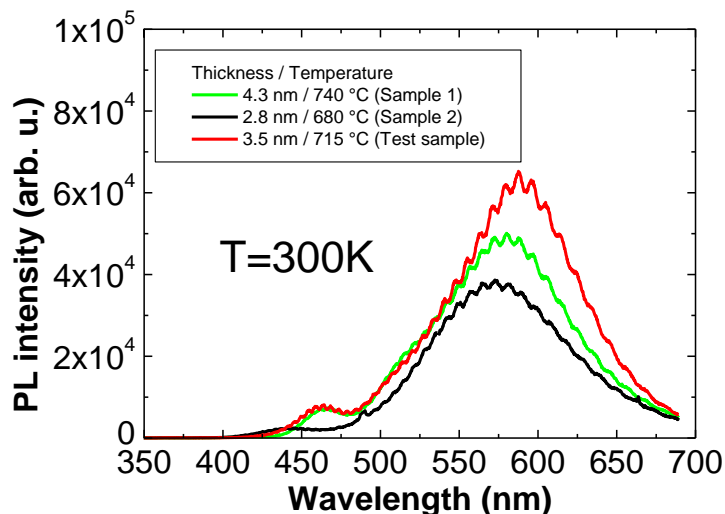


Figure 4-8: Room temperature photoluminescence of sample 1 and 2.

Thus we can adjust indium composition and QW thickness value to compensate the QCSE effect and improve the material quality of a sample to have better PL performance. For example, we have grown a test sample, where the QWs were grown at 715°C with growth duration of 3 minutes and found that it is promising as it allows us to have higher intensity emission than that of our studied samples as shown in Figure 4-8. The obtained maximum intensity of the test sample was around 580 nm of wavelength. From AFM analysis, we have found the total TDD of the test sample to be  $7.3 \times 10^9$  per  $\text{cm}^2$  and we assumed the average indium composition and QW thickness of the sample to be about 21% and 3.5 nm, respectively from XRD simulation.

In fact, these results seem to indicate that the optimal structure may result from a balance between the QW thickness and the indium composition. For thick QWs, the QCSE reduces the intensity. For high indium compositions, structural defects are created. It has also to be noted that the QCSE is an intrinsic property whereas the creation of structural defects depends on the growth conditions. There is maybe room for improvement of the structural quality at high indium composition.

### 4.3 Study of InGaN/GaN structure with AlGaIn capping layer (sample A to D)

In this part, we study the impact of a few monolayers of AlGaIn layer as a capping layer on top of InGaN QW layers. We have grown three samples (B to D) with AlGaIn capping layers after the InGaIn active QW layers growth. The AlGaIn growth temperature was varied and growth interruptions have been performed or not while increasing the reactor temperature to grow later layers. Another sample is grown following the standard growth process as a reference one

(sample A), i.e., without any AlGaN capping layer deposition after the low temperature InGaN QW growth and without any growth interruption while increasing the growth temperature of the reactor to grow the GaN barrier layer. The growth process differences of the sample series are discussed in detail in the following sub-section.

### 4.3.1 Growth process of samples A to D

The structure of this sample series (samples A to D) and the precursors used for the growth of the different layers were the same as mentioned in section 4.1 (TMG and TEG were 1 and 5 sccm, respectively for this sample series). The change in growth processes of the AlGaN capping layers between the samples are schematized in Figure 4-9.

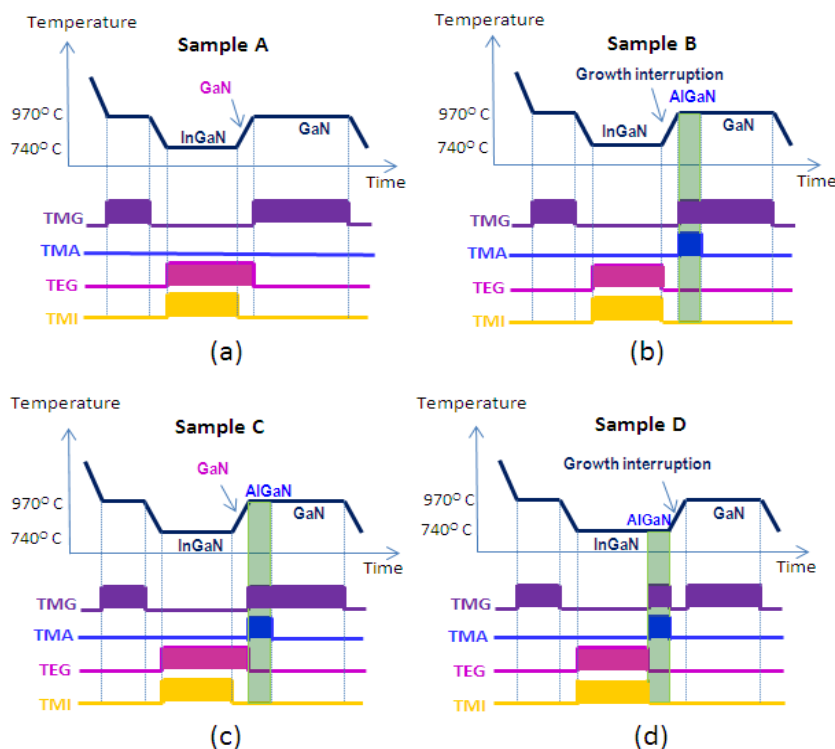


Figure 4-9: (a)-(d) Schematic diagram of the growth processes of samples A to D. The color bar below each graph indicates the 'ON' and 'OFF' state of different gas flow. The 'ON' state corresponds to filled rectangles.

For sample A (reference sample), after each InGaN QW layer growth, there was no growth interruption (TEG and  $\text{NH}_3$  flows were 'ON') while the reactor temperature was raised from 740°C to 970°C for the GaN barrier layer growth (Figure 4-9 (a)). But for sample B, the growth was interrupted after the InGaN QW layer growth and the reactor temperature was raised to 970°C for high temperature deposition of a few monolayers of AlGaN layers before the GaN

barrier layer deposition at the same temperature (Figure 4-9(b)). Sample C was grown exactly the same way as sample B except that there was no growth interruption (TEG and  $\text{NH}_3$  flows were 'ON') after the InGaN QW layers growth (Figure 4-9(c)). Finally, for sample D, AlGaIn layers were deposited after InGaN QW layers at low temperature ( $740^\circ\text{C}$ ) and a growth interruption was made while increasing the temperature to  $970^\circ\text{C}$  for the GaN barrier layer growth.

The depositions of InGaN QW layers were conducted for 4 minutes at  $740^\circ\text{C}$ , the GaN barrier layers were deposited for 2 minutes at  $970^\circ\text{C}$  whereas for AlGaIn layer deposition, the process was run only for 6 seconds at different temperature (either  $740^\circ\text{C}$  or  $970^\circ\text{C}$ ) as illustrated in Figure 4-9. Moreover, the temperature was ramped from  $740^\circ\text{C}$  to  $970^\circ\text{C}$  in 2 and half minutes in each case and the GaN thickness during the ramp time was estimated to be less than 2 nm.

### 4.3.2 Structural and optical properties of the second sample series (samples A to D)

We are going to present the obtained results about structural and optical properties of this sample series in the following sub-sections.

#### 4.3.2.1 AFM analysis

We have measured the average threading dislocation density (TDD) and surface roughness of this sample series following the procedure described in section 3.5. Figure 4-10 shows two images where the measured TDD are about  $1.2 \times 10^9 \text{ cm}^{-2}$  and  $0.9 \times 10^9 \text{ cm}^{-2}$  and the surface roughness (in rms) are about 0.30 nm and about 0.56 nm, for sample C and D, respectively. It has to be noted that the other two samples (sample A and B) have surface morphology similar to that of sample C and we have found some V-defects only in sample D.

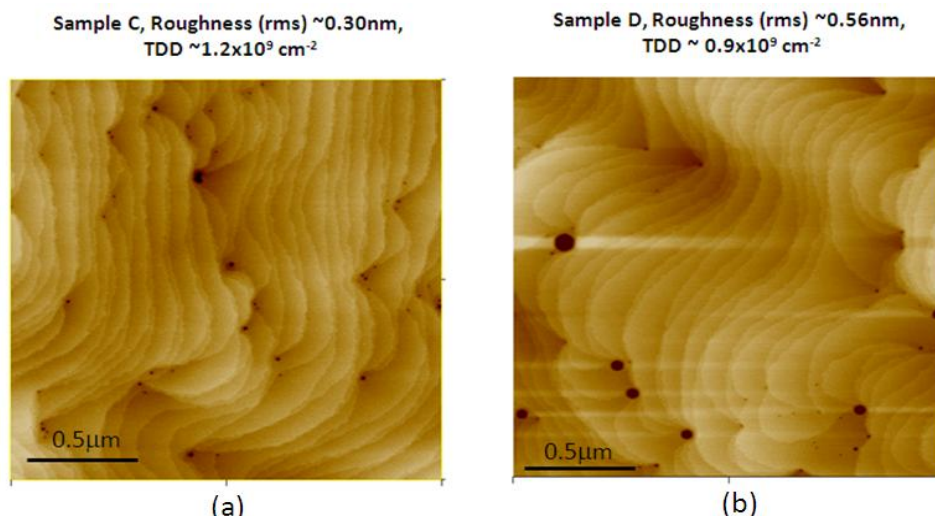


Figure 4-10: Atomic force microscopy image of a  $2 \times 2 \mu\text{m}^2$  scan area for (a) sample C and (b) sample D. The measured threading dislocation density (TDD) and the surface roughness values of the images are mentioned on top.

Table 4-2: Summary of the threading dislocation density (per  $\text{cm}^2$ ) and root mean square (RMS) values of the surface roughness of the sample series.

Sample	Threading dislocation density per $\text{cm}^2$	RMS surface roughness (nm)
Sample A	$7.9 \times 10^8$ ( $\pm 3.0 \times 10^8$ )	0.33 ( $\pm 0.07$ )
Sample B	$6.1 \times 10^8$ ( $\pm 1.3 \times 10^8$ )	0.29 ( $\pm 0.06$ )
Sample C	$1.0 \times 10^9$ ( $\pm 2.5 \times 10^8$ )	0.33 ( $\pm 0.08$ )
Sample D	$6.6 \times 10^8$ ( $\pm 1.7 \times 10^8$ )	0.66 ( $\pm 0.10$ )

Table 3-3 summarizes the measured values of both TDD and RMS surface roughness of each sample of the series. From the table, we find that the average TDD per  $\text{cm}^2$  of the samples is only slightly different from each other except for sample C ( $1.0 \times 10^9$  per  $\text{cm}^2$ ). Similarly, the surface RMS roughness values of the samples are the same except for sample D (0.66 nm). This higher value of surface roughness ( $0.66 \pm 0.10$  nm) for sample D may be due to the presence of big pits (typical diameter of about 100 nm) as observed in the AFM image (Figure 4-10 (b)). We are going to discuss the origin of higher TDD for sample C and the shape and position of V defects in sample D in the discussion section.

#### 4.3.2.2 TEM and XRD analysis of the sample series

Following the procedure described in section 3.2 of chapter 3, we have observed a large area of each sample to obtain statistical data concerning individual layer thickness (QW and barrier layer) and indium composition of InGaN QWs of the series, as explained by Figure 3-14.

For this sample series we have observed atomically flat interfaces with no crystal defects such as voids, stacking faults, misfit dislocations, additional threading dislocations, In-rich clusters or V-defects as reported elsewhere<sup>2,3,4</sup>, except few V-defects within sample D. For example, Figure 4-11 shows an image taken along  $\langle 14-50 \rangle$  zone axis with low magnification of sample D, which allows us to observe almost the whole structure from QW 1 to QW 9.

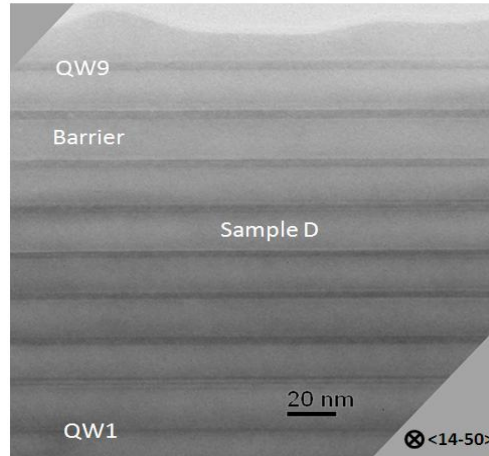


Figure 4-11:  $\langle 14-50 \rangle$  zone axis image of sample D, demonstrating that no voids, V-defects nor strong indium clustering can be detected within the quantum wells. A homogeneous contrast of quantum well and atomically flat interfaces between the barrier layers and the quantum well layers are observed.

The summary of layer average thicknesses and overall indium composition values of the sample series is listed in Table 4-3. We have found that individual QW thickness values of all samples are almost equal to their measured overall mean QW thicknesses as listed in the summary table, except for sample A.

Table 4-3: Summary data of the sample series

Sample	Mean Indium composition within QWs % In	Mean barrier thickness $L_{\text{BARRIER}}$ (nm)	Mean QW thickness value $L_{\text{QW}}$ (nm)	FWHM value of Gaussian fit of QW thickness distribution (nm)	Observed total lateral length L (nm)
Sample A	$18 \pm 1$	$17 \pm 1$	2.75	1.54	4201
Sample B	$18 \pm 1$	$17 \pm 1$	2.45	0.75	8986
Sample C	$14 \pm 1$	$17 \pm 1$	3.00	0.94	4195
Sample D	$18 \pm 1$	$17 \pm 1$	3.50	0.88	2230

For example, Figure 4-12 shows the average thickness variation of each QW for sample A and B. This figure demonstrates that the thicknesses of sample A have an increasing trend from the first QW (0.4 nm) to the last QW (3.3 nm), whereas such a trend does not exist for sample B. Except the first QW of sample A, we can note that the increases in QW thickness values are not as large as we found for sample 1 and 2 of the first sample series.

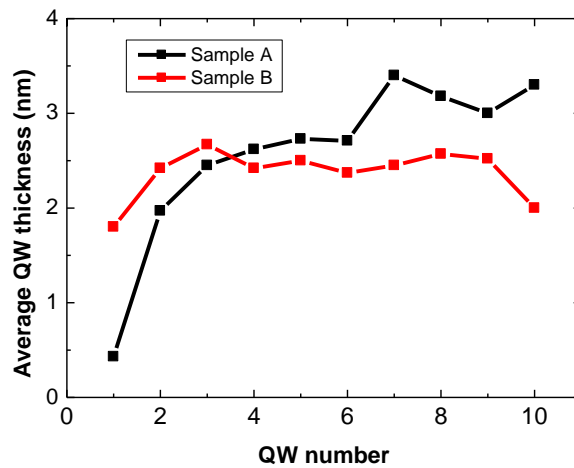


Figure 4-12: Average thickness value for each InGaN quantum well of sample A and sample B.

Moreover, while calculating the individual QW thickness for each sample, we found that for sample A, QW thickness variations occur more frequently than in the other samples (sample B to D). For example, Figure 4-13 (a) and (b) illustrate cs-HRTEM images of sample A, which are taken along  $\langle 14\text{-}50 \rangle$  zone axis and at a distance of about  $0.5 \mu\text{m}$  apart from each other. These two images demonstrate QW thickness variation for sample A, as QW number 5 has 2.0 and 2.9 nm of thicknesses, whereas the QW number 4 has 2.6, 1.4 and 2.8 nm of thickness with a clear step in Figure 4-13 (b), whereas Figure 4-14 illustrates with a large field of view for sample B, that it has more homogeneous QW thicknesses. In Figure 4-14, InGaN QW number 7 has thickness of 2.5 nm and the AlGaIn capping layer has thickness of 1.5 nm, as shown.

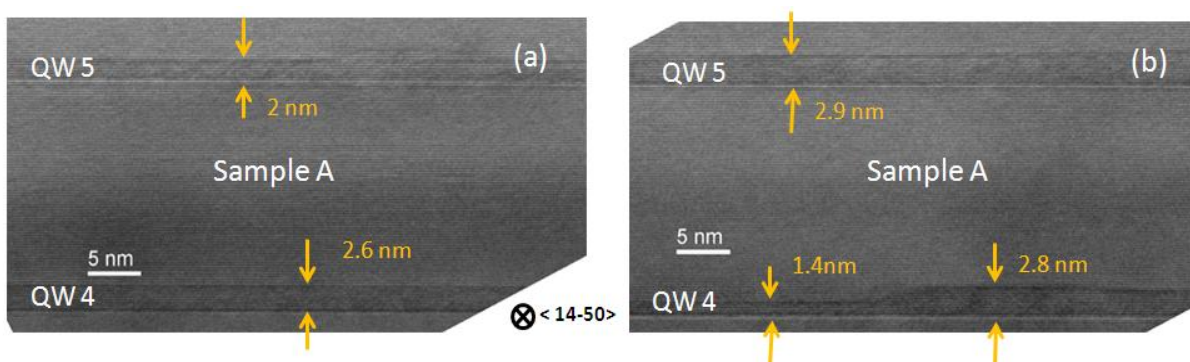


Figure 4-13: Cross-sectional high resolution transmission electron microscopy images of sample A, both images taken along  $\langle 14\text{-}50 \rangle$  zone axis and about  $0.5 \mu\text{m}$  apart. Comparing (a) and (b), quantum well number 5 has two different thickness values of 2.0 and 2.9 nm, whereas quantum well number 4 has thickness values of 2.6, 1.4 and 2.8 nm with a clear step in (b).

We can also confirm the more frequent QW thickness variation phenomena of sample A by comparing the thickness distribution plot for each QW of sample A to that of other samples (sample B to D) of the series, For example, Figure 4-15 shows the thickness distribution plot of QW number 9 for both samples A and B, where sample A has broadest distribution of the ratio as a function of QW thickness. Thus we can conclude that sample A has higher thickness variation occurrence than that of sample B. Please note that the parameters used in these plots are already explained in section 3.2.1 of chapter 3.

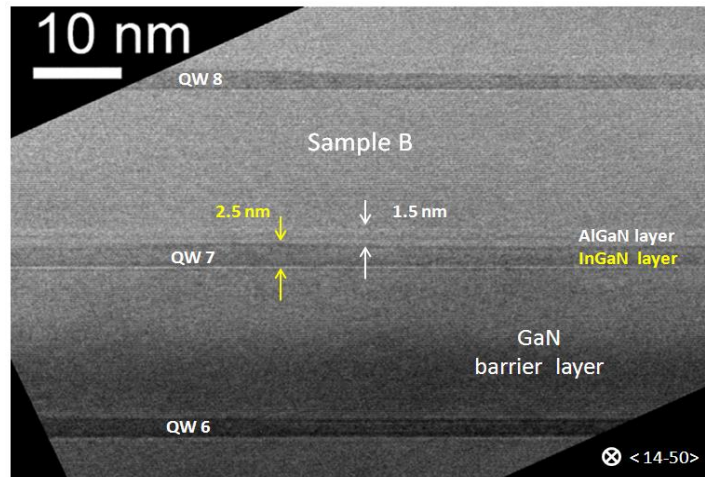


Figure 4-14: Cross-sectional high resolution transmission electron microscopy image of sample B, showing the homogeneity of quantum well thickness due to AlGaIn capping layer deposition. The thicknesses of the InGaIn layer and the AlGaIn layer for quantum well 7 are 2.5 and 1.5 nm, respectively.

From summary Table 4-3 of this sample series we can also note the FWHM value of sample A (1.54) is significantly larger than for any other samples of the series (0.74, 0.94 and 0.88 nm for sample B, C and D, respectively). Note that for calculating FWHM values of this sample series, we did not consider the QW thickness data of first QW of sample A, as its average value is significantly lower than any other QWs. Considering the growth processes of sample B to D and the above observed results, we can conclude that a few monolayers of AlGaIn capping layer after each InGaIn QW surely reduce the occurrence of thickness variations and help to have more homogeneous QWs in terms of thickness.

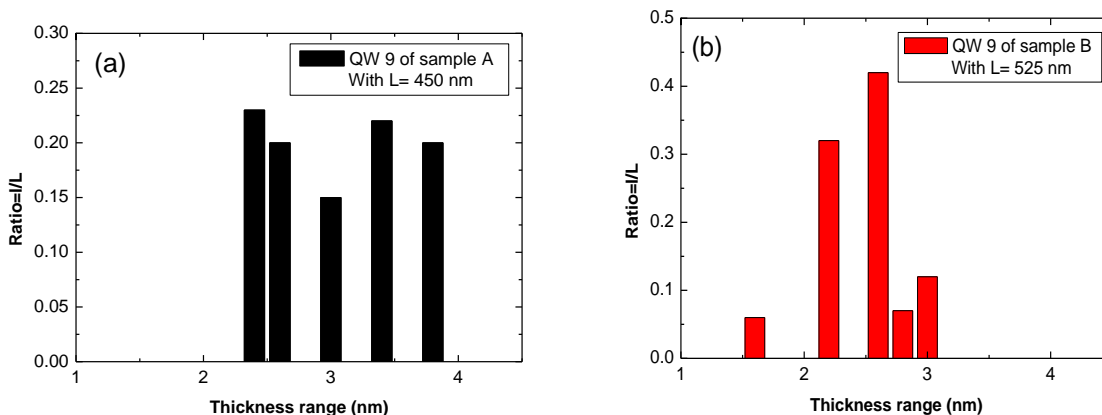


Figure 4-15 (a) Thickness distribution plot of individual quantum well number 9 for (a) sample A and (b) sample B with total observed lateral length  $L$  for the plots are 450 nm and 525 nm, respectively.

From the mean QW thickness ( $L_{QW}$ ) values summarized in Table 4-3, it is certain that the growth process has a strong impact on the QW thickness. The mean QW thickness of sample A ( $L_{QW}=2.75$  nm) is higher than sample B ( $L_{QW}=2.45$  nm). This difference in mean QW thickness value can be explained by comparing the growth process of sample A and B (Figure 4-9). Due to the growth interruption in sample B and the raise of the samples' growth temperature, InGaN is evaporated more easily than in sample A (as there is no growth interruption for sample A) or indium incorporation at the beginning of the ramp under non-growth interruption case (TEG was 'ON' at ramp time for sample A) helps sample A to achieve a little higher QW thickness. Here it is assumed that the process with no growth interruption (sample A) helps to avoid the evaporation of InGaN.

Diffusion of indium from QWs and/or indium surface segregation can also play a role in our overall mean QW thickness measurement. Comparing the growth process difference between sample A and sample D along with their measured mean QW thickness ( $L_{QW}= 2.75$  nm and  $L_{QW}= 3.5$  nm for sample A and sample D respectively), sample D demonstrates that AlGaIn layer helps to limit the indium diffusion during the high temperature GaN barrier growth. The measured mean QW thicknesses of sample A and sample C ( $L_{QW}= 2.75$  nm and  $L_{QW}= 3.0$  nm for sample A and sample C respectively) are in the range of measurement error limit ( $1ML=0.259$  nm for GaN).

For samples A and B, during the temperature ramp we have some evaporation and/or diffusion of InGaN layers from the top part of QWs. So an indium composition gradient may exist at the upper part of each QW. Now as discussed in section 3.2.2 on the limitations of the GPA technique<sup>5</sup> it is obvious that the GPA technique will not be able to correctly analyze the strain in areas where the image contrast changes (interfaces), so for indium composition determination,

following the procedure explained in the section 3.2.2.2 of chapter 3 (GPA method), we have intentionally considered the average lattice deformation value from the middle of each QW and average out the strain value to correlate it to the Indium composition value of the QW. Due to the limitations of GPA, we are not able to determine the indium concentration gradient at the top part of QWs. For example, Figure 4-16 illustrates the obtained lattice deformation map of sample A and the corresponding laterally averaged lattice deformation profile from a particular region marked by white dashed rectangle of the deformation map and we have considered the deformation value ( $e_{zz}$ ) of 0.027 and correlate it to the indium composition value of 17 percent, considering the bi-axial stress state condition (Figure 1-11).

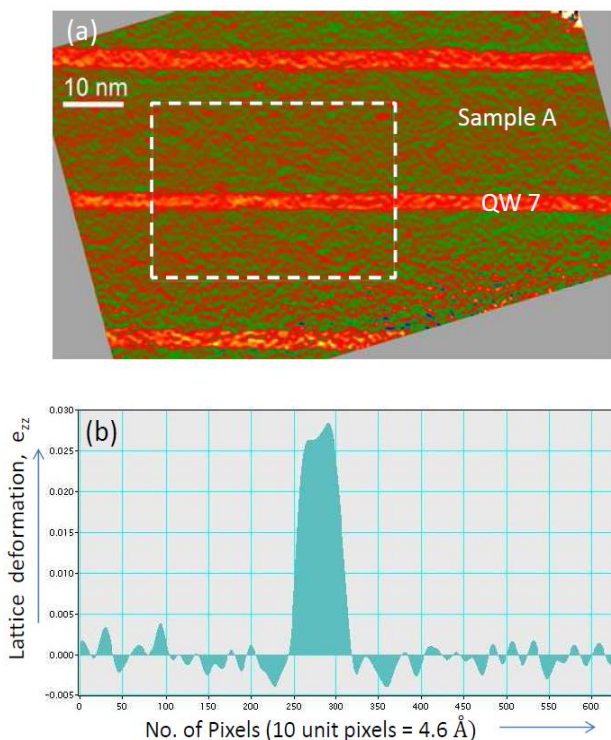


Figure 4-16: (a) (0002) plane lattice deformation map of sample A. (b) Profile of laterally averaged lattice deformation done in the area indicated by the white dashed rectangle in (a).

Therefore, the tabulated indium composition value (Table 4-3) corresponds to the average indium composition at the middle of each QW. We find that for sample A, B and sample D, the average indium composition is about  $18\pm 1\%$  but for sample C, it is only about  $14\pm 1\%$  (Table 4-3). As we have analyzed the TEM sample from about  $5\pm 1$  mm away from the center of the wafer for sample C, whereas the same analysis were conducted within  $2\pm 1$  mm of the center of the wafer for all other samples, we assume that this position variation is the origin of these differences in mean indium composition values. The temperature inside the homemade MOCVD reactor chamber is not uniform as it has slightly higher temperature on the edge than at the center of the reactor substrate, thus this temperature difference made the change in

obtained composition value for sample C than that of other samples. We also assume that the indium composition at the middle of each QW is not affected through evaporation or diffusion processes and that is why we have the same indium composition of  $18\pm 1\%$  for samples A, B and D.

Thus the average indium composition values confirm that the different growth processes have impact on thickness but not in indium composition values at the center of the QWs.

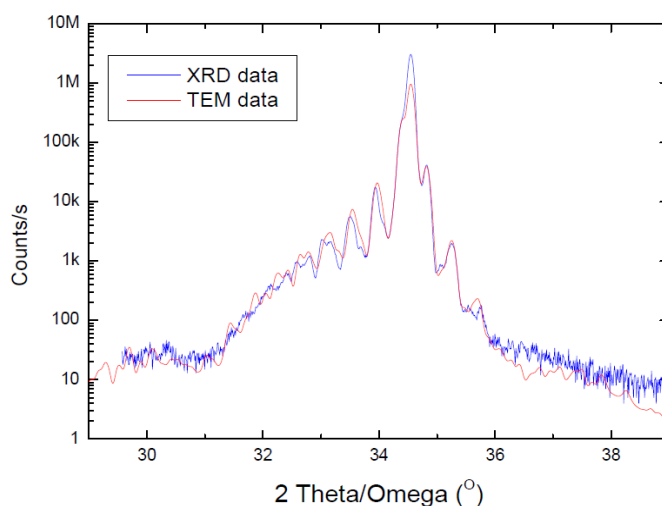


Figure 4-17: Fit of the  $\omega$ - $2\theta$  x-ray diffraction scan data for sample D, using thickness and composition data deduced from the quantitative transmission electron microscopy analysis.

The AlGaIn capping layer thickness was relatively small compared to that of the QW and barrier layers of the samples (sample B to D). Due to the limitation of the GPA technique<sup>5</sup>, we were not able to determine precisely the Al composition of this AlGaIn capping layer. Thus to estimate the Al composition value and to verify that our prediction about overall average indium composition values considering the bi-axial stress state within the *cs*-TEM samples are right, we have simulated the 0002  $\omega$ - $2\theta$  XRD data using the tabulated TEM data. Figure 4-17 illustrates one such simulation fit of XRD data to that of tabulated TEM data (Table 4-3) for sample D. In this simulation we have considered the Al composition to be of 5%. Thus according to all the simulation of the XRD  $\omega$ - $2\theta$  scan, we deduce an aluminum composition of 3 to 5% for sample B to D and the tabulated data for all the samples are quite relevant.

#### 4.3.2.2.1 Dislocation analysis of samples A to D

To analyze the dislocations of the sample series, we have conducted the experiment following the process described in section 3.2.3 of chapter 3. Following the visibility criteria of dislocation contrast, we have found that most of the pre-existing threading dislocations are either  $\langle a \rangle$  or  $\langle a+c \rangle$  types and we have rarely observed any  $\langle c \rangle$  type pre-existing threading dislocations within the samples.

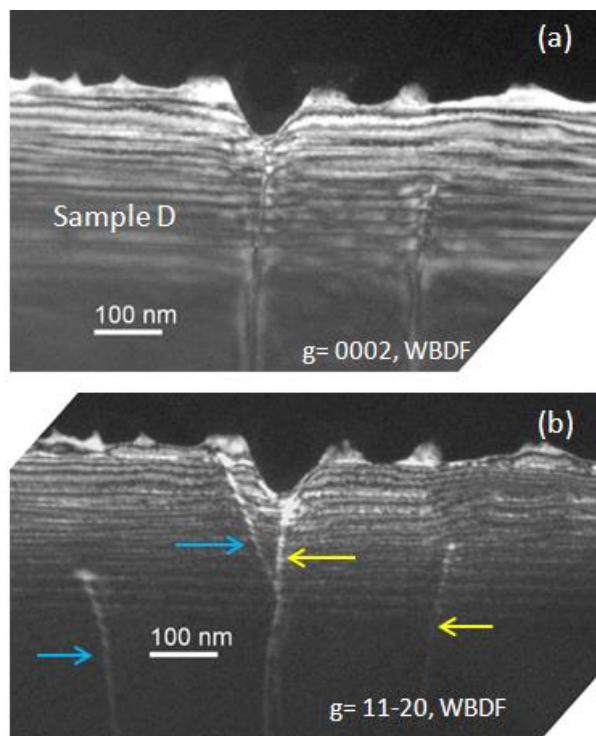


Figure 4-18: Dislocation analysis of sample D: Weak beam dark field (WBDF) images with (a)  $g=0002$  and (b)  $g=11-20$  diffraction spots. Following the visibility criteria of dislocation contrast, the blue and yellow arrows indicate the  $\langle a \rangle$  and  $\langle a+c \rangle$  type of dislocations, respectively.

We did not observe any additional threading dislocation generated from the samples of this series. However, only in sample D, we have observed a few V-defects generated in the top part of the structure. Figure 4-18 illustrates one such V-defect. Using equation 4.1, we have measured the elastic stress energy per unit area per QW ( $E_{\text{elastic}}$ ) of all the samples of the series. For each sample, we have considered the parameters of equation 4.1 with an InGaN composition value of 18%. The obtained elastic stress energy per unit area per QW ( $E_{\text{elastic}}$ ) for samples A to D depends on its average QW thickness and we have about 0.43, 0.38, 0.48 and 0.55  $\text{J}/\text{m}^2$ , respectively. Thus from obtained values we may assume that due to the highest elastic stress energy value of sample D (0.55  $\text{J}/\text{m}^2$ ), it has V-defects in its structure.

Now to confirm that the higher TDD of sample C ( $1.0 \times 10^9 \pm 2.5 \times 10^8 \text{cm}^{-2}$  as mentioned in Table 3-3) is from pre-existing TD of the GaN template, we have observed the sample under WBDF image conditions at low magnification using STEM. It allows us to see the threading dislocations contrast more clearly in the image as we know that sample thickness variation, bend contour and auxiliary contrast effects have less impact on STEM images than that of TEM images.<sup>6</sup>

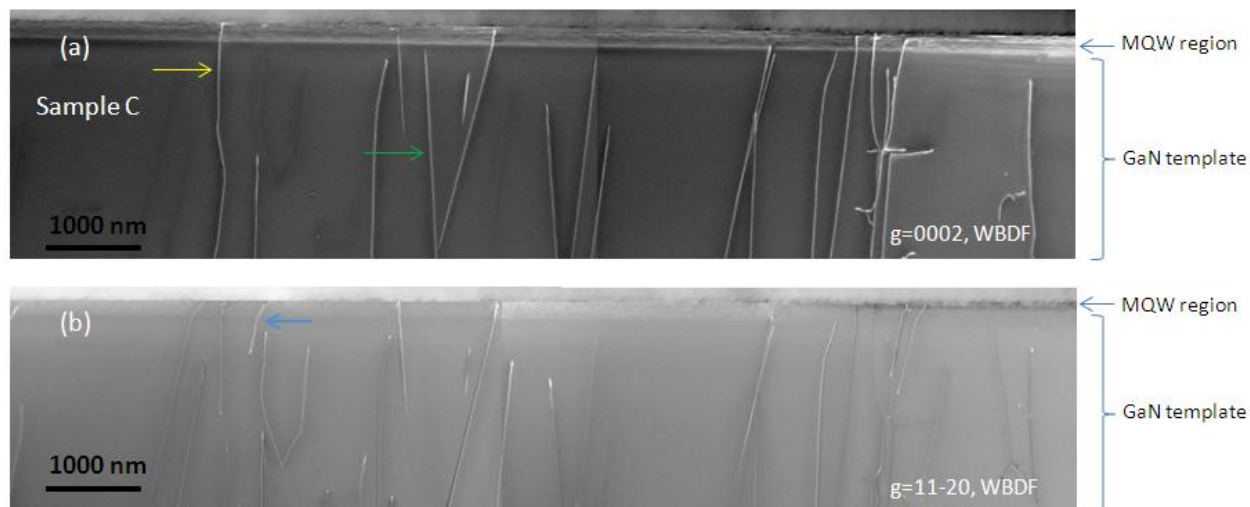


Figure 4-19: Dislocation analysis in a large field of view for sample C. Depending on visibility criteria of dislocation contrast blue, yellow and green arrows indicate the  $\langle a \rangle$ ,  $\langle a+c \rangle$  and  $\langle c \rangle$  type dislocations, respectively in weak beam dark field images with (a)  $g=0002$  and (b)  $g=11-20$  diffraction beam spots.

Figure 4-19 illustrates the dislocations in sample C. Each image of Figure 4-19 has been constructed from 3 consecutive images taken side by side at low magnification and under weak beam dark field (WBDF) image condition with either  $g=11-20$  or  $g=0002$  diffraction beam spots. These two images allow us to see the dislocations of the sample in a large field of view. They confirm that no additional threading dislocation has been created from the MQW region of the sample structure and the observed higher TDD per  $\text{cm}^2$  for sample C is only due to its pre-existing threading dislocations of different types within the template.

#### 4.3.2.3 Room temperature photoluminescence (RT-PL) analysis

The integrated RT-PL data of the sample series are shown in Figure 4-20. The RT-PL data of the samples are from exactly the same position from where the TEM analysis was conducted. For samples A, B and D, the indium composition is of  $18 \pm 1\%$  and the corresponding RT-PL wavelengths are 531, 499 and 540 nm. We recall that the emission wavelength increases when the QW thickness increases, so it is an expected behavior. We can also notice that samples A and B have similar mean QW thickness (2.75 nm and 2.45 nm, respectively) but very different wavelength emissions. We attribute the longer wavelength emission of the sample A to the fact that the QW interfaces of this sample are rougher and therefore electrical carriers have a larger probability to localize in deeper potential minima due to these potential fluctuations. But for sample C, though it has higher mean QW thickness (3.0 nm), it emits at shorter wavelength (513 nm) than sample A, due to the lower indium composition (about  $14 \pm 1\%$ ).

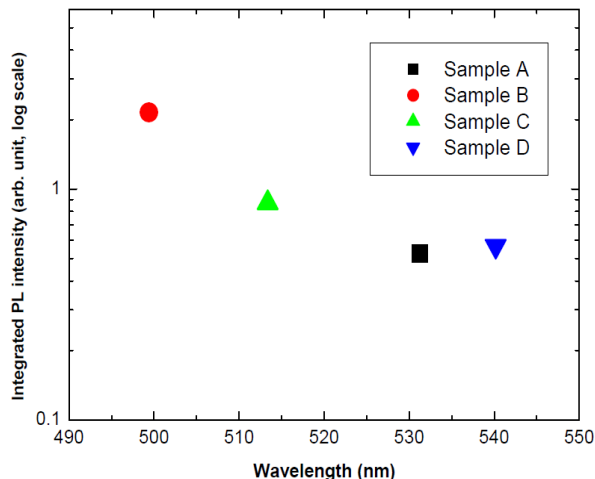


Figure 4-20: Integrated room temperature photoluminescence for samples A to D.

However, the integrated PL intensity of the samples with an AlGaIn capping layer is larger than that of the reference sample A. As sample B has thinner QWs (2.45 nm) and sample C has smaller indium composition ( $14\pm 1\%$ ) to that of sample A (2.75 nm and  $18\pm 1\%$ ), their larger intensity is expected owing to smaller impact of the quantum confined Stark effect (QCSE)<sup>7</sup> as explained in section 1.4.1 of chapter 1. But for sample D, the mean QW thickness is larger than that of sample A, while there is a slight improvement of the PL intensity. This means that by using the growth conditions of sample D for the AlGaIn capping layer, we can extend the QW emission at longer wavelength without degradation of the RT-PL efficiency compared to the reference.

The strain states of this sample series are going to be presented in section 4.5.

#### 4.4 Comparative study of low temperature capping processes: GaN Vs AlGaIn

As mentioned in the introduction section, in order to determine the impact of large capping layer thickness at low temperature ( $740^\circ\text{C}$ ), we have analyzed 3 samples (sample X to Z) with 10 MQW structure where two of them (sample X and Y) have GaN and the other one (sample Z) has AlGaIn as capping layers after each InGaIn QW. The precursors and the growth time of the capping layers have been modified between the samples. The growth process details of the samples are presented in the next section. Both the structural and optical properties have been studied for comparative analysis of this sample series.

##### 4.4.1 The growth processes of samples X to Z

The structure of this sample series (samples X to Z) and the precursors used for the growth of the different layers were exactly the same as mentioned in section 4.1 (TMG and TEG were 1 and 10 sccm for GaN and InGaIn layers, respectively for this sample series). All the GaN barriers

and the InGaN QW regions of this sample series (samples X, Y and Z) were grown under same growth conditions i.e., the GaN barrier layers were grown at 940°C for 2 minutes and the InGaN QW layers were grown at 740°C for 1 and half minutes.

However, for sample X, we have used TEG and NH<sub>3</sub> as precursors to deposit a GaN capping layer after each InGaN QW. Due to the low deposition rate (about 1 nm/min) of GaN layers with TEG precursor at 740°C, we allowed 3 minutes of deposition time. But for sample Y, we have used TMG and NH<sub>3</sub> precursors to deposit GaN capping layers and allowed only 30 seconds of deposition time due to high growth rate (about 6-7 nm/min) with TMG precursor at the same growth temperature (740°C).

Finally, for sample Z, we have used TMG, TMA and NH<sub>3</sub> as precursors to deposit AlGaIn capping layers and allowed only 30 seconds of deposition time.

Note that after the low temperature capping layer deposition, the growth process was interrupted to raise the temperature from 740°C to 940°C within 2 and half minutes for later GaN barrier layer growth. Figure 4-21 summarizes the sample structures along with their growth parameters. The growth time of different layers are provided in parentheses with the standard notation (prime representing minutes and double prime seconds).

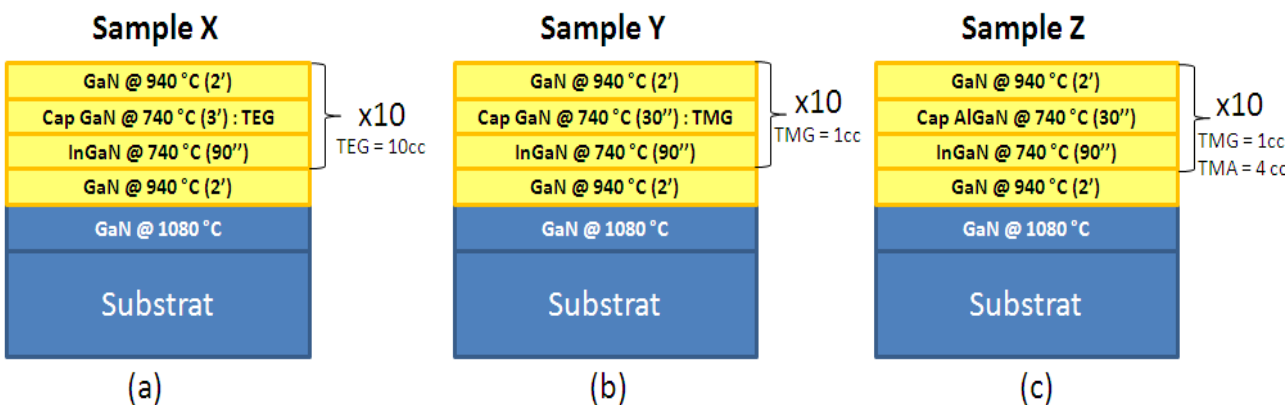


Figure 4-21: Summary of the sample structure along with their growth parameters shown for (a) sample X, (b) sample Y and (c) sample Z.

#### 4.4.2 Structural and optical properties of the last sample series (samples X to Z)

We are going to present the studied structural and optical results in detail for these three samples in the following subsections.

##### 4.4.2.1 AFM analysis

For this sample series, we also conducted the AFM imaging at or near the center of the 2 inch wafers. Following the measurement process described in section 3.5, we have taken a large

scan area of  $5 \times 5 \mu\text{m}^2$  and calculated the TDD and RMS surface roughness for each sample. Analyzing the AFM images, we have found that RMS surface roughness values of the samples are proportional to their TDD per  $\text{cm}^2$ . Figure 4-22 illustrates the images along with their measured TDD and surface roughness values. From these images we can assume that each sample has V-defects along with clustering of threading dislocations. Thus to identify and observe the origin of such V-defects as well as the clustering of threading dislocations in the samples, we tried to analyze each of our samples using different TEM techniques by preparing cross sectional TEM (cs-TEM) samples using standard preparation processes.

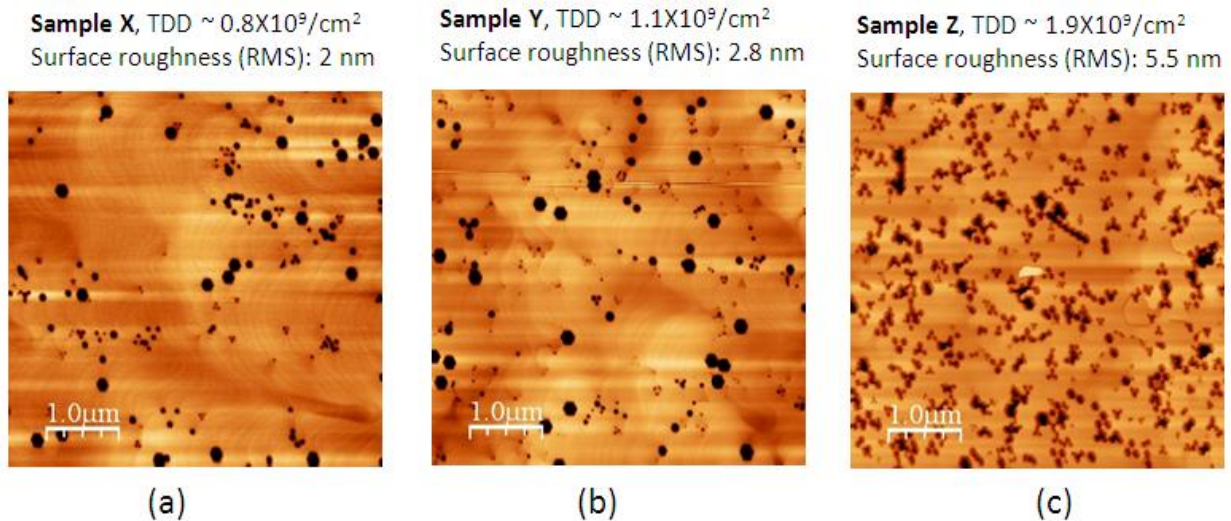


Figure 4-22: AFM images of  $5 \times 5 \mu\text{m}^2$  scan size for (a) sample X, (b) sample Y and (c) sample Z. On top of each image the corresponding threading dislocation density (TDD) per  $\text{cm}^2$  and the root mean square (RMS) surface roughness value in nm scale are provided.

#### 4.4.2.2 TEM and XRD analysis

For this sample series we have also conducted the same kind of experiments as mentioned earlier for other sample series. Following the experimental procedures described in section 3.2 of chapter 3, we have analyzed different areas of each QW of the samples to obtain data on individual QWs' thickness, overall average thickness of different layers and composition values of QWs. Figure 4-23 illustrates the average individual QW thickness for this sample series. From this figure, we can note that the thickness of QWs does not increase from the 1<sup>st</sup> QW to the last QW as much as we have found for the first sample series (Figure 4-6). The summary of the obtained data of this sample series is presented in Table 4-4.

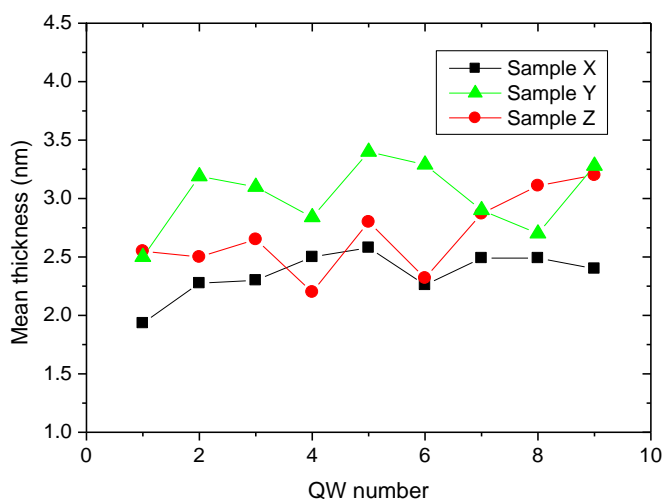


Figure 4-23: Average thickness value for each InGaN quantum well of samples X to Z.

Table 4-4: Summary table of low temperature capping sample series

Sample	Mean Indium composition within QWs % In	Mean barrier thickness $L_{\text{BARRIER}}$ (nm)	AlGaIn- cap thickness $L_{\text{CAP}}$ (nm)	Mean QW thickness value $L_{\text{QW}}$ (nm)	FWHM value of Gaussian fit of QW thickness distribution	Observed total lateral length $L$ (nm)
Sample X	20±1	22±1	-	2.41	0.35	2533
Sample Y	20±1	22±1	-	3.02	0.31	1885
Sample Z	20±1	20±1	3.4±0.5	2.75	0.52	1593

Now to confirm our data through TEM analysis, we have simulated the 0002  $\omega$ - $2\theta$  XRD scan data and compared with the obtained TEM data for each sample of the series. In each case, we have a good correlation of the simulation fits to that of 0002  $\omega$ - $2\theta$  XRD scan data observed at the center of the sample wafer. Note that as the thickness of the AlGaIn capping layers was relatively large (3.40 nm) for sample Z in this series, we were able to determine the average Al composition value considering the center part of the deformation map and found it to be around 8 to 10%. For example, Figure 3-27 in chapter 3 shows the simulation fit constructed from the tabulated values of the Table 4-4 along with Al composition value of 8%, which fit quite well with the XRD scan data. Thus again, we have confirmed our measured values of the sample series through TEM analysis.

From the mean QW thickness values of the sample series, it is certain that the growth process differences of capping layers have impact on overall QW thickness values as the average QW thickness of sample X (2.41 nm) is different from the other two samples (3.02 and 2.75 nm for

sample Y and Z, respectively). We are going to discuss more about this observed QW thickness difference in discussion section.

Finally, the FWHM values of the Gaussian fit from the QW thickness distribution plots suggest us that in any case the QW thickness variation is quite low (as FWHM values are only of 0.35, 0.31 and 0.52 nm for sample X, Y and Z, respectively), so we can conclude that the low temperature capping process without growth interruption is necessary to compensate the QW thickness variation and to have more homogeneous QWs in the structure.

#### 4.4.2.2.1 Dislocation analysis of samples X to Z

We have taken several images in different parts of the samples. Now analyzing all the images, we found that additional dislocations were generated from each sample and they are of  $\langle a \rangle$  type. Maximum  $\langle a \rangle$  type additional dislocations are created after QW number 5. For example, Figure 4-24 illustrates such a situation at one place of sample Y. Considering the visibility criteria of dislocation contrast in weak beam dark field (WBDF) images (Figure 4-24(a) and (b)), we are certain that all the additional dislocations are of  $\langle a \rangle$  type. Moreover, we have found that for this sample series some of these additional threading dislocations were assisting to form V-defects within the sample.

We have calculated the elastic stress energy per unit area ( $E_{\text{elastic}}$ ) for each QW of the sample series from equation 4.1 and found it to be about 0.46, 0.57 and 0.53 J/m<sup>2</sup> for sample X, Y and Z, respectively.

To identify whether we have any  $\langle a \rangle$  type misfit dislocations in our samples, we have considered WBDF images using the diffraction beam spot  $g=11-20$ , after tilting the cs-TEM samples from  $\langle 1-100 \rangle$  zone axis by about 6-7 degree around  $\langle 11-20 \rangle$  direction. But we did not observe any bright contrast at different layer interfaces within such WBDF images showing that we do not have misfit dislocations in our sample.

Similarly, to identify whether we have stacking fault in our sample we used diffraction beam spot  $g=1-100$ , after tilting the sample from  $\langle 11-20 \rangle$  zone axis by about 5-6 degree around the  $\langle 1-100 \rangle$  direction to obtain the WBDF images. Again, we did not observe any bright contrast at different layer interfaces within such WBDF images, which confirms the non-existence of stacking faults (based on the  $\mathbf{g} \cdot \mathbf{R}$  criterion for stacking faults contrast<sup>8</sup>) in our samples.

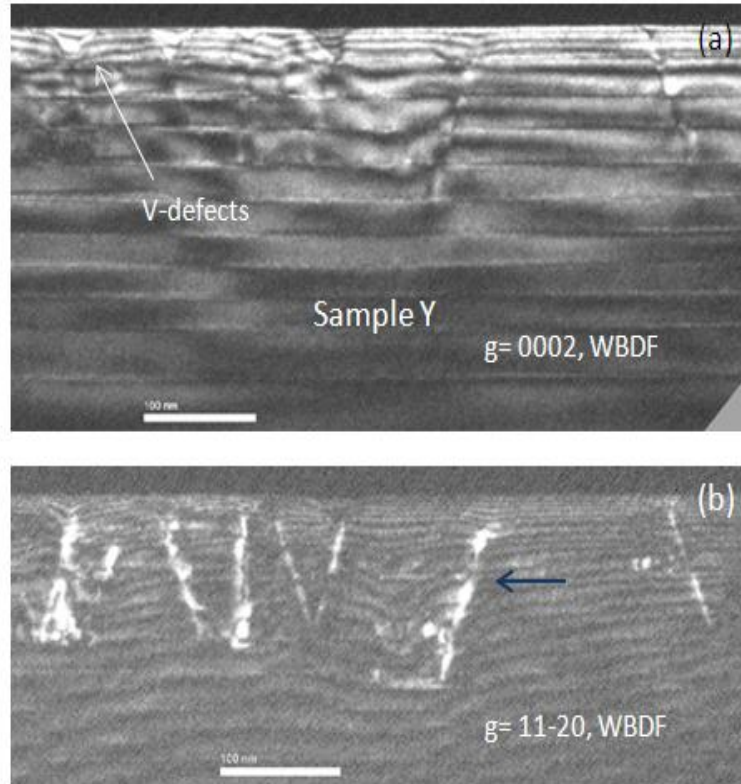


Figure 4-24: Dislocation analysis of sample Y: Weak beam dark field (WBDF) images with (a)  $g=0002$  and (b)  $g=11-20$  diffraction spots. Analyzing the Images, we can conclude that additional threading dislocations of  $\langle a \rangle$  type are generated after QW number 5 and V-defects are formed at the end of almost each dislocation. The white and dark blue arrow in image (a) and (b) show one V-defect and a  $\langle a \rangle$  type dislocation, respectively.

As discussed in section 3.1.4 of chapter 3, the HAADF images allow us to see contrast from chemical composition, so we took HAADF images or Z-contrast images of the samples to see whether any indium clustering within the QWs are promoting such  $\langle a \rangle$  type additional dislocations or not. We took several HAADF images at places, where we initially identified the presence of several additional threading dislocations from bright field imaging. Figure 4-25 illustrates such a region of sample Z.

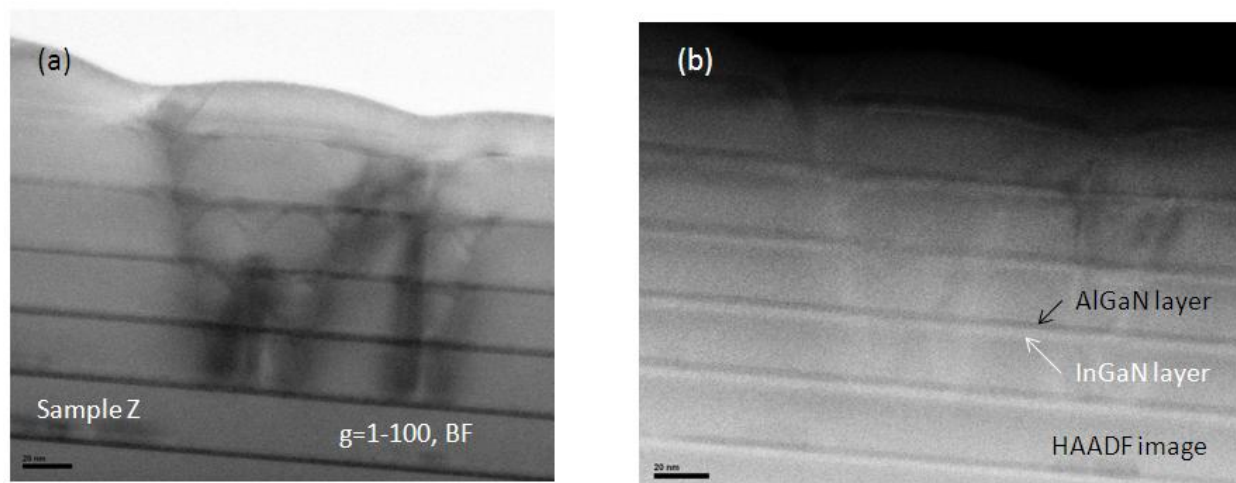


Figure 4-25: (a) The bright field (BF) image of sample Z and (b) its corresponding high angle annular dark field (HAADF) image, demonstrating no indium clustering within the QWs.

From the HAADF image (Figure 4-25(b)) taken at the same place of the sample, we can recognize the InGaIn QW and the AlGaIn capping layer from their relative intensity contrast difference. The brighter region indicates the InGaIn QW region and the darker layer as AlGaIn layer in the image. This image confirms that we do not have any indium clustering in the QW regions as we could not see any drastic brightness change within any InGaIn QW regions.

We are going to discuss more about the limiting factors of identifying indium clustering through HAADF imaging from a cs-TEM sample in discussion section.

#### 4.4.2.3 Room temperature photoluminescence (RT-PL) analysis

The integrated RT-PL data of the sample series (sample X to Z) are shown in Figure 4-26. The RT-PL data of the samples are from exactly the same position from where the TEM analysis was conducted. For all the samples (sample X to Z), we have determined that the indium composition of InGaIn QW regions are of about  $20\pm 1\%$  but the corresponding RT-PL wavelengths are of 500, 532 and 542 nm for sample X, Y and Z, respectively. This difference in RT-PL wavelength can be explained by considering the overall average QW thickness values as tabulated in Table 4-4 and the growth process difference of the samples.

We know that the emission wavelength increases when the QW thickness increases, as an expected behavior. Thus we can attribute the shorter wavelength emission (500 nm) of sample X due to its lowest average QW thickness (2.41 nm) compared to the other two samples Y and Z (sample Y and Z have 3.02 and 2.75 nm, respectively).

We can also remark that samples Y and Z have almost similar mean QW thickness (3.02 nm and 2.75 nm, respectively) but very different wavelength emissions as well as relative intensity values. In this case we may attribute the longer wavelength emission of the sample Z due to the

growth processes difference between the two samples (Figure 4-21). We note that for sample Z, AlGaIn layers have been deposited as capping layers of certain thickness (3.4 nm) after each InGaIn QW layer. This pseudomorphic deposition of AlGaIn layer has certainly increased the electrical field ( $\vec{E}_W$ ) within the QW region of sample Z as compared to the other two samples (samples X and Y). Using the equations 1.25 and 1.26, we have calculated the electrical field within each quantum well of the samples. We found that the electric field ( $\bar{E}_W$ ) within each QW of the samples are about 3.12, 3.05, 3.22 MV/cm for sample X, Y and Z, respectively. Thus comparing the electric field value for sample Y and Z, we can assume that AlGaIn capping layer certainly increase the electric field within QW and thus has higher overall impact of quantum confined Stark effect (QCSE)<sup>7</sup> as explained in section 1.4.1 of chapter 1. We attribute this fact to explain the longer wavelength emission. It can also be the reason for the relatively lower emission intensity of sample Z than that of sample Y. Another explanation of low intensity is related to the growth temperature of AlGaIn which is far from the optimum one.

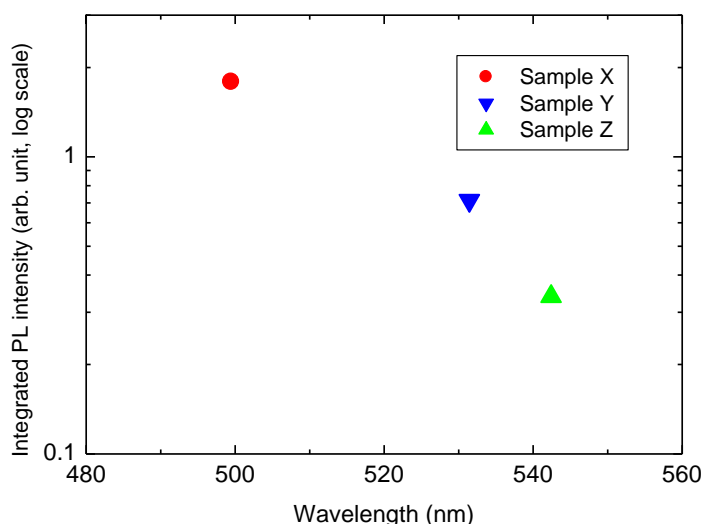


Figure 4-26: Integrated room temperature photoluminescence for samples X to Z.

#### 4.5 Strain state of some samples of the studied series

From the basic idea developed on reciprocal space map (RSM) and analysis process discussed in section 3.3.2.2, we have conducted the RSM at the diffracted beam spot of (20-25) plane for some samples of our series. The samples with higher TDD per  $\text{cm}^2$  and/or large number of V-defects on their surface have been observed through RSM. We have conducted the RSM for sample 2 of first sample series, as it has high TDD ( $7.8 \times 10^9$  per  $\text{cm}^2$ ) and for sample Z of third sample series, because of the presence of both high TDD ( $1.9 \times 10^9$  per  $\text{cm}^2$ ) and V-defects in it.

Figure 3-28 of chapter 3, shows the RSM of sample Z. Both obtained RSMs only indicate a slight relaxation of the samples as we found about 0.02% and 0.03% of relaxation for sample 2 and sample Z, respectively.

## 4.6 Discussion

It is well known that pseudomorphic growth of an InGaN layer on top of a GaN layer causes strain on the epilayer due to lattice mismatch. In chapter 2, we have discussed some observed structural characteristics such as indium clustering, threading dislocation, misfit dislocation, V-defects and QW thickness variation of InGaN/GaN system. It is assumed that some of these observed characteristics are generated from relaxation of built-in stress energy of the grown epilayer.

As we studied 10 periods of InGaN/(Al)GaN multi quantum well (MQW) samples, we also observed some structural defects within our samples. In some samples, we have observed additional <a> type threading dislocations along with V-defects (for example, third samples series) whereas, in some samples, we only observed <a> type threading dislocations (first sample series). However, from our RSM analysis, we have obtained a percentage of relaxation of only about 0.02% for sample 2 (first sample series) and 0.03% for sample Z (third sample series), though they have relatively higher TDD per  $\text{cm}^2$  and presence of V-defects in them.

Moreover, from our earlier discussion (in section 2.2.1 of chapter 2), we also know that it is not possible for <a> type threading dislocation to follow Matthew-Blakeslee<sup>9</sup> or energy balance model<sup>10,11</sup> to relax the strain, as only <a+c> type dislocations can participate in such relaxation mechanism.

Thus we are going to discuss in detail about our observed structural characteristics, their origin and role in strain state of the samples.

### 4.6.1 Strain relaxation

#### 4.6.1.1 V-defects and additional threading dislocations

V defect (also known as V-pits or pinholes) is known as a plastic deformation which helps to relax elastically the strain of the layer at or near its surface. Thus the formation of V-defects in the InGaN epitaxial layer is due to the elastic relaxation of strain in the surface area of the layer<sup>12</sup>. Two dimensional finite-element calculations of pit like structure show that such pits may efficiently reduce the strain by elastic relaxation.<sup>13</sup> In our case we have observed V-defects in some of our samples.

The presence of two different shapes of V-defects has already been reported for an InGaN/GaN MQW structure. For example, Nikhil Sharma et al<sup>14</sup> found that after the initial formation of V-

defects, there is no QW region grown at the inclined plane  $\{1-101\}$  of V defects on later MQW growth, whereas X. H. Wu et al<sup>15</sup> reported finding thin QW regions within the  $\{1-101\}$  plane of the V-defects as schematically shown in Figure 4-27. In our case, we have observed both types of V-defects. In case of first sample series (sample D) we have V-defects, where no QW regions were grown on the  $\{1-101\}$  planes of the V-defects but for last sample series (samples X to Z) we have observed thin QW regions on the  $\{1-101\}$  planes of the V-defects. Figure 4-28 illustrates one such formation of thin QW regions at  $\{1-101\}$  plane of the V-defect for sample Y, as we can see a very thin dark region in bright field and similarly a very thin bright region on the HAADF image representing the QW regions on that plane. V-pits introduction allow relaxation in our samples but the difference of behavior of QWs in the pits remains unclear.

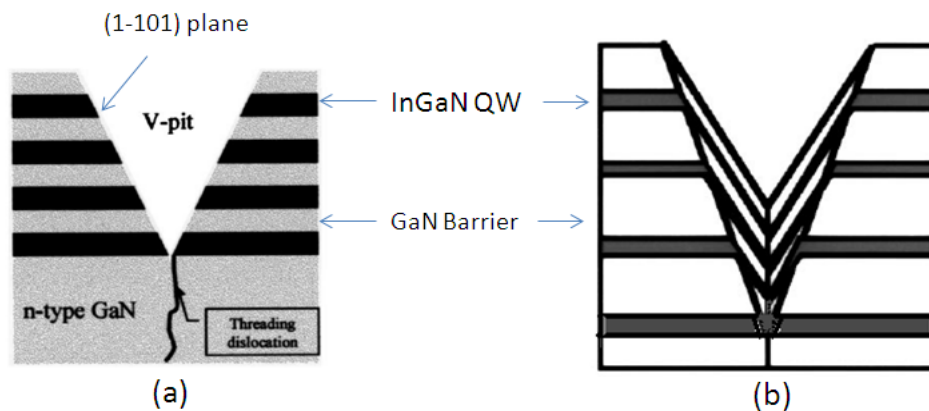


Figure 4-27: Schematic diagram showing the (1-101) plane of V-defects where (a) no QW and (b) thin QW regions were grown in a multi-quantum well (MQW) structure.<sup>14,15</sup>

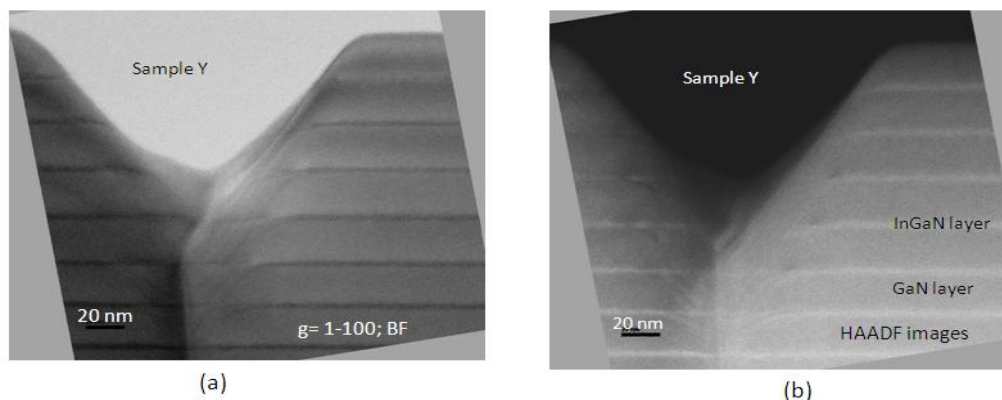


Figure 4-28: (a) Bright field and (b) HAADF Image of sample Y near a V defect, demonstrating growth of thin QW regions on (1-101) plane of the V-defect.

As discussed in section 2.2.3 of chapter 2, B. Jahnke et al<sup>16</sup> reported that when the V-defects reach the heteroepitaxial interface,  $\langle a \text{-type} \rangle$  misfit dislocations may be created and propagate through the basal  $\{0001\}$  plane to relax the strain at the apex of V-defects. A similar type of

relaxation has also been observed by R. Lui et al<sup>17</sup>, where they describe the propagation of <a-type> dislocation as radial-shape dislocation half loops. They clearly identified that <a-type> dislocation has been created at the interface of the two layers exposed by V-defects, while the diameter of the half loops in basal plane depends on the amount of strain relaxation. But in our case, we did not observe any misfit dislocation at the interface of our studied samples, thus such a generation process of additional <a> type dislocations to relax the strain does not exist in our samples.

However, we have observed very few segments of misfit dislocations appearing at different QW interfaces of one sample (sample 1) (Figure 4-7) while observing large area of the cs-TEM sample (Total lateral length  $L = 3.6\mu\text{m}$ ). The total length of such MD segments is measured to be less than 100 nm. Thus the contribution of such MD in strain relaxation is negligible.

Moreover, F.Y. Meng et al<sup>18</sup> have reported that stacking faults at the interface of two different layers form <a> type threading dislocation in the epilayer. The experimental observation confirms that we did not have any stacking fault at the layer interfaces of our MQW structure, thus we rule out such an <a> type threading dislocation generation mechanism for our studied samples, as well. This lack of stacking faults in our samples also allows us to rule out the possibility of formation of V-defects from stacking faults as reported by H. K. Cho et al<sup>19</sup> in their work.

Mingwei Zhu et al<sup>20</sup> propose another mechanism of additional dislocation formation, where dislocations are generated in pairs and propagate in a particular direction within the InGaN layer. In our case, we have observed clusters of threading dislocations generated in our InGaN layers and they are not inclined in any particular direction while propagating through the layer. Thus such a formation mechanism of additional dislocation does not exist in our case.

#### 4.6.1.2 Inclined threading dislocation

P. Cantu et al<sup>21</sup> and A. E. Romanov et al<sup>22</sup> reported a mechanism of strain change by inclination of threading dislocations for AlGaIn/GaN system. This inclination of TDs is referred to as an effective dislocation climb process.<sup>22</sup> The exact mechanism for such an inclination is still under discussion but seems not to be an actual climb process but rather a bending during growth<sup>22,23</sup>. The pre-existing <a> type threading dislocation inclined from the [0001] direction towards a particular <1-100> direction by an angle  $\alpha$  ( $\sim 15^\circ$ - $25^\circ$ ) while propagating through GaN layer. The projection of such an inclined dislocation in the interface plane is a segment of misfit dislocation. They have modeled such phenomenon and calculate the strain change of one epilayer with thickness  $h$ , following the equation below:

$$\varepsilon_{pl} = \frac{1}{2} b \rho_{TD} h \tan \alpha \quad (4.2)$$

where  $\varepsilon_{pl}$  stands for the amount of strain change in the epilayer due to the inclination of threading dislocation at the stressed and buffer layer interface,  $b$  the length of Burger vector and  $\rho_{TD}$  is the average TDD per  $\text{cm}^2$ . Due to this strain change process the strain at the top surface of the epilayer will become:

$$\varepsilon_{mes} = |\varepsilon_m - \varepsilon_{pl}| = \left| \frac{a_x - a_o}{a_o} \right| \quad (4.3)$$

$$\text{And, } \varepsilon_m = \left| \frac{a - a_o}{a_o} \right|$$

where,  $\varepsilon_m$  is the mismatch strain of the epilayer,  $a$  is the lattice parameter of fully strained epilayer i.e., the lattice parameter of the buffer layer,  $a_x$  represents the partially relaxed lattice parameter of the top surface of the epilayer and  $a_o$  is the relaxed lattice parameter of the epilayer as illustrated in Figure 4-29 for one epilayer. Thus after such a process the percentage of relaxation becomes:

$$r = \left| \frac{a_x - a}{a} \right| \times 100 (\%) \quad (4.4)$$

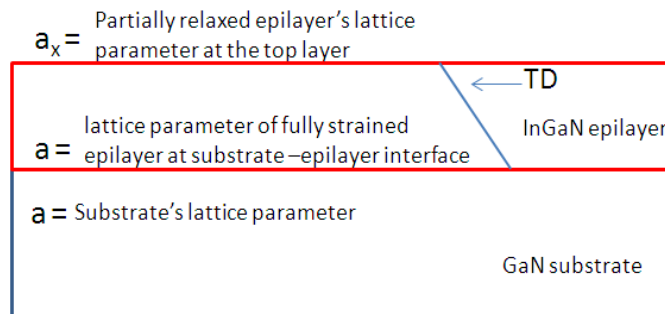


Figure 4-29: Schematic diagram of strain relaxation process due inclined threading dislocation within one epilayer.

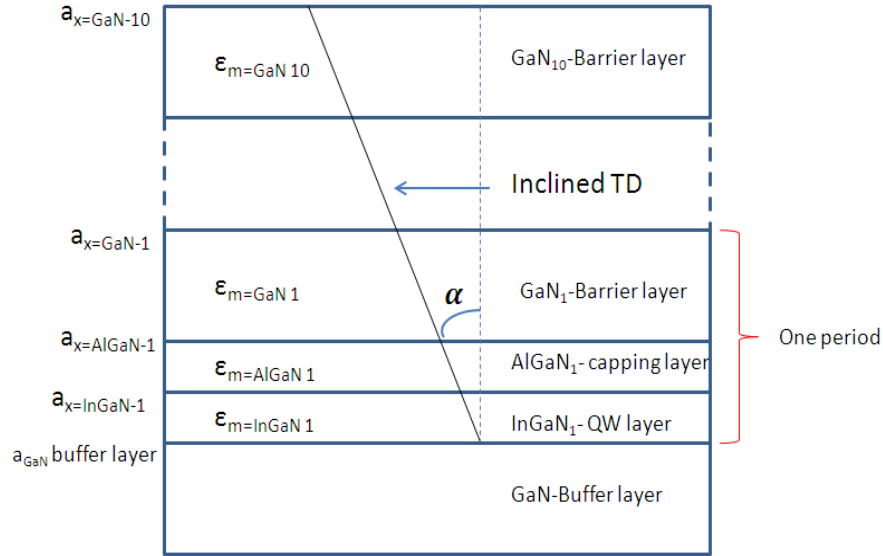


Figure 4-30: Schematic illustration of relaxation process through bending of pre-existing threading dislocations, where  $a_x$  represents the partially relaxed lattice parameter at each interface and  $\varepsilon_m$  corresponding strain at different layers.

Following the same hypothesis, we may also calculate the amount of strain change within our samples due the presence of inclined dislocations. Most of these inclined dislocations do not result from the bending of pre-existing ones but are additional dislocations created in the QW region. In our case, some parameters are not known (direction of dislocations inclination, exact angle of inclination, character of the dislocations). For the calculation, we assume that these parameters are the most favorable for relaxing the strain in InGaN QWs: direction of inclination towards  $\langle 10\text{-}10 \rangle$  directions,  $25^\circ$  of inclination (maximum measured in our images) and a pure edge-character for the projected misfit segments in the interfaces. Figure 4-30 schematically represents the strain change processes within the epilayers due to inclination of threading dislocations for an InGaN/AlGaIn/GaN structure (sample Z). For example, if we consider the parameters of sample Z (for sample Z:  $\text{TDD}=1.9 \times 10^9$  per  $\text{cm}^2$ ,  $h_{\text{InGaIn}}=2.75$  nm,  $h_{\text{AlGaIn}}=3.4$  nm,  $h_{\text{GaN}}=19.7$  nm,  $\alpha=25^\circ$  and  $b=0.3189$  nm), then following equation 4.2, we can calculate the strain change  $\varepsilon_{pl}$  for the different layers as:

$$\varepsilon_{pl_{\text{InGaIn}}} \cong 3.88 \times 10^{-6}$$

$$\varepsilon_{pl_{\text{AlGaIn}}} \cong 4.80 \times 10^{-6}$$

$$\varepsilon_{pl_{\text{GaN}}} \cong 2.78 \times 10^{-5}$$

However, the mismatch strain  $\varepsilon_m$  at different epilayers will be different owing to the evolution of the in-plane lattice parameter ( $a_x$ ) at different interfaces as shown in Figure 4-30. For example, the mismatch strain of the 1<sup>st</sup> InGaIn QW layer depends on the in-plane lattice

parameter of the GaN buffer layer ( $\varepsilon_{m=InGaN1} = \left| \frac{a_{GaN\ buffer\ layer} - a_o}{a_o} \right|$ ), whereas in case of the 2<sup>nd</sup> InGaN QW layer the mismatch strain depends on the in-plane lattice parameter at the surface of the 1<sup>st</sup> GaN barrier layer ( $\varepsilon_{m=InGaN2} = \left| \frac{a_{x=GaN1} - a_o}{a_o} \right|$ ).

Thus considering these facts and considering that the InGaN layers have 20% of indium and AlGaN layers have 10% of Al composition with their relaxed lattice parameters as  $a_{oIn(0.2)Ga(0.8)N} = 3.2558 \text{ \AA}$  and  $a_{oAl(0.1)Ga(0.9)N} = 3.1814 \text{ \AA}$ , we have calculated the in plane lattice parameters at different interfaces of 1<sup>st</sup> period of the structure (sample Z) as follows:

$$a_{x=InGaN1} \cong 0.318901 \text{ nm}$$

$$a_{x=AlGaN1} \cong 0.318902 \text{ nm}$$

$$a_{x=GaN1} \cong 0.318908 \text{ nm}$$

To relax the strain in an InGaN QW, an inclined dislocation has to increase the in-plane parameter. The inclination direction of the inclined dislocations being constant, this in-plane lattice parameter increase also occurs in AlGaN and GaN layers, thereby increasing the strain in these layers.

After one period of the structure, following equation 4.4, the percentage of relaxation ( $r$ ) for InGaN becomes:

$$r = \left| \frac{a_{x=GaN1} - a_{GaN\ buffer\ layer}}{a_{GaN\ buffer\ layer}} \right| \times 100 \text{ (\%)}$$

$$r = \left| \frac{0.318908 - 0.3189}{0.3189} \right| \times 100 \cong 0.002 \text{ \%}$$

where  $a_{x=GaN1}$  is the in-plane parameter at the surface of the 1<sup>st</sup> GaN barrier and at the beginning of the 2<sup>nd</sup> InGaN QW.

Following the same procedure for all other layers, we finally obtain a percentage of relaxation at the surface of the last InGaN epilayer of the structure of about 0.02%. The measured relaxation by XRD being 0.03%, the role of inclined dislocations in the relaxation seems to be important. But, XRD measured the percentage of relaxation of the whole structure whereas the value of 0.02% due to inclined dislocations is at the surface of the last InGaN QW. Moreover, we chose parameters which maximize the effect of inclined dislocations on the percentage of relaxation. Therefore, we conclude that inclined dislocations play a minor role on the relaxation of strain in the InGaN QWs of our structures.

Taking into account this minor role of inclined dislocations on the relaxation of InGaN and the fact that these inclined dislocations increase the strain in the AlGaN and GaN layers, we consider that the driving force for the introduction of additional dislocations is not related to a strain relaxation process.

#### 4.6.2 Indium clustering

We next assumed that indium clustering within our QW region may be at the origin of such dislocation creation as these additional dislocations are helping to relax the excessive strain within the high indium concentrated region. The explanation of the formation of In-rich InGaN clusters close to the core of pre-existing TDs may be similar to the one proposed by Rouvière et al<sup>24</sup> for the preferential nucleation of GaN quantum dots on AlN layers. In the presence of a vertically threading dislocation with an a-component, there are compressed and expanded regions around the dislocation core. InGaN clusters may preferentially nucleate in the tensely strained region (larger in plane parameter).

Thus we took HAADF images or Z-contrast images of the samples. But we could not find any strong evidence of indium clustering within the QWs in our samples. Figure 4-31 schematically illustrates the possibility of having the exact location of indium clustering within a cs-TEM sample. For example, if we have an indium cluster in a region of an InGaN layer (black bounded region), as shown in the 3D view of the layer (Figure 4-31 (a)), then preparing the cs-TEM sample from the black bounded region of the InGaN layer will allow us to observe the pre-existing TD which is the origin of additional TDs and therefore an eventual In-rich cluster. On the other hand, if it is not the case then only additional TDs would be observed (Figure 4-31(c)). If we assume a pre-existing TDD of  $5 \times 10^8 \text{ cm}^{-2}$ , there is one TD every  $0.2 \text{ } \mu\text{m}^2$ . With a cs-TEM sample which is 50 nm thick and 5  $\mu\text{m}$  large, the intercepted surface is  $0.25 \text{ } \mu\text{m}^2$ . The probability of intercepting the origin of additional TDs is therefore close to 1. Moreover, we have observed several samples. Therefore, if detectable In-rich clusters exist, we should have observed some of them. On the other hand, if In-rich clusters have a very small size compared to the TEM object thickness (a few nanometers in assumed 50 nm thick object), they will not have contrast in a HAADF image. Therefore, we can certainly exclude the existence of large In-rich clusters but we cannot be conclusive about the presence of small clusters.

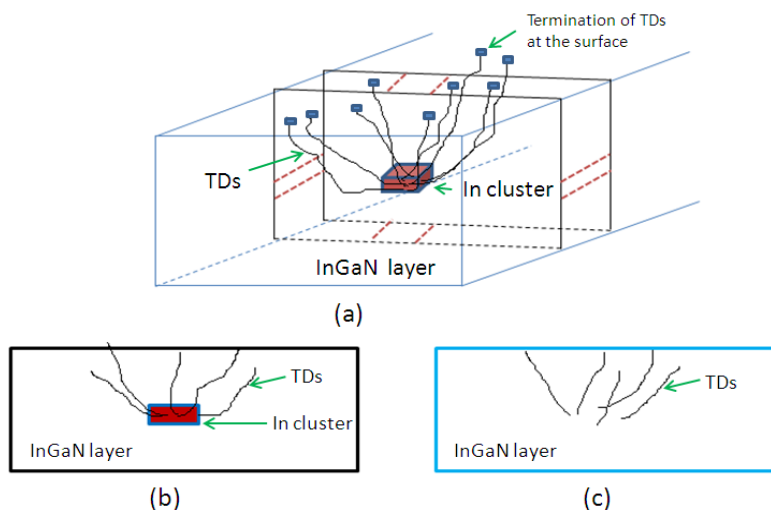


Figure 4-31: Schematic diagram representing the rare chance of having indium clustering within a cs-TEM sample. (a) 3 dimensional (3D) view of an InGaN layer with indium cluster as represented by red box. Cross sectional (cs) views of the InGaN layer where (b) cs-TEM sample prepared from within the black boundary region and (c) outside the black boundary region of image (a).

We can make another hypothesis about the origin of additional TDs. We observe that the density of additional TDs is related to the indium composition. But our way to obtain high indium compositions is to reduce the growth temperature from the optimum one for the GaN growth. In fact, the mobility of adatoms is drastically reduced at these low temperatures and the probability of point defect creation is increased. The formation of additional dislocations may be the result of the agglomeration of point defects in the core of pre-existing TDs.

#### 4.6.3 QW thickness increment

Several research groups, for example N. Grandjean et al<sup>25</sup> and N. Duxbury et al<sup>26</sup> have already reported a small increment of QW thicknesses from initial to final QW in their multi-quantum well samples grown either by molecular beam epitaxy (MBE) or MOCVD growth techniques.<sup>25,26,27</sup> They have associated this phenomenon to the effect of indium surface segregation, which is well known to occur during ternary alloy semiconductor compound growth.<sup>28</sup>

It is assumed that in such indium surface segregation process, after initial QW growth, the top-most layer of the QW becomes indium rich<sup>29,30</sup>. Depending on the growth process of the following GaN barrier layer, these accumulated indium atoms may further segregate without incorporation in the GaN barrier layer and become available to the growth front of next QW. These extra indium adatoms then will participate in the next QW growth process and make the later QW a little thicker than the previous one.

However, the amount of available indium adatoms on the growth front of the next QW depends entirely on growth rate, growth temperature and deposition time of the GaN barrier layers. It is assumed that while growing a relatively thick GaN barrier at high temperature, no such indium adatoms will be available at the growth front of next QW due to evaporation and diffusion processes.

In some of our studied samples (sample 1, 2 and sample A), we have observed an increment of average QW thicknesses from initial QW to at least 4-5<sup>th</sup> QWs (Figure 4-6 and Figure 4-12). But this observation is quite abnormal as we have grown all our GaN barrier layers at high temperature ( $\geq 940^{\circ}\text{C}$ ) with large thickness ( $\geq 14$  nm) and moreover the differences between the QW thickness are quite large (0.5 nm and 1.8 nm for first two QWs of sample 1) to assume any indium surface segregation to cause such QW thickness increment. Thus we conclude that it is not related to indium surface segregation, rather it is related to the stability of our home made MOCVD reactor, as we have observed quite stable average QW thickness for later QWs ( $> 4^{\text{th}}$  QWs) in those samples.

On the other hand, comparing the growth processes of third series (samples X to Z) (Figure 4-21) along with their overall average QW thickness, we can attribute the lower average QW thickness of sample X (2.41 nm) compare to other two samples (3.02 and 2.75 nm for sample Y and Z, respectively), to a relatively stronger indium surface segregation effect in sample X as the GaN capping layers were deposited at low growth rate for much longer growth time (3 minutes). This growth process may allow floating indium atoms at top layer of the QW to segregate more easily into the GaN capping layer than the other two samples (Note that the capping layer deposition times for sample Y and Z are only 30 seconds).

In section 3.4 of chapter 3, we have discussed that we used a frequency-doubled argon ion ( $\text{Ar}^+$ ) laser as a source (emitting at 244 nm) in our RT-PL experiment, which has a penetration depth of around 50 nm for our InGaN/GaN system. Thus the obtained PL data correspond to the optical behavior of top 2-3 QWs of all the studied samples. Moreover, note that we have ignored the lower QW thickness data when calculating the mean QW thickness and the FWHM values for samples with such QW thickness increment phenomena. Thus we were able to ignore the impact of this abnormality of the MOCVD reactor in our obtained results. Moreover, we can mention that an increase in QW thickness may be advantageous in our case. In fact, it results in a broad spectrum emission of the converter as different QWs will emit at different wavelength.<sup>31</sup> The resulting white emission is also broad which is better for domestic applications.

#### 4.6.4 QW thickness variation

Several research groups have observed QW thickness variation and reported on their impact on optical properties.<sup>32,33,34</sup> It is assumed that thickness variation occurs due to growth temperature and process differences between different layers.<sup>35,36</sup> We also found QW thickness variations in our samples. The full width half maximum (FWHM) values of the Gaussian fit obtained from the QW thickness distribution plots (discussed in section 3.2.1) confirm that samples without any capping layers have much more frequent and/or higher QW thickness variation (FWHM values are of 1.70, 1.0 and 1.54 nm for samples 1, 2 and sample A, respectively) than other samples (<1.0 nm). Thus to reduce the occurrence of thickness variation we should implement a capping process after each InGaN QW. Moreover, depositing capping layer at the low temperature (i.e. the same growth temperature as for InGaN QW layers) without growth interruption helps to limit the diffusion and evaporation of indium atoms from the QWs more effectively and thus compensate the occurrence of thickness variation.

However, the exact mechanism of thickness reduction in definite areas of QW is still unknown. We can assume that QW thickness variation within a QW is occurring due to the presence of threading dislocations within the sample as schematically shown in Figure 4-32. But we could not confirm such assumption from our cs-TEM observation.

The presence of such QW thickness variation near a TD may allow electrical carriers to localize in deeper potential minima (in thick QW regions) therefore minimizing the detrimental effect of TD on optical performances of QWs structures.

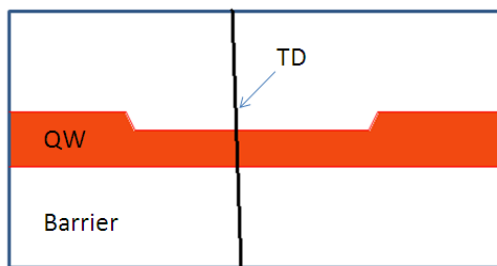


Figure 4-32: Schematic diagram showing the quantum well thickness variation due to a threading dislocation.

#### 4.6.5 Impact of AlGa<sub>N</sub> capping layer deposition

From our analysis, we have found that capping InGa<sub>N</sub> QWs at low temperature with AlGa<sub>N</sub> layers helps us to achieve relatively higher wavelength emission. This phenomenon has two reasons. Firstly, It helps to achieve relatively thick QWs within the structure (sample D) as it blocks the diffusion and evaporation of indium atoms from the QWs and secondly, it increases the overall quantum confined Stark effect (QCSE)<sup>7</sup>, as AlGa<sub>N</sub> layer increases the internal electric field ( $\vec{E}_w$ ) within the QWs depending on its composition and thickness values (sample Z).

On the other hand, as discussed in section 1.4.1 of chapter 1, both the QW thickness and the electric field within the QWs may play a role in emission intensity of the sample due QCSE. Comparing sample Y and Z, we found that sample Z has higher wavelength emission (542 nm) with less intensity than sample Y (532 nm) (Figure 4-26). Note that sample Z has AlGa<sub>N</sub> as capping layers with about 10% of Al composition and 3.4 nm thicknesses. However, we can attribute the lower intensity of sample Z not only to QCSE but also to the poor material quality due to the low growth temperature. But, comparing the intensity of sample D to that of sample A, the reference, we found a higher wavelength emission with slight increase in intensity (Figure 4-20), which is quite remarkable as we deposited a few monolayers of AlGa<sub>N</sub> (about 1.5 nm) with low Al composition (about 5%) in sample D.

Thus, by adjusting the composition and thickness values of the AlGa<sub>N</sub> capping layer along with the InGa<sub>N</sub> QWs, we may achieve higher wavelength emission with reasonable intensity. And finally, optimizing the growth conditions of AlGa<sub>N</sub> capping layer at low temperature can lead us to achieve improved PL efficiency.

### Summary

In this work, we have tried to construct an efficient InGa<sub>N</sub>/Ga<sub>N</sub> based MQW structure with bright emission at green-yellow spectral range by changing different growth parameters and processes. The motivations of such approaches were to identify the impact of different growth processes on the MQW structure and achieve an effective growth process which will eventually help us to construct a phosphor free white LED structure<sup>37</sup>.

In this work initially, we have constructed 10 periods of InGa<sub>N</sub>/Ga<sub>N</sub> MQW structures either of high indium composition and low thickness or low indium composition and high thickness QWs without any capping layer deposition. Following such approaches, we were able to construct MQW structures emitting at around 570 nm wavelengths but with poor intensity as observed from room temperature photoluminescence (RT-PL) experiments. From our analysis, we have

confirmed that additional threading dislocations of <a> type have been generated from QWs and the occurrences of thickness variation within each QW were relatively high (FWHM  $\geq 1.0$  nm). We did not observe any indium clustering, stacking faults and/or misfit dislocations to be a source of such additional threading dislocation in the structure.

These dislocations did not relax the strain of the InGaN epilayer as we have found the percentage of relaxations to be negligible (relaxation of 0.02% for sample 2) but they certainly hamper achieving high intensity light from the structure as dislocations act as non-radiative recombination centers for the electron-hole carriers<sup>38,39</sup>. In our assessment, indium clustering of small volume and/or point defects within QWs may be the prime reason for such <a> type additional threading dislocations in the structure.

We tried to investigate the impact of a few monolayers of AlGa<sub>N</sub> as capping layer and its growth process after each QW. We were able to identify that it is possible to have a green light (540 nm) emission with a higher room temperature photoluminescence (RT-PL) efficiency than the reference one by a low temperature (740°C) deposition of the AlGa<sub>N</sub> capping layer above relatively low indium composition and low thickness InGa<sub>N</sub> QWs (average composition of 18% and 3.5 nm-sample D). The AlGa<sub>N</sub> layer helps to reduce the evaporation and/or diffusion of Indium from InGa<sub>N</sub> quantum wells and compensates the occurrence of thickness variations (FWHM  $\leq 1.0$  nm), which are detrimental effects of the high temperature processing. Moreover, we did not observe any additional <a> type threading dislocations generated from low composition and low thickness QWs samples.

Finally, to distinguish the impact of low temperature (740°C) deposition of Ga<sub>N</sub> to that of AlGa<sub>N</sub> as capping layer, we have analyzed last sample series (sample X to Z). From the obtained results, we may conclude that deposition time of any capping layer should be short and growth rate of the capping layer should be high, as otherwise it may cause indium atoms to segregate and/or diffuse into the barrier layer. It will reduce the expected QW thickness and eventually have impact on optical performance of the structure (sample X). This series also confirms that it not only AlGa<sub>N</sub> but also Ga<sub>N</sub> can be used as capping layer to compensate the QW thickness variation (from its FWHM values  $< 1.0$  nm). Moreover, AlGa<sub>N</sub> capping layer with relatively high Al composition (about 10 %) and thickness value (3.4 nm) may allow us to have longer wavelength emission with less intensity than that of Ga<sub>N</sub> capping layer owing to the quantum confinement Stark effect<sup>7</sup>. Thus depending on the goal, we can manipulate the AlGa<sub>N</sub> capping layers' composition and thickness value to balance between the targeted wavelength and intensity from such MQW structure.

**References:**

- 1 J. F. Nye, *Physical properties of crystals: Their Representation by Tensors and Matrices*. (Oxford University Press, USA, 1985).
- 2 Y. Chen, T. Takeuchi, H. Amano, I. Akasaki, N. Yamada, Y. Kaneko, and S. Y. Wang, *Applied Physics Letters* **72** (6), 710 (1998).
- 3 M. D. McCluskey, L. T. Romano, B. S. Krusor, D. P. Bour, N. M. Johnson, and S. Brennan, *Applied Physics Letters* **72** (14), 1730 (1998).
- 4 D. Gerthsen, B. Neubauer, A. Rosenauer, T. Stephan, H. Kalt, O. Schon, and M. Heuken, *Applied Physics Letters* **79** (16), 2552 (2001).
- 5 M. Korytov, PhD thesis, Universite de Nice- Sophia Antipolis, France, 2010.
- 6 S.J. Pennycook and P.D. Nellist, *Z- Contrast Scanning Transmission Electron Microscopy*. (Kluwer Academic Publishers, The Netherlands, 1999).
- 7 N. Grandjean, B. Damilano, S. Dalmaso, M. Leroux, M. Laugt, and J. Massies, *Journal of Applied Physics* **86** (7), 3714 (1999).
- 8 F. Y. Meng, M. Rao, N. Newman, R. Carpenter, and S. Mahajan, *Acta Materialia* **56** (15), 4036 (2008).
- 9 J. W. Matthews and A. E. Blakeslee, *Journal of Crystal Growth* **27**, 118 (1974).
- 10 R. People and J. C. Bean, *Applied Physics Letters* **47** (3), 322 (1985).
- 11 L. B. Freund and S Suresh, *Thin Film Materials: Stress, Defect Formation and Surface Evolution*. (Cambridge University Press, Cambridge, 2003).
- 12 F. C. Frank, *Acta Crystallographica* **4** (6), 497 (1951).
- 13 D. Vanderbilt and LK. Wickham, *Material Research Society Symposium Proceedings* **202**, 555 (1991).
- 14 Nikhil Sharma, Paul Thomas, David Tricker, and Colin Humphreys, *Applied Physics Letters* **77** (9), 1274 (2000).
- 15 X. H. Wu, C. R. Elsass, A. Abare, M. Mack, S. Keller, P. M. Petroff, S. P. DenBaars, J. S. Speck, and S. J. Rosner, *Applied Physics Letters* **72** (6), 692 (1998).
- 16 B. Jahnen, M. Albrecht, W. Dorsch, S. Christiansen, H. P. Strunk, D. Hanser, and Robert F. Davis, *MRS Internet Journal Nitride Semiconductor Research* **3**, 39 (1998).
- 17 R. Liu, J. Mei, S. Srinivasan, F. A. Ponce, H. Omiya, Y. Narukawa, and T. Mukai, *Applied Physics Letters* **89** (20) (2006).
- 18 F. Y. Meng, H. McFelea, R. Datta, U. Chowdhury, C. Werkhoven, C. Arena, and S. Mahajan, *Journal of Applied Physics* **110** (7) (2011).
- 19 H. K. Cho, J. Y. Lee, G. M. Yang, and C. S. Kim, *Applied Physics Letters* **79** (2), 215 (2001).
- 20 Mingwei Zhu, Shi You, Theeradetch Detchprohm, Tanya Paskova, Edward A. Preble, Drew Hanser, and Christian Wetzel, *Physical Review B* **81** (12), 125325 (2010).
- 21 P. Cantu, F. Wu, P. Waltereit, S. Keller, A. E. Romanov, S. P. DenBaars, and J. S. Speck, *Journal of Applied Physics* **97** (10) (2005).
- 22 A. E. Romanov and J. S. Speck, *Applied Physics Letters* **83** (13), 2569 (2003).
- 23 Srinivasan Raghavan, Ian C. Manning, Xiaojun Weng, and Joan M. Redwing, *Journal of Crystal Growth* **359** (0), 35 (2012).
- 24 J. L. Rouvière, J. Simon, N. Pelekanos, B. Daudin, and G. Feuillet, *Applied Physics Letters* **75** (17), 2632 (1999).
- 25 N. Grandjean, J. Massies, S. Dalmaso, P. Vennéguès, L. Siozade, and L. Hirsch, *Applied Physics Letters* **74** (24), 3616 (1999).

- 26 N. Duxbury, U. Bangert, P. Dawson, E. J. Thrush, W. Van der Stricht, K. Jacobs, and I. Moerman, Applied Physics Letters **76** (12), 1600 (2000).
- 27 H. Chen, A. R. Smith, R. M. Feenstra, D. W. Greve, and J. E. Northrup, MRS Internet J. Nitride Semicond. Res. **451**, 695 (1999).
- 28 J. Massies, F. Turco, A. Saletes, and J. P. Contour, Journal of Crystal Growth **80** (2), 307 (1987).
- 29 K. Muraki, S. Fukatsu, Y. Shiraki, and R. Ito, Applied Physics Letters **61** (5), 557 (1992).
- 30 A. Dussaigne, B. Damilano, N. Grandjean, and J. Massies, Journal of Crystal Growth **251** (1–4), 471 (2003).
- 31 A. Dussaigne, J. Brault, B. Damilano, and J. Massies, physica status solidi (c) **4** (1), 57 (2007).
- 32 Nicole K. van der Laak, Rachel A. Oliver, Menno J. Kappers, and Colin J. Humphreys, Applied Physics Letters **90** (12) (2007).
- 33 W. S. Fu, G. R. Olbright, A. Owyong, J. F. Klem, R. M. Biefeld, and G. R. Hadley, Applied Physics Letters **57** (14), 1404 (1990).
- 34 A. V. Filinov, C. Riva, F. M. Peeters, Yu E. Lozovik, and M. Bonitz, Physical Review B **70** (3), 035323 (2004).
- 35 S. Kret, F. Ivaldi, K. Sobczak, R. Czernecki, and M. Leszczyński, physica status solidi (a) **207** (5), 1101 (2010).
- 36 L. Hoffmann, H. Bremers, H. Jönen, U. Rossow, M. Schowalter, T. Mehrrens, A. Rosenauer, and A. Hangleiter, Applied Physics Letters **102** (10) (2013).
- 37 Benjamin Damilano, Hyonju Kim-Chauveau, Eric Frayssinet, Julien Brault, Sakhawat Hussain, Kaddour Lekhal, Philippe Vennéguès, Philippe De Mierry, and Jean Massies, Applied Physics Express **6** (9) (2013).
- 38 S. J. Rosner, E. C. Carr, M. J. Ludowise, G. Girolami, and H. I. Erikson, Applied Physics Letters **70** (4), 420 (1997).
- 39 Sugahara Tomoya, Sato Hisao, Hao Maosheng, Naoi Yoshiki, Kurai Satoshi, Tottori Satoru, Yamashita Kenji, Nishino Katsushi, T. Romano Linda, and Sakai Shiro, Japanese Journal of Applied Physics **37** (4A), L398 (1998).

**Sample References:**

Sample 1 and 2 = G2986 and G2987

Test sample = G2988

Sample A to D=G2788 to G2791

Sample X=G3127

Sample Y=G3132

Sample Z= G3131

## Conclusion and perspective



## Conclusion and perspective

In this work, we have studied  $\text{In}_x\text{Ga}_{1-x}\text{N}/(\text{Al})\text{GaN}$  multiple quantum well (MQW) structures with the goal of obtaining bright emission at green-yellow spectral range. By analyzing the impact of different structures, growth processes and parameters, we have tried to understand the mechanisms of defect formation and to identify the best conditions that can be implemented to achieve our goal.

To obtain yellow emission with  $\text{In}_x\text{Ga}_{1-x}\text{N}/\text{GaN}$  MQWs, large indium composition and/or thick  $\text{In}_x\text{Ga}_{1-x}\text{N}$  wells are necessary. In theory, it is better to use thin  $\text{In}_x\text{Ga}_{1-x}\text{N}$  QWs with a large indium composition in order to limit the decrease of the oscillator strength of the optical transitions due to the quantum confined Stark effect. From the practical point of view, we have shown that the situation is more complex since we are facing material problems related to the growth of high indium content  $\text{In}_x\text{Ga}_{1-x}\text{N}$  layers on GaN (high stress, low temperature growth to incorporate large indium compositions). In this work we have mainly used transmission electron microscopy techniques to analyze the structural properties of our samples to extract data on layer thicknesses and compositions through quantitative analysis. We have systematically confronted these data to photoluminescence measurements in order to be able to contribute to the sample optimization. This correlation is not obvious since the typical scale for TEM analysis is on the order of a few hundreds of nm while for photoluminescence measurements we are exciting the sample with surfaces much larger than the squared micrometer. Therefore the analysis of our cross-section TEM samples was extended to a few  $\mu\text{m}$ s in order to have representative statistics on indium composition and quantum well thickness.

Thanks to this method, we have been able to reveal that in our standard growth processes (low temperature  $\text{In}_x\text{Ga}_{1-x}\text{N}$  quantum well growth and high temperature GaN barrier growth), strong in-plane thickness variations of the  $\text{In}_x\text{Ga}_{1-x}\text{N}$  quantum wells are present. These variations can be useful for some applications because it induces a modulation of the energy potential in the quantum well plane and as a consequence provides localization centers for carriers. This localization can be beneficial to increase the radiative efficiency in a material with a large dislocation density. But in other applications (such as lasers) where the spectral purity is important, these variations have to be avoided. We have then studied the impact of different capping processes of the  $\text{In}_x\text{Ga}_{1-x}\text{N}$  quantum wells before the GaN barrier growth: low or high growth temperature, GaN or AlGa<sub>N</sub> capping layer. Our results clearly show that using a low temperature cap layer, GaN or AlGa<sub>N</sub>, of the  $\text{In}_x\text{Ga}_{1-x}\text{N}$  quantum well results in a homogenization of the in-plane quantum well thickness. The conclusion regarding the photoluminescence efficiency of  $\text{In}_x\text{Ga}_{1-x}\text{N}$  QWs capped by GaN or Al<sub>γ</sub>Ga<sub>1-γ</sub>N is less clear but we

think that with an appropriate optimization of the Al composition, the thickness and the growth conditions of the  $\text{Al}_y\text{Ga}_{1-y}\text{N}$  layer is a good way to obtain high photoluminescence efficiency at long wavelength. This is also supported by the very recent results of Toshiba: by using  $\text{In}_x\text{Ga}_{1-x}\text{N}$  QWs capped with  $\text{Al}_y\text{Ga}_{1-y}\text{N}$  they were able to demonstrate high efficiency yellow and red light emitting diodes (Shinji Saito *et al* 2013 *Appl. Phys. Express* **6** 111004, Jong-Il Hwang *et al* 2014 *Appl. Phys. Express* **7** 071003).

One of the main issues regarding  $\text{In}_x\text{Ga}_{1-x}\text{N}$  quantum wells with a large indium composition is the formation of extended defects. We have found that in structures containing  $\text{In}_x\text{Ga}_{1-x}\text{N}/\text{GaN}$  MQWs with relatively high indium composition ( $> 18\%$ ) and thickness ( $> 3.5$  nm),  $\langle a \rangle$  type threading dislocations are generated from the  $\text{InGaN}$  QWs. These defects are not significantly relaxing the strain of the epilayers but have a negative effect on the room temperature photoluminescence efficiency of the  $\text{In}_x\text{Ga}_{1-x}\text{N}/\text{GaN}$  MQWs. We have discussed the origin of such additional dislocations and concluded that it is probably due to indium-rich clustering and/or point defect formation which occur during the QW growth in our samples. Unfortunately, we could not provide strong evidence for these hypotheses. Two possibilities may be considered to support the formation of indium-rich clusters near the origin of additional threading dislocations. The multiplication of observed samples would increase the probability to intercept such regions in the investigated volume. On the other hand, site specific-TEM preparation would allow us to be sure to observe the places where additional dislocations are formed. Nevertheless, it will be difficult to definitively conclude about the presence of clusters if their size is nanometric or sub-nanometric.

We have observed that it was possible to decrease the dislocation density by increasing the growth temperature of the  $\text{In}_x\text{Ga}_{1-x}\text{N}$  quantum well. But this induces a decrease in the indium composition and in order to avoid a blue-shift of the QW emission energy, we have to increase the QW thickness. This is not a perfect solution since in this case, we have wider QWs and then the oscillator strength of the optical transition is reduced due to the quantum confined Stark effect. Actually, there is no ideal solution to get high efficiency  $\text{In}_x\text{Ga}_{1-x}\text{N}$  quantum wells emitting at long wavelength: a compromise has to be found between the  $\text{In}_x\text{Ga}_{1-x}\text{N}$  material quality (growth temperature) and the quantum well thickness. To go further, a way would be to increase the indium composition while keeping a (relatively) high growth temperature. However, the indium composition is limited by the solubility limit of indium in GaN. In order to go beyond this limit we have to use specific growth conditions far from thermodynamic equilibrium. For example, larger  $\text{In}_x\text{Ga}_{1-x}\text{N}$  growth rates can be used. The other advantage of a larger growth rate is also to limit the effect of indium surface segregation. However, we can anticipate that there will be a maximum limit for the growth rate due to  $\text{In}_x\text{Ga}_{1-x}\text{N}$  material degradation at high growth rate and again a compromise has to be found. One other possibility which has been proposed to increase the indium composition in  $\text{In}_x\text{Ga}_{1-x}\text{N}$  layers is to increase

of the pressure in the reactor. The polish company TOPGaN is working on this subject but the first results obtained are mixed and depend on the reactor which is used (Mike Leszczynski, private communication).

Finally, we want to point out that the internal quantum efficiency of  $\text{In}_x\text{Ga}_{1-x}\text{N}/\text{Al}_y\text{Ga}_{1-y}\text{N}$  depends on the optimization of many different parameters: growth conditions, structure (In and Al compositions, layer thicknesses), capping layers, quantum confined Stark effect. For long wavelength emission (yellow, red), there is no ideal solution due to material limitations and a compromise has to be found between all these parameters. In this thesis, we hope to have contributed to establish some general rules useful for the optimization of these parameters.



## Conclusion et perspective

Dans ce travail de thèse, nous avons étudié des structures multi puits quantiques (MPQs) formées d'empilements de couches  $\text{In}_x\text{Ga}_{1-x}\text{N}/(\text{Al})\text{GaN}$ . L'objectif final de cette étude étant d'obtenir une émission lumineuse intense dans la zone spectrale du vert-jaune. Nous avons aussi essayé de comprendre les mécanismes de formation des défauts et tenté d'identifier clairement les meilleures conditions de croissance permettant d'obtenir une telle émission lumineuse.

Pour avoir une émission dans le jaune avec un empilement  $\text{In}_x\text{Ga}_{1-x}\text{N}/\text{GaN}$  (MPQs) une concentration importante d'indium et/ou des puits relativement épais de  $\text{In}_x\text{Ga}_{1-x}\text{N}$  sont nécessaires. Théoriquement, il est plus avantageux d'utiliser des PQs relativement fins avec une concentration élevée d'indium afin de limiter la diminution (due à l'effet Starck confiné quantique) de la force d'oscillateur associé aux transitions optiques.

D'un point de vue pratique, la situation est plus compliquée qu'il n'y paraît. En effet, nous fûmes confrontés à des difficultés liées au matériau, et plus particulièrement à la croissance des couches d' $\text{In}_x\text{Ga}_{1-x}\text{N}$  avec une forte composition en indium sur des couches de GaN (contraintes élevées, dépôt à basse température pour obtenir une plus forte composition en indium). Nous avons principalement utilisé dans ces travaux de thèse des techniques de microscopie électronique à transmission (MET) pour analyser les propriétés structurales de nos échantillons. Cela nous a permis de rassembler les informations nécessaires à la détermination par des méthodes d'analyses quantitatives des épaisseurs et des compositions des couches. Nous avons confrontés ces résultats de manière systématique avec ceux obtenus par photoluminescence afin de pouvoir optimiser la réalisation de nos échantillons. Cette corrélation n'est pas évidente. En effet l'échelle de grandeur typique des analyses MET est de l'ordre de la centaine de nanomètres. Tandis que dans le cas de la photoluminescence, l'échantillon est analysé sur une surface beaucoup plus grande se situant au-delà de  $1 \mu\text{m}^2$ . Par conséquent, pour avoir des valeurs statistiques représentatives de la composition en indium et de la taille des puits quantiques, l'analyse des échantillons sur leur section par MET a été étendue à quelques micromètres.

Grâce à cette méthode, nous avons été capables de montrer que dans nos conditions de croissance standards (croissance des puits quantiques d' $\text{In}_x\text{Ga}_{1-x}\text{N}$  à basse température et croissance de la barrière GaN à température élevée), des fluctuations importantes de l'épaisseur des puits quantiques  $\text{In}_x\text{Ga}_{1-x}\text{N}$  apparaissent dans le plan de croissance. Ces fluctuations peuvent être utiles pour certaines applications car elles induisent une modulation de l'énergie potentielle dans le plan de croissance des puits quantiques, fournissant de ce fait des centres de localisation pour les porteurs de charges. Cette localisation peut être bénéfique car elle favorise l'augmentation de l'efficacité radiative dans un matériau présentant une densité de dislocations élevée. En revanche, pour d'autres applications (comme les lasers) où la pureté spectrale est importante, ces fluctuations doivent être évitées.

Nous avons étudié ensuite l'impact des différents procédés de protection des puits quantiques en  $\text{In}_x\text{Ga}_{1-x}\text{N}$  avant la croissance de la couche barrière en GaN : influence de la température,

utilisation de GaN ou d'AlGaIn comme matériau pour la couche de protection. Nos résultats montrent clairement que l'utilisation d'une couche de protection déposée à basse température, en GaN ou en AlGaIn, résulte en une homogénéisation de l'épaisseur des puits quantiques en  $\text{In}_x\text{Ga}_{1-x}\text{N}$  dans le plan de croissance. La conclusion en ce qui concerne l'efficacité de la photoluminescence pour des PQs d' $\text{In}_x\text{Ga}_{1-x}\text{N}$  protégés par une couche en GaN ou en  $\text{Al}_y\text{Ga}_{1-y}\text{N}$  est moins claire. Mais nous pensons qu'en optimisant la concentration en Al, l'épaisseur et les conditions de croissances, l'utilisation d'une couche de couverture  $\text{Al}_y\text{Ga}_{1-y}\text{N}$  est une bonne méthode pour atteindre une haute efficacité de photoluminescence à des longueurs élevées d'ondes (vert-jaune). Cette hypothèse est soutenue par des résultats publiés récemment par Toshiba : en utilisant des PQs d' $\text{In}_x\text{Ga}_{1-x}\text{N}$  recouvert avec de l' $\text{Al}_y\text{Ga}_{1-y}\text{N}$ , des diodes électroluminescentes avec une efficacité importante dans le jaune et dans le rouge ont été démontrées (Shinji Saito et al. 2013 Appl. Phys. Express 6 111004, Jong-Il Hwang et al. 2014 Appl. Phys. Express 7 071003).

Un des problèmes essentiels concernant les puits quantiques d' $\text{In}_x\text{Ga}_{1-x}\text{N}$  avec une forte composition d'indium est la formation de défauts étendus. Nous avons trouvé que dans une structure de PQs d' $\text{In}_x\text{Ga}_{1-x}\text{N}/\text{GaN}$  avec une composition en indium relativement élevée (>18%) et d'épaisseur importante (>3.5 nm) des dislocations traversantes de type <a> sont générées à partir des PQs d' $\text{InGaIn}$ . Ces défauts ne relaxent pas significativement les contraintes dans la couche mais ils ont un effet négatif sur l'efficacité de la photoluminescence des PQs d' $\text{InGaIn}$  à température ambiante. Nous avons aussi discuté l'origine de ce type de dislocation et nous en avons déduit qu'ils proviennent probablement de la formation d'îlots riches en indium et/ou de la formation de défauts ponctuels qui apparaissent dans les PQs lors de la croissance. Malheureusement, nous n'avons pas été capables de montrer directement une preuve expérimentale de ces suppositions. Deux pistes de travail sont à considérer pour renforcer l'hypothèse se basant sur le fait que la formation de d'îlots riches en indium est à l'origine de la formation de ces dislocations traversantes additionnelles. D'une part, l'augmentation du nombre d'échantillons observés pourrait augmenter significativement la probabilité d'observer une de ces régions. D'autre part, une préparation MET localisée pourrait aussi nous permettre de nous assurer que l'on observe bien les endroits où ces dislocations additionnelles sont formées. Néanmoins, il sera épineux de conclure de manière péremptoire sur la présence d'îlots riches en indium et de déterminer si leurs tailles est de l'ordre nanométrique ou sous-nanométrique.

Nous avons observé qu'il est possible de réduire la densité de dislocations en augmentant la température de croissance des PQs d' $\text{In}_x\text{Ga}_{1-x}\text{N}$ . Mais cela induit une réduction de la concentration d'indium, et pour éviter un décalage vers le bleu de l'émission des PQs, il faut donc augmenter l'épaisseur des PQs. Ceci n'est pas la meilleure des solutions, car des PQs plus larges entraîneront une réduction (due à l'effet Stark de confiné quantique) de la force d'oscillateur des transitions optiques. En fait, il n'y a pas de solution idéale pour obtenir des PQs d' $\text{In}_x\text{Ga}_{1-x}\text{N}$  avec une efficacité élevée et qui émettent à des longueurs d'ondes importantes (vert-jaune): un compromis doit être trouvé entre la qualité du matériau d' $\text{In}_x\text{Ga}_{1-x}\text{N}$  (température de croissance) et l'épaisseur des PQs. Pour aller plus loin, on peut proposer d'augmenter la concentration d'indium en gardant la température de croissance

(relativement) élevée. Cependant, la composition en indium est limitée par la solubilité maximale de l'indium dans le GaN. Pour passer outre cet écueil, il faut utiliser des conditions de croissances spécifiques situées loin de l'équilibre thermodynamique. Par exemple, l'augmentation des vitesses de croissance d' $\text{In}_x\text{Ga}_{1-x}\text{N}$  peut être mise en œuvre. L'autre intérêt de l'augmentation des vitesses de croissance est de permettre de limiter l'effet de ségrégation de surface de l'indium. Néanmoins, nous pouvons anticiper la présence d'une limite maximum à l'augmentation vitesses de croissance en raison de la dégradation de la qualité du matériau d' $\text{In}_x\text{Ga}_{1-x}\text{N}$  lors de l'utilisation de vitesses de croissances élevées. A nouveau un compromis devra être trouvé.

Une solution alternative qui a été proposé pour augmenter la concentration d'indium dans les couches d' $\text{In}_x\text{Ga}_{1-x}\text{N}$  est d'augmenter la pression à l'intérieur du réacteur de croissance. L'entreprise polonaise TOPGaN travaille sur ce sujet mais les premiers résultats obtenus ne permettent pas de conclure et, de plus, dépendent du type de réacteur utilisé (Mike Leszczynski, communication privée).

Finalement, nous tenons à souligner que l'efficacité quantique interne des empilements  $\text{In}_x\text{Ga}_{1-x}\text{N}/\text{Al}_y\text{Ga}_{1-y}\text{N}$  dépend de l'optimisation de plusieurs paramètres différents: conditions de croissance, structure (composition en In et Al, épaisseur des couches), couche de protection, effet Stark confiné quantique. Pour les émissions à des longueurs d'ondes élevées (jaune, rouge), il n'y a pas une solution idéale en raison des limitations dues au matériau, en conséquence un compromis doit être trouvé entre tous les paramètres précédents. Dans cette thèse, nous espérons avoir réussi à contribuer de manière significative à l'établissement de règles générales et utiles dans le but d'optimiser ces différents paramètres.



## Appendix

### Derivation of some equations presented in section 1.3.1

In chapter 1, we have discussed that depending on the cs-TEM sample thickness, the sample may become either in bi-axial stress or uni-axial stress state (Figure 1-10 of chapter 1), thus considering the growth direction of our sample along Z axis, we derive some important equations used in section 1.3.1 following Hooke's law.

The Hooke's law allows us to relate the crystal stress to that of the crystal strain as follows:

$$\vec{\sigma} = C \cdot \vec{\epsilon} \quad (1)$$

where  $\vec{\sigma}$  and  $\vec{\epsilon}$  are stress and strain tensors and C is the elastic coefficient tensor. Using Voigt notation for hexagonal crystal system, we can expressed equation (1) as follows:

$$\vec{\sigma} = \begin{bmatrix} \sigma_{xx} \\ \sigma_{yy} \\ \sigma_{zz} \\ \sigma_{yz} \\ \sigma_{zx} \\ \sigma_{xy} \end{bmatrix} = \begin{bmatrix} C_{11} & C_{12} & C_{13} & 0 & 0 & 0 \\ C_{12} & C_{11} & C_{13} & 0 & 0 & 0 \\ C_{13} & C_{13} & C_{33} & 0 & 0 & 0 \\ 0 & 0 & 0 & C_{44} & 0 & 0 \\ 0 & 0 & 0 & 0 & C_{44} & 0 \\ 0 & 0 & 0 & 0 & 0 & C_{66} \end{bmatrix} \cdot \begin{bmatrix} \epsilon_{xx} \\ \epsilon_{yy} \\ \epsilon_{zz} \\ \epsilon_{yz} \\ \epsilon_{zx} \\ \epsilon_{xy} \end{bmatrix} \quad (2)$$

where  $\sigma_{ij}$  is stress tensor,  $\epsilon_{ij}$  is strain tensor and  $C_{ij}$  is stiffness tensor.

#### For bi-axial stress state:

From equation (2), we can write stress along growth direction (Z-axis) as,

$$\sigma_{zz} = C_{13}\epsilon_{xx} + C_{13}\epsilon_{yy} + C_{33}\epsilon_{zz} \quad (3)$$

Considering the sample in bi-axial stress state, i.e, strain along in-plane directions are equal ( $\epsilon_{xx} = \epsilon_{yy} = \epsilon$ ) and the stress along growth direction is zero ( $\sigma_{zz} = 0$ ), we can re-write equation (3) as,

$$0 = C_{13}\epsilon_{xx} + C_{13}\epsilon_{xx} + C_{33}\epsilon_{zz}$$

$$\text{Or,} \quad C_{33}\epsilon_{zz} = -2C_{13}\epsilon_{xx}$$

$$\text{Thus,} \quad \epsilon_{zz} = \frac{-2C_{13}\epsilon}{C_{33}} \quad \text{[Equation 1.7 of chapter 1]} \quad (4)$$

Similarly, the stress along any in-plane direction (X or Y axis) can be expressed from equation (2) as:

$$\sigma_{xx} = \sigma_{yy} = C_{11}\varepsilon_{xx} + C_{12}\varepsilon_{yy} + C_{13}\varepsilon_{zz} \quad (5)$$

Putting the expression of  $\varepsilon_{zz}$  from equation (4) into equation (5), we can re-write the equation (5) as:

$$\sigma = \left( C_{11} + C_{12} - \frac{2C_{13}^2}{C_{33}} \right) \varepsilon \quad \text{[Equation 1.6 of chapter 1]} \quad (6)$$

where,  $\varepsilon_{xx} = \varepsilon_{yy} = \varepsilon$  and  $\sigma_{xx} = \sigma_{yy} = \sigma$  has been considered.

We may consider the relaxed lattice parameters of InGaN layer as  $a_0$  and  $c_0$ , whereas the lattice parameters for GaN layer are  $a$  and  $c_{GaN}$  along in-plane and out of plane direction, respectively. Now considering the pseudomorphic growth of InGaN as epilayer on top of GaN substrate layer, the in plane lattice parameter of the epilayer becomes equal to that of substrate in plane lattice parameter, as illustrated in Figure 1.

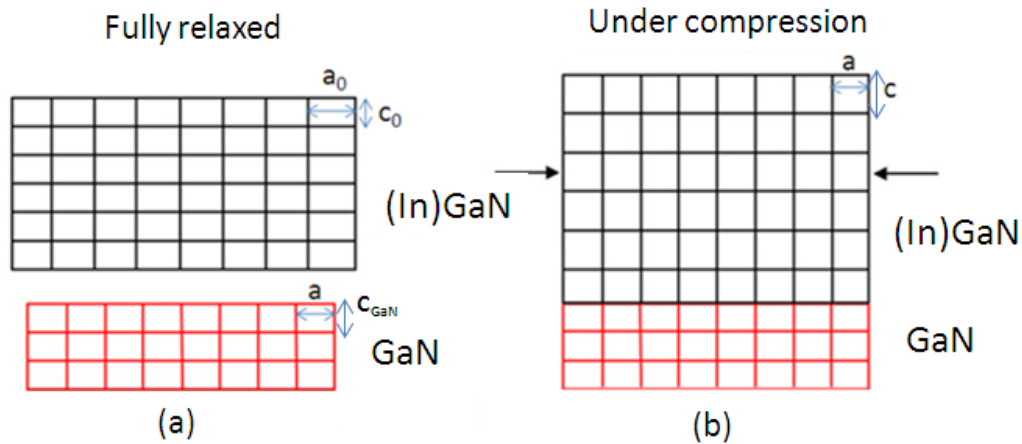


Figure 1: Schematic diagram showing (a) the fully relaxed InGaN and GaN layers and (b) the strained InGaN layer due to pseudomorphic growth on top of GaN layer.

Thus the strain along growth direction (Z-axis) can be expressed as:

$$\varepsilon_{zz} = \frac{c - c_0}{c_0} \quad (7)$$

where,  $c$  is the out of plane lattice parameter of strained epilayer.

And the strain along in-plane directions can be expressed as:

$$\varepsilon_{xx} = \varepsilon_{yy} = \varepsilon = \frac{a-a_0}{a_0} \quad (8)$$

Thus, putting the in-plane and out of plane strain expressions from equations (7) and (8) into equation (4), we can have:

$$\frac{c-c_0}{c_0} = -\frac{2C_{13}}{C_{33}} \left( \frac{a-a_0}{a_0} \right) \quad (9)$$

Thus after rearranging this equation (9), we obtain the expression as:

$$c = c_0 \left[ 1 - \frac{2C_{13}}{C_{33}} \left( \frac{a-a_0}{a_0} \right) \right] \quad \text{[Equation 1.9 of chapter 1]} \quad (10)$$

### For uni-axial stress state:

As we discussed in section 1.3.1 that in case of uni-axial stress state, in addition to the growth direction, the epilayer becomes stress free along one in-plane direction due to sample thickness. Here we have considered the sample to become stress free along e-beam direction (Y axis) as illustrated in Figure 1-10 in chapter 1. Thus we can write for uni-axial stress state case:

$$\sigma_{zz} = \sigma_{yy} = 0 \quad (11)$$

From equation (2) we can express the stresses as:

$$\sigma_{yy} = C_{12}\varepsilon_{xx} + C_{11}\varepsilon_{yy} + C_{13}\varepsilon_{zz} \quad (12)$$

$$\sigma_{zz} = C_{13}\varepsilon_{xx} + C_{13}\varepsilon_{yy} + C_{33}\varepsilon_{zz} \quad (13)$$

However, for uni-axial stress state condition, the strain along in-plane directions are not equal as stress are different in two directions, i.e.,  $\varepsilon_{xx} \neq \varepsilon_{yy}$ .

Thus, we can re-write equation (12) as:

$$0 = C_{12}\varepsilon_{xx} + C_{11}\varepsilon_{yy} + C_{13}\varepsilon_{zz}$$

$$\text{Or, } \varepsilon_{yy} = \frac{-C_{12}\varepsilon_{xx} - C_{13}\varepsilon_{zz}}{C_{11}} \quad (14)$$

Now putting this expression of  $\varepsilon_{yy}$  from equation (14) into equation (13), we will get

$$0 = C_{13}\varepsilon_{xx} + C_{13} \left[ \frac{-C_{12}\varepsilon_{xx} - C_{13}\varepsilon_{zz}}{C_{11}} \right] + C_{33}\varepsilon_{zz}$$

$$\text{Or, } 0 = \varepsilon_{xx} \left( C_{13} - \frac{C_{12}C_{13}}{C_{11}} \right) - \frac{C_{13}^2}{C_{11}}\varepsilon_{zz} + C_{33}\varepsilon_{zz}$$

$$\text{Or, } \varepsilon_{zz} = \frac{\left[ \frac{C_{13} - C_{12}C_{13}}{C_{11}} \right]}{\left[ \frac{C_{13}^2}{C_{11}} - C_{33} \right]} \cdot \varepsilon_{xx}$$

$$\text{Or, } \varepsilon_{zz} = \frac{-C_{13}(C_{11} - C_{12})}{C_{11}C_{33} - C_{13}^2} \cdot \varepsilon_{xx} \quad \text{[Equation 1.8 of chapter 1]} \quad (15)$$

Thus again putting expression of  $\varepsilon_{zz}$  and  $\varepsilon_{xx}$  from equation (7) and (8), respectively into equation (15), we can re-write the equation (15) as:

$$\frac{c - c_0}{c_0} = \left[ \frac{-C_{13}(C_{11} - C_{12})}{C_{11}C_{33} - C_{13}^2} \right] \cdot \left( \frac{a - a_0}{a_0} \right)$$

Or,

$$c = c_0 \left[ 1 - \left\{ \frac{C_{13}(C_{11} - C_{12})}{C_{11}C_{33} - C_{13}^2} \right\} \cdot \left( \frac{a - a_0}{a_0} \right) \right] \quad \text{[Equation 1.10 of chapter 1]} \quad (16)$$

Thus, we have derived some important equations that are presented in chapter 1 (as indicated in bold letters) and used in this work.

